2021

# Tension Propagation Along Tip-Link Cadherins: Regulation and Implications for the Auditory System

Daniel M. Firester


# TENSION PROPAGATION ALONG TIP-LINK CADHERINS: REGULATION AND IMPLICATIONS FOR THE AUDITORY SYSTEM

A Thesis Presented to the Faculty of
The Rockefeller University
in Partial Fulfillment of the Requirements for
the degree of Doctor of Philosophy

by
Daniel M. Firester
June 2021

# Tension Propagation Along Tip-Link Cadherins: Regulation and Implications for the Auditory System

Daniel M. Firester, Ph.D.
The Rockefeller University 2021

Hair bundles detect sound by shearing in response to vibrations spanning orders of magnitude in intensity and frequency. Their responsiveness stems from mechanosensitive ion channels that sit atop the stereocilia and are gated by tension in tip links. Experimental evidence and theoretical arguments implicate a soft compliant element, with a stiffness of 1-4 mN/m, as necessary for mechanotransduction. Although the identity of this element remains an open question, direct measurements of a component of the tip link have highlighted entropic elasticity as one relevant characteristic.

A tip link comprises a heterotetremer of protocadherin-15 and cadherin-23, arranged in a loose helical configuration and joined at their amino-terminals through a calcium ion-dependent interaction. As for many other biopolymers, the tip link's stiffness is several times greater than that of the empirically measured gating spring. To remain a viable candidate as a compliant element, entropic elasticity in the tip link must therefore be shown to support the full frequency and intensity range of auditory stimuli.

In the present work, we model the tip link as a worm-like chain and evaluate its fast dynamic response using theoretical and numerical calculations. Our analysis uncovers frequencies at which the tip link exhibits viscoelastic behavior, and we evaluate how this behavior might alter auditory function. Critical to modulating the tip link's frequency-dependent response is the resting tension, which controls both the frequency above which the tip link behaves viscoelastically and the tip-link's local nonlinear stiffness. Under low resting tensions, we find that tension pools at the ends of the tip link and propagates poorly into the bulk of the chain. Upon application of high resting tensions, the frequency above which the tip link shows non-equilibrium behavior shifts beyond the range of human hearing.

*To my family and my parents, who practice wisdom and humanity in all aspects of life*

*To Caroline, my foundation and inspiration, who brings me ceaseless joy in the humblest of times*

*To my brother Jesse, whose perseverance in the face of difficulty is of everlasting marvel*

## Acknowledgements

The path to this point has been marred with pitfalls, bumps, quicksand, and all other matter of obstacle. Without those who have remained at my side, I surely would have stumbled to my demise a thousand times over. This work could not have been completed without their unwavering support, love, patience, kindness and understanding. In turn I must thank them, though the words are sure to fail to describe the magnitude of their importance and contribution therein.

First and foremost, I must thank my family for their steadfast support in times of both difficulty and success. My parents, Sharon and Glenn, have helped guide me every step of the way, and will always be figures I look to for wisdom and advice. Their patience and understanding is unmatched, and they have always responded to adversity with kindness and humanity. Their unending support of my brother serves as a constant reminder of how dedicated they are to our family, no matter the challenges. I also owe my aunts, Gwen and Cindy, unfathomable gratitude for their instrumental role in my upbringing, and for the countless joy-filled summers spent reflecting by the shore. They always ask questions that cut to the heart of the matter, and they remain figures I can rely on in times of need.

My interest in science began when I worked at the now historical St. Vincents Hospital, which inspired in me the desire to pursue a career in science. Through the careful guidance of Dr. Patricia Walker, I embarked on my first informal research project, and shadowed doctors who treated patients with Cystic Fibrosis. My experience at St. Vincents marked the first turning point in my professional career, and helped foster my enthusiasm for science. Dr. Walker's professionalism and level of care for her patients remains a standard to which I strive to replicate, and her never-ending patience and enthusiasm I hold in utmost esteem.

I am thankful to have had excellent mentorship and guidance in my undergraduate career. In particular, I must thank Dr. Robert Leheny at the physics department of Johns Hopkins, whose lab I worked in during my sophomore through senior years. I owe much of my current position to Bob, who helped build the foundation of my scientific knowledge and who shaped

my understanding of the physical world. Bob was a mentor who passed no judgment, and whose encouragement allowed me to thrive and always remain inquisitive. I must also thank the two graduate students I worked under; Joel Rovner, who helped me launch my research career, and later Daniel Allen, who made the late nights and countless hours of research so lighthearted, yet instructive. Daniel would never shy away from discussing any manner of scientific problem, and I will always remember the countless hours we whittled away programming in Python or solving a problem on the whiteboard. I owe additional thanks to Dr. Doug Barrick and Dr. Karen and Patrick Fleming at the Biophysics department, who encouraged me to pursue a doctorate degree no matter the destination.

My arrival at Rockefeller was a return home of sorts, as I had passed by the gates countless times as a child. Within I found an unrivaled scientific community, and I have since had the pleasure to work with many fantastic scientists. When I first joined Jim's lab, I was welcomed with enthusiasm by two students, Josh Salvi and Julien Azimzadeh, who were instrumental my training. Josh and Julien were always there to answer the most trivial of questions, and their scientific insight and thoughtful experimental design was nothing short of inspirational. I must also give a special thanks to Brian Fabella, who spent many hours helping lift my project off the ground, and who acted as my moral support through the hardest years of graduate career. I would be remiss to not mention the others in the lab who I frequently conversed and worked with, including Corstiaen, Yuttana, Sanjee, Andrew, Agnik, Anna E. and Anna K., Nathaniel, Aaron, Felicitas, Gogui, Florian, and more recently Ahmed, Caleb, and Yuval. I must also thank Camila Villesante, who first joined the lab last year and brought a good deal of lighthearted fun into the drudgery of sample preparation. Thank you for always humoring my rants about physics, or bread, or whatever else it is that has captured my attention for the day.

My sincerest thanks goes to Tobias Bartsch, whose contribution to the work within these pages cannot possibly be understated. I had known Tobias for many years when I changed projects, and was always in awe of his work ethic and dedication to science. He is not

only one of the most brilliant, hardworking individuals I have ever met, but he is kind and forgiving, and brings humor to the most stressful of situations. And in the darkest years of my graduate career, Tobias' door was always open. I was honored to work with Tobias, and am forever indebted to his mentorship in charting my course over the past years.

Of utmost importance I must thank my mentor, Dr. Jim Hudspeth, for his continued belief in me even when I was unable to see a path forward. Jim is a man of unrivaled scientific and intellectual integrity, and an inspiration to all who have ever had the opportunity to hear him speak. His breadth of knowledge is unmatched, and the rapid-fire pace at which he processes and generates ideas is, quite frankly, frightening. But Jim is kind as well, and even when I doubted my own abilities, Jim never stopped encouraging me to push forward. I cannot possibly count the hours I spent in his office discussing science, bread, family, and all manner of topic, and I thank him for his continued kindness and understanding. I am greatly honored to have had the opportunity to work with Jim over these past years.

I must also thank my past committee member, Vanessa Ruta, and current committee members, Stanislas Leibler, Marcelo Magnasco, and Alipasha Vaziri, for their dedication to the project and for pruning away my forest of ideas to keep me focused. In addition, the graduate school would not function without the continued dedication of the deans Emily Harms and Sid Strickland, as well as Cristian Rosario, Stephanie Fernandez, and Kristen Cullen. I must also thank Marcos Sotomayor for serving as my external examiner.

Finally, to Caroline, who has grounded me and kept me sane these past several years. Caroline's humility and kindness belie her absolute brilliance, and I could not have completed a fraction of the work enclosed without her continued love and support. She encourages in me exploration and confidence, and has stood by me when I needed her most. Without her I would have spent the last several years never leaving the city, and would have missed out on some of the greatest experiences of my life. She brings out the very best in me.

# TABLE OF CONTENTS

# List of Figures

# Chapter 1: Mechanics of Hearing

The auditory system is a marvel of biophysics. Through the detection of environmental stimuli that ranges in orders of magnitude in frequency and intensity, its job is to decompose longitudinal pressure waves into transmissible electrical signals that are sent through the auditory nerve into the cochlear nuclei, where they are further processed before ultimately being sent to higher-order areas of the brain. This process results in the sensation of sound. Studies suggest fine-tuning at every level of the auditory pathway, from optimal propagation of energy through the middle ear, to passive tonotopic separation of frequencies along the basilar membrane, to active processes within the mechanoreceptive cells that amplify and tune signals, and finally to higher-order processing of neural signals within the brain [1, 2, 3, 4]. Before sounds are even converted to electrical signals, passive and active processes within the middle and inner ear act to tune and regularize the response, making further deconvolution of complex auditory sensation a significantly less intensive neural task. This is for a good reason - sound is perhaps the most useful stimulus for detecting threats necessary for survival, and the auditory system has consequently evolved for efficiency and speed.

Detection of sound underlies nearly every aspect of life. We owe our enjoyment of musical melodies, our ability to verbally communicate, and our fast reaction time to environmental

noises and vibrations all to the auditory system. Our ability to remain upright and balanced, preform acrobatic feats, and visually track targets while in motion we likewise owe to the closely associated vestibular system. Long has the scientific community searched for the sources responsible for the empirically observed acuity of hearing. For instance, humans are capable of detecting signals that vibrate the eardrum by no more than the width of a hydrogen atom, corresponding to energy on the order of thermal fluctuations themselves [5, 6]. Despite such high sensitivity, the dynamic range of the auditory system still spans a trillion-fold change in acoustic power, allowing us to perceive both the rustle of grass and the boom of celebratory fireworks [7]. And temporal performance is no less impressive. From 20 Hz to 20 kHz, trained musicians may distinguish tones separated by a 0.1% difference in frequency [8]. In fact, human resolution of frequency and temporal changes is up to a factor of ten more exact than values predicted by the Fourier uncertainty principle [9]. These tremendous feats have long begged explanation.

In this chapter we discuss the anatomy of the auditory system and its functional processes, including the active process of the sensory cells and the central role of filamentous tip links in mechantransduction. In particular we focus on the role of the gating spring in transducing motion into graded force signals. We continue with a review of the structure of tip links and their known properties; we discuss some recent crystallographic studies on the structure of linked cadherin domains, as well as high-precision optical trapping experiments that implicate entropic elasticity as a significant contribution in at least one tip-link-constituent's mechanical response.

## 1.1 Sound Transmission and Basilar-Membrane Mechanics

Sound and acceleration are detected through fluid motion in the cochlea and associated vestibular organs. The process by which this occurs begins at the level of the external ear - involved in sound collection and phase detection - and ends at the hair cells, the sensory cells of the auditory system. To begin, longitudinal pressure waves are collected by the external ear and enter the auditory canal where they impinge upon the tympanic membrane, evoking oscillations of the tympanum as small as 1 pm at the threshold of hearing [5]. Vibration of the tympanic membrane sets into motion the three ossicles in the middle ear: the maleus, incus, and stapes [10]. Motion of the tympanum is elastically coupled to the arm of the maleus, which acts as a leaver to drive a piston-like motion in the incus and stapes. The stapes is directly coupled to the oval window of the cochlea, and motion in the stapes drives fluid motion in the inner ear. This arrangement of the middle ear allows impedance-matched transmission of pressure waves from air to water, and is further controlled by the stapedius and tensor tympani-muscles of the middle ear involved in the acoustic reflex, which act quickly to attenuate sound transmission at the level of the ossicles [3, 11].

Upon deflection of the stapes, the oval window sets into motion the fluid-filled compartments of the inner ear. The inner ear comprises of several interconnected organs involved in both the detection of auditory stimuli – in the cochlea – and also the detection of acceleration and orientation necessary for balance – in the vestibular system. The vestibular system consists of three semicircular canals – slender ducts through which fluid flows in response to angular acceleration and which are critical to maintaining the integrity of the vestibulo-ocular reflex – and the vestibule – containing the utricle and saccule necessary for detection of linear accelerations. We do not discuss further the vestibular system of the mammal, except to note that the sensory cells on which we focus our discussion are ubiquitous throughout the inner ear, including the vestibular system.

The spiral cochlea contains the primary auditory organ of the mammal, and is involved in detection of sound stimuli ranging in frequency from 20 Hz up to 20 kHz in humans, and even up to 100 kHz in some species such as bats [12, 13]. The cochlea comprises of three fluid-filled compartments: the scala tympani, scala media, and scala vestibuli (Figure 1.1) [14]. Isolation of chambers and integrity of their ionic concentration are maintained through separation by two membranes: Reissner's membrane, which separates the scala vestibuli from the scala media, and the basilar membrane, which separates the scala media from the scala tympani. Ionic concentrations and electric potentials (+80 mV) vary significantly across the chambers - the scala vestibuli and scala tympani are filled with $Na^+$-rich solution (4 mM $K^+$, 130 mM $Na^+$, 2 mM $Ca^{2+}$) at the body's zero potential, and the scala media is filled with $K^+$- rich and $Ca^{2+}$-poor solution (150 mM $K^+$, 2mM $Na^+$, 20 $\mu$M $Ca^{2+}$) at a positive relative potential [15, 16]. Critical to maintaining this so-called endochochlear potential is the stria vascularis, which lines the walls of the scala media and pumps ions necessary to maintain the potential difference [15]. Sandwiched between the scala tympani and scala media, sitting atop the basilar membrane, is the organ of Corti which contains both the sensory hair cells, named for their apical hair-like protrusions into the scala media, and accessory supporting cells [17, 18, 19].

Detection of sound by the cochlea begins with the oscillatory motion of the oval window driven by the piston motion of the stapes, which acts to displace fluid within the cochlea in the form of a long-wavelength pressure wave [3]. These waves travel from the base of the cochlea to the apex within the scala vestibuli, and then through the scala tympani from the apex back to the base. To good approximation the fluid in the cochlea is incompressible, and pressure changes at the oval window must ultimately be relieved at the round window, which sits at the base of the scala tympani.

Pressure differentials within the compartments entrain surface waves along the basilar membrane. These surface waves take the form of traveling waves, which increase in amplitude and decreases in wavelength before reaching a frequency-dependent characteristic point

along the spiral of the cochlea, whereafter they quickly disperse. Gradients in stiffness and mass along the cochlear spiral of the basilar membrane permit this passive frequency decomposition. For instance, the stiffness of the basilar membrane at the base of the cochlea, which is involved in sensation of high-frequency auditory stimuli, is much higher than the stiffness at the apex, which is involved in low-frequency sensation [20]. This remarkable passive frequency deconvolution property of the basilar membrane allows the cochlea to decompose complex auditory stimuli tonotopically for ease of processing by the brain; sounds with similar frequency stimulate similar areas of the cochlea. In this sense, the cochlea is not dissimilar to a player piano, whereby it collects melodies and converts them back to strikes along a keyboard.

Sitting atop the basilar membrane lies the organ of Corti, the primary receptor organ for auditory sensation, which runs the length of the cochlea and contains both supporting cells and mechanoreceptive hair cells, so named for their hair-like protrusions at the apical surface of the cell bodies. This hair-like protrusion is termed the hair bundle [21, 22, 23]. In the mammalian cochlea, hair cells come in two varieties: the outer hair cells, which are thought to be involved in amplification and tuning of stimuli and receive primarily efferent innervation, and the inner hair cells, which primarily receive afferent innervation and are responsible for sending signals to the brain [24]. Homologous structures in other non-mammalian species, such as the *Gekko gecko*'s basilar papilla, have similar divisions between cell types, and the analogous outer hair cells - termed tectorial hair cells in the gecko - receive little to no innervation at all [25].

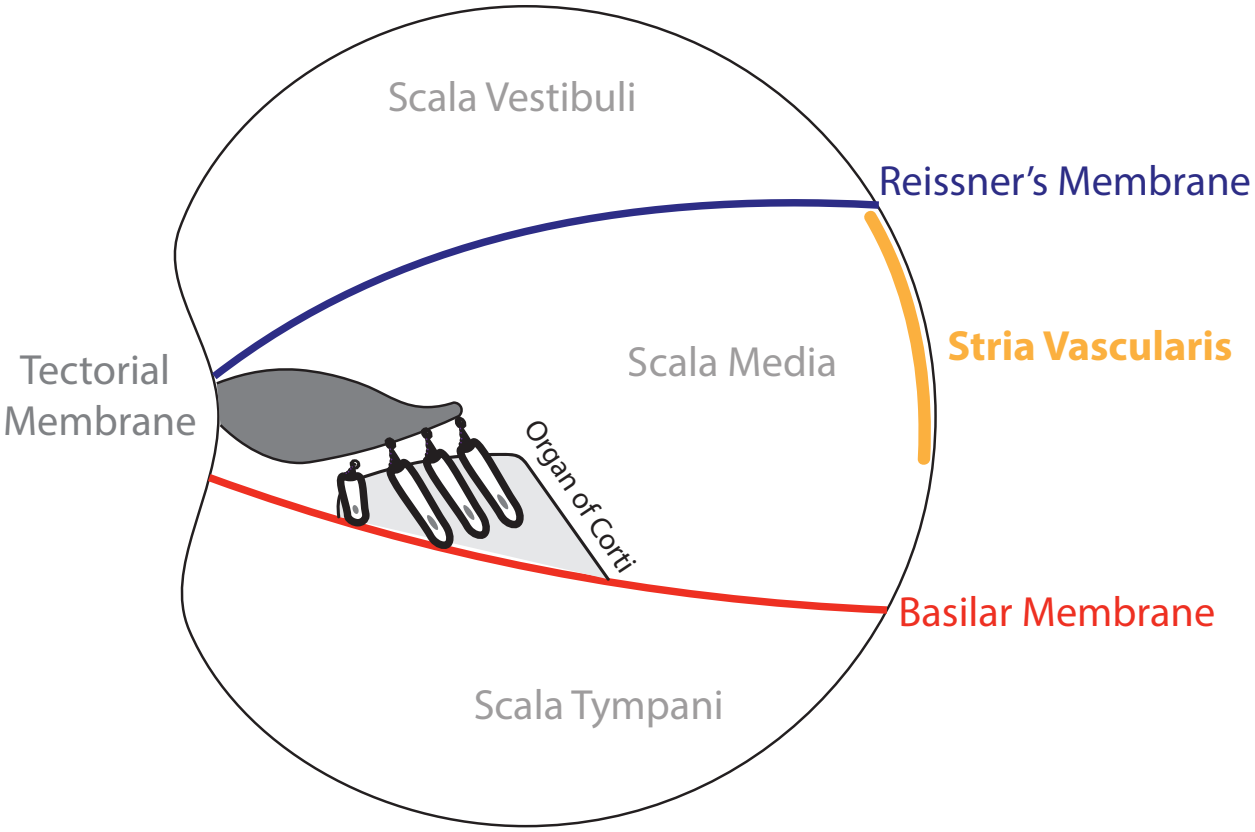


Figure 1.1: **Cross Section of the Cochlea**. A schematic diagram of a cross section of the cochlea, showing the three main fluid-filled compartments: the scala vestibuli, the scala media, and the scala tympani. Dividing the compartments and maintaining their ionic integrity are the Reissner's membrane and the basilar membrane. The stria vascularis lines the scala media and helps maintain the endocochlear potential. Fluid motion induced by motion of the stapes causes the basilar membrane to vibrate, stimulating the hair bundles within the organ of Corti by shearing them with respect to the overlying tectorial membrane. The three outer hair bundles (per characteristic frequency) maintain direct contact with the overlying tectorial membrane, whereas the inner hair bundle is deflected from fluid motion alone.

## 1.2 The Structure and Function of the Hair Bundle

Each hair cell possesses a specialized organelle, the hair bundle, which acts as a mechanoreceptive sensor for the auditory system. Hair bundles not only detect stimuli passively; they also employ strategies to amplify vibrations and offset viscous damping [1, 26, 2]. The hair bundle is composed of tens to over one hundred of actin-filled stereocilia arranged in a staircase-like pattern of increasing heights (Figure 1.2) [27]. Each stereocilium is connected to its next tallest neighbor by a filamentous link, and is attached tightly to the cell body at the cuticular plate where it may rotate with some associated stiffness [28]. Upon deflection towards its taller edge, the distance between the tip of each stereocilium and that of its taller neighbor increases due to a shearing motion of the entire hair bundle (Figure 1.2b). The hair bundle exploits this effect both by positioning mechanoelectrical transduction channels (MET channels) precisely at the tip of each stereocilium, and by tying the MET channel to its adjacent stereocilium through a filamentous polymer termed the tip link. The identity of the transduction channel remains unknown, though several candidate proteins have been suggested as either the channel, or as portions of a larger pore-forming complex [29, 30, 31, 32]. Regardless, deflection of the hair bundle increases tension in the tip links, biases the MET channel towards an open state, and allows an influx of cations into the hair cell and leading to membrane depolarization. The cascade ends at the basolateral surface of the hair cell, which releases neurotransmitter in response to depolarization.

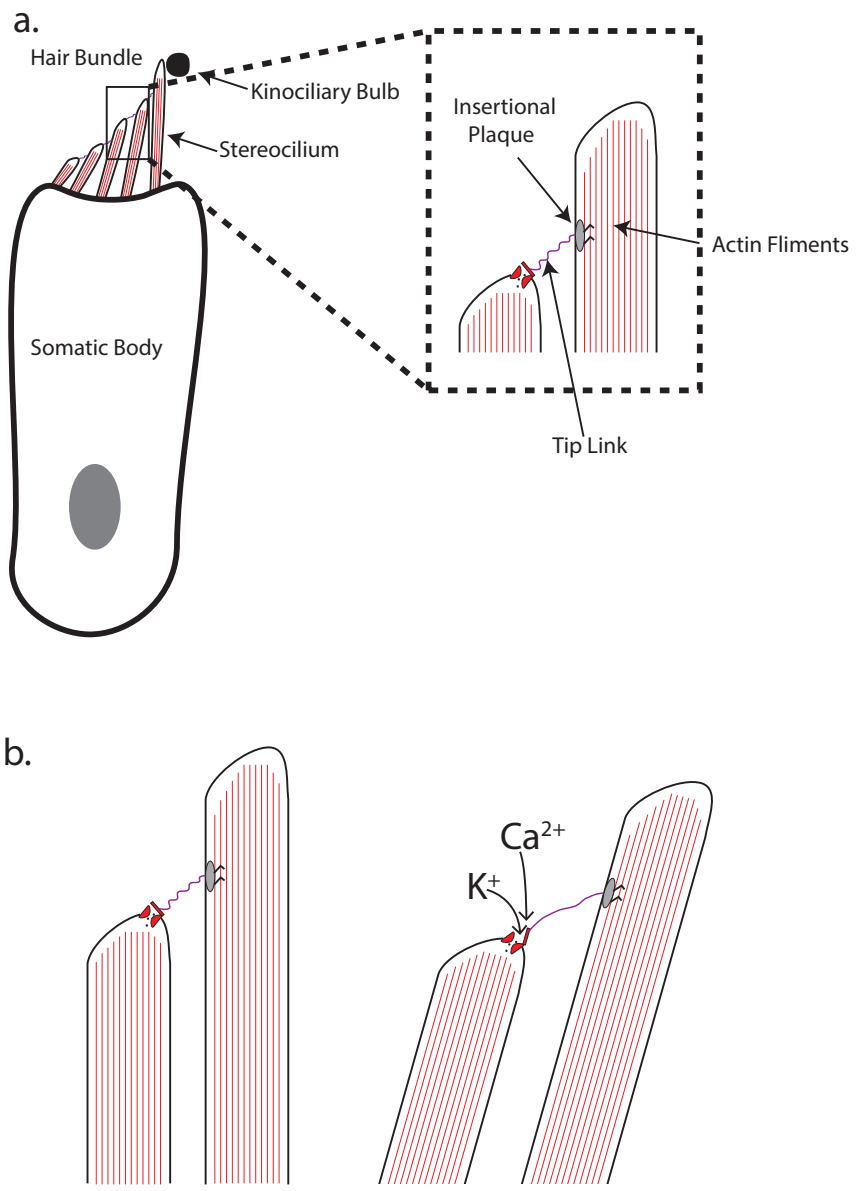


Figure 1.2: **The Hair Cell**. Schematic diagrams of a hair cell and hair bundle found in the sensory organs of the inner ear. In (a), the full hair cell, with actin-filled stereocilia protruding from its apical surface. The stereocilia are of differing heights, and are arranged in a staircase-like pattern from shortest to tallest. At the tallest edge, a true cilium called a *kinocilium*, which may possess a kinociliary bulb in certain species. A closer look at the tips of each stereocilia reveals the mechanoreceptive ion channel, which is linked to the tallest adjacent stereocilium through a filamentous tip link. In (b), as the hair bundle is deflected, the stereocilia pivot about their insertional points, causing an increase in the distance between adjacent stereocilia and increasing tension in the tip link and ion channel. Upon opening, calcium and potassium ions diffuse into the stereocilia.

Central in the role of channel gating is the tip link, which helps transduce force to the MET channel either directly, or through additional components in series with the transduction apparatus. Each tip link forms a helical dimer of dimers, and each dimer is composed of two polymers, cadherin-23 (CDH23) and protocadherin-15 (PCDH15), joined by an "extended handshake" interaction [33]. The basal edge of each tip link is either coupled directly to a component of the MET channel, or to some other intracellular cytoskeletal components [34]. The apical edge is coupled to an upper insertional plaque within the stereocilia, with myosins 1c, 3a, and 7a and other structural proteins such as Harmonin-b implicated as primary constituents [35, 36]. These proteins form a complex which is thought to crawl and slide along the bundled actin filaments and play a key role in adaptation. This provides one convenient method by which the hair bundle may tune the tension in the tip link, and adjust the resultant open probability of the MET channel.

Hair bundles range in length from tens of micrometers down to less than one micrometer [37, 38], and vary depending on characteristic frequency and organ. Hair bundles also change architecture depending on their specific role, from cylindrical shapes in the bullfrog sacculus, to "W" and "U" configurations found in the inner and outer hair bundles of the mammalian cochlea [39, 40]. Although hair-bundle height is correlated inversely with intrinsic frequency, the geometry of the bundle also influences the geometric gain of length change between adjacent stereocilia during deflection. These geometric factors play a pivotal role in transduction of force to the channel, and range in value from 0.14 in the bullfrog's sacculus to 0.06 in the Tokay gecko [41, 25]. While our focus will ultimately be on understanding the mechanics of the mammalian hair bundle, we note that much experimental work to date has been on other, more easily accessible species such as the Tokay gecko [41, 25] or American bullfrog (*Rana catesbeiana*). As such, we will generally refer to experiments that have been conducted in non-mammalian preparations, and fill in details known with regards to the mammalian system where applicable.

## 1.3 The Active Process and Adaptation

Although extensive in vitro and interferometric studies over the past several decades have revealed subtleties in the motion of both the hair bundle and the basilar membrane that cannot be explained through passive motion alone, it was much earlier that physicists suggested the auditory system was acting as an active amplifier. Beginning in the 1940s, Thomas Gold hypothesized that if the cochlear basilar membrane acted as only a passive receiver, its resonant capabilities would be in sharp contrast to those measured by the auditory psychological studies of the time [42]. In short, the viscous damping of the basilar membrane would need to be overcome by an active amplification process, which he envisioned as a negative stiffness [43]. To generate this behavior, the ear would need to expend metabolic energy to enhance its resonant capabilities. This hypothetical process was subsequently termed the active process.

Years later, researchers outlined four key auditory phenomena that could be explained only by an active process in the ear [44, 45, 46]. These were amplification of small stimuli, precise frequency discrimination, a compressive nonlinearity of the trillion-fold range in input power to a hundred-fold range in auditory response [47], and the epiphenomena of otoacoustic emissions, in which ears spontaneously emit sound in a quiet environment [48, 49].

Recognition of the hair bundle as a mechanosensitive element [50] lead to a unifying critical-instability model that incorporates these four observations as consequences of a singular process. The details of the specific model have been described elsewhere [51, 52]: it has been shown that as the hair bundle's operating point in physical parameter space approaches a critical value, it may become unstable and begin to oscillate spontaneously [53]. This qualitative change in behavior is known as a Hopf bifurcation, whereby a system exhibits a phase change from quiescence to spontaneous oscillation. As mathematical models of hair bundles approach the Hopf bifurcation, they exhibit amplification of small stimuli, compressive nonlinearity, and sharp frequency tuning. Upon traversing the bifurcation, a hair bundle

may produce spontaneous limit-cycle oscillations of varying frequency and amplitude. Thus, the four key components of the active process may be explained as the consequence of hair bundles operating near a Hopf bifurcation [4, 54].

Recent work has shown direct evidence for the Hopf bifurcation in the saccular hair bundles of the American bullfrog (*Rana catesbeiana*) [51, 55]. Under mechanical stimulation, individual hair bundles exhibit all four characteristics of the active process. Additional epiphenomena of the auditory system, such as the distortion products first documented by the violinist Giuseppe Tartini [56] and later by Helmholtz [57], have also been demonstrated at the level of the individual hair bundle [58, 59]. Taken together, nearly every auditory characteristic has been recapitulated at the level of the individual hair bundle.

The active process is thought to be controlled through feedback on channel gating through the motion of the insertional plaque, which can expend ATP in order to amplify and adapt to stimuli. In a simple two-state model for MET channel opening, the open probability of the channel is given by the Boltzmann distribution:

$$P_o = \frac{1}{1 + e^{+\frac{\Delta G}{k_B T}}} \tag{1.1}$$

where $P_0$ is the equilibrium open probability of the channel, and $\Delta G$ is the free-energy difference between the open and closed state of the channel. The form above can be modified when the channel is connected to a spring which pulls on the channel with force $F = \kappa_s x_s$, where $\kappa_s$ is a linear spring constant and $x_s$ is the displacement of the spring. The new open probability is given by [60]:

$$P_o = \left(1 + e^{\frac{\Delta G - d\kappa_s(\gamma x + x_0)}{k_B T}}\right)^{-1} \tag{1.2}$$

where $\gamma$ is the geometric factor described in the previous section, $x$ is the displacement of the tip of the hair bundle, $x_0$ is the resting extension of the spring, and $d$ is the distance by which the channel swings when moving from the closed to open state. Measurements of ionic

influx into hair cells in the absence of stimulation shows a resting open probability of $\sim 15\%$ [60]. As the hair bundle is deflected, the increase or decrease of force on the channel biases it to either the opened or closed configuration. Upon deflection, the ionic current into the bundle does not remain constant – it decays over time, with both fast and slow components on the order of a millisecond and on the order of tens of milliseconds, respectively [61].

The source of slow adaptation is well understood, and involves calcium ion and force-induced slippage of the motor complex along actin filaments after deflection of the hair bundle towards its tall edge. This changes the $x_0$ term cited above and allows the bundle to modulate its open probability. This adaptive process also underlies the active process in at least some hair bundles, whereby the motor can climb and slip at such a frequency as to engender oscillations in the bundle. The fast component of adaptation is poorly understood, but several models have proposed fast calcium-ion regulated reclosure of channels as a likely culprit [62].

Key to proper functioning of the active process and adaptation is the spring constant of the gating spring, which grades the open probability of the MET channel with respect to deflection (Figure 1.3, Figure 1.4). With the geometric factor set by the static architecture of the hair bundle, the stiffness value of the spring that tugs on the channel must be tightly controlled to allow for a continuum of responses. The stiffness of the gating spring has been measured on the order of 1-10 mN/m [38], though its identity remains uncertain.

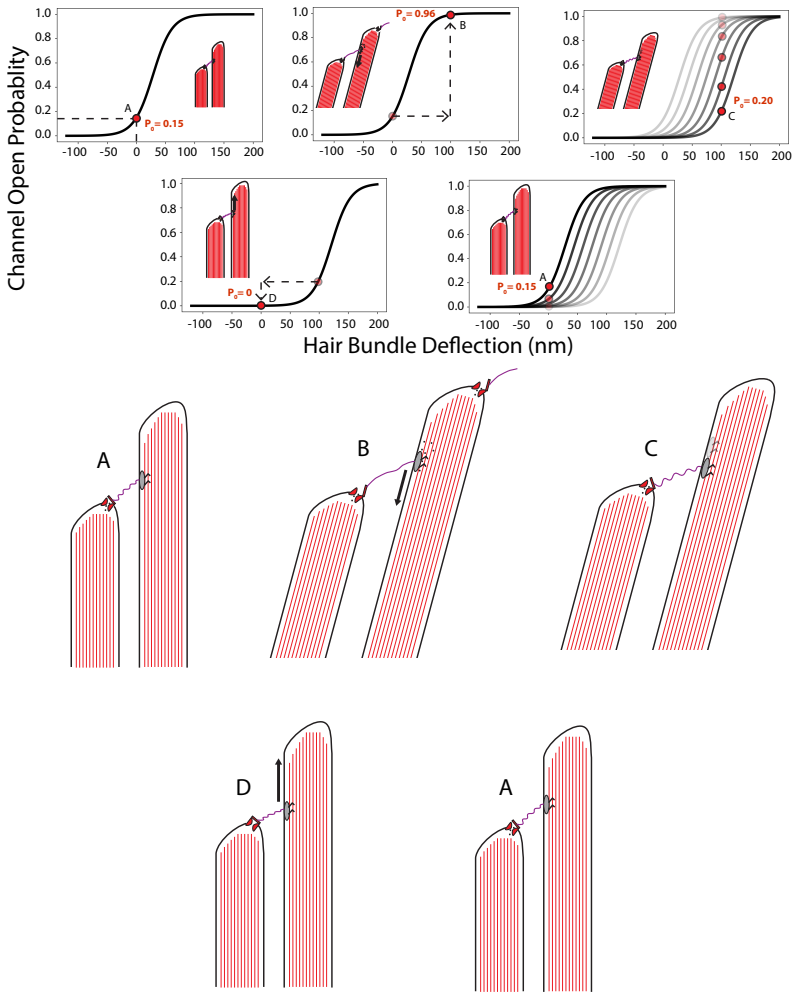


Figure 1.3: **Adaptation of the Hair Bundle**. Upon deflection, the hair bundle adapts and changes the open probability of the MET channel. At (A), the hair bundle is in a resting state and the channel has a resting open probability of $P_0 \sim 0.15$. Once the bundle is deflected quickly in (B), the open probability follows the curve up to a high open probability ($\sim 0.96$) before adaptation begins. Opening of MET channels allows calcium ions into the stereocilia, which interact with myosin motors in the insertional plaque and causes slippage. In (C), the motor complex has slid down the actin filaments and restored the open probability to close to its original value. Adaptation remains complete indefinitely. Upon release in (D), tension is released in the link and the channel closes with near certainty. The lack of tension allows the motor complex to climb, eventually resetting the bundle to its original state.

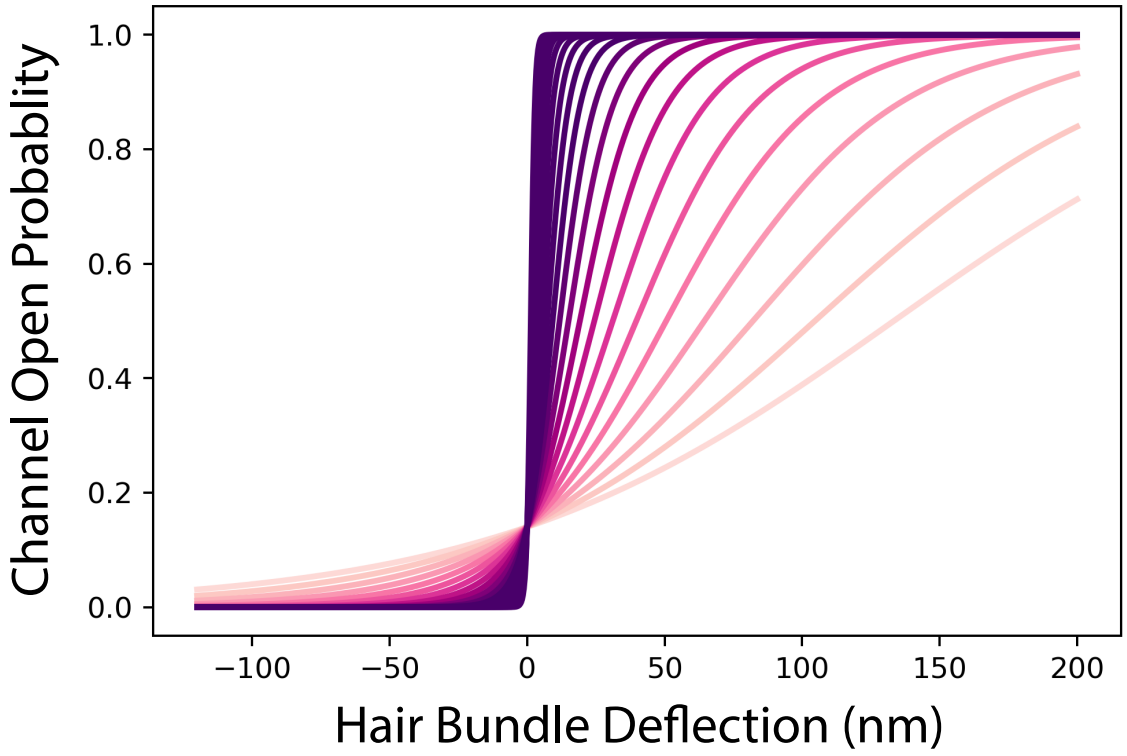


Figure 1.4: **Gating-Spring Stiffness Changes the Open Probability of the MET Channel.** The curvature of the open probability of the MET channel modeled by Equation 1.2 is dependent on the gating stiffness. At resting position, $x_0$ was chosen such that the channels always had open probability $P_0 \sim 15\%$ at zero deflection. Gating-spring stiffnesses between 0.1 and 10 mN/m were sampled (light to dark). At low stiffnesses, a large bundle deflection leads to little change in channel open probability, and sensitivity to weak stimuli is diminished. At high stiffness, the open probability approaches a step function with no dynamic range. Parameters chosen: $\Delta G = 10 k_B T$, $d = 4$ nm, $\gamma = 0.14$.

## 1.4 The Elusive Gating Spring

A mechanically gated ion channel requires an associated transducer that converts mechanical strain (extension) into actionable stress (force) for proper functioning. This element, termed a gating spring, was first proposed to be essential for mechanotransduction in the hair cells of vertebrates [63], and has since been identified as the cell membrane itself for Piezo channels, and as ankryin repeat domains in NOMPC [67, 68, 69, 82]. The identity of the gating spring in hair bundles remains controversial. Due to the nature of hair-bundle architecture, the gating spring must either be the tip link itself, or some other component in series with it. Whether it is the tip link, the cellular membrane, or other associated elastic proteins that act as the gating spring has been the subject of debate for the past decades.

The gating spring was originally measured to have a stiffness on the order of 1 mN/m in bullfrog saccular hair cells [63]. More recent measurements of the hair bundles within the rat cochlea by fluid-jet stimulation have shown a tonotopic gradient of individual gating-spring stiffnesses, ranging in value from 1 to 4 mN/m from the 1 to 4 kHz positions along the basilar membrane [38]. Because the compliance of springs (even nonlinear springs) in series adds as the sum of their reciprocal values, gating-spring stiffness is dominated by the least stiff element.

## 1.5 The Tip Link as the Gating Spring

The identity of the gating spring remains unknown. One obvious candidate is the tip link itself, which remains an object of controversy despite intensive structural study [28, 70, 71, 72, 73, 74, 75]. The tip link comprises a helical dimer of dimers, and each (*cis*) dimer is composed of two polymers, cadherin-23 (CDH23) and protocadherin-15 (PCDH15), joined

at their amino-terminal sites by a (*trans*) extended-handshake interaction that is $Ca^{2+}$-dependent [33, 76, 33]. Indeed, the presence of calcium-ion chelators such as BAPTA disrupts tip links [28, 77, 78]. Several hereditary diseases, such as Usher's Syndrome, are associated with mutations in PCDH15 and CDH23, implicating their proper functioning as contingent for auditory sensation [79, 80].

A dimer of PCDH15 forms the lower one-third of the tip link, and each PCDH15 monomer consists of 11 EC domains along with a membrane-proximal PICA domain. Dimerization sites at the PICA domain and EC3 stabilize the dimer, and introduce a half-helical turn along the length of the two strands. PCDH15 EC1-2 interacts with EC1-2 of CDH23, which also forms a helical dimer that revolves approximately 2.5 turns before interacting with the insertional plaque at its C-terminus [156]. CDH23 consists of 27 EC domains and forms the upper two-thirds of the tip link.

Each dimer of PCDH15 and CDH23 exists in its native state as a series of tightly folded beta-sheet units connected by small linker regions that contain up to three calcium binding sites [81]. Crystal structures with bound calcium-ions show the linker regions to be stiff, though additional study of CDH23 linker regions revealed several atypical calcium-ion binding sites, with binding affinities ranging from 5 $\mu$M to 80 $\mu$M [74]. Furthermore, crystal structures of PCDH15 EC9-12 revealed a calcium-ion free linker region between EC8-9, which under molecular dynamic simulations provides an elastic elongation of a few nanometers. The stretching of individual cadherin domains under molecular dynamic simulations suggests an enthalpic stiffness on the order of 60 mN/m [74], rendering them unlikely contributors to the gating-spring's elasticity in the folded state.

Recent high-precision optical trap measurements on a monomeric PCDH15 construct, however, suggest that entropic elasticity could play a significant role in the mechanics of the tip link, and that the linkers between EC domains are flexible under a wide range of calcium-ion concentrations [82]. Under physiological concentrations (20 $\mu$M $Ca^{2+}$) and pulling forces (10 - 60 pN), Bartsch et al. observed a nonlinear elastic mechanical response

consistent with the predictions for a semiflexible biopolymer [82]. In particular, they found that entropic stiffness – owing to the pulling out of thermal undulations in the chain – contributed significantly to the extension change of PCDH15 under low and moderate forces. In addition, they observed reversible unfolding events, which occurred for individual cadherin domains at rates ranging from 0.01 $s^{-1}$ to 1 $s^{-1}$, suggesting that over many cycles the tip links of the hair bundle may adopt heterogeneous conformations. The 34 nm chain-length change observed in a large fraction of these unfolding events is in agreement with the prediction of full EC domain unfolding, and smaller unfolding events of size 16 nm and 4 nm are posited to be the result of partial unfolding and calcium-ion unbinding.

The role of entropic fluctuations in the mechanics of tip links under normal physiological conditions is not well understood. In particular, unlike the enthalpic stiffness associated with stretching bonds which acts near instantaneously, the entropic stiffness associated with stretching a semiflexible polymer is limited by the speed at which the chain may rearrange and sample energetically accessible conformations. Although unimportant for most stressed biopolymers, this consideration has practical implications for the auditory system, in which stimulation frequencies can climb into the tens of kilohertz. If the tip link is to plausibly act as an entropic spring, it must be able exert its "springiness" at these high frequencies, or otherwise modify its behavior in some novel way to enhance audition.

From the perspective of polymer physics, the tip link falls into a wider category of biopolymers for which work has been done to answer these same questions [83, 84, 109, 85, 86]. Although semiflexible biopolymers have been investigated extensively, analysis is often performed under quasi-static conditions. The reason for this is obvious; most biopolymers are never subjected to high-frequency oscillatory motions, and if they are, their response in lower-frequency modes is of overriding concern. The addition of dynamics into the picture leads to surprising results which have been noted before, but have not been evaluated in the context of large oscillatory motion so critical to the tip link's function.

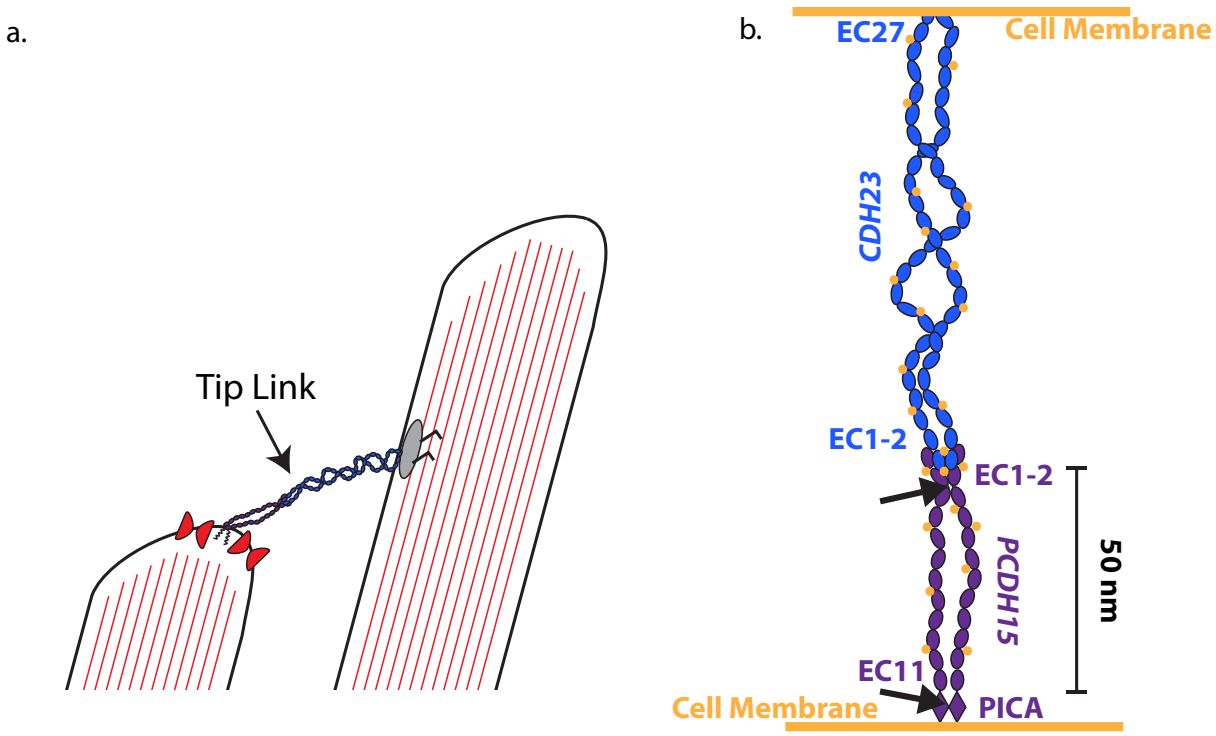


Figure 1.5: **Detailed Model of Tip-Link's Structure**. The tip link comprises of PCDH15 and CDH23 dimers, which interact at their amino termini in a calcium-ion-mediated extended-handshake interaction to form a heterotetramer. In (a), a modified model in which the tip link is treated as a polymer with significant thermal bends, and is also not attached directly to the MET channels. In (b), a schematic diagram of the tip link. Arrows indicate known dimerization sites. Calcium ions depicted as yellow circles bind in the linker regions between two successive EC domains, and inhibit flexibility. Calcium-ions stabilize the handshake interaction of PCDH15 EC1-2 and CDH23 EC1-2. PCDH15 makes one half-helical turn along its length, and CDH23 makes two helical turns along its length.

## 1.6 Outline of Thesis

In this thesis, we explore the implications of a model of entropic elasticity as suggested by recent optical-force microscopy measurements and considerations of flexibility of linker regions between cadherin domains in the absence of bound calcium-ions. Although the enthalpic stiffness of individual cadherin domains is too high to account for the measured compliance of the gating spring, entropic effects due to the thermal undulation of the tip link are still a prime candidate. The stretching of thermal bends forms the basis of an entropic spring, for which work is not done to change the configurational energy of the polymer, but instead to reduce the allowed number of configurations that the polymer may adopt. Many biopolymers display entropic elasticity with well-documented characteristics.

We discuss the implications of modeling the tip link as a semiflexible polymer, with focus given to the effects of high-frequency stimulation. Both polymer networks and individual polymers can display viscoelastic behavior, which may significantly alter the frequency-dependent response upon deflection of the hair bundle.

In the next chapter, we review the properties of polymers in equilibrium and recover some important force-extension relations that are used to model polymers during quasi-static pulling experiments. The models that we discuss in Chapter 2 will form the bedrock for further analysis in Chapter 3, in which we discuss the implications of adding drag and thermal motion into the model. The study of polymer dynamics will naturally lead to the conclusion that tension cannot instantaneously propagate down a chain, but instead forms a moving boundary layer over which only a portion of the chain has equilibrated. We end our discussion with the derivation of a master partial integro-differential equation, which governs the dynamics of tension propagation down the length of a polymer. We study the numerical solutions to this equation in Chapter 4, and subject a chain with tip-link-like parameters to sinusoidal forcing at high frequencies. We find that resting tension plays a crucial role in regulating the response, echoing our earlier asymptotic analysis in Chapter 3. In Chapter

5, we take a more systematic approach to studying the viscoelastic behavior of tip-link-like chains under small forcing amplitudes, which are highly relevant in the context of normal auditory function. Finally, in Chapter 6 we present work on the development of new Monte Carlo sampling algorithms for polymers with fixed end-to-end distances, which we hope will be used for further study on the effects of steric interactions between the parallel strands of the dimeric tip link, and as a basis to build new dynamic simulations of polymers without the need for explicit Langevin integration.

# Chapter 2: Linear Polymers in Equilibrium

Polymers are diverse objects, occurring both naturally in the form of biopolymers such as dsDNA and f-actin, and generated through human synthesis [87, 88, 89]. Beginning in the 1800s, scientists began modifying existing polymeric materials, such as natural rubber, into stable forms that could be manufactured on a large scale for commercial profit [90]. Though the physics of polymeric materials was poorly understood at the time, chemists nevertheless succeeded in discovering and manufacturing novel materials through the turn of the century. It was not until Staudiger proposed the atomic chain model, or macromolecule model, of polymers in the 1920s that the materials being produced could be studied systematically – a discovery which won him the Nobel Prize in 1953 [91].

The rigorous physical study of polymers did not begin until World War II, when the demand for synthetic cloth substitutes skyrocketed. In the following years, new polymeric materials were created and manufactured at a rapid pace, including polyester, polypropylene, Kevlar, Teflon, and additional plastics ubiquitous in the modern world [92, 93]. In tandem, theoretical works by Flory and de Gennes formed the foundation of modern polymer physics, and groundbreaking work by Doi and Edwards contributed to our modern understanding of the dynamics of polymers [94, 95, 96]. Since then, modern approaches using path-integral

interpretations of polymers, as well as computational studies, have shed light on the more subtle aspects of polymer physics [97, 98, 99]. Still, the field of polymer physics remains young.

The tip link is one such polymer, whose entropic properties may be important in auditory sensation [82]. In this chapter, we review the mathematics of several models that may be used to describe polymers in equilibrium, before turning our discussion to polymer dynamics in Chapter 3. As such, this chapter forms the foundation which we expand upon in later chapters. From the view of tip links, the equilibrium behavior to first order describes the response of a tip link to low-frequency auditory stimuli.

We begin with the simplest polymer model, a random flight of uncorrelated random chains, termed the freely-jointed chain (FJC). We continue with an overview of some discretized polymer models that have additional constraints or energetic costs, such as volume exclusion. Next we turn to continuous polymers, for which the chain may be viewed as a continuous curve through space. In particular, we will focus on the inextensible worm-like chain (WLC) model [100] which have had great success in describing the results of single-molecule-force-microscopy experiments [101]. In fact, the force-extension relation for a single WLC was derived specifically to help fill the gap between experiment and theory for semi-flexible biopolymers such as DNA. Throughout the chapter, we focus our discussion on the readily available observables to a single-molecule experimentalist, namely, the probability distribution of the end-to-end distances.

## 2.1 The Freely-Jointed Chain

One may imagine the simplest of polymer models, in which $N+1$ beads are linked together by $N$ rigid bonds of length $b$. The total length of the unfurled chain is $l_c = Nb$. For simplicity, we assume there is no energetic cost to bending – that is, each bond is free to orient in any direction and is completely independent of the previous orientations and any future orientations, or $\langle \vec{r}_i \cdot \vec{r}_j \rangle = \delta_{ij} b^2$, where $\vec{r}_i$ is the orientation of the $i$th bond and $\delta_{ij} = 1$ if $i = j$ and $\delta_{ij} = 0$ if $i \neq j$. This model is termed the freely-jointed chain (FJC) model, inasmuch as its bonds may be rotated freely with no associated energetic cost. The total potential energy of the chain, independent of conformation, is exactly zero. In thermal equilibrium, each conformation or micro-state of the chain is equally likely. The statistics of the chain are thus governed completely by entropic effects. We postpone discussion of volume exclusion effects to Section 2.4.

We define the end-to-end vector as the sum over all bonds in the chain, $\vec{R} = \sum_{i=1}^{N} \vec{r}_i$. $\vec{R}$ will play a primary role in our analysis, and represents an easily measurable observable of a polymer. The first moment, or expected value, of the end-to-end vector $\langle \vec{R} \rangle = \sum_{i=1}^{N} \langle \vec{r}_i \rangle = 0$, because each bond vector is symmetric and has no preferred orientation. The second moment is non-negligible, and is given by:

$$\langle \vec{R}^2 \rangle = \sum_{i=1}^{N} \sum_{j=1}^{N} \langle \vec{r}_i \cdot \vec{r}_j \rangle = \sum_{i=1}^{N} b^2 = Nb^2 \tag{2.1}$$

By this result, the mean-squared value of the end-to-end vector scales with the square root of $N$ in solution. Doubling the length of the chain increases the average size of the globule by only $\sqrt{2}$.

We also are interested in the full probability distribution of the chain - in particular, when the chain has many "links". The small-$N$ case is nontrivial, and we postpone its discussion until Chapter 6. In the large-$N$ limit, each bond vector $\vec{r}_i$ acts as a random variable, and is independent of all other bond vectors. We may split the end-to-end distance

into Cartesian coordinates, $\langle R^2 \rangle = \langle x^2 \rangle + \langle y^2 \rangle + \langle z^2 \rangle$. Because there is no special direction – that is, changing basis to another Cartesian coordinate system renders the system invariant – and noting that we have already derived $\langle R^2 \rangle = Nb^2$, length must be stored equally along all three directions: $\langle x^2 \rangle = \langle y^2 \rangle = \langle z^2 \rangle = Nb^2/3$. In the limit of large $N$, the probability distribution along each axis (and for the end-to-end distance vector) approaches a normal distribution, $P(x) = \sqrt{\frac{3}{2\pi Nb^2}} e^{-\frac{3x^2}{2Nb^2}}$. The probability distribution of the end-to-end distance vector $\vec{R}$ is thus given by:

$$P(\vec{R}) = P(x)P(y)P(z) = \Big(\frac{3}{2\pi Nb^2}\Big)^{3/2} e^{-\frac{3R^2}{2Nb^2}} \tag{2.2}$$

which is indeed Gaussian. The probability distribution of the magnitude of the end-to-end distance vector, $P(R)$, is found by integrating over the shell of radius R:

$$P(R) = 4\pi R^2 \Big(\frac{3}{2\pi Nb^2}\Big)^{3/2} e^{-\frac{3R^2}{2Nb^2}} \tag{2.3}$$

By Equation (2.2), the chain is more likely to be found in a crumpled configuration than in an extended configuration. On one hand, this may be viewed statistically; there are far more ways for the chain to be in a crumpled configuration than in an extended configuration. On the other hand, we may ask what is physically driving the system away from an extended state and into a crumpled state. Because there is only one source of energy – the thermal energy of the bath – it must be that the solution in which the polymer is dissolved drives it into a crumpled configuration. To good approximation, water molecules in solution bombard the polymer with spatially- and temporally-independent correlations of energy $k_B T$, which introduce undulations in the chain and act to crimp it. In order to stretch out the chain, then, it is necessary to do work on the system against the bath. The work necessary to extend the chain in solution is the basis of an entropic spring.

## 2.2 Force Extension of the Freely-Jointed Chain

In this section, we explicitly derive the force-extension relation for a FJC, for the derivation is elementary and demonstrates some fundamental properties we exploit in later sections. We define the direction $\vec{z}$ to be the direction in which we apply a pulling force. The average end-to-end distance along the axis of pulling is given by $R = \vec{R} \cdot \vec{z}$, or expanding, $R = b \sum_i \vec{t}_i \cdot \vec{z}$, where $\vec{t}$ is the direction of the $i$th bond. The potential energy of the system is given by $E = -Fb \sum_i^N \vec{t}_i \cdot \vec{z} = -Fb \sum_i^N \cos\theta_i$, where $\theta_i$ defines the angle between the local tangent of the chain and the pulling direction. Thus, rotating a segment of chain to align with the direction of pulling force lowers its energy. Armed with the energy of the system, we may easily construct the partition function for this model, which is the sum (or in this case, integral) of the Boltzmann factors over all tangent orientations:

$$Z(F) = \int \int ... \int d\vec{t}_1 d\vec{t}_2 ... d\vec{t}_N e^{\frac{Fb}{k_b T} \sum_i^N \cos\theta_i} \tag{2.4}$$

where the $N$ integrals run along all orientations of the tangent along the unit sphere. Once the partition function is solved, one may easily extract the average end-to-end distance by noting that $\langle R \rangle = k_b T \partial_F \log Z$, since $\partial_F \log Z = \frac{\partial_F Z(F)}{Z(F)}$ and:

$$\partial_F \log Z(F) = \frac{\int \int ... \int d\vec{t}_1 d\vec{t}_2 ... d\vec{t}_N \frac{R}{k_B T} e^{\frac{Fb}{k_B T} \sum_i^N \cos\theta_i}}{Z(F)} = \langle R \rangle / k_B T \tag{2.5}$$

We will always take *log* to refer to the natural logarithm *ln*, unless otherwise noted. $Z(F)$ is easily expressed in polar coordinates as:

$$Z(F) = \int_0^\pi \int_0^{2\pi} d\theta_1 \sin\theta_1 d\phi_1 ... \int_0^\pi \int_0^{2\pi} d\theta_N \sin\theta_N d\phi_N e^{\frac{Fb}{k_B T} \sum_i^N \cos\theta_i} \tag{2.6}$$

which may be integrated to yield $Z(F) = (2\pi)^N \left(\frac{2 \sinh Fb/k_B T}{Fb/k_B T}\right)^N$. Differentiating the logarithm of this function yields the average end-to-end distance:

$$\langle R \rangle = k_B T \partial_F \log Z(F) = Nb\Big[\coth\Big(\frac{Fb}{k_B T}\Big) - \frac{k_B T}{Fb}\Big] \tag{2.7}$$

As we will see, the corresponding calculation for the semiflexible chain we consider later in the chapter is far more involved.

## 2.3 Scaling Argument for the Freely-Jointed Chain

Under small forces, the first-order Taylor expansion of Equation (2.7) is $\langle R \rangle = \frac{NFb^2}{3k_b T}$. Thus, the FJC acts as a linear spring under small forces with spring constant $\frac{3k_b T}{Nb^2}$. There is another method to arrive at this answer, which involves a scaling argument that will become important when we revisit the idea of stretching dynamics in later chapters [102]. The idea is straightforward - at a certain length scale $l_{\text{blob}}$, the chain goes from experiencing the effects of tension to behaving like a freely-floating chain without tension. Below this characteristic length scale, the thermal energy outweighs the energy gained by aligning the small segment of chain in the direction of the pulling force. Above this length scale, rotating the chain in the direction of the pulling force decreases the potential energy of the system in a meaningful way (on the scale of $k_B T$), and must be accounted for. The length scale should be force-dependent, because a stronger aligning field increases the energy associated with rotation away from the axis of pulling.

Applying tension $F$ to the ends of the chain stretches it to a length $R > bN^{1/2}$ which is greater than the average end-to-end length of the free chain. If we break the chain into $M$ segments of $N/M$ bonds each, the chain length of each segment is $l_c = \frac{Nb}{M}$, with a corresponding free (tensionless) average length $l_{\text{blob}} = b\sqrt{\frac{N}{M}}$. We posit this blob length to be the same as characteristic length scale $l_{\text{blob}}$ described in the previous paragraph. By construction, the only way for the chain to extend is for these blobs to be aligned in the

direction of pulling, such that they roughly follow the axis of pulling $\vec{F}$. The length of the entire stretched chain is then simply $R = Ml_{\text{blob}}$. Rearranging, and using the definition of the blob size $l_{\text{blob}} = b\sqrt{\frac{N}{M}}$:

$$l_{\text{blob}} \approx \frac{Nb^2}{R} \tag{2.8}$$

This is the characteristic size of the blobs, but we need an additional argument to approximate the energy. The energy of the chain within each blob is unchanged by stretching, but in order to approximate the chain length, we assumed that the blobs were all aligned in the same direction. By the Equipartition Theorem, each degree of freedom of a system in equilibrium corresponds to $k_BT/2$ of energy. By assuming all $M$ blobs are aligned along a single axis, we restrict a single degree of freedom per blob. The energy change to extend the chain is therefore approximated as [102]:

$$\Delta E \approx \frac{k_BT}{2}M = \frac{Nb^2k_BT}{2l_{\text{blob}}^2} = \frac{R^2k_BT}{2Nb^2} \tag{2.9}$$

Taking the derivative with respect to the end-to-end distance $R$ gives $F \approx \frac{Rk_BT}{Nb^2}$, and rearranging gives $R \approx \frac{FNb^2}{k_BT}$, which up to a numerical factor correctly predicts the force-extension relation.

Armed with the knowledge of blobs, we also may rewrite the force equation with respect to blob size. The blob size scales with the force as $l_{\text{blob}} \propto \frac{1}{F}$. In subsequent sections and chapters, we will find that the blob size does not always scale as $\propto \frac{1}{F}$.

The tension blob picture is useful to gain an intuitive understand of the effects of tension on a polymer, and also provides a useful tool with which to understand the fast tension dynamics of semiflexible and flexible chains for which force may not be distributed equally across the chain. In particular, works on polymer translocation through small pores predicts a "trumpet" configuration of blobs [103], and we will encounter non-uniform blob size when we discuss worm-like chain dynamics.

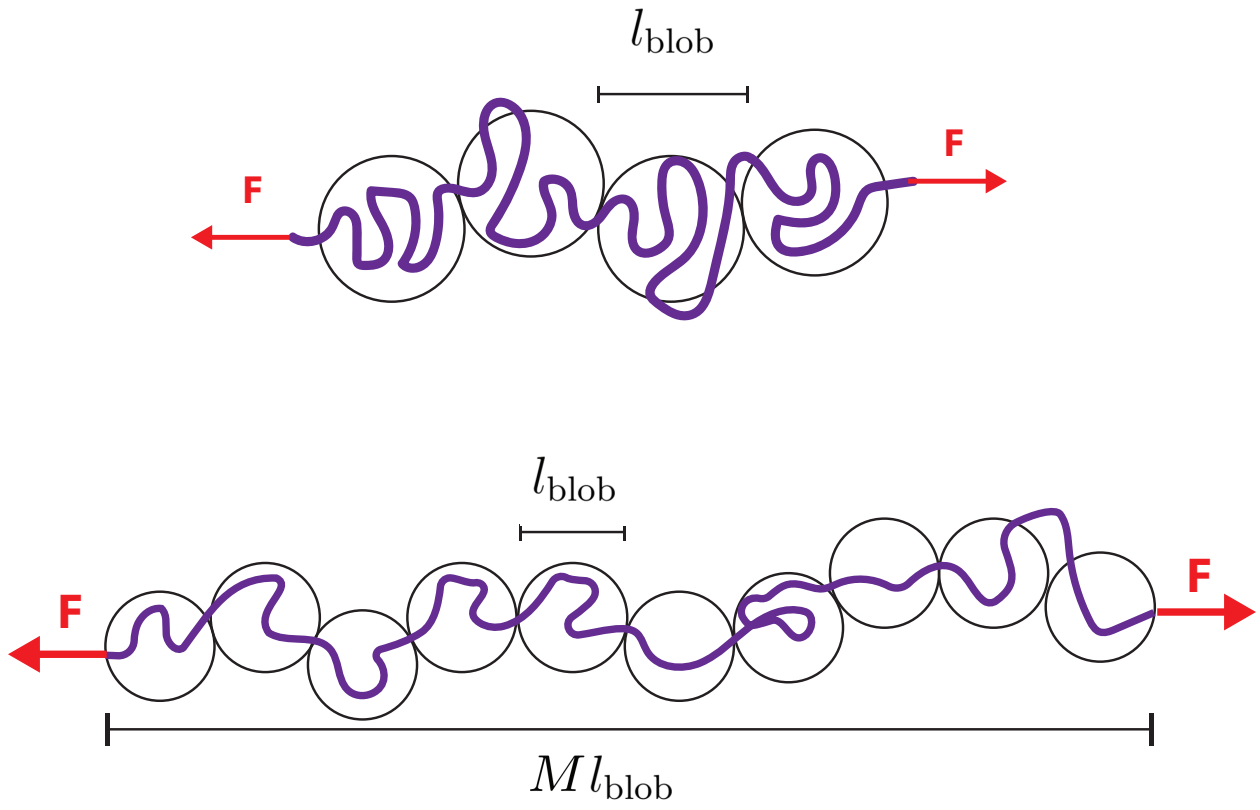


Figure 2.1: **Tension Blobs**. Schematic diagram of tension blobs described in Section 2.3. At the top, a polymer is held under low tension at its ends. The corresponding blob size is large, but its length grows only as $\propto \sqrt{N}$, the number $N$ being the links in the blob. Upon applying a larger force, the blob size shrinks but the number of blobs increases. Within each blob, the chain may be treated as free (tensionless).

## 2.4 The Real Freely-Jointed Chain

Real polymers are not infinitesimally thin. Proteins consist of strings of amino acids connected by their backbones, with potentially large side chains that interact with distant sites on the chain. An actin filament cannot cross over itself, with very real effects on extension behavior in the low-force regime. Real chains in solution thus exhibit properties not fully captured by the ideal chain model. It is necessary to slightly modify the results from the previous section, in order to account for more subtle effects like volume exclusion.

In solution, especially in cases where the chain is not found in an extended state, distant segments along the polymer may interact. This is in stark contrast to our previous assumption, in which segments only interacted locally. This additional interaction becomes highly probable as the length of the chain grows. Heuristically, volume-exclusion effects cause the polymer to swell in size because there are fewer available crumpled conformations. The first successful theory to take into account volume-exclusion effects was developed by Flory in 1949 [104, 105], whereas more recent computational efforts have refined the theory considerably [106].

To predict the average-squared end-to-end distance of the real chain, $\langle R_r^2 \rangle$, we may consider the free energy of the system, which must equal zero in equilibrium. The free energy of the system in the simplest model of a real chain consists of two factors: the energetic cost associated with stretching the chain, and the energetic cost associated with compressing the chain into a small volume in the presence of volume exclusion. Because the volume-exclusion effect is expected to cause the chain to swell, we may use the result from Section 2.3 to estimate the energy associated with stretching the chain to an end-to-end distance $R_r$, $E_{\text{stretch}} \approx \frac{R_r^2 k_B T}{2Nb^2}$. At a size $R_r$, the pervaded volume of the polymer is $\frac{4}{3}\pi R_r^3$. If we assume each monomer of the chain occupies a volume $v \ll \frac{4}{3}\pi R_r^3$, then the ratio of the filled to unfilled volume is $\frac{3vN}{4\pi R_r^3}$. The probability of the addition of a new monomer overlapping with another monomer is proportional to this ratio, such that $P_{\text{overlap}} = \frac{3vN}{4\pi R_r^3}$. Summing over the

$N$ monomers gives the expected number of overlaps, all of which are forbidden by steric interactions. Each expected overlap results in $k_BT/2$ of free energy, as each forbidden site acts as a degree of freedom for the system. On average, then, we expect $E_{\text{excluded volume}} \approx \frac{3k_BTvN^2}{8\pi R_r^3}$. The total free energy of the system is then:

$$E_{\text{total}} = E_{\text{stretch}} + E_{\text{excluded volume}} = k_BT\Big(\frac{R_r^2}{2Nb^2} + \frac{3vN^2}{8\pi R_r^3}\Big) \tag{2.10}$$

and the minimum of the free energy occurs when:

$$R_{\text{real}} \approx v^{1/5}b^{2/5}N^{3/5} \tag{2.11}$$

where the numerical factor is close to unity, and can be disregarded as the Flory theory was approximate to begin with. Of note is the scaling of $R_{\text{real}}$ with $N^{3/5}$ instead of $N^{1/2}$ as is the case with ideal polymers. In general, a polymer's mean squared average length $R \propto N^{\nu}$. More rigorous theories have approximated $\nu \approx 0.588$ for the real FJC [107].

One may repeat the blob argument from the previous section, using the new value of $R_{\text{real}} \propto N^{\nu}$, and noting that the size of the blob again should roughly scale with $b$ (implying $v \sim b^3$). Doing so yields blobs of size $l_{\text{blob}} = b^{1/(1-\nu)}\big(\frac{N}{R}\big)^{\nu/(1-\nu)}$, and energy change $\Delta E \approx \frac{k_BT}{2}b^{1/(\nu-1)}N^{\nu/(\nu-1)}R^{1/(1-\nu)}$. Again differentiating with respect to stretched end-to-end distance yields:

$$F \approx \frac{k_BT}{b^{1/(1-\nu)}}\Big(\frac{R}{N}\Big)^{\nu/(1-\nu)} \tag{2.12}$$

This more general formula reduces to the low-force limit of Equation (2.7) when $\nu = 1/2$. When $\nu > 1/2$ and there are repulsive long-range interactions between monomers (such as steric effects and electrostatic repulsion), the chain behaves as a nonlinear spring with increasing spring constant as it becomes extended. In the case for which $\nu < 1/2$ and there are attractive long-range interactions between monomers, the chain again behaves as a nonlinear spring, but with decreasing spring constant as the spring becomes extended. For

a real chain with $\nu = 0.588$, the force required to pull a chain apart scales as $F \propto R^{1.43}$, whereas the ideal chain scales as $F \propto R$.

Volume-exclusion effects are mostly important in the context of crumpled polymer configurations. Why then do we spend time discussing the results, when the tip link is expected to remain in the extended state under physiological resting tensions? The reason is that the intertwined strands of the native dimer are thought to bond only at sparsely spaced sites along the tip links length. Volume-exclusion interactions are thereby necessarily encountered when stretching the tip link, which draws the chains closer together and affects the entropic stiffness. Although the degree to which this effect occurs is unknown, it would be expected in increase the energetic cost of extending the tip link.

## 2.5 The Worm-Like Chain Model

In many cases, the FJC model fails to describe experimental force-extension data. This is due to the overly simplified model, which ignores the significant resistance to bending observed in many biopolymers [64, 65, 66]. Instead, we may take the continuous version of a FJC, termed either a semiflexible chain or a worm-like chain (WLC). In keeping with historical notation, a polymer is considered *semiflexible* when the energy associated with bending the chain significantly alters the conformation from a FJC model. For many biopolymers the rigidity is great enough that they may to first order be approximated as straight over short lengths. Nevertheless, random thermal fluctuations drive the polymer away from the exactly straight conformation, and the statistics of biopolymers exhibit unique and diverse properties [108].

We consider a simplified model of a chain that does not twist - it is simply a filament that winds through space and resists bending. There are two length scales to consider. The

first is the total arclength of the chain, $l_c$, which characterizes the total length of the chain if one were to completely straighten it. The second is the persistence length, $l_p$, which can intuitively be through of as the length scale on which the polymer remains approximately straight before thermal motion bends it. If we define $\kappa$ as the bending modulus of the chain, to first order the energy associated with bending the chain is proportional to the local change in curvature, or in other words, $\kappa\big(\frac{\partial \hat{t(s)}}{\partial s}\big)^2$ where $\hat{t}(s)$ is the local tangent. Integrating over the entire chain, the total energy of any particular conformation is given by [109]:

$$H_{\text{WLC}} = \frac{\kappa}{2}\int_0^{l_c}\Big(\frac{\partial^2 \vec{r}(s)}{\partial^2 s}\Big)^2 = \frac{\kappa}{2}\int_0^{l_c}\Big(\frac{\partial \hat{t}(s)}{\partial s}\Big)^2 \tag{2.13}$$

The bending modulus $\kappa$ has units of energy and length. Because the persistence length is a measure of the point at which the bending energy, parameterized by the bending modulus, and the thermal energy, $k_BT$, are approximately equal, dimensional analysis yields for the persistence length $l_p = \kappa/k_BT$. Fortuitously, this expression is exactly correct in the case of a WLC in $\mathbb{R}^3$, and is incorrect by a factor of two in $\mathbb{R}^2$ [110].

## 2.6: The End-to-End Probability Distribution of a Worm-Like Chain

Unlike the FJC, the full end-to-end probability distribution is difficult to compute. To first order, the mean-squared end-to-end distance can be shown to follow [102]:

$$\langle R^2\rangle = 2\Big(l_p l_c - l_p^2\Big[1 - e^{-l_c/l_p}\Big]\Big) \tag{2.14}$$

In the limit of a long chain, $l_p \ll l_c$, the mean-squared end-to-end distance reduces to $2l_pl_c$, and we may identify the Kuhn length $b = 2l_p$ to be the same bond length we considered in the FJC model. For long chains, then, the WLC is expected to behave like a FJC, with bond length given by $2l_p$.

While only approximate solutions to the full probability of the end-to-end distance of a semiflexible chain were historically available [111], recovery of the full probability distribution

of the end-to-end radial distribution was completed recently in the Fourier-Laplace domain [112]. Here, we recapitulate a formulation by Mehraeen et al. that is valid in arbitrary dimensions and for any persistence length, and show an alternative strategy in Appendix I using Python libraries for computation of the Fourier-Laplace inversion by taking advantage of the recursion relations of a generalized continued fraction [113]. For ease of comparison, we assume that the total chain length $l_c = 1$ exactly, and note that the results hold for any arbitrary chain length by scaling the probability distribution isotropically by $l_c$, and taking the appropriate persistence length. As can be shown by considering the Green's function (or transition probability) of a worm-like chain to snake a total end-to-end distance $r$, and by summation of stone-fence paths in Fourier-Laplace space, the transition probability in arbitrary dimensions is given by [113]:

$$G_0(\vec{K}, p) = \cfrac{1}{P_0(p) + \cfrac{\alpha_1 K^2}{P_1(p) + \cfrac{\alpha_2 K^2}{P_2(p) + \cfrac{\alpha_3 K^2}{P_3(p) + \cfrac{\alpha_4 K^2}{\cdots}}}}} \tag{2.15}$$

where $\vec{K} = 2l_p\vec{k}$ with $\vec{k}$ the wave vector of $\vec{r}$ after Fourier transform, $P_i = p + i(i + D - 2)$ with D the dimensionality of the chain and p the conjugate variable of $N = 1/2l_p$ , and $\alpha_i = \frac{i(i+D-3)}{(2i+D-2)(2i+D-4)}$. For D = 2, the forms reduce to $P_i = p + i^2$ and $\alpha_1 = 1/2$ and $\alpha_{i\geq 2} = 1/4$. For D = 3, the forms reduce to $P_i = p + i(i + 1)$ and $\alpha_i = \frac{i^2}{4i^2-1}$ which approaches 1/4 in the limit $i \gg 1/2$. This Green's function is found by integrating over the more general Green's function for fixed orientation at the start and end of the chain, $\psi(\vec{u}_0, s = 0)$ and $\psi(\vec{u}, s = 1)$. Integrating over the starting and end orientations yields Equation (2.15), which is valid in the case that both ends are free to rotate.

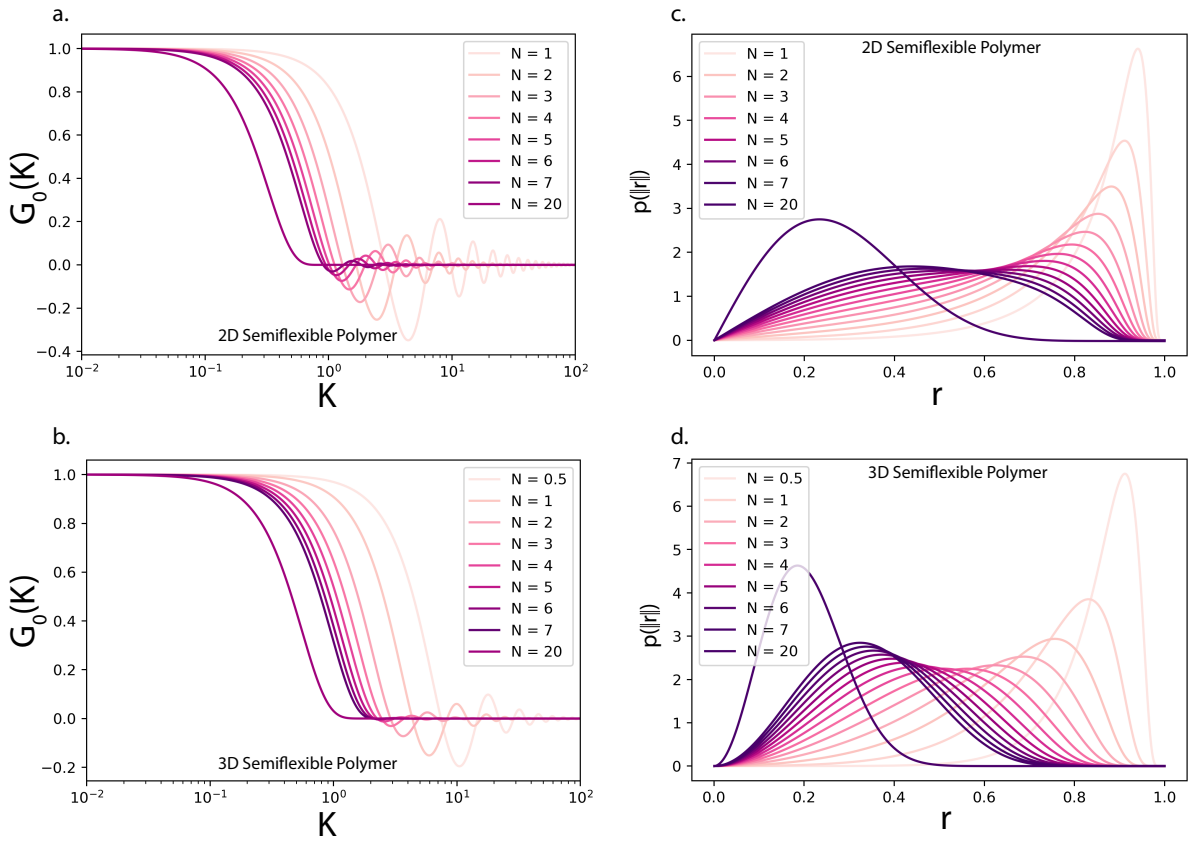


Figure 2.2: **End-to-end Distance Probability Distribution of Semiflexible Polymers** Inverse Fourier-Laplace transforms of Equation (2.15) for semiflexible polymers in $\mathbb{R}^2$ and $\mathbb{R}^3$ with total chain length $l_c$ scaled to unity. The infinite continued fraction was truncated after 12 iterations. In (a,b), the inverse Laplace transforms of the Green's function for several values of $N = 1/2l_p$, with smaller $N$ representing stiff chains and larger $N$ representing a flexible chains. In (c,d), the explicit probability distributions of the end-to-end distance of a semiflexible polymer in $\mathbb{R}^2$ and $\mathbb{R}^3$, respectively. In the limit that $N \to \infty$, the distributions converge to a Gaussian, reflecting their convergence to FJC behavior. An additional $N = 0.5$ was chosen in (b,d) to show the stiff-chain limit in $\mathbb{R}^3$, which requires additional bending rigidity to overcome fluctuations in the additional degree of freedom.

Figure 2.2 shows the results of the calculations for values of $N$ ranging from 1 to 20 for $\mathbb{R}^2$, and from 0.5 to 20 for $\mathbb{R}^3$. These values correspond to a persistence length from $l_p = l_c$ to $l_p = l_c/40$. The non-gaussian nature of the radial distribution function in $\mathbb{R}^2$ is particularly striking, and has been noted in prior work [111].

These probability distributions are to be expected for a freely-floating WLC in solution. As with the FJC, stretching the WLC requires that work be performed on the system in order to overcome the bends introduced by thermal bombardments. In the next section, we will review some force-extension relations for the WLC.

## 2.6 Force Extension in the Worm-Like Chain

Of primary interest to the single-molecule biophysicist is the force-extension relation, measured under quasi-static conditions in which a polymer is stretched between two substrates. From the force-extension curve, one may extract the persistence length and total chain length by standard least-squares fitting. Historically, fits to a FJC model fail to capture the more subtle behavior found in experimental data.

For brevity, we review some results found previously and offer minimal commentary. The force-extension relation for a WLC was calculated by Marko and Siggia in 1995, and is approximately given by the interpolation formula [101]:

$$F = \frac{k_B T}{l_p}\Big[0.25\Big(1 - \frac{r}{l_c}\Big)^{-2} - 0.25 + \frac{r}{l_c}\Big] \tag{2.16}$$

The force required to extend the chain to the exactly straight configuration diverges for finite $l_p$. At low extensions, the force approximates to $F \approx \frac{3k_BT}{2l_p l_c}x$, identical to the result for the FJC if we take $2l_p = b$. In the high force limit, or large extension limit, the force approximates to $F \approx \frac{k_BT}{4l_p(1-r/l_c)^2}$, or inverting, $r \approx l_c\big(1 - 0.5\sqrt{\frac{k_BT}{l_pF}}\big)$.

Additional approximations have been proposed, adding terms that correct for divergences in the non-matching asymptotic crossover regime [114]:

$$F = \frac{k_B T}{l_p}\Big[0.25\Big(1 - \frac{r}{l_c}\Big)^{-2} - 0.25 + \frac{r}{l_c} - 0.8\Big(\frac{r}{l_c}\Big)^{2.15}\Big] \tag{2.17}$$

An additional method to compute the force extension exists, through the use of the continued fraction form of the partition function in Laplace space [112]. The equation is similar to that in section 2.5, with $G_0$ replaced by the partition function $Z(F)$ and $K^2$ replaced by $-F^2$ [113]:

$$Z(F,p) = \cfrac{1}{P_0(p) - \cfrac{\alpha_1 F^2}{P_1(p) - \cfrac{\alpha_2 F^2}{P_2(p) - \cfrac{\alpha_3 F^2}{P_3(p) - \cfrac{\alpha_4 F^2}{\cdots}}}}} \tag{2.18}$$

where the functions $P_i(p)$ and $\alpha_i$ are identical to those given in the previous section, and $F = 2l_p f$ with $f$ the real pulling force measured in units of $k_B T$. Numerically taking the inverse Laplace transform from $p$ to $N = l_c/(2l_p)$, and using our result for the mean end-to-end distance in Section 2.3, $\langle R \rangle = k_B T \partial_F \log Z$, we may numerically calculate the force-extension relationship to arbitrary precision. In particular, Equation (2.18) has the advantage of being applicable in arbitrary dimensions, and can furthermore be used to calculate the higher-order moments of the end-to-end distribution. In Figure 2.3, we show typical force-extension curves for the WLC calculated using Laplace inversion of Equation (2.18), for a variety of values of $N$.

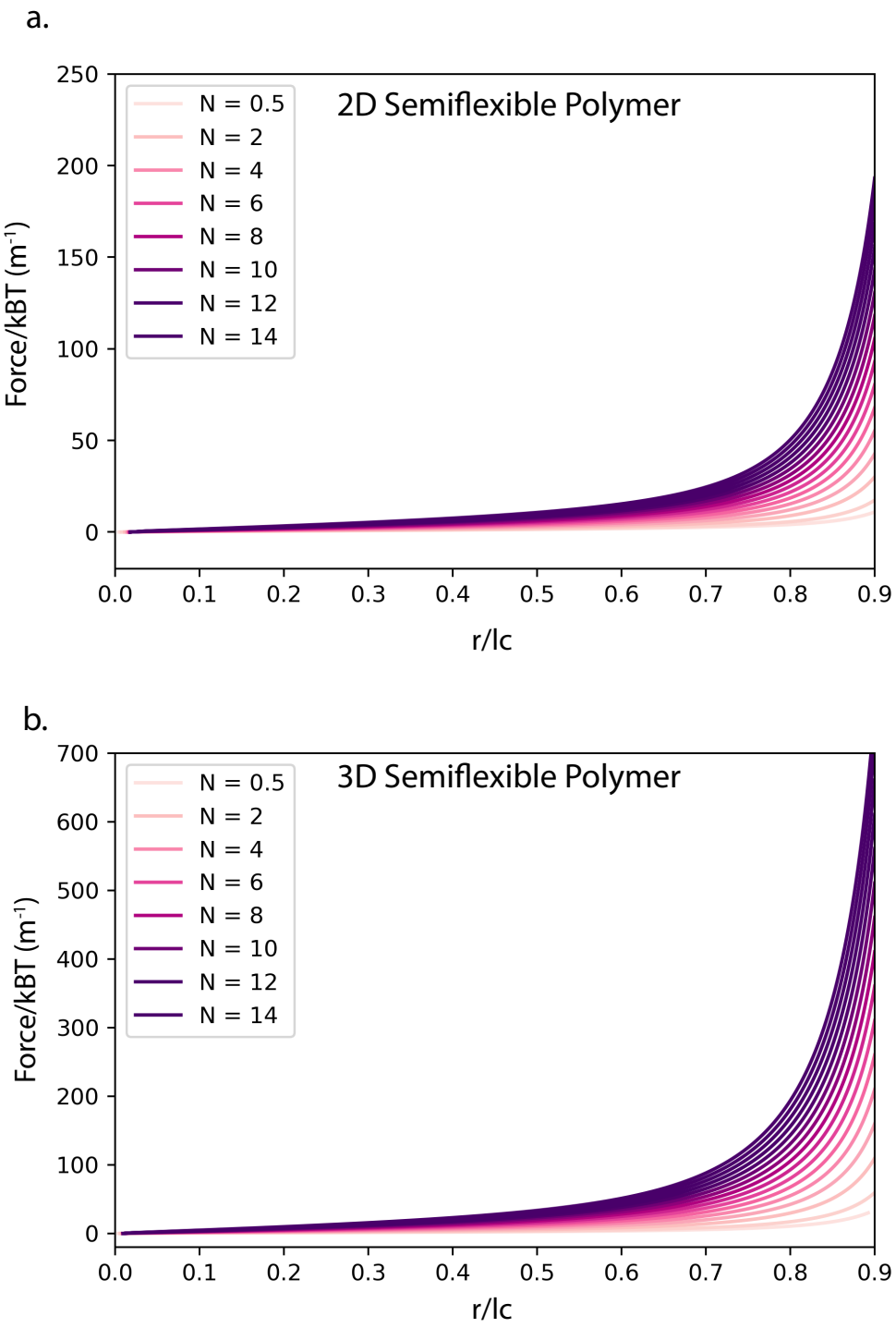


Figure 2.3: **Force-Extension Curves of the Worm-Like Chain** Inverse Laplace transforms of Equation (2.18) for semiflexible polymers in $\mathbb{R}^2$ and $\mathbb{R}^3$ with total chain length $l_c$ scaled to unity. The infinite continued fraction was truncated after 12 steps. The inverse Laplace transform was preformed for 1001 force values spaced equal distance apart. The $\mathbb{R}^2$ and $\mathbb{R}^3$ instances show little difference in their force-extension relationships, besides different scaling of force magnitude.

## 2.7 Conclusions

In this chapter we reviewed the FJC and WLC models of polymers and showed that even without backbone elasticity, a polymer acts as a spring with variable resistance to stretching. The source of this springiness was not due to bending - as straightening a semiflexible polymer actually decreases its energy - but solely a result of entropic, statistical effects. Entropic springs are ubiquitous in nature, with the most common example being that of a rubber band.

In terms of describing the behavior of a single monomer of PCDH15 under slow pulling conditions, a combination of the FJC and WLC model captures the nonlinear spring behavior of the monomer [82]. However, the critical assumption of thermal equilibrium was made throughout the chapter, and is made (to good approximation) in most single-molecule pulling experiments. In contrast, the auditory system supports ramping of the tip link's end-to-end distance at frequencies up to 20 kHz, leaving open the possibility that the polymer is far from thermal equilibrium. In order to address the effect of this high frequency regime on the entropic springs we have considered, we must modify the static picture of a chain to include dynamics. This is the topic of discussion in the next chapter.

# Chapter 3: Polymer Dynamics

In the previous chapter, we considered the equilibrium properties of polymers. The same force that acts to crimp the chain and governs its equilibrium properties, thermal motion, is also responsible for drag forces that prevents the polymer from instantaneously rearranging its conformation. The inclusion of drag in the model of a polymer can drastically change its behavior [102, 94, 109]. For instance, pulling a polymer through solution introduces a drag force along its length, acting to straighten the polymer into a rare configuration under equilibrium conditions [85]. Pulling a polymer too quickly at its ends causes a spike in force, due to the significant energy dissipated into the solution through viscous drag.

The field of polymer dynamics is rich with subtlety, and advances in computational techniques have allowed for us to gain insight into polymers far from equilibrium. Traditionally, polymer dynamics has been concerned with studying semi-dilute and concentrated polymer networks and their reactions to shearing motion [94]. In the context of the auditory system, each tip-link exists in the absolute dilute state, since there is only one chain linking each end of a stereocilia. Upon potentially fast oscillation of the hair bundle, the single polymer may be pulled out of equilibrium, influencing its behavior in a subtle manner not easily accessible to modern experimental techniques [82]. For these reasons, a full analytical picture of single-chain polymers is necessary to understand how the tip link behaves under fast oscillatory

conditions.

In this chapter, we will briefly discuss the Rouse model and its predictions on the probability distribution of end forces for the static end-to-end condition. We then move onto a thorough discussion of the dynamics of semiflexible polymers, which has been treated from first principles by Hallatschek et al. [85]. We follow the general outline of their procedure, but make several additions to the theory that allow comparison to tip-link behavior. This includes an asymptotic analysis of tension propagation along a polymer under considerable prestress, which drastically changes the scaling behavior from the unstressed condition. To conclude, we arrive at a partial integral-differential equation that describes the local changes in backbone tension along an inextensible semiflexible chain.

## 3.1 The Rouse Model

The Rouse model, which was developed in the 1950s, represents one of the first successful models to include dynamics in polymer motion [153]. The model consists of breaking a polymer into discrete units, which are treated as beads with significant size so as to introduce drag, connected by elastic springs, which are assumed massless and without volume (Figure 3.1). The average distance between beads is given by $\langle l \rangle = b$. We assume the springs connecting adjacent beads are idealized and harmonic, such that probability distribution of distance between beads is given by $P(l) = \frac{1}{\sqrt{2\pi k_B T/k_s}} e^{-\frac{k_s (l-b)^2}{2k_B T}}$ where $k_s$ is the spring constant of the link. The spring constant can be chosen, for the three-dimensional chain, to be $k_s = 3k_B T/b^2$ in order to enforce the $\langle l \rangle = b$ condition. Individual beads are assumed to be spherical, and have drag coefficients given by Stoke's law $\zeta = 6\pi\eta r$ [115], where $\eta$ is the viscosity of the surrounding solution and $r$ is the radius of the individual bead.

If we drag the chain through solution, it experiences a drag force from each bead. If there are $N$ beads in the chain, the drag force to pull the entire chain through solution is

$F_{\text{drag}} = N\zeta v$, where $v$ is the velocity of motion. This suggests we define a drag coefficient for the entire chain, which we call $\zeta_R = N\zeta$. From the Einstein relation, the drag coefficient and diffusion constant of a molecule are related through thermal energy, $\zeta D = k_B T$. The diffusion constant of the entire chain is thus given by $D_R = k_B T / N\zeta$. There are three length scales in the system - the first is the bond length $b$, the second is the chain length $l_c = Nb$, and the third is the size of the chain in equilibrium, shown in Chapter 2 to be $\langle R^2 \rangle = Nb^2$. The third length scale is most relevant in solution to relate $\zeta_R$ to a time, and suggests we set a timescale $\tau_R$ which is the time it takes a chain to diffuse across its own size:

$$\tau_R = \frac{Nb^2}{2D_R} = \frac{N^2 b^2 \zeta}{2k_B T} \tag{3.1}$$

The first length scale $b$ can also be used to relate $\zeta$ to a timescale. We define a timescale $\tau$ as the time it takes a monomer to diffuse a chain length $b$:

$$\tau = \frac{b^2}{2D} = \frac{b^2 \zeta}{2k_B T} \tag{3.2}$$

Clearly, $\tau_R = N^2 \tau$. The Rouse chain can be broken into modes of oscillation, each containing N/q number of segments. This is equivalent to a modal decomposition of the chain. Since the chain is equivalent on any length scale, the timescale of relaxation for any mode involving N/q monomers is $\tau_p = (N/p)^2 \tau$. This is the time it takes a segment of the chain to relax and fully explore its conformational space. As we see from the $1/p^2$ scaling, longer-wavelength (shorter wave-mode) oscillations take much longer to come to equilibrium.

We now shift focus to explore the predictions of the Rouse model on tension for a fixed end-to-end distance $\mathbf{R}$. This is equivalent to holding the chain at fixed positions, and asking what local force is required to keep the chain glued to its boundary conditions. The $n$th monomer in the chain feels a force:

$$\mathbf{F}_{n,tot} = \mathbf{F}_{n,chain} + \mathbf{F}_{n,drag} + \boldsymbol{\xi}_n \tag{3.3}$$

Where the chain force $\mathbf{F}_{n,chain} = \frac{3k_BT}{b^2}(\mathbf{x}_{n+1} + \mathbf{x}_{n-1} - 2\mathbf{x}_n)$, the drag force is approximated by $\mathbf{F}_{n,drag} = \zeta\partial_t\mathbf{x}$, and the thermal force $\xi_n$ is formally equivalent to the time derivative of a scaled standard Weiner process. This Langevin equation is simplified by treating the inertial term as negligible, and hence treating the total force on each bead as balanced to zero, $\mathbf{F}_{\mathrm{n,tot}} = 0$.

In the continuum limit, we may reduce the equations of motion of the Rouse model links into a diffusion-type equation. The governing equation then reads [115]

$$\zeta\partial_t\mathbf{x}(t,n) = \frac{3kT}{b^2}\partial_n^2\mathbf{x}(t,n) + \boldsymbol{\xi}(t,n) \tag{3.4}$$

In the case of fixed end-to-end distance, we may define the boundary conditions on this equation as $\mathbf{x}(0,t) = \mathbf{x}_0$ and $\mathbf{x}(N,t) = \mathbf{x}_N$. The tension exerted by the chain on the boundaries is given by $\frac{3kT}{b^2}\frac{dx}{dn}|_{0,N}$, the arclength derivative of the link position evaluated at the boundary. Alternatively, this may be thought of as the force exerted locally by stretching the bond between the $x_0$ and $x_1$ links, or the $x_{N-1}$ and $x_N$ links.

A suitable choice of Fourier decomposition that obeys the boundary conditions yields a solution in the form

$$\mathbf{x}(n,t) = \mathbf{x}_0 + \frac{n}{N}\mathbf{R} + 2\sum_{q=1}^{\infty}\mathbf{a}_q(t)\sin(\frac{\pi qn}{N}) \tag{3.5}$$

One may check this satisfies the imposed boundary conditions, if we identify $\mathbf{R} = \mathbf{x}_N - \mathbf{x}_0$ as the end-to-end distance vector. $\mathbf{a}_q(t)$ is the wave amplitude of wave-mode $q$. Substituting Equation (3.5) into Equation (3.4) then yields a system of equations of the form:

$$\zeta\partial_t\mathbf{a}_q(t) = -\frac{3\pi^2kTq^2}{b^2N^2}\mathbf{a}_q(t) + \boldsymbol{\xi}_q(t) \tag{3.6}$$

where $\boldsymbol{\xi}_q(t)$ is given by the Fourier Transform

$$\boldsymbol{\xi}_q(t) = \frac{1}{N}\int_0^N \sin(\pi qn/N)\boldsymbol{\xi}(t,n)dn \tag{3.7}$$

The first and second moments of the random force in wave-mode space are computed as

$$\langle\boldsymbol{\xi}_p(t)\rangle = \frac{1}{N}\int_0^N \sin(\pi qn/N)\langle\boldsymbol{\xi}(t,n)\rangle dn = 0 \tag{3.8}$$

and

$$\langle\boldsymbol{\xi}_p(t)\boldsymbol{\xi}_q(s)\rangle = \frac{1}{N^2}\int_0^N\int_0^N \sin(\pi pn/N)\sin(\pi qn'/N)\langle\boldsymbol{\xi}(n,t)\boldsymbol{\xi}(n',s)\rangle dndn' = \frac{\zeta k_B T}{N}\delta_{pq}\delta_{\alpha\beta}\delta(t-s) \tag{3.9}$$

where $\alpha$ and $\beta$ are indices of an orthonormal coordinate system. The differential equation given in Equation (3.6) can be solved by the method of Green's functions, and yields a solution:

$$\mathbf{a}_q(t) = \frac{1}{\zeta}\int_{-\infty}^t dt' e^{-\frac{t-t'}{\tau_q}}\boldsymbol{\xi}_q(t') \tag{3.10}$$

with $\tau_q = \frac{N^2b^2\zeta}{3\pi^2kTq^2}$. Note that the expectation value of $\mathbf{a}_q(t)$ is zero, due to the expected value of the random force being zero.

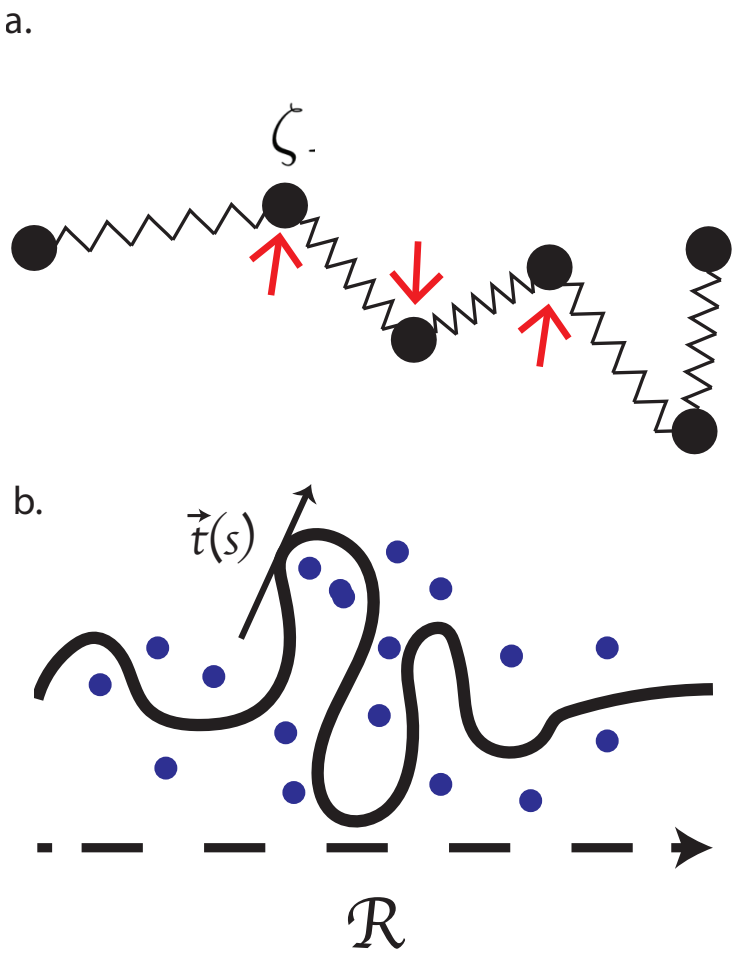


Figure 3.1: **Schematic Diagrams of Rouse and WLC models** Schematic diagrams of both the Rouse and inextensible worm-like chain models. In (a), the bead and spring model fitting the simplified polymer description. Each of the N beads is assumed spherical and large, such that it has a non-negligible drag coefficient given by $\zeta$. Force from the thermal bath, in red arrows, only exerts force on the beads and not the springs. The only energy in the system comes from the stretching of springs, not from bending. In (b), the continuous worm-like chain model is parameterized by arclength coordinate $s$. Central to the study of the WLC is the value of the tangent, $\vec{t}(s)$. A change in tangent with arclength induces bends. In the WLC model, bends are energetically unfavorable. The two models have the same end-to-end vector $\vec{R}$, in this case.

From here, we are interested in computing the expected value and correlation function for the tension $f(t)$ on either end of the Rouse chain. The last piece of mathematics needed is the correlation function of $\langle \mathbf{a}_p(t)\mathbf{a}_q(0)\rangle$, which is exactly the same as in the case of free ends, and can be shown analogously to be

$$\langle \mathbf{a}_p(t)\mathbf{a}_q(0)\rangle = \delta_{pq}\frac{3k_BT\tau_p}{\zeta}e^{-\frac{t}{\tau_p}} \tag{3.11}$$

Armed with these relations, we are ready to compute the expected tension and correlation of the boundary tension. For the expected value of the tension along the $\mathbf{R}$ axis, using Equation (3.10) and Equation (3.5) we find

$$\langle f(t)\rangle = \frac{3k_BT}{b^2}\langle\frac{dx}{dn}|_{0,N}\rangle = \frac{3k_BT}{b^2}\Big(\frac{R}{N} - \frac{2\pi}{N}\sum_{p=1}^{\infty} p\langle a_p(t)\rangle\cos(\pi p)\Big) = \frac{3k_BTR}{b^2N} \tag{3.12}$$

Where R is the norm of the end-to-end distance. For the correlation of tension along the $\mathbf{R}$ axis, we find:

$$\begin{aligned}\langle f(t')f(t'+t)\rangle = \frac{9(k_BT)^2}{b^4}\Big(\frac{R^2}{N^2} + \frac{4\pi}{N}\sum_{p=1}^{\infty} p\langle a_p(t)\rangle\cos(\pi p) + \\ \frac{4\pi^2}{N^2}\sum_{p=1}^{\infty}\sum_{q=1}^{\infty} pq\langle a_p(t)a_q(t+t')\rangle\cos(\pi q)\cos(\pi p)\Big)\end{aligned} \tag{3.13}$$

The second term in the brackets goes to zero because $\langle a_p(t)\rangle = 0$, whereas the double summation is simplified to a single summation by the delta function in the correlation of wave-mode amplitude terms. Substituting and subtracting the mean value, we find:

$$\langle f(t')f(t'+t)\rangle - \mathbf{E}[f]^2 = \frac{28(k_BT)^2}{b^2}\sum_{q=1}^{\infty} e^{-\frac{q^2t}{\tau_1}} \tag{3.14}$$

where we define the lowest Rouse relaxation mode $\tau_1 = \frac{N^2b^2\zeta}{3\pi^2k_BT}$. In the limit $t > \tau_1$, the higher

wave-modes in the summation deteriorate rapidly and the correlation is approximated by

$$\langle f(t')f(t'+t)\rangle - \mathbf{E}[f]^2 = \frac{28(kT)^2}{b^2} \tag{3.15}$$

In the opposing short time scale limit that $t < \tau_1$, we can approximate the summation as an integral because the wave-mode $p$ slowly varies the exponent. In this case, we have

$$\langle f(t')f(t'+t)\rangle - \mathbf{E}[f]^2 \approx \frac{28(k_BT)^2}{b^2}\int_1^\infty e^{-q^2t/\tau_1}dq \tag{3.16}$$

where the integral may be approximated by

$$\frac{28(k_BT)^2}{b^2N}\int_1^\infty e^{-q^2t/\tau_1}dq = \frac{14\sqrt{\pi}(k_BT)^2}{b^2\sqrt{t/\tau_1}}\,\mathrm{erfc}(\sqrt{t/\tau_1}) \approx \frac{14\sqrt{\pi}(k_BT)^2}{b^2\sqrt{t/\tau_1}} - \frac{28(k_BT)^2}{b^2} \tag{3.17}$$

where erfc(x) is the complementary error function. Finally, rearranging terms and substituting the value for the slowest Rouse relaxation time, we find for fast time scales $t < \tau_1$ that

$$\langle f(t')f(t'+t)\rangle - \mathbf{E}[f]^2 \approx \frac{14N(k_BT)^{3/2}\zeta^{1/2}}{\sqrt{3\pi}b}t^{-1/2} - \frac{28(k_BT)^2}{b^2} \tag{3.18}$$

Of surprise is that, as the lag time $t$ goes to zero, we find that the total variance of the tension goes to infinity. This indicates that the distribution of tensions on the end is heavy-tailed, and not well described by a Gaussian random variable. In the physical limit, however, there will never be a total divergence of the tension. Notably, the integral in Equation (3.16) does not extend to infinity; this would be equivalent to a continuous chain in which the bond length goes to zero. In real chains, the bond length always remains finite, and thus the wave modes must truncated after some value such that $1/q \sim b$. This truncation implies a finite variance in real chains, but still a heavy tailed distribution.

## 3.2 Inextensible Worm-Like Chains

Real biopolymers are not composed of discrete blocks, but have continuous length and drag associated with them. To first approximation, ignoring twisting and stretching that may occur from motion of the two monomeric chains, we set out to describe the tip-link dynamics analytically using the convenient worm-like chain (WLC) model. The model consists of a single continuous linear chain with no branch points. The position of any point along the chain is given by $\mathbf{r}(s)$, parameterized by an arclength $s$ that runs from 0 to $l_c$, the total contour length of the chain. Additionally, we may describe the tangent at any point $s$ as the arc-length derivative of the chain $\hat{\mathbf{t}} = \mathbf{r}'(s)$.

We introduce two physical parameters, the bending stiffness $\kappa$ and the drag coefficient $\hat{\zeta}$, which may have both longitudinal and transverse components with respect to the local tangent. One may think of the bending stiffness as a resistance to any turns or bends in the chain, and to lowest order the energy associated with bending is quadratic in the change in the tangent, $E_{bend} = \frac{\kappa}{2}\hat{\mathbf{t}}'^2$. Associated with the chain is a persistence length $l_p$ over which correlations in the tangent decline. The persistence length is defined exactly as $\langle \hat{\mathbf{t}}(s) \cdot \hat{\mathbf{t}}(s') \rangle = e^{-\frac{s'-s}{l_p}}$. The bending stiffness is directly related to the persistence length $l_p$ by $\kappa = k_B T l_p$ [109].

In low Reynolds number conditions, the effects of inertia may be considered subdominant to other relevant forces. This assumption immediately allows us to write a Langevin equation, expressing that at any point along the chain, all forces are balanced. That is,

$$0 = \sum F_i = F_{drag} + F_{WLC} + F_{therm} \tag{3.19}$$

where $F_{drag}$ is the drag force on a segment of the chain, $F_{WLC}$ is the force from internal bending and stretching of the chain, and $F_{therm}$ is a random thermal force often denoted $\xi$.

$F_{drag}$ is given by $F_{drag} = -\hat{\zeta}\partial_t \hat{\mathbf{r}}$, and where $\hat{\zeta} = \zeta_\perp(1 - \hat{\mathbf{t}} \otimes \hat{\mathbf{t}}) + \zeta_\parallel \hat{\mathbf{t}} \otimes \hat{\mathbf{t}}$ has been chosen to allow for separate drag coefficients parallel and perpendicular to the tangent. Likewise, the random thermal force is chosen such that the equation obeys the fluctuation-dissipation theorem, and can be modeled as a white noise process described by its mean

$$\langle \xi(s,t) \rangle = 0 \tag{3.20}$$

and variance

$$\langle \xi(s,t)\xi(s',t') \rangle = 2k_B T \hat{\zeta} \delta(s-s')\delta(t-t') \tag{3.21}$$

The force from the WLC may be constructed by considering the Hamiltonian of the system,

$$H_{\mathrm{WLC}} = \frac{1}{2} \int_0^{l_c} ds[\kappa \mathbf{r}''^2 + f(s,t)\mathbf{r}'^2] \tag{3.22}$$

which has contributions both from the bending stiffness and from a Lagrangian multiplier term enforcing the inextensibility constraint $\mathbf{r}'^2 = \mathbf{t}^2 = 1$. The force from the combined energetics of the WLC, then, is given by the functional derivative of $H$ with respect to the contour function $\mathbf{r}(s,t)$

$$F_{WLC} = -\frac{\delta H}{\delta \mathbf{r}} \tag{3.23}$$

The functional derivative may be defined for the following form of a functional $F(r) = \int L(s, \mathbf{r}, \mathbf{r}', \mathbf{r}'', ...)ds$ as [116]

$$\frac{\delta F}{\delta \mathbf{r}} = \frac{\partial L}{\partial \mathbf{r}} - \frac{\partial}{\partial s}\frac{\partial L}{\partial \mathbf{r}'} + \frac{1}{2}\frac{\partial^2}{\partial^2 s}\frac{\partial L}{\partial \mathbf{r}''} - ... \tag{3.24}$$

Inserting Equation (3.24) into Equation (3.23) and applying the definition given in Equation (3.22) we find:

$$F_{WLC} = -\kappa \mathbf{r}'''' + (f\mathbf{r}')' \tag{3.25}$$

where $f$ is identified as the backbone tension and is in general a function of both time and arclength, $f(s,t)$. Returning now to the Langevin equation, we may write a master equation that describes the motion of a chain in time and space. This equation is given as a stochastic partial-differential equation (SPDE) of the form

$$\hat{\zeta}\partial_t \mathbf{r} = -\kappa \mathbf{r}'''' + (f\mathbf{r}')' + \hat{\xi} \tag{3.26}$$

Solutions to this partial differential equation are in general difficult. We parameterize the problem using the semiflexible limit, in which the chain is predominantly in a straight configuration. In this instance, we may parameterize the curve by a transverse component $\mathbf{r}_\perp(s)$ and a longitudinal component $s - r_{||}(s)$. In the limit that we pull on the ends of the polymer with enough force to extend it, or conversely, if the polymer is only weakly bending, we may define a small parameter $\epsilon$ such that the bending is small, $(\partial_s \mathbf{r}_\perp)^2 = \mathcal{O}(\epsilon)$. Combining this with the inextensibility constraint, $(\partial_s \mathbf{r})^2 = 1$, we have:

$$\begin{aligned}
&\partial_s \begin{pmatrix} \mathbf{r}_\perp(s) \\ s - r_{||}(s) \end{pmatrix}^2 = \mathbf{r}_\perp'^2(s) + (1 - r_{||}'(s))^2 = 1 \\
&\Rightarrow 1 - r_{||}'(s) = \sqrt{1 - \mathbf{r}_\perp'^2(s)} \approx 1 - \frac{1}{2}\mathbf{r}_\perp'^2(s) + O(\epsilon^2) \\
&\Rightarrow r_{||}'(s) \sim \frac{1}{2}\mathbf{r}_\perp'^2(s) \text{ as } \epsilon \to 0
\end{aligned} \tag{3.27}$$

The total length of the polymer along the longitudinal axis is given by $l_c - \mathbf{r}_{||}(l_c)$, and the change in length from the fully extended length $l_c$ is $\mathbf{r}_{||}(l_c)$. This suggests that there is $\mathbf{r}_{||}'(s)$ length stored locally in thermal kinks, since $\int_0^{l_c} ds \mathbf{r}_{||}'(s) = \mathbf{r}_{||}(l_c) - \mathbf{r}_{||}(0) = \mathbf{r}_{||}(l_c)$. Using Equation (3.27), we can identify this stored-length density $\rho(s)$ as:

$$\rho(s) = \mathbf{r}'_{||}(s) \approx \frac{1}{2}\mathbf{r}'^2_{\perp}(s) \tag{3.28}$$

The stored-length density represents the local excess length stored in the random displacements away from the straight configuration. Intuitively, this indeed should be proportional to the tangent of $\mathbf{r}_\perp$, because when the tangent is large the polymer is facing away from the main axis (Figure 3.2). Once the stored-length density is solved, we may recover the end-to-end distance $R$ by $R = \int_0^{l_c} 1 - \rho(s)ds$.

For simplicity, we assume isotropic friction for the chain in the longitudinal and transverse direction. Doing so, we may expand Equation (3.26) in terms of its longitudinal and transverse components:

$$\begin{aligned}
\zeta\partial_t\mathbf{r}_\perp &= -\kappa\mathbf{r}''''_\perp + (f\mathbf{r}'_\perp)' + \xi_\perp \\
\zeta\partial_t\mathbf{r}_{||} &= \kappa\mathbf{r}''''_{||} - f' + (f\mathbf{r}'_{||})' - \xi_{||} - F_{||}(s)
\end{aligned} \tag{3.29}$$

Here $F_{||}(s)$ is externally applied tensions in the longitudinal direction, which will be of primary interest when we consider pulling on the chain at one or both ends. In the asymptotic limit that $\epsilon \to 0$, we may take the arclength derivative of the longitudinal component of Equation (3.29) and using Equation (3.27) find:

$$f''(s) = -\xi_{||} - F'_{||}(s) \tag{3.30}$$

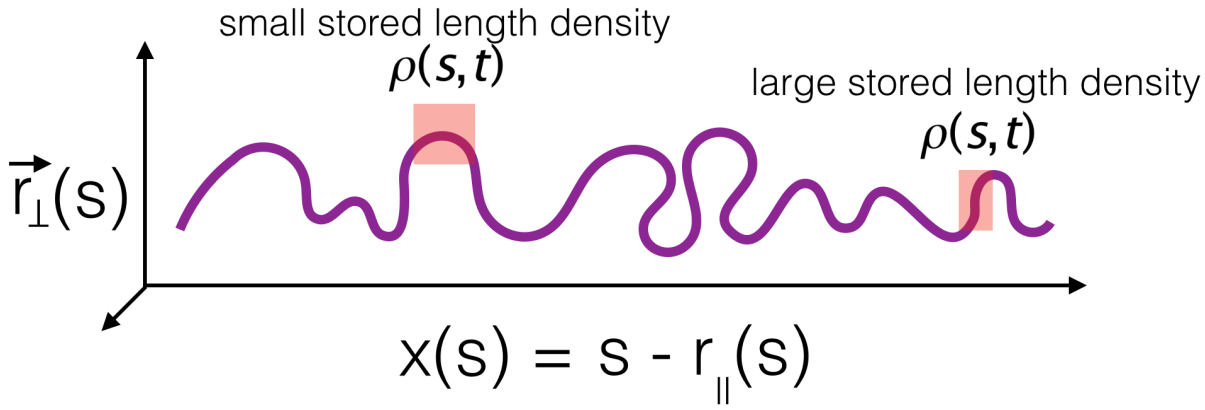


Figure 3.2: **Coordinate System of the WLC** The coordinate system of the WLC is taken to have tangental components, in the $\hat{r}_\perp$ direction, and longitudinal components, in the orthogonal direction to the perpendicular direction, or in the direction of the end-to-end distance vector $\vec{R}$. When the slope of $\hat{r}_\perp$ is small, the chain is directed mostly in the longitudinal direction, and has small amounts of length stored in thermal undulations. When the slope of $\hat{r}_\perp$ is large, there is significant arclength being stored in the transverse direction.

This equation corresponds to the zeroth-order expansion in $\epsilon$, and implies that the average tension along the backbone of the chain is linear at all times. For instance, if we pull the chain with equal and opposing forces in opposite directions, the tension is equilibrated instantly all along the chain. Clearly, this cannot be true; if tension were to propagate instantaneously across the chain, it would imply instantaneous rearrangement of configuration over the entire chain length and subsequently an infinite drag force. However, on small spatial scales, $\epsilon$ really is small, and Equation (3.30) becomes valid.

We solve Equation (3.29) to zeroth order, with $f(s)$ a constant given by $F(0) = F(l_c) = f$. After taking the thermal average, Equation (3.29) becomes:

$$\zeta \partial_t \mathbf{r}_\perp(s,t) = -\kappa \mathbf{r}_\perp''''(s,t) + f\mathbf{r}_\perp''(s,t) \tag{3.31}$$

where we have included back the arclength and time dependence of $\mathbf{r}_\perp(s,t)$. Using a Fourier decomposition of the form

$$\mathbf{r}_{\perp}(s,t) = \sum_{q} \mathbf{u}_q(t)\sin\big(qs\big) \tag{3.32}$$

and substituting into Equation (3.31) yields a modal decomposition of the form:

$$\begin{aligned} \zeta\partial_t \mathbf{u}_q(t) &= -\kappa q^4 \mathbf{u}_q(t) - fq^2\mathbf{u}_q(t) \\ \Rightarrow \mathbf{u}_q(t) &\propto e^{-\frac{\kappa q^4 + fq^2}{\zeta}t} \end{aligned} \tag{3.33}$$

From the equipartition of energy, each wave mode acts as an independent degree of freedom. The energy of each wave mode can be solved by Fourier decomposition of Equation (3.22), and is given by [109]:

$$E_q = \frac{l_c}{4}\Big(\kappa q^4 + fq^2\Big)\langle u_q^2\rangle = \frac{k_b T}{2} \tag{3.34}$$

Combining Equation (3.34) and Equation (3.33) gives:

$$\begin{aligned} \langle \mathbf{u}_q(t)\mathbf{u}_q(0)\rangle &= \frac{2k_bT}{l_c(\kappa q^4 + fq^2)}e^{-t/\tau(q)} \\ \text{with } \tau(q) &= \frac{\zeta}{q^2(\kappa q^2 + f)} \end{aligned} \tag{3.35}$$

Low-wavelength modes (small $q$) of the chain come to equilibrium much slower than higher wavelengths. On average, the long-wavelength undulation modes contain the majority of the stored-length, and also are the ones that relax to thermal equilibrium the slowest. Under no tension, the time constant of this decay scales as $\tau \sim q^{-4}$, and thus long-wavelength modes predominantly set the limit on relaxation. The effect of tension acts to lower the time constant associated with long-wavelength relaxation, such that when $q$ is such that $\kappa q^2 \ll f$, $\tau \sim q^{-2}$.

Before moving onto a full solution to the zeroth order partial-differential equation, we consider the effect of tension on a semiflexible polymer using the same arguments as in Section 2.3. In this case, we find that tension significantly changes the amplitude of only the longest wavelength, that is, of wave modes such that $\kappa q^2 < f$. Because wave-mode $q$ corresponds to a wavelength of $\lambda_q$, we may posit that there exists a wave-mode $q$ such that for wave modes greater than $q$, the effects of tension are negligible, whereas above $q$, the effects of tension are outweighed by the intrinsic bending energy. This suggests a separation of length scales when $l_{\text{blob}} \approx \sqrt{\frac{\kappa}{f}}$, or in terms of the persistence length:

$$l_{\text{blob}} \approx \sqrt{\frac{k_B T}{l_p f}} \tag{3.36}$$

This scaling is qualitatively different than that found for the generalized FJC with scaling parameter $\nu$. This is because the interaction energy is short range rather than long range.

## 3.3 Formal Solution of $\mathbf{r}_\perp$

The formal solution to Equation (3.31) is found by the method of Green's functions. The Green's function $G(s, s', t, t')$ satisfies the equation:

$$\big(\zeta \partial_t + \kappa \partial_s^4 - f(t)\partial_s^2\big) G(s, s', t, t') = \delta(s - s', t - t') \tag{3.37}$$

where we have introduced a possible time dependence in the chain tension $f(t)$. Multiplication by $\xi(s', t')$ and subsequent integration over $s' \in (0, l_c)$ and $t' \in (-\infty, \infty)$ recovers Equation (3.31), and thus a solution to $\mathbf{r}_\perp(s, t)$ is given by:

$$\mathbf{r}_\perp(s, t) = \int_0^{l_c} ds' \int_{-\infty}^{\infty} dt' G(s, s', t, t') \xi(s', t') \tag{3.38}$$

In the bulk of the chain, the Green's function is invariant to shifts in position, and is thus a function of $G(s-s') \equiv G(s)$. Solving Equation (3.37) is more readily transparent in the Fourier domain, where:

$$(\zeta_\perp \partial_t + \kappa q^4 + f(t)q^2)\bar{G}(q,t,t') = \delta(t-t') \tag{3.39}$$

since $\int_{-\infty}^{\infty} ds\delta(s)e^{-iqs} = 1$. The equation is solved by the method of integration factors, whereby the solution to the equation below is given by:

$$\partial_x y(x) + p(x)y(x) = q(x) \tag{3.40}$$

$$\Rightarrow y(x) = e^{-v(x)} \int e^{v(x)} q(x) dx \tag{3.41}$$

where $v(x) = \int p(x)dx$. Solving Equation (3.39) using this formula gives:

$$\bar{G}(q,t,t') = \frac{1}{\zeta_\perp} e^{-\int_{t'}^{t} q^2(\kappa q^2 + f(t'))/\zeta_\perp} \tag{3.42}$$

which may be inverted to recover $G(s,t,t')$:

$$G(s,t,t') = \int_0^\infty dq \bar{G}(q,t,t')\cos\big(qs\big) \tag{3.43}$$

## 3.4: Formal Solution of $\langle \Delta\rho \rangle$

The stored-length density is related to the transverse displacement by Equation (3.28). Of primary interest is the change in stored-length density, $\Delta\rho(s,t) = \rho(s,t) - \rho(s,0)$, caused by a change in tension along the chain $f(t)$. From the change in stored-length density, it is trivial to recover the change in the end-to-end distance of the chain $\Delta R$, which may be recovered by integrating $\Delta\rho(s,t)$ along the length of the chain. Taking the arclength

derivative of Equation (3.38), we may express Equation (3.28) as:

$$\rho(s,t) = \frac{1}{2}\int_0^{l_c} ds' \int_{-\infty}^{t} dt' \int_0^{l_c} ds'' \int_{-\infty}^{t} dt'' \partial_s G(s,s',t,t') \partial_s G(s,s'',t,t'') \vec{\xi}_\perp(s',t') \cdot \vec{\xi}_\perp(s'',t') \tag{3.44}$$

This equation may be solved for a particular random spatiotemporal white noise $\vec{\xi}$ by naive Monte Carlo integration. If we are only interested in the mean value, however, we may compute the thermal average $\langle \rho(s,t) \rangle$, which using Equation (3.21) gives:

$$\langle \rho(s,t) \rangle = 2k_B T \zeta_\perp \int_0^{l_c} ds' \int_{-\infty}^{t} dt' \partial_s G^2(s,s',t,t') \tag{3.45}$$

Using $k_B T = \kappa / l_p$ and Equation (3.42) we can write the stored-length density in the $q$-domain:

$$\langle \bar{\rho}(s,t) \rangle = \frac{2q^2 \kappa \zeta_\perp}{l_p} \int_{-\infty}^{t} \bar{G}^2(q,t,t') dt' \tag{3.46}$$

The stored-length density, then, is simply the inverse Fourier transform:

$$\langle \rho(s,t) \rangle = \frac{2\kappa}{\zeta_\perp \pi l_p} \int_0^{\infty} q^2 dq \int_{-\infty}^{t} dt' e^{-2q^2(\kappa q^2 (t-t') + \int_{t'}^{t} f(t'') dt'')/\zeta_\perp} \tag{3.47}$$

Where the $\cos(sq)$ term is negated away from the boundaries [85].

We consider the case where the force is held constant at $f_0$ during $t \in (-\infty, 0]$, and thereafter the force is allowed to have time dependence $f(t)$. We alternatively will refer to $f_0$ as the prestress, or the resting tension at which the polymer is held before we begin an experiment or analysis. Because $f(t)$ is constant throughout the chain in this approximation, $f(t)$ is equivalently the force at which we pull on the chain. To find the change in stored-length density, then, we take:

$$\begin{aligned}\langle \Delta\rho(s,t)\rangle &= \langle \rho(s,t)\rangle - \langle \rho(s,0)\rangle \\ &= \frac{2\kappa}{\zeta_\perp \pi l_p}\int_0^\infty dq\Big\{q^2\int_{-\infty}^{t} dt' e^{-2q^2(\kappa q^2(t-t')+\int_{t'}^{t} f(t'')dt'')/\zeta_\perp} - \frac{1}{q^2+f_0/\kappa}\Big\} \\ &= \frac{1}{\pi l_p}\int_0^\infty dq\Big\{\frac{e^{-2q^2[q^2t\kappa+F(s,t)]/\zeta_\perp}-1}{q^2+f_0/\kappa} + \frac{2q^2\kappa}{\zeta_\perp}\int_0^t dt' e^{-2q^2[q^2\kappa(t-t')+F(s,t)-F(s,t')]/\zeta_\perp}\Big\}\end{aligned}$$

where we have split the time integral into two subsets, $t' \in (-\infty, 0]$ and $t' \in [0, t]$ and defined the time integrated tension $F(t) = \int_0^t dt f(t)$.

This integral equation can be solved for any temporal form of pulling tension $f(t')$, and consists of two parts. We consider the reference frame at time $t > 0$ where $f(t') \neq f_0$ for some $t' \in (0, t]$. From here, the first component depends only on the current value of the time integrated tension, $F(t)$, and decays rapidly to $\frac{1}{q^2+f_0/\kappa}$. If we consider a constant pulling tension $f(t') = f \neq f_0$, then $F(t) = ft$ and the term decays rapidly towards a time-independent constant as long as the wave-mode $q$ is large. When $q$ is small, or equivalently for large-wavelength modes, the exponential term decays as $e^{-2q^2t[q^2\kappa+f]/\zeta_\perp}$. Comparing this term to Equation (3.35), we find the decay rate is equivalent to the simplified linear averaged equation where we did not consider the effects of Brownian motion on the system. This first term in Equation (3.28), then, can be thought of as deterministic relaxation of the chain to its new length, where the wavelength-dependent relaxation time scales as $\tau(q) = \frac{\lambda^4}{(\kappa+f\lambda^2)}$. The effect of increasing tension is to suppress the scaling of relaxation time with wavelength, causing long wavelength modes to come to equilibrium much faster. This conclusion is identical to that which we found in Section 3.2.

The second part of Equation (3.28) is dependent on the entire history of the pulling tension $f(t')$, and introduces hysteresis into the system. It may be thought of as the average response of the system to Brownian motion, which due to the nonlinearity of the system still enter into the dynamics of the average response [117]. The exponential decay with respect to time elapsed, $t - t'$, reflects the intuitive notion that more recent tension values – again,

from the reference frame of time t – are most important in describing the system. This decay, however, is again complicated by the existence of small wavemode $q$, corresponding to long-wavelength amplitudes that retain pertinent memory of the entire tension history. As $t$ increases, the number of wavemodes that retain a long memory scales anywhere from $q \propto t^{1/2}$ to $q \propto t^{1/4}$, depending on the force. Due to the nature of this slow decay, the second term cannot be easily approximated, and reflects the long-term memory of long wavelength modes.

There is a logical fallacy in the solution to the stored-length density: it is independent of arclength $s$. The logical inconsistency becomes more readily apparent when considering the change in total length of the chain, given by:

$$\langle \Delta R \rangle = \int_0^{l_c} ds \langle r'_{||}(s,0) - r'_{||}(s,t) \rangle = -\int_0^{l_c} ds \langle \Delta\rho(s,t) \rangle = -l_c \langle \Delta\rho(t) \rangle \tag{3.48}$$

where in the last operation we used the arclength independent property of Equation (3.28). The only way for the chain to gain end-to-end distance is through motion of its internal elements a distance $l_c\langle\Delta\rho(t)\rangle$. In the case where the chain length $l_c$ is very large, any minute change in the stored-length density results in a large change in end-to-end distance, creating drag force roughly equal to $F_{\text{drag}} \approx \zeta_{||} l_c^2 \partial_t \langle \Delta\rho(t) \rangle$. By definition, the only force that can do work on the system to extend the chain is the pulling force $f(t)$, which is finite and positive definite. The drag force, then, can never exceed this pulling force, or else the chain would be drawing energy from the bath in an unphysical way. In order for $F_{\text{drag}}(t) \leq f(t)$ for all $t$, it cannot be true that the stored-length density is changing everywhere along the chain instantaneously. Instead, only a subsection of the chain $l_{||}(t)$ can change its stored-length density, corresponding to a time-dependent boundary layer of tension propagation through the chain. In other words, the simple linearized system suggests that that a tension change cannot propagate instantaneously throughout a polymer, and that there must be some time delay associated with dragging the chain through solution.

In the following sections, we elaborate on the predictions of this model for the case of

fast ramping of a pulling force, and ask how long it takes for tension to become equilibrated along the entire length of a chain.

## 3.4 Asymptotic Expansion of $\langle \Delta\rho(t) \rangle$

The exact scaling of the boundary layer $l_{||}(t)$ with time is determined by calculating the change in stored-length density along the chain, and setting the drag force induced by this stored-length change to the pulling force $f(t)$. This leads to results consistent with higher order approximations, and provides a convenient shortcut to understand tension propagation.

We begin by recapitulating the result for the change in stored-length density of a chain where at time $t = 0$, the pulling force at one end suddenly changed from $f_{t<0} = 0$ to $f_{t\geq 0} = f$. For ease of calculation, we work with redimensionalized units, taking $f \to \kappa f$ and $t \to \zeta_\perp t/\kappa$. Solving Equation (3.28) for $f_0 = 0$ and $f(t) = f$ yields:

$$\langle \Delta\rho(t) \rangle = \frac{1}{\pi l_p} \int_0^\infty dq \frac{f}{q^2(q^2+f)} (e^{-2q^2(q^2+f)t} - 1) \tag{3.49}$$

The addition of a resting tension results in a qualitative shift in the form of the stored-length density. We modify the stored-length density to have both a nonzero prestress term and nonzero pulling force. We find the change in stored-length density (with respect to the length density at time $t = 0$) to be of the form

$$\langle \Delta\rho(t) \rangle = \frac{1}{\pi l_p} \int_0^\infty dq \frac{f - f_0}{(q^2+f)(q^2+f_0)} (e^{-2q^2(q^2+f)t} - 1) \tag{3.50}$$

We examine the two asymptotic limits of Equation (3.50), where $t \to 0$ and $t \to \infty$. In the first case, as $t$ becomes small, we may easily find the correct asymptotic limit of $\langle \Delta\rho(t) \rangle$ by a clever change of variables $q^2 = k^2 f$ and $\tau = f^2 t$, which gives

$$\langle \Delta\rho(t) \rangle = \frac{f - f_0}{\pi l_p} \int_0^\infty dq \frac{1}{\sqrt{f}(fk^2 + f_0)(k^2 + 1)} (e^{-2k^2(k^2+1)\tau} - 1) \tag{3.51}$$

Transforming variables again to $\hat{k} = k\tau^{1/4}$ gives

$$\langle \Delta\rho(t) \rangle = \frac{f - f_0}{\pi l_p} \int_0^\infty dk \frac{1}{\tau^{1/4}\sqrt{f}(\frac{f\hat{k}^2}{\tau^{1/2}} + f_0)(\frac{\hat{k}^2}{\tau^{1/2}} + 1)} (e^{-2\hat{k}^2(\frac{\hat{k}^2}{\tau^{1/2}}+1)\tau^{1/2}} - 1) \tag{3.52}$$

which reduces in the asymptotic limit $\tau \to 0$ to

$$\langle \Delta\rho(t) \rangle \sim -\frac{t^{3/4}(f - f_0)}{\pi l_p} \int_0^\infty d\hat{k} \frac{(1 - e^{-2\hat{k}^4})}{\hat{k}^4} \tag{3.53}$$

In the final equation, we have replaced $\tau$ with $f^2 t$ and moved all variables outside of the integral. The integral may be solved numerically, and gives a value of 2.03251.

In the asymptotic limit that $t \to \infty$, a similar rescaling approach may be attempted. This time, we start from Equation 3.50, and now define a different variable transform $\bar{k} = k\tau^{1/2}$. Doing so gives

$$\langle \Delta\rho(t) \rangle = \frac{f - f_0}{\pi l_p} \int_0^\infty d\bar{k} \frac{1}{\tau^{1/2}\sqrt{f}f_0(\frac{f\bar{k}^2}{f_0\tau} + 1)(\frac{\bar{k}^2}{\tau} + 1)} (e^{-2\bar{k}^2(\frac{\bar{k}^2}{\tau}+1)} - 1) \tag{3.54}$$

which reduces in the asymptotic limit that $\tau \to \infty$ to

$$\langle \Delta\rho(t) \rangle \sim -\frac{f - f_0}{t^{1/2} f^{3/2} f_0 \pi l_p} \int_0^\infty d\bar{k} (1 - e^{-2\bar{k}^2}) \tag{3.55}$$

The scaling of the change in stored-length density is easily seen in this form. Regrettably, Equation (3.55) is insufficient for our calculations, due to the divergence of the integral $\int_0^\infty dx(1 - e^{-2x^2}) \to \infty$. This is not actually a problem for the convergence of the change in stored-length density, for the $t^{1/2}$ in the denominator is also going to infinity. In order for the change in stored-length density to be bounded, we must require that the limit

$$\lim_{t\to\infty} \frac{\int_0^\infty d\bar{k}(1-e^{-2\bar{k}^2})}{t^{1/2}} \sim N \tag{3.56}$$

where $N$ is bounded. This immediately implies that the divergent integral scaling is bounded by $t^{1/2}$, but may also scale more slowly. To first order, then, the stored-length density change may be written as

$$\langle \Delta\rho(t) \rangle \sim N \frac{f - f_0}{f^{3/2} f_0 \pi l_p} \tag{3.57}$$

where $N$ is some number that might be dependent on other parameters. Clearly, this asymptotic form is not useful, as we have lost the time dependence of the stored-length density. Instead, we use a different approach in order to approximate the integral from the original Equation (3.50). First, we examine the integrand $I(q) = -\frac{1-e^{-2q^2(q^2+f)t}}{(q^2+f)(q^2+f_0)}$ and note that in the limit $t \to \infty$, the exponent in the numerator is very close to zero, except when $q$ is also close to 0. This suggests that we split the integral into two parts,

$$\frac{f - f_0}{\pi l_p} \int_0^\infty dq I(q) = \frac{f - f_0}{\pi l_p} \Big[ \int_0^\delta dq I(q) + \int_\delta^\infty dq I(q) \Big] = \frac{f - f_0}{\pi l_p} (I_1 + I_2) \tag{3.58}$$

where $\delta \to 0$ as $t \to \infty$.

We approach the $I_2$ term first, as it will set a lower bound for $\delta$. In the limit that $t \to \infty$ and sufficiently large $\delta$, $I_2$ may be approximated as

$$I_2 = -\int_\delta^\infty dq \frac{1 - e^{-2q^2(q^2+f)t}}{(q^2+f)(q^2+f_0)} \sim -\int_\delta^\infty dq \frac{1}{(q^2+f)(q^2+f_0)} \tag{3.59}$$

How large should $\delta$ be such that this asymptotic approximation is valid? The requirement that the exponential term be much less than 1 sets a minimum bound on $\delta$. By requiring that $2\delta^2(\delta^2+f)t > 1$ as $t \to \infty$, $\delta$ must scale at least as fast as $t^{-1/2}$. More precisely, if we

set some value $a > 1$, and assume $\delta^2 \ll f$, we find that $\delta \sim \sqrt{\frac{a}{2tf}}$ as $t \to \infty$. $I_2$ can now be approximated as

$$\begin{aligned} I_2 &\sim -\int_{\delta}^{\infty} \frac{dq}{(q^2+f)(q^2+f_0)} = -\int_{0}^{\infty} \frac{dq}{(q^2+f)(q^2+f_0)} + \int_{0}^{\delta} \frac{dq}{(q^2+f)(q^2+f_0)} \\ &= -\frac{\pi}{2(f\sqrt{f_0}+f_0\sqrt{f})} + \int_{0}^{\delta} \frac{dq}{(q^2+f)(q^2+f_0)} \sim -\frac{\pi}{2(f\sqrt{f_0}+f_0\sqrt{f})} + \frac{\delta}{ff_0} \\ &\sim -\frac{\pi}{2(f\sqrt{f_0}+f_0\sqrt{f})} + \frac{a^{1/2}}{\sqrt{2}t^{1/2}f^{3/2}f_0} \text{ as } t \to \infty \end{aligned} \tag{3.60}$$

At this point, it is notable that the integral has two very different components that have been uncovered from the asymptotic approximation. The first component is time-independent, as predicted by our original analysis. The second component, however, is explicitly dependent on time, and gives a scaling similar to that found Equation (3.55).

To finish the problem, we must also find $I_1$. This is an easier exercise, as the integral is, in the limit $\delta \to 0$, asymptotic to

$$I_1 = -\int_{0}^{\delta} dq \frac{1-e^{-2q^2(q^2+f)t}}{(q^2+f)(q^2+f_0)} \sim -\int_{0}^{\delta} dq \frac{2q^2ft}{ff_0} \sim -\frac{a^{3/2}}{3\sqrt{2}t^{1/2}f^{3/2}f_0} \text{ as } t \to \infty \tag{3.61}$$

Note that the asymptotic approximation for this integral is valid only in the case that $\delta^2(\delta^2+f)t < 1$, that is, that the exponent is small. Under this assumption, then, we find the constraint that $\delta \sim \sqrt{\frac{a}{2tf}}$ where $a < 1$. Comparing the two definitions for the asymptotic form of $\delta$, we find that our approximation for $I_1$ sets an upper bound for $\delta$, whereas $I_2$ sets a lower bound for $\delta$. This at first seems problematic, for we cannot have both $a > 1$ and $a < 1$. However, we note that in the limit $t \to \infty$, the actual value of $\delta$ becomes asymptotically close to 0, and thus the overlap region in which our approximations fails also approaches zero. In fact, the region of error converges for large t much faster than $\delta$, and corresponds

to a higher order correction in our asymptotic expression. This suggests that we choose the natural midpoint for the two asymptotic forms of $\delta$, namely, that $a = 1$. Figure 3.2 shows the validity of these approximations by examining the integrand values over several values of time and for difference force conditions $f_0 = 1$ and $f = 2, 10$. Indeed, as $t$ becomes large, the value of $\delta$ becomes small, and the region in which the two limits fail to overlap approaches zero. The approximation that $I_2 \approx -\int \frac{1}{(q^2+f)(q^2+f_0)}$ is extremely accurate for most values of $q > (2tf)^{1/2}$, while the approximation that $I_1 \approx -\int \frac{2q^2t}{f_0}$ incurs small errors close to $q = (2tf)^{1/2}$.

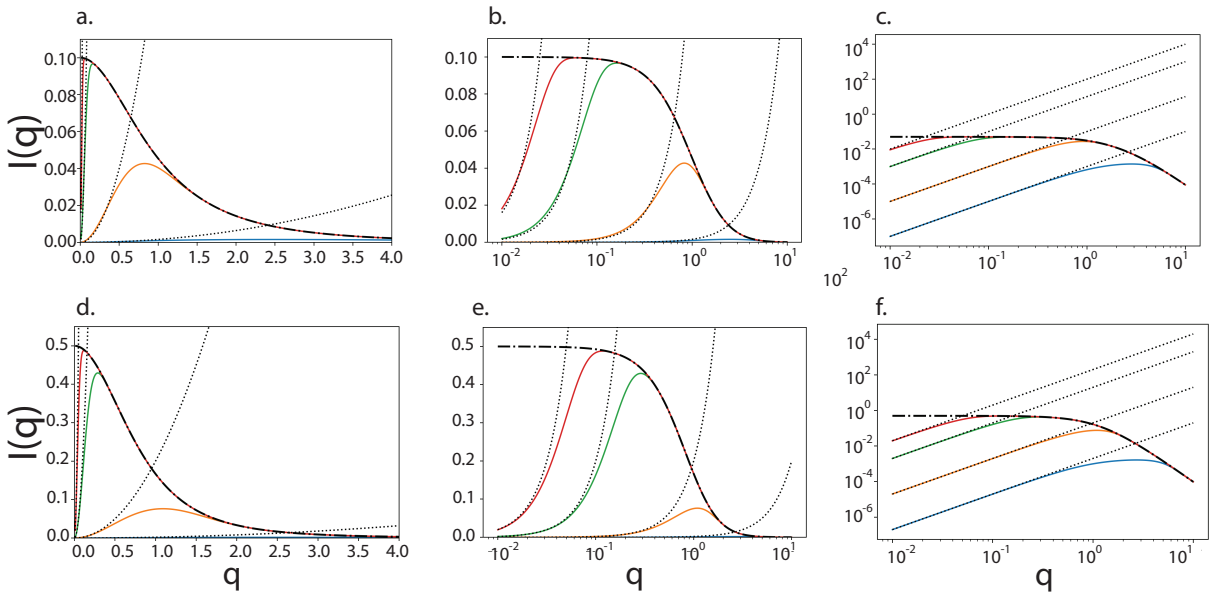


Figure 3.3: **Integrand Scaling with Wave Mode** Validity of the approximations to the integrands used in Equations (3.59 and 3.61), where we replaced the exponential form with the large or small $q$ limit. In color, numerical solutions to Equation (3.50), at times t = 0.001, 0.1, 10, and 100 (blue, orange, green, red). Overlaid in dashed, the large $q$ approximation to the integrand used in Equation (3.59). In dotted, the small $q$ approximation to the integrand given in Equation (3.61). In (a,b,c), alternative views in linear, semi-logrithmic, and logrithmic coordinates of the $f_0 = 2$, $f = 10$ condition. In (d,e,f), we examined different parameters $f_0 = 1$, $f = 2$ to show the robustness of our approximation to changes in force scales. In all cases, the small $q$ approximation diverges quickly from the numerical solution curves. The large-$q$ approximation is robust after a critical point, and represents an increasing portion of the curve as $t$ increases.

Finally, combining our approximations with Equation (3.58) and restoring physical units, we find

$$\langle \Delta\rho(t) \rangle \sim -\frac{\kappa^{1/2}(f - f_0)}{2l_p(f\sqrt{f_0} + f_0\sqrt{f})} + \frac{\sqrt{2}\kappa\zeta_\perp^{1/2}(f - f_0)}{3\pi f^{3/2} f_0 t^{1/2} l_p} + \mathcal{O}(t^z) \text{ as } t \to \infty \tag{3.62}$$

where $z < -1/2$.

Equation (3.62) is our main novel result for the asymptotic scaling of the stored-length density, and assumes that both $f$ and $f_0$ do not approach zero but remain finite. Equation (3.62) thus does not collapse onto known scaling forms when setting $f_0$ to 0 [85]. As $t \to \infty$, the second term of Equation (3.62) decays away while the first term remains constant with time. After some algebra, we find $\lim_{t\to\infty} \langle \Delta\rho(t) \rangle = -\frac{\kappa^{1/2}/2l_p}{(\sqrt{f} - \sqrt{f_0})}$. This may be directly compared with the high force limit of the WLC model:

$$R(f) = l_c \Big[ 1 - \frac{1}{2} \Big( \frac{\kappa}{l_p^2 f} \Big)^{1/2} \Big] \tag{3.63}$$

and taking the change in end-to-end distance:

$$\Delta R(f, f_0) = l_c \frac{\kappa^{1/2}/2l_p}{(\sqrt{f} - \sqrt{f_0})} \tag{3.64}$$

Since in the large-$t$ limit the tension should be equilibrated everywhere along the chain, our asymptotic approach recovers the predicted worm-like chain behavior. In addition, our result gives additional information about the long timescale relaxation of the chain, and shows how the stored-length changes in the limit that $t$ becomes large.

To review, we have solved for the change in the stored-length density in both the large- and small-$t$ limits:

$$\langle \Delta\rho(t) \rangle \sim -2.033 \frac{t^{3/4}(f - f_0)}{\pi l_p \kappa^{1/4} \zeta_\perp^{3/4}} \text{ as } t \to 0$$

and

$$\langle \Delta\rho(t) \rangle \sim -\frac{\kappa^{1/2}(f - f_0)}{2l_p(f\sqrt{f_0} + f_0\sqrt{f})} + \frac{\sqrt{2}\kappa\zeta_\perp^{1/2}(f - f_0)}{3\pi f^{3/2} f_0 t^{1/2} l_p} + \mathcal{O}(t^z) \text{ as } t \to \infty \tag{3.65}$$

Figure 3.4 shows the validity of these approximations for several values of $f$ and $f_0$, in comparison to the exact numerical solution to Equation (3.49). While examining the approximate forms, we found that adjusting the numerical factors slightly significantly extended the validity of each individual approximation. In particular, we used the updated forms:

$$\langle \Delta\rho(t) \rangle \sim -2.435 \frac{t^{3/4}(f - f_0)}{\pi l_p \kappa^{1/4} \zeta_\perp^{3/4}} \text{ as } t \to 0$$

and

$$\langle \Delta\rho(t) \rangle \sim -\frac{\kappa^{1/2}(f - f_0)}{2l_p(f\sqrt{f_0} + f_0\sqrt{f})} + \frac{6}{5}\frac{\sqrt{2}\kappa\zeta_\perp^{1/2}(f - f_0)}{3\pi f^{3/2} f_0 t^{1/2} l_p} + \mathcal{O}(t^z) \text{ as } t \to \infty \tag{3.66}$$

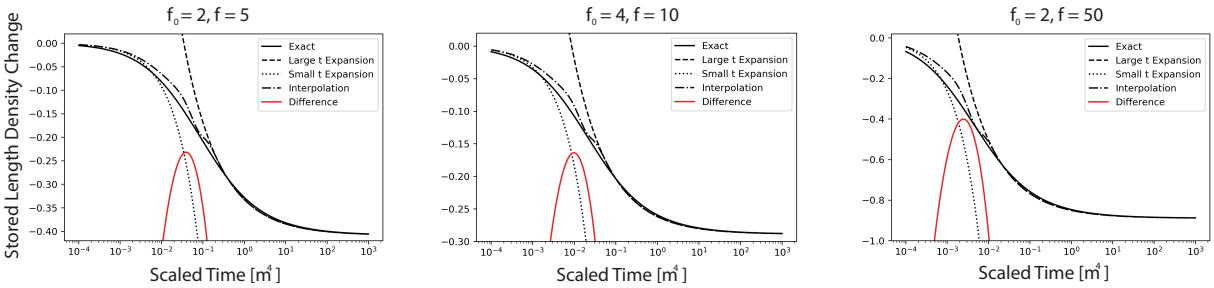


Figure 3.4: **Validity of Asymptotic Approximations** Numerical solutions to Equation (3.50) along with the asymptotic approximations in the small- and large-$t$ limits given by Equations (3.66). In solid black, the exact solutions for three test conditions ($f_0 = 2$, f = 5), ($f_0 = 4$, f = 10), ($f_0 = 2$, f = 50), chosen to widely sample possible resting and pulling tension dependence of validity. In all conditions, the large $t$ asymptotic expansion (dashed line) yielded impressive results for the long-term behavior of the stored-length density, confirming our scaling dependencies. The small-$t$ asymptotic expansion diverges quickly. The two expansions undergo strong divergence before they cross over at time $t_c$, where the two expansions are have the smallest difference (red). The strong divergence leads to complications in asymptotic matching techniques. Since the order of scaling is known for each approximation, we employed a exponential suppression of the each term which matches the time scaling of the individual asymptotic expansion (see Equation 3.68). In dotted dash, the interpolation is shown, which retains many of the characteristics of the small and large asymptotic regimes and closely matches the exact value. The interpolation is not sufficient to gain insight into the boundary layer behavior in the intermediate regime, due to artificial variations in the slope close to time $t_c$.

Figure 3.4 shows that a significant region exists where both of these approximations fail. This corresponds to the intermediate scaling region, which depend nontrivially on both $f$ and $f_0$. Due to the divergence of each asymptotic regime outside of the area of validity, the difference between the two approximations is maximal exactly at this intermediate time point. Solving for the maximal value, we find the crossover time $t_c$ occurs at:

$$t_c = \left(\frac{4\sqrt{2}}{15}\right)^{4/5} \frac{\kappa\zeta_\perp}{2.038 f^{6/5} f_0^{4/5}} \tag{3.67}$$

Through the method of matched asymptotic expansions, we may interpolate between these

two expansions in order to construct an approximate form that is valid over all time [154]. Beyond the crossover time, the small-$t$ expansion grows as $t^{3/4}$, whereas before the crossover time, the large-$t$ expansion grows as $t^{-1/2}$. In order to suppress these effects, we construct the following solution:

$$\langle \Delta\rho(s,t)\rangle \approx -2.435\frac{t^{3/4}(f-f_0)}{\pi l_p \kappa^{1/4}\zeta_\perp^{3/4}}e^{-(t/t_c)^{4/3}} - \Big[\frac{\kappa^{1/2}(f-f_0)}{2l_p(f\sqrt{f_0}+f_0\sqrt{f})} - \frac{6}{5}\frac{\sqrt{2}\kappa\zeta_\perp^{1/2}(f-f_0)}{3\pi f^{3/2}f_0 t^{1/2}l_p}\Big]\big(1-e^{-(t/t_c)^2}\big) \tag{3.68}$$

which is approximately valid over all time.

## 3.5 Boundary-Layer Dynamics

In order to gain more insight into the boundary-layer dynamics, we review the heuristic argument made in the previous section, and combine the predictions made for the asymptotic scaling of $\langle\Delta\rho\rangle$ with the approximate force-balance constraint. Again, the pulling force $f$ sets a limit on the drag force of a filament. That is, as the stored-length density changes uniformly along the bulk of the chain, it results in a longitudinal drag that must be less than or equal to the pulling force. This condition may be expressed as

$$f \geq -\zeta_{||} l_c \int_0^{l_c} \partial_t\langle\Delta\rho(t)\rangle = -\zeta l_c^2 \partial_t\langle\Delta\rho(t)\rangle \tag{3.69}$$

Clearly, this condition can only be met if $l_c$ remains finite - that is, for an infinitely long semi-flexible chain, this condition is never met. This implies that the the bulk value of the stored-length density change must break down at some length $l_{||}(t)$. Physically, this implies that tension does not propagate instantaneously down the length of the chain. Rather,

a boundary layer denoted by $l_{\|}(t)$ grows, over which tension has propagated. $l_{\|}(t)$ grows monotonically with $t$, until it reaches the other end of the chain, at which point tension has now equilibrated over the entire chain. We calculate the values of $l_{\|}(t)$ for the prestressed condition in the small and large time limit from Equation (3.66) and find

$$\begin{aligned} l_{\|}(t) &\sim N_0 t^{1/8} \sqrt{\frac{f\kappa^{1/4} l_p \hat{\zeta}}{\zeta_{\perp}^{1/4}(f-f_0)}} \text{ as } t \to 0 \\ l_{\|}(t) &\sim N_{\infty} t^{3/4} \sqrt{\frac{f^{5/2} f_0 l_p \hat{\zeta}}{\zeta_{\perp}^{3/2}\kappa(f-f_0)}} \text{ as } t \to \infty \end{aligned} \tag{3.70}$$

Where $\hat{\zeta}$ is the possible non-unity value of the ratio of the transverse and longitudinal drag coefficients $\zeta_{\perp}/\zeta_{||}$, and $N_0$ and $N_{\infty}$ are numerical factors of approximate value 1.312 and 3.333 respectively.

At some critical time $t_c$, the two asymptotic approximations cross and become equivalent. This happens at

$$t_c = \left(\frac{N_0}{N_{\infty}}\right)^{8/5} \frac{\zeta_{\perp}\kappa}{f^{6/5} f_0^{4/5}} \tag{3.71}$$

which is the exact result we found previously for the critical point where the two asymptotic approximations have the smallest difference. We may also define a new time, $t^*$, which is the total time it takes the tension to propagate down the length of the chain such that $l_c \approx l_{||}(t^*)$. As long as $t_c$ is much less than the time $t^*$ for the $t \to \infty$ asymptotic regime, then we may assume that the critical time $t^*$ is well approximated by the $\lim_{t\to\infty} l_{||}$ form of Equation (3.70). This limit is given by $t_c < t^*$, or rewriting it into a parameter we label $H = t_c/t^*$, our condition reads $H < 1$ . The exact form of $H$ is given by

$$H = \frac{N_0^{8/5} \kappa^{1/3} f^{7/15} l_p^{2/3} \hat{\zeta}^{2/3}}{N_{\infty}^{4/15} l_c^{4/3} f_0^{2/15} (f-f_0)^{2/3}} \tag{3.72}$$

We find that at almost all values for the resting tension $f_0$ and reasonable changes in force such that $\delta f = |f - f_0|$ is non-negligible, that the value of the $H$ parameter is much less than one. To good approximation, we may replace the two scaling forms of $l_\parallel(t)$ with the $t \to \infty$ limit, and solve for $t^*$ such that the boundary layer length is exactly $l_c$. Doing so gives an expression for $t^*$, the characteristic time for tension to propagate the total length of the chain:

$$t^* = N_\infty^{-4/3} l_c^{4/3} \frac{\zeta_\perp \kappa^{2/3} (f - f_0)^{2/3}}{f^{5/3} f_0^{2/3} l_p^{2/3} \hat{\zeta}^{2/3}} \text{ for } H < 1 \tag{3.73}$$

This time roughly corresponds to the time it takes tension to come to equilibrium in a polymer. For typical values of a biopolymer such as the tip link ($l_p = 10$ nm, $l_c = 150$ nm, $\zeta_\perp = 10^{-1}$ N·s·m$^{-2}$, $f_0 = 5$ pN, $f = 6$ pN), this timescale is about 1 $\mu$s, which is insignificant on the timescale of hair-bundle dynamics.

Compared to the result for the time of tension propagation for the chain under zero prestress, this characteristic time is orders of magnitude shorter. For the case of no prestress, the time of tension propagation $t^* \propto l_c^4 l_p^3$, which depends critically on the total chain length [85]. Why are these results for the two cases, with and without prestress, so different? In the wave-mode picture, this is due to the action of the prestress pulling out the largest-wavelength undulations in the chain, and it is precisely these wave modes which govern the long reaction time of the chain. We emphasize that the scaling of the equilibrium time could not have been guessed using dimensional analysis, and the fractional exponential dependence on parameters in characteristic of polymer scaling forms analyzed previously [118].

## 3.6 Multiple-Scale Analysis

The results found for the stored-length density in Section 3.4 result in a physical breakdown beyond a critical boundary layer $l_{||}(t)$. To first order, we treated the tension as undergoing a step change at $l_{||}(t)$ from $f_0$ towards the center of the chain to $f$ towards the edges of the chain. In general, one can imagine any complex $f(t)$ such that the tension in the middle of the chain need not be strictly less than the pulling force at the ends. This introduces wavelets of tension that propagate down the chain, with characteristic timescale set by the tension profile of the chain.

During our derivation of the linearized system, we found that to zeroth order, the tension must be continuous across the chain. We now relax this assumption, and assert that this is only strictly true when $\epsilon \to 0$. That is, locally along the arclength of the chain, the linearized system applies exactly. As we transverse the arclength of the chain, $\epsilon$ need not be 0, and can grow quite large. This suggests we solve Equation (3.26) through a multiple-scale-perturbation approach, where we define a short- and a long-arclength coordinate system. The exact analysis has been completed by Hallatschek et al., and involves matching of the full equation to the order of $\epsilon^{1/2}$ [85].

Here, we arrive at the same result by considering physical constraints on the system. First, we generalize our solution to allow the stored-length density change $\langle \Delta\rho(s,t) \rangle$ and the backbone tension $f(s,t)$ to have an arclength dependence, as we have already argued in Section 3.6 must be the case. To zeroth order, we found a jump step-change in the tension upon pulling, which is unphysical. Instead, the arclength derivative of the local tension $\partial_s f(s,t)$ must exist and remain finite everywhere, as defined in the zeroth order expansion. Comparing two adjacent small segments, we also find that the second arclength derivative of the local tension $\partial_s^2 f(s,t)$ must exist and remain finite everywhere, due to the arclength invariance of the system parameters. Thus, tension must be twice differentiable everywhere along the chain (Figure 3.5).

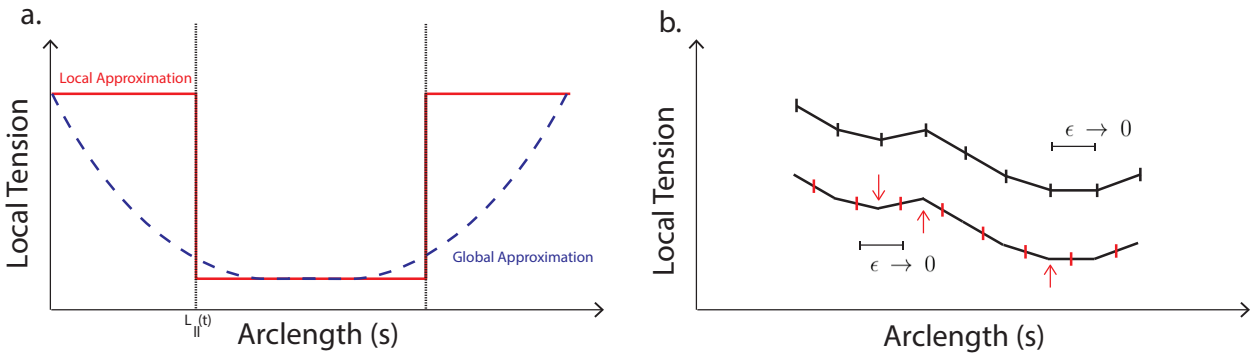


Figure 3.5: **Physicality of Tension Profiles** Comparison of the stepwise tension profile predicted by the zeroth-order perturbation theory, contrasted with the continuous curvature predicted by physical arguments. In (a), the zeroth order approximation (red) predicts regions of constant tension up to a time-dependent distance $l_{||}(t)$ away. This boundary layer grows rapidly with time, but is in general less than the entire chain length $l_c$ at small times. After passing over this boundary layer, the tension profile suddenly drops to its pre-pulled state $f_0$. In dotted blue, the global approximation is shown in which $\partial_s^2 f(s,t)$ exists everywhere. In (b), a sample piecewise tension profile in which $\partial_s^2 f(s,t)$ becomes infinite (red arrows). Black partitions represent a valid partitioning of the tension profile where the tension in each partition is continuous and has constant arclength derivative. Red partitions represent an invalid partitioning of the tension profile, for the profile contains discontinuities that are disallowed by the zeroth-order equations.

Each segment of the chain experiences a local tension at its ends $f(s+\epsilon,t)$ and $f(s-\epsilon,t)$, inducing a change in the local stored-length density and subsequent local extension of the chain. The drag force must again be balanced by the tension, though now both the drag force and the tension under consideration are local. This may be formalized as follows:

$$f(s,t) = -\zeta_{||} \int_{s-\epsilon}^{s+\epsilon} \int_{s-\epsilon}^{s+\epsilon} \partial_t \langle \Delta\rho \rangle ds^2 \tag{3.74}$$

where the double integral is due to the counting of both the length change, and then again as a measure of the segment length involved in the local drag. Taking a double arclength derivative, which is allowed since we have argued already that $\partial_s^2 f(s,t)$ must exist, we arrive at:

$$\partial_s^2 f(s,t) = -\zeta_{||}\partial_t\langle\Delta\rho\rangle \tag{3.75}$$

which can be integrated with respect to time to yield:

$$\partial_s^2 F(s,t) = -\zeta_{||}\langle\Delta\rho\rangle \tag{3.76}$$

where $F(s,t)$ is the time integrated tension. This result agrees exactly with the full multiple scale perturbation analysis, and represents our best model for understanding polymer dynamics. In general, this equation is not exactly solvable and requires either scaling arguments or numerical solutions to recover the full tension dynamics. In the next chapter, we will discuss strategies for numerical solutions to Equation (3.76).

## 3.7 Extensible Chains

So far we have only considered the dynamics of inextensible chains. The treatment over the past chapter is easily extended to the relaxed scenario in which the chain has a stiffness associated with extending the backbone of the chain. In general, biopolymers are highly resistant to stretching [119, 120]. Under low resting and pulling tensions, the chain can effectively be considered as inextensible. In certain cases, such as under a highly-prestressed condition, the energy associated with backbone stretching becomes relevant. In this case, we may rewrite the energy of the system as:

$$H_{\text{eWLC}} = \frac{1}{2}\int_0^{l_c} ds[\kappa\mathbf{r}''^2 + k_s(\mathbf{r}' - 1)^2] \tag{3.77}$$

where we have introduced a spring constant $k_s$ to be the spring constant associated with

stretching the backbone of the polymer. Again taking the functional derivative yields:

$$F_{\text{eWLC}} = -\kappa \mathbf{r}'''' + \kappa_s \mathbf{r}'' \tag{3.78}$$

This is analogous to the case in which we treated the backbone tension as constant in the inextensible case. As for the inextensible case, however, the actual backbone tension $f(s,t) = \kappa_s(\mathbf{r}' - 1)\mathbf{r}''$ need not be constant along the arclength, and may be recovered after solving for $\mathbf{r}_\perp$ though the methods discussed in this chapter.

## 3.8 Summary

In this chapter, we have considered the dynamics of polymer motion in a solvent. We found that the presence of thermal motion, along with local energetic constraints, gave rise to nonlinear dynamics that depend on parameters with a fractional dependence. The field of polymer dynamics is rich with subtlety, and mathematical studies have often arrived at divergent results depending on the regime in which the polymer is considered. Here, we reviewed the dynamics of a WLC from first principles, and used a local tension constraint to arrive at intuitive pictures of tension propagation down a chain. In the next Chapter, we will numerically solve the more rigorous Equation (3.76), which predicts the average response of a polymer in conditions far from equilibrium.

# Chapter 4: Numerical Solutions to Tension Propagation Along The Tip Link

In the previous chapter, we arrived at a partial differential equation linking the local change in stored-length density to the curvature of the time integrated local backbone tension. Except under special cases, the local tension cannot be solved analytically [86]. Although scaling solutions allow for asymptotic analysis of simple pulling, release, and towing cases, the full profile of local backbone tension is not exactly solvable. For scenarios in which the pulling frequency drives the system far out of equilibrium, difficulties arise in finding both the short-term and limit-cycle behavior. To circumvent these issues, we develop a numerical approximation that allows computation of solutions to an arbitrary pulling force at the boundaries.

In this chapter, we will review the mathematical results of the previous chapter and rewrite the differential equation as an optimization problem. We discuss strategies for computation, as well as an importance-sampling approach that results in almost no loss of accuracy, but greatly diminishes the bottleneck for finding long-term solutions and lowers the computational complexity from $\mathcal{O}(n^2)$ to $\mathcal{O}(n \log n)$. With these approaches, we are able to compute the backbone tension profiles for the parameters of tip-link-like polymers

when subjected to high-frequency sinusoidal forcing. We show that our model of the tip link remains in equilibrium under high-frequency auditory stimulation, except when the resting tension is low. Finally, we discuss complications in determination of the end-to-end distance change for our model, which may be solved by combining the local backbone tension with the blob pictures developed in Chapter 2 and 3.

## 4.1 Applicability of Model to Tip Links

To review, the tip link comprises of a dimer of PCDH15 and a dimer of CDH23, joined together through an extended handshake interaction mediated by $Ca^{2+}$ ions. Each PCDH15 monomer contains 11 extracellular cadherin domains (EC1-EC11), along with a PCDH15-interacting channel-associated (PICA) domain. The dimerization of PCDH15 occurs at the EC3 and PICA sites, and completes a half-helical turn along its length. CDH23 contains 27 extracellular domains [121]. In total, the tip link completes about 2.5 helical turns along its length, leaving two helical turns for CDH23 [28].

Electron-microscopic studies suggest the tip link exists as a rigid structure, tightly bound between adjacent stereocilia. Furthermore, molecular-dynamics simulations have suggested that individual cadherin domains are highly resistant to stretching over short timescales [122]. In contrast, single-molecule optical-trap measurements of a monomers of mouse PCDH15 expressed in HEK293 cells suggest that entropic elasticity contributes dominantly to the nonlinear stiffness measured in slow force-ramping experiments [82]. Fits to a model of a worm-like chain and a freely-jointed chain in series imply a persistence length $l_p$ on the order of 4 nm, suggesting that the tip link behaves more like a freely-jointed chain than a semiflexible chain. While we leave open the possibility of extension modes due to unwinding of the

tip link, we also note studies suggesting that unwinding of the helical structure contributes only in the high-force limit [123].

Single-molecule measurements of dimers of PCDH15 (unpublished results) suggest a larger persistence length, on the order of 10 nm, consistent with additional rigidity due to the dimerization interaction. Parallels between the helical structure of DNA and the helical structure of the tip link suggest that the tip link can be modeled using the WLC model [101]. In the following, we model the entire tip link as a worm-like chain with low bending rigidity. This poises the tip link in a regime between the semiflexible limit and the flexible limit - a regime that has poorly characterized. Here, we treat the tip link with the same mathematics used in the semiflexible limit derived earlier, and note that the approach of the multiple scale perturbation allows us to examine locally the line tension along the chain, while the global effects of pulling may be inaccurate. We address this issue at the end of the chapter, where we combine the blob picture of force propagation with the predictions of local backbone tension.

## 4.2 Mathematical Preliminaries

As shown in the Chapter 3, tension propagates along a polymer in a highly nonlinear fashion. Random thermal motion act to crimp the chain, whereas the local tension felt by each segment depends on its precise internal configuration and the external force exerted on it. Even in equilibrium, recovering the force-extension relationship for a chain with internal bending energy, volume-exclusion effects, and a stiff bond coefficient is a non-trivial calculation [101]. The full dynamic picture, including a transition probability function, remains elusive and highly dependent on particular conditions. Progress can be made by confining

our inquiry to the ensemble-averaged response of a chain, which may be sufficient to develop an understanding of expected behavior over the entire hair bundle. In particular, a mammalian hair bundles possess up to one-hundred tip links arranged in a parallel configuration, and for purposes of modeling the expected behavior of the hair-bundle's dynamics, the average response is sufficient for a first-order approximation over many cycles of oscillation. In contrast, understanding the entire distribution of tip-link tension gives precise information about the local tension the channels and insertional plaques experience.

As shown previously, tension does not in general propagate instantaneously along a polymeric chain [85]. Rather, there is a timescale associated with rearrangements of chain segments owing to viscous drag. The full dynamics of the system are given by the following Fredholm-like partial integro-differential equation derived previously [124]

$$\partial_s^2 F(s,t) = \frac{\zeta_{||}}{\pi l_p}\int_0^\infty dq\Big\{\frac{1-e^{-2q^2[q^2t\kappa+F(s,t)]/\zeta_\perp}}{q^2+f_0/\kappa} - \frac{2q^2\kappa}{\zeta_\perp}\int_0^t dt' e^{-2q^2[q^2\kappa(t-t')+F(s,t)-F(s,t')]/\zeta_\perp}\Big\} \tag{4.1}$$

where $\zeta_\perp$ and $\zeta_{||} \approx \zeta_\perp/2$ are the transverse and longitudinal drag coefficient per unit length, $f_0$ is the equilibrium resting tension along the chain up to time 0, $\kappa$ is the bending modulus of the chain, $l_p$ is the persistence length of the chain, and $F(s,t) = \int_0^t f(s,t'')dt''$ is the time integrated local backbone tension of the chain at arclength $s$. Equivalently, the right-hand side may be rewritten to express its relation to the ensemble-averaged change in stored-length density $\rho$:

$$\partial_s^2 F(s,t) = -\zeta_{||}\langle\Delta\rho(s,t)\rangle \tag{4.2}$$

taken with respect to the stored-length density at the start of the experiment, or more explicitly, with respect to the holding tension going back sufficiently far in time such that the chain is in equilibrium with average tension $f_0$ at time $t = 0$. For clarity of this point, we may rewrite Equation (4.1) as:

$$\partial_s^2 F(s,t) = \frac{\zeta_{||}}{\pi l_p}\int_0^\infty dq\Big\{\frac{1}{q^2+f_0/\kappa} - \frac{2q^2\kappa}{\zeta_\perp}\int_{-\infty}^t dt' e^{-2q^2[q^2\kappa(t-t')+F^\infty(s,t)-F^\infty(s,t')]/\zeta_\perp}\Big\} \quad (4.3)$$

where $F^\infty(s,t) = \int_{-\infty}^t f(s,t'')dt''$. Assuming that at time $t<0$ the prestress $f_0$ is constant in time and arclength, or in other words that the chain has come to equilibrium, we may reduce $F^\infty(s,t) - F^\infty(s,t')$ to $F(s,t) - f_0 t'$. Separation of the hysteresis integral $\int_{-\infty}^t f(t')dt'$ into two integrals from $-\infty$ to 0 and from 0 to $t$, and integration of the integral from $-\infty$ to 0, recovers Equation (4.1).

While we will be primarily focused on computing the tension profile along the chain, we also would like to keep observables in mind to make contact with experiments. In this case, the most readily available observable is the end-to-end distance change of the chain, which may be measured through optical-trapping experiments or other single molecule techniques [82]. The end-to-end distance change of the chain $\langle \Delta R(t)\rangle$ may be computed by combining Equations (4.1) and (4.2), and integrating along the arclength coordinate

$$\begin{aligned}\langle \Delta R(t)\rangle &= -\int_0^{l_c}\langle \Delta\rho(s,t)\rangle ds \\ &= \int_0^{l_c}\left(\frac{1}{\pi l_p}\int_0^\infty dq\Big\{\frac{1-e^{-2q^2[q^2t\kappa+F(s,t)]/\zeta_\perp}}{q^2+f_0/\kappa} - \frac{2q^2\kappa}{\zeta_\perp}\int_0^t dt' e^{-2q^2[q^2\kappa(t-t')+F(s,t)-F(s,t')]/\zeta_\perp}\Big\}\right) ds \\ &\quad + \mathcal{O}(ds) \end{aligned} \quad (4.4)$$

where the error term arises due to non-applicability of Equation (4.1) very close to the ends of the chain, which quickly equilibrate to the external pulling force.

Before progressing to a solution, we note that the form of this equation links the arclength spacial curvature of the accumulated local tension to the entire history of stored-length density. This realization is evident in the second term of Equation (4.1), which is expressed as a nonlinear convolution hysteresis integral. Additionally, solving the equation analyti-

cally is nontrivial due to the implicit nature of the problem. In the following, we device a computational strategy for constructing solutions for any boundary condition.

## 4.3 Computational Strategy for Solution

We considered the scenario of symmetric pulling, most relevant in the context of the auditory system, but note that the strategy developed can easily be extended to the case of asymmetric pulling. Although it is possible to compute alternative force conditions whereby force is exerted along the entire length of the chain, we limit our discussion to forces that are exerted at the boundaries only. This is equivalent to a local force condition, whereby the force at the ends of the chain is fixed based on our experimental procedure, or the force exerted on the tip link by shearing of the hair bundle.

Solutions to Equation (4.1) are driven by the boundary conditions, including both the equilibrium prestress before the experiment and the tension exerted at the boundaries by pulling. The boundary conditions may be written in either Dirichlet or Neumann form:

$$
\begin{aligned}
f(0,t) = f(l_c,t) &= f_{pull}(t) \\
f(s,0) &= f_0 \\
&or \\
\partial_t F(0,t) = \partial_t F(l_c,t) &= f_{pull}(t) \\
\partial_t F(s,0) &= f_0
\end{aligned}
\tag{4.5}
$$

In order to construct a numerical solution to Equation (4.1), we discretize the solution space. More specifically, we break the solution space into a grid in arclength space and time

coordinates, with arclength spacing $\delta s$ and time spacing $\delta t$, and define the target solution $F_{target}(s,t)$ to be the solution satisfying Equation (4.1) exactly. Due to intrinsic errors owing to the discretization procedure, we allow for the possibility of an approximate solution with relaxed conditions on satisfying the master equation. We define the approximate solution $F_{test}(s,t)$ to satisfy a modified form of the equation:

$$\partial_s^2 F_{test}(s,t) = \hat{H}(F_{test}(s,t)) + E(s,t) \tag{4.6}$$

where $\hat{H}$ is the nonlinear operator defined by the right-hand side of Equation (4.1), and $E$ is an error term defined explicitly by the difference $\partial_s^2 F_{test}(s,t) - H(F_{test}(s,t))$. Minimization of $E$ corresponds to convergence between the test solution $F_{test}$ and target solution $F_{target}$, since in the limit that $E$ goes to zero everywhere, $F_{test}(s,t)$ satisfies the equation exactly. In this framework, we have transferred the problem of finding the exact solution $F_{target}$ to the optimization problem of minimizing $E(s,t)$ everywhere.

In general, the optimization problem described above is non-trivial owing to the highly nonlinear operator $\hat{H}$. To make progress, we assume some knowledge of the target solution, and take an educated guess as to what it might look like for a given moment in time. If the test solution and target solution are sufficiently close, the test solution can be expanded as:

$$F_{test}(s,t) = F_{target}(s,t) + d(s,t) \tag{4.7}$$

where we assume $d$ to be small. Substituting into Equation (4.6), and taking the first order Taylor expansion yields

$$\begin{aligned} E(s,t) &\approx \partial_s^2 F_{target}(s,t) + \partial_s^2 d(s,t) - H(F_{target}) - d\frac{\delta H}{\delta F_{test}}\Big|_{F_{test}} \\ &= \left[\partial_s^2 - \frac{\delta H}{\delta F_{test}}\Big|_{F_{test}}\right] d(s,t) \end{aligned} \tag{4.8}$$

Or, rearranging into matrix form,

$$\vec{E}(t) = \hat{\mathbf{J}}\vec{d}(t) \tag{4.9}$$

where $\hat{\mathbf{J}}$ is the Jacobian matrix with elements $J_{ij} = d\hat{\mathbf{T}}(F_{test}(s_i,t))/dF_{test}(s_j,t)$, with $\hat{\mathbf{T}}$ the operator $\partial_s^2 - \hat{H}$. Rearranging Equation (4.7) to $\vec{F}_{target}(t) = \vec{F}_{test}(t) - \vec{d}(t)$, inverting Equation (4.9), and combining the two yields an updated guess for the target solution:

$$\vec{F}_{target}(t) \approx \vec{F}_{test}(t) - \hat{\mathbf{J}}(\vec{F}_{test}(t))^{-1}\vec{E}(t, \vec{F}_{test}(t)) \tag{4.10}$$

where we have written out the explicit dependence of the Jacobian matrix and the error term on the test solution. In practice, the use of Equation (4.10) acts only to improve the approximate test solution $F_{test}$, and does not exactly solve for $F_{target}$. Instead, Equation (4.10) can be iterated $k$ times to yield the improved solution:

$$\vec{F}_{k+1} = \vec{F}_k - \hat{\mathbf{J}}^{-1}\vec{E}_k \tag{4.11}$$

This strategy represents a Newton's Method of optimization, where at each step we consider the first derivative in solution space and descend along the local gradient. At each step, the error term is explicitly recomputed for use in the next iteration, and can be monitored for convergence to zero everywhere along the arclength. After a sufficient number of iterations, the error term will be small, indicating the test solution has successfully converged to the target solution.

## 4.4 The Jacobian

The Jacobian may be calculated explicitly by separating it into two parts, $J_1 = \partial_s^2$ and $J_2 = \frac{\delta H}{\delta F_{test}}\Big|_{F_{test}}$. The first component, $J_1$, is trivial to calculate. It is given by the matrix representation of $\partial_s^2$ in the discretized arclength basis, which to first order is given by the approximate form:

$$J_1 = \frac{1}{(\delta s)^2}\begin{pmatrix} -2 & 1 & 0 & \cdots & 0 & 0 \\ 1 & -2 & 1 & \cdots & 0 & 0 \\ 0 & 1 & -2 & \cdots & 0 & 0 \\ \vdots & \vdots & \ddots & \vdots & \vdots & \vdots \\ 0 & 0 & 0 & \cdots & -2 & 1 \\ 0 & 0 & 0 & \cdots & 1 & -2 \end{pmatrix} \tag{4.12}$$

The second component of the Jacobian, $J_2$, is highly nonlinear in nature due to the nonlinearity present in the operator $\hat{H}$. The operator is explicitly given by the right hand side of Equation (4.1), and consists of an inverse integral transform from wave-mode $q$ back to solution space $F(s,t)$. The $q$-integral contains two components, one that is primarily generated from the effects of resting tension that decays as $t \to \infty$, and the second that involves a convolution between the current tension and the entire tension history of the chain. We revisit this point in the next section, for the time decay of the tension hysteresis affords us opportunities for approximation.

$J_2$ can be explicitly calculated, but due to strong divergencies in the integral in $\hat{H}$ near $t' = t$ it can be resolved only by defining an interpolation between points $F(s,t_{i-1})$ and $F(s,t_i)$. For simplicity, we choose the linear interpolation:

$$F(s,t') = F(s,t_i) + \frac{t_i - t'}{t_i - t_{i-1}}\Big[F(s,t_{i-1}) - F(s,t_i)\Big], \text{ where } t_{i-1} < t' < t_i \tag{4.13}$$

With this interpolation, the hysteresis integral may be evaluated explicitly between times 0 and $t$ by breaking it into smaller integrals between each time $t_i$ to $t_{i+1}$ and taking their sum. Doing so yields:

$$\begin{aligned}
&\int_0^\infty \frac{2q^2\kappa}{\gamma_\perp} dq \int_0^t e^{-2q^2[q^2\kappa(t-t')+F(s,t)-F(s,t')]/\gamma_\perp} dt' \\
&= \sum_{i=1}^{n} \int_0^\infty dq \frac{e^{-2q^2[q^2 t\kappa+F(s,t)]/\gamma_\perp}}{q^2 + \frac{F(s,t_i)-F(s,t_{i-1})}{\kappa(t_i-t_{i-1})}} \left[ e^{2q^2[q^2 t_i\kappa+F(s,t_i)]/\gamma_\perp} - e^{2q^2[q^2 t_{i-1}\kappa+F(s,t_{i-1})]/\gamma_\perp} \right]
\end{aligned} \tag{4.14}$$

where $t_0 = 0$ and $t_n = t$. Combining Equation (4.1) and (4.14), the entire term $H(F(s,t))$ can be written as

$$\begin{aligned}
H(F(s,t)) = \frac{\zeta_{||}}{\pi l_p} \Big\{ &\int_0^\infty dq \frac{1 - e^{-2q^2[q^2 t\kappa+F(s,t)]/\zeta_\perp}}{q^2 + f_0/\kappa} \\
&- \sum_{i=1}^{n} \int_0^\infty dq \frac{1}{q^2 + \frac{F(s,t_i)-F(s,t_{i-1})}{\kappa(t_i-t_{i-1})}} \Big[ e^{-2q^2[q^2(t-t_i)\kappa+F(s,t)-F(s,t_i)]/\zeta_\perp} \\
&- e^{-2q^2[q^2(t-t_{i-1})\kappa+F(s,t)-F(s,t_{i-1})]/\zeta_\perp} \Big] \Big\}
\end{aligned} \tag{4.15}$$

The calculation of $H(F(s,t))$ at time $t$ explicitly involves the solutions at all previous time points $0 \leq t_i < t$, imparting directionality in the construction of our solutions. Additionally, the nonlinear term depends only on values of $F(s,t)$ at that particular arclength, so that the calculation of $H(F(s',t))$ is independent of $H(F(s'',t))$. $H(F(s,t))$ may thus be computed point-wise along the arclength coordinate and stitched together at the end. The nonlinear part of the Jacobian is also diagonal by this property, which may be expressed as $\frac{\partial H(F(s_i,t))}{\partial F(s_j,t)} = \delta_{ij} \frac{\partial H(F(s_i,t))}{\partial F(s_j,t)}$

Calculation of the derivative is straightforward, except in the case that $i = n$ in the summation term, where care must be exercised to avoid the singularity at large $q$ and small $t - t'$. In practice, this requires us to treat the $i = n$ term as a separate case, and calculate

the derivative for only that component. Doing so yields an additional two terms in the derivative. Finally, after taking the derivative, we find the nonlinear portion of the Jacobian may be written as:

$$
\begin{aligned}
J_2 = \hat{\mathbf{I}}\frac{\zeta_{||}}{\pi l_p}\Big\{ & \int_0^\infty dq \frac{2q^2 e^{-2q^2[q^2 t\kappa + \vec{F}(t)]/\zeta_\perp}}{\zeta_\perp(q^2 + f_0/\kappa)} \\
& + \sum_{i=1}^{n-1} \int_0^\infty dq \frac{2q^2}{\zeta_\perp\left(q^2 + \frac{\vec{F}(t_i)-\vec{F}(t_{i-1})}{\kappa(t_i - t_{i-1})}\right)} \left[ e^{-2q^2[q^2(t-t_i)\kappa + \vec{F}(t) - \vec{F}(t_i)]/\zeta_\perp} - e^{-2q^2[q^2(t-t_{i-1})\kappa + \vec{F}(t) - \vec{F}(t_{i-1})]/\zeta_\perp} \right] \\
& + \int_0^\infty dq \frac{1}{\kappa\zeta_\perp\left(q^2 + \frac{\vec{F}(t)-\vec{F}(t_{n-1})}{\kappa(t-t_{n-1})}\right)^2} \frac{1}{t - t_{n-1}} \left[ 1 - e^{-2q^2[q^2(t-t_{n-1})\kappa + \vec{F}(t) - \vec{F}(t_{n-1})]/\zeta_\perp} \right] \\
& - \int_0^\infty dq \frac{2q^2 e^{-2q^2[q^2(t-t_{n-1})\kappa + \vec{F}(t) - \vec{F}(t_{n-1})]/\zeta_\perp}}{\zeta_\perp\left(q^2 + \frac{\vec{F}(t)-\vec{F}(t_{n-1})}{\kappa(t-t_{n-1})}\right)} \Big\}
\end{aligned}
\tag{4.16}
$$

where $\hat{\mathbf{I}}$ is a $s$x$s$ identity matrix, with $s$ the number of points taken in the discretization of the arclength. This completes our expression for $J_2$.

Combining Equations (4.12) and (4.16) yields the Jacobian matrix to be computed at each step. To solve Equation (4.11) requires the computation of the inverse Jacobian matrix. Due to discretization errors in computing the arclength's second derivative, and from solving the time-dependent nonlinear term $\hat{H}(F(s,t))$ using a linear interpolation, it is often the case that the Jacobian matrix is not exactly invertible. To circumvent this problem, we instead calculate the pseudo-inverse $J^+$ using the Moore-Penrose pseudo-inverse algorithm from the NumPy library [125, 126]. In the case that $\mathbf{J}$ is exactly invertible, $\mathbf{J}^+$ and $\mathbf{J^{-1}}$ are identical. In noninvertible cases, $\mathbf{J}^+\mathbf{J} \approx \hat{\mathbf{I}}$. In either case, we use $\mathbf{J}^+$ in place of $\mathbf{J^{-1}}$ to solve Equation (4.11).

Ideally, the iterative solution can be run indefinitely towards convergence with the target solution, but in practice we define a threshold in the global error term $\sum_{i=0}^{s} E(i,t)$. After the error of the test solution at a given time point is below this threshold, we lock in the best solution and advance the computation to the next time point.

## 4.5 Strategies for Expediency

Although the computational method outlined above provides a framework for building numerical approximations to governing Equation (4.1) subject to boundary conditions (4.5), the feasibility of computation beyond simple scenarios is precluded by the scaling of operations. Due to the hysteresis in the system, each vector solution at a time point requires the evaluation of $(N_s - 2)(2n_t + 3)$ integrals in $q$-space, where $N_s$ is the number of points along the arclength axis we are sampling, and small $n_t$ is the number of time points we have sampled, $n_t = t/\delta t$, or equivalently the step of the calculation. Each integral involves evaluation of $\mathcal{O}(100)$ points, and we iterate the process a variable number $N_e$ times until the error is sufficiently small to advance. In total, the number of operations grows as $200N_e(N_s - 2)n_t + C$, where $C$ accounts for both the constant operations owing to both the static integrals and additional operations for matrix manipulation that remain constant in $n_t$. The time complexity of this algorithm is linear, $\mathcal{O}(n_t)$, but must be repeated for each time point. In order to solve the system up to time $T$, then, the number of operations scales as $\mathcal{O}(n_t^2)$. This results in an algorithm that fails to probe long time scales of complex polymer dynamics. This restriction stems from the highly nonlinear computations, which must be evaluated with small time spacing close to the current time point in order to ensure applicability of the linear interpolation, and to ensure a small error. Examination of the value of the hysteresis integral for simple time-dependent local forces revealed no obvious approximations, owing to the highly nonlinear nature of the operator (Figure 4.1). Even in the case of a constant history of holding tension, the integral decays with a long timescale, precluding the use of linear or constant approximations to the exponential (Figure 4.1(a)).

Because error accumulates in the hysteresis of the system, it is important that the threshold to move the computation forward remains low. These considerations produce an algorithm that can succeed in evaluating simple changes in boundary condition such as a step change in pulling force, but that fails for complex pulling forces like ramps and oscillations.

To overcome these difficulties, we conceded to the use of approximations by consulting the form and physical properties of the hysteresis. We note that the dependengrce of the term decays exponentially with both time and time-integrated tension, and that physically, the chains memory is heavily weighted towards its recent past. Intuitively, the chain's memory of its tension history decays rapidly as thermal fluctuations bombard it. What is left is the ghost of past configurations – the more recent tension history – which has only implicit dependence on states far in the past. This Markov-like property can be exploited by sampling densely in the recent past, and sparsely in the distant past. This procedure is equivalent to an importance-sampling algorithm, and arises naturally due to the linear interpolation already taken in Section 4.4. Many sampling algorithms are possible, but we sample by always including the first point ($t = 0$), the last 30 points, and stepping backwards in increasing step size by 1 for every step. This strategy results in roughly logarithmic growth of sampled points, that is, $n_{sample} \sim \log n$ in the limit of large $n$. Using this sampling decreases the large $n$ time complexity of the algorithm to $\mathcal{O}(n_t \log n_t)$. Between sampled points, we again use a linear interpolation, with now $t_{i,sample}$ and $t_{i-1,sample}$ being chosen from the collection of sparely sampled time-points $\{t_{n_{sample}}, t_{n_{sample}-1}, ..., t_0\}$.

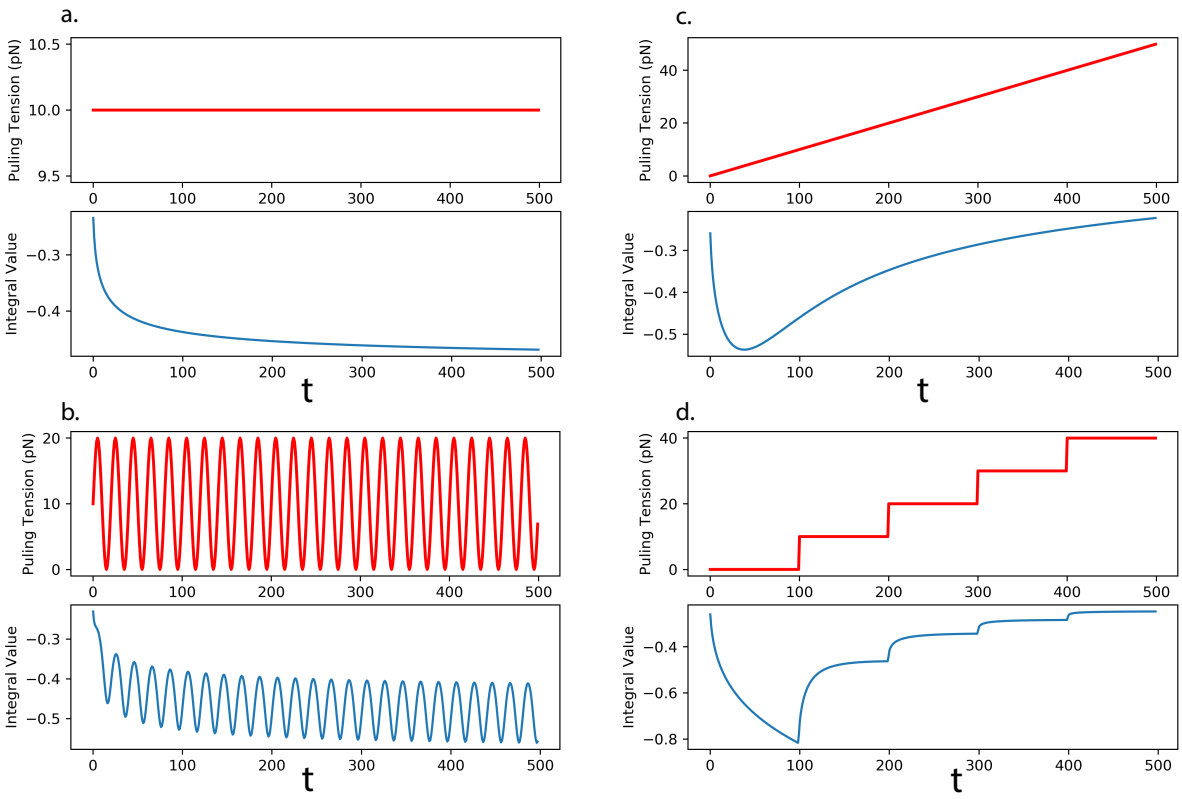


Figure 4.1: **Nonlinear Behavior of the Hysteresis Integral for Tension Histories**. Evaluation of the right-hand side of Equation (4.1) for different tension histories. Time and force were rescaled according to $f \to \kappa f$ and $t \to \zeta_\perp t/\kappa$. In (a), the output of the operator to a constant-valued force history. The integral value decays slowly, with significant creep at long times. The slow decay renders approximation difficult, for we cannot replace the operator function with a constant or linear function. In (b), the response to a sinusoidal tension history. The overall waveform matches that in (a), but displays phase-shifted oscillations with amplitude and phase that are frequency-dependent (not shown). In (c), the response to a linear ramp in tension. The initial decay component corresponds to an initial effect of the resting tension. In (d), a stepped force ramp. The output of the operator again resembles the overall waveform given in (c), but with nearly exponential decay after a step change in force. The amplitude of response decreases as tension is increased.

To allow the use of a variable time step $\delta t$ in order to widely apply our algorithm to different scenarios, we choose a target number of iterations $N_e$. We keep track of the number of iterations before reaching the error threshold, and variably adjust the time step $\delta t$ up or down to decrease or increase the expected value of iterations for the next time point. Choice

of target $N_e$ is empirical, but clearly if $\delta t$ becomes too small there would be no change in the tension profile, whereas for $\delta t$ too high the solution would over-smooth the dynamics. We found a range of reasonable values to be $5 < N_e < 10$.

Finally, multiprocessing has become a standard tool in intensive computational tasks. Here, we make use of the independence along arclength of Equations (4.15) and (4.16) in order to parallelize the computation.

## Section 4.6: Numerical Solutions to Force Jumps

We considered the case of a force jump with the following boundary conditions

$$f(0,t) = f(l_c,t) = \begin{cases} f_0, & \text{if } t \leq 0. \\ f_{pull}, & \text{if } t > 0. \end{cases} \tag{4.17}$$

and evaluated the tension profile, time integrated tension profile, stored-length density, and end-to-end distance change of the chain. The exact time-course of the solution depended on the choice of $f_0$, $f_{pull}$, $l_p$, $l_c$, and the transverse drag-coefficient-per-unit-length $\zeta_\perp$. Here, we considered a chain with $l_c = 100$ nm subjected to an initial prestress of 5 pN, and jumped instantaneously to a tension of 50 pN at the ends. Generally, the tension profile followed the jump change closely at the boundaries, where the curvature rapidly increased (Figure 4.2). This curvature propagated through the chain, before eventually reaching the midpoint. After, the global tension curvature became linear across most of the chain, only changing rapidly around the midpoint. As time progressed the profile decayed as the global tension asymptotically approached its equilibrium value set by the boundaries. We found the tension histories for individual segments of the chain to be highly nonlinear, and they displayed distinct rates of increase that were time-dependent (Figure 4.2(b)). We also examined a heatmap of the tension profile history, which shows a clear overall picture of the response of the chain (Figure 4.2(c)). As expected, at short times the bulk of the chain was unable to

feel the effects of the tension increase at the boundaries. It was only after a finite time, here about 1 $\mu$s, that the tension finally began to change everywhere along the chain. The chain tension then increased rapidly to its equilibrium value.

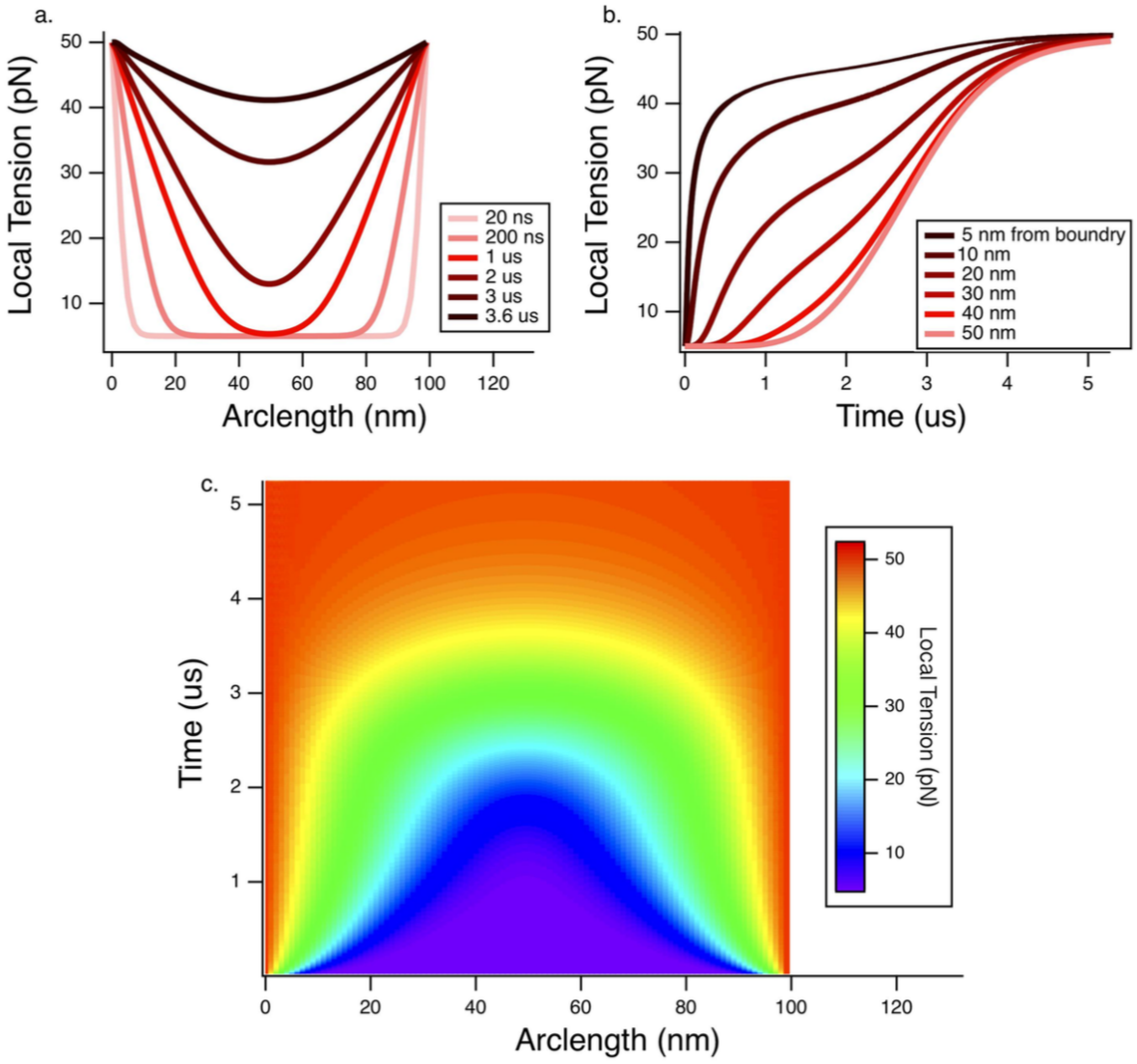


Figure 4.2: **Tension Profiles of a Jump Stimulus** Numerical tension profiles calculated as solutions to Equation (4.1) under jump pulling conditions. At time 0, the tension at the boundaries jumps from 5 pN to 50 pN. Parameters values used in model were $l_p = 1$ nm, $l_c = 100$ nm, and $\gamma_\perp = 100$ mN·s·m$^{-2}$. In (a), snapshots of local tension along the entire chain at times after the jump in force occurred. First, the tension change takes about 1 $\mu$s have an effect at the midpoint. Thereafter, the tension of the entire chain relaxes to its equilibrium value. In (b), time courses of local tension profiles at various positions away from the ends. Close to the ends, the tension rapidly rises in response to the jump, while close to the midpoint the response lags behind. In (c), a heatmap of the tension profile for the time course of the solution at each arclength along the chain.

Our results agree closely with those found by previously, confirming the validity of our computational approach [124]. Of particular note is the timescale on which these effects occur, which was found to be extremely fast (of order 5 $\mu$s). Part of this speed was due initial choice of re-dimensionalized parameters, which allowed for exploration of only high pre-stresses and pulling forces. Lower forces are expected to propagate more slowly through the chain. Additionally, the chain length chosen here is smaller than even that of the tip link, which is small on the scale of most polymers. By our asymptotic analysis in Section 3.5, timescales are expected to increase more than linearly with increasing chain length, implying potential relevance in longer biopolymers.

## 4.6 Numerical Solutions to Tension Profiles in the 1 MHz Limit

A primary interest in our work was elucidating the dynamics of a polymeric chain subject to sinusoidal forcing at its ends. Previous studies, and current experimental work, has shown the entropic elasticity of a monomer of PCDH15 to be the overwhelming balancing force encountered while slowly extending a single molecule in an optical trap [82]. What remained unclear was what role dynamics played in the response of entropic elasticity, and under what conditions the chain could be driven out of thermal equilibrium. The answer was not clear at the outset, and arguments have been made that entropic elasticity is too slow to support the full auditory frequency spectrum. This argument would implicate enthalpic stretching near the ends of the of the tip link as the dominant contribution to channel gating, acting through a soft compliment element. For these reasons, it was important to explore the numerical solutions to a polymeric chain under high-frequency pulling.

We began by considering the regime well above the frequency sensitivity of any known auditory process, 1 MHz. While not applicable in the context of the auditory system, the response under fast oscillatory shear is of theoretical interest in understanding general polymer behavior. In the following computations, the parameters chosen were $l_c = 150$ nm, $l_p = 10$ nm, and $\zeta_\perp = 100$ mN·s·m$^{-2}$ and $\zeta_{||} = 50$ mN·s·m$^{-2}$ set as an upper limit to the drag derived from the slender rod approximation, taking into account additional drag from the nearby stereocilia and hydrodynamic coupling of chain segments. We chose values of the resting tension $f_0 = 1$, 5, 10, 20 pN, and chose the amplitude of the sinusoidal forcing values $f_0/2$ and $f_0$, representing both medium and large amplitude forcing. Attempts were made to compute the response at a lower sinusoidal forcing value of $f_0/10$, but errors in our computational approach caused the time steps to grow too large for sufficient resolution.

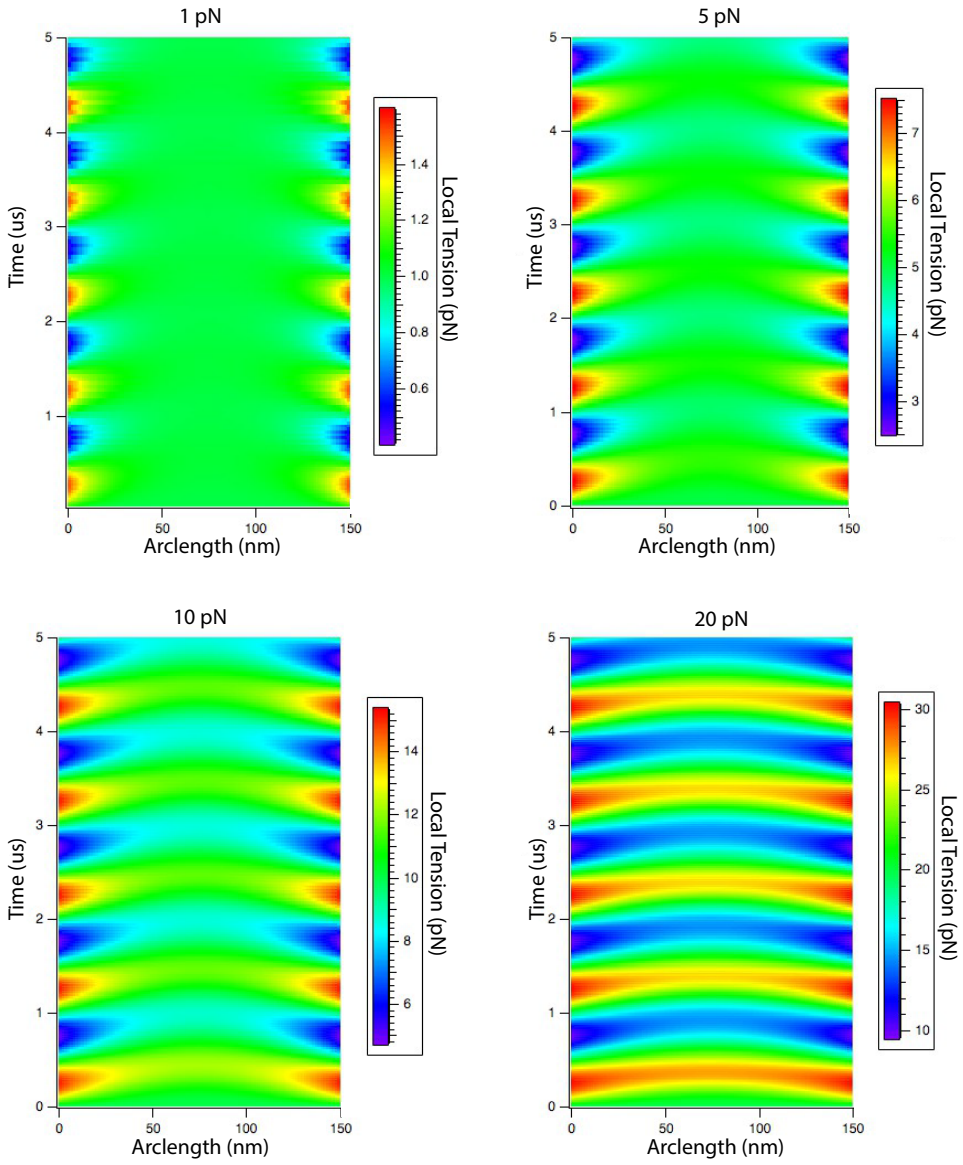


Figure 4.3: **Tension Profiles For Tip-Link-Like Polymers Under Tension I** Numerical tension profiles calculated as solutions to Equation (4.3) under a sinusoidal forcing of 1 MHz, well above the auditory range of hearing. Parameters used in the numerical simulation were $l_p = 10$ nm, $l_c = 150$ nm, $\zeta_\perp = 100$ mN·s·m$^{-2}$. The average force in this calculation is set exactly at the resting tension, and varied to 1/2 the resting tension's value at the ends. For each case, then, the sinusoidal pulling at the ends is given by $f(s = 0, l_c) = f_0 + \frac{f_0}{2}\sin(\omega t)$ with $\omega$ the angular frequency. At low resting tensions, the tension change at the ends does not propagate far into the bulk of the chain. At higher resting tensions (10 pN), tendrils form to bridge the pulling force at the end into the center of the chain. At high resting tension, the middle of the chain approaches values in tension close to the ends, but with significant phase lag. Wavefronts become evident in the 10 pN and 20 pN condition, indicating a phase shift between the response at the center of the chain to the pulling at the ends of the chain.

In Figure 4.3, we show the tension profile history of the $f_0/2$ forcing amplitude. At low 1 pN resting tensions, the value at the boundaries for both an increase and a decrease in tension away from the resting tension did not penetrate into the bulk of the chain, indicating that the majority of the chain was unable respond to the tension change at the ends. Instead, the energy of pulling dissipated into the surrounding bath due to the large viscous drag of pulling the ends straight over small timescales. At higher 5 pN resting tensions, the penetration of the tension change into the bulk increased. Close to the boundaries, the local tension closely followed the pulling tension, but with significant time lag. As tension was increased further to 10 and 20 pN, tension significantly propagated into the bulk of the chain. Unlike the case of instantaneous tension ramping, the tension was found to propagate $\propto t$ close the the boundaries, and $\propto t^{\alpha}$ with $\alpha < 1$ as it approached the midpoint of the chain.

These results suggest that as resting tension is increased, the degree to which the entire chain feels the effect of a tension change at the boundaries increases. Still, there is a significant time lag associated with tension propagation through the bulk, causing a ripple-like wavefront effect. Wavefront ripples travel at different speeds (interpreted as the angle with respect to the horizontal axis in Figures 4.3 ,4.4, 4.5, 4.6) depending whether the tension is dropping or rising. This distinction reflects the increased time it takes a chain to crumple due to thermal forces with energy $k_BT$ as opposed to the time it takes a chain to extend as a result of a pulling force $f_{\text{pull}}$ with energy much greater than $k_BT$.

We also examined the scenario in which the amplitude of stimulation was identical to that of the resting tension, such that at certain times the local tension at the boundaries dropped to exactly 0. Surprisingly, the addition of even stronger forcing did little to change the qualitative picture of tension propagation down the chain (Figure 4.4). The resistance of the system to changes in forcing amplitude is surprising, since a larger change in boundary tension is predicted to increase the rate of tension propagation down the length of the chain in the zeroth-order approximation. The effect for the full multiple-scale perturbation differential equation, however, is subtle.

In Figure 4.7, we show snapshots of the tension profile taken at different approximate time points separated by 50 ns and 500 ns for the 1 MHz and 100 kHz cases respectively, for the sinusoidal amplitude equal to the resting tension $f_0$. In the left-hand column, we show the results of the 1 MHz pulling solutions as resting tension increases. The effect of increasing resting tension changes the shape of the "finger trap" profile in a nonlinear way. At 1 pN resting tension, the chain is unable to respond at all in the bulk to the action at the edges. In contrast, the 5 pN resting tension chain is able to respond minimally to activity at the edges. At 10 pN, the system comes almost to equilibrium, but the phase delay of tension response at the center of the chain in the release portion of the oscillation is greater than that of the pulling portion. Surprisingly, at 20 pN resting tension, the system falls further out of equilibrium, possibly reflecting the short timescale behavior of the onset of oscillation associated with the resting tension history being constant before the simulation.

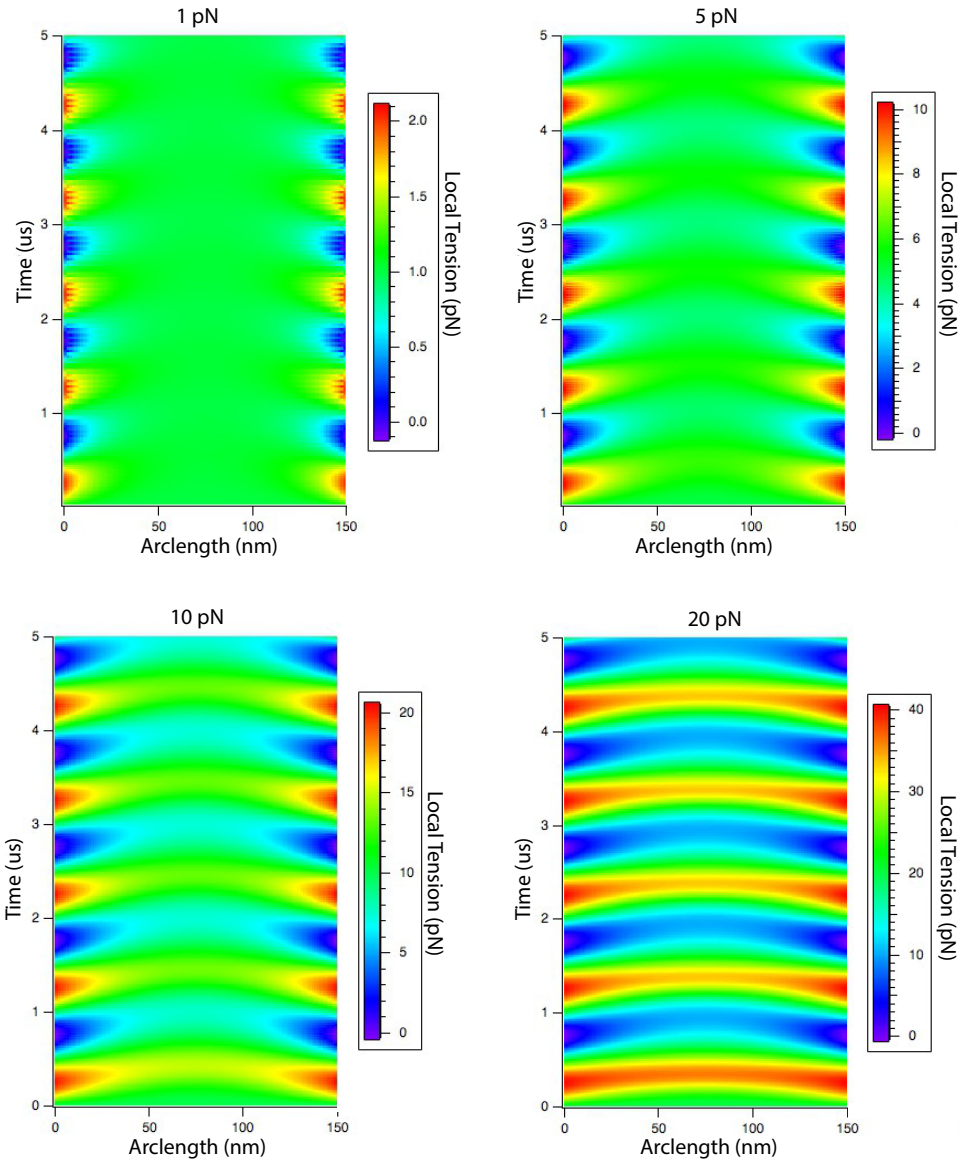


Figure 4.4: **Tension Profiles For Tip-Link-Like Polymers Under Tension II** Identical numerical computation as in Figure 4.3, but with increased sinusoidal forcing amplitude equal to the entirety of the resting tension, so that the tension felt at the ends oscillates between 0 and $2f_0$ (1 MHz). The results are nearly identically to the previous case, indicating that the addition of stronger pulling forces does little to change the dynamic behavior of the polymer from the perspective of the tension profile. Subtle differences may be observed, such as the increased penetration of the pulling force into the bulk of the $f_0 = 10$ pN case.

## 4.7 Numerical Solutions to Tension Profiles in the 100 kHz Limit

We repeated the calculations of the previous section, but for the high-frequency limit of the known auditory system in certain mammals, 100 kHz. The tension profiles were calculated in the same manner as in Section 4.7. The results are shown in Figures 4.5 and 4.6 for a low-amplitude $f_0/10$ and high-amplitude $f_0$ forcing, respectively. We begin by examining the tension profiles under low-amplitude forcing. The behavior under low 1 pN resting tension was similar to that observed for the 1 MHz stimulating frequency, with tension attenuating before transversing the length of the chain. In contrast to the 1 MHz forcing amplitude, the strong attenuation effect was completely diminished by increasing the resting tension to 5 pN, whereupon the tension was able to propagate into the center of the chain. Increasing the resting tension further, to 10 pN and 20 pN, caused the system to nearly come into equilibrium, reflected by the "90's striped-shirt" pattern in the 20 pN $f_0$ computation. For these values of resting tension and sinusoidal forcing frequency, the chain was able to follow nearly in phase with the response at all times, though slight bowing of the wavefronts was observed for the 10 pN case. The asymmetry in phase lag during pulling as opposed to release was diminished in the 10 pN case.

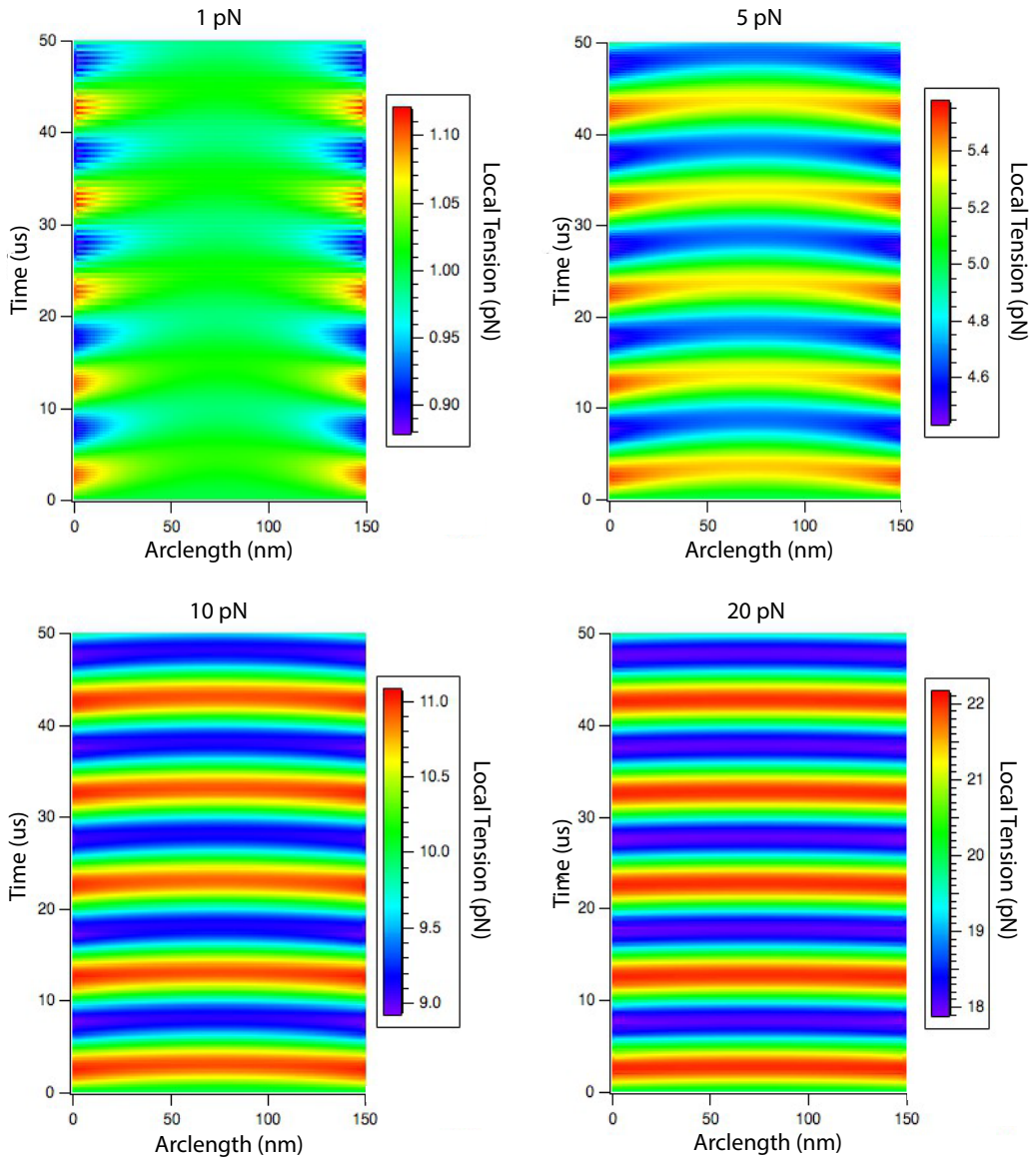


Figure 4.5: **Tension Profiles For Tip-Link-Like Polymers Under Tension III** Numerical tension profiles computed with a lower sinusoidal forcing frequency of 100 kHz, which is above the frequency of human hearing but approaches the upper limit of frequency sensitivity in bats. Sinusoidal forcing of the form $f(s = 0, l_c) = f_0 + \frac{f_0}{10}\sin(\omega t)$, where the amplitude of sinusoidal forcing is small in comparison to the resting tension. These calculations were possible due to the slow variation of the tension profile with time, which allowed our computational method to converge well in comparison to the same type of stimulus attempted in the 1 MHz case (not shown). At 1 pN resting tension, the tension at the ends is unable to penetrate far into the bulk, while increasing the resting tension to 5 pN results in full penetration into the center of the chain. At higher resting tensions, the phase shift of the wavefronts decreases, until the entire chain is nearly in equilibrium at all times for the 20 pN case.

In the high-amplitude-forcing case (Figure 4.6), we again observed qualitatively similar tension profiles to those obtained in the low-amplitude-forcing case. The major difference was observed in the phase delay of the wavefronts up to the 20 pN resting tension case, which was not present in the low amplitude forcing. These subtle changes, while small in the tension profiles, create large discrepancies in the behavior of the stored-length densities (Figures 4.9, 4.10). On the right hand column of Figure 4.7, we show the snapshots of tension profiles taken at time points separated by 500 ns seconds under different resting conditions. As in the higher frequency 1 MHz forcing computations, increasing the resting tension does not guarantee that the chain will approach equilibrium monotonically.

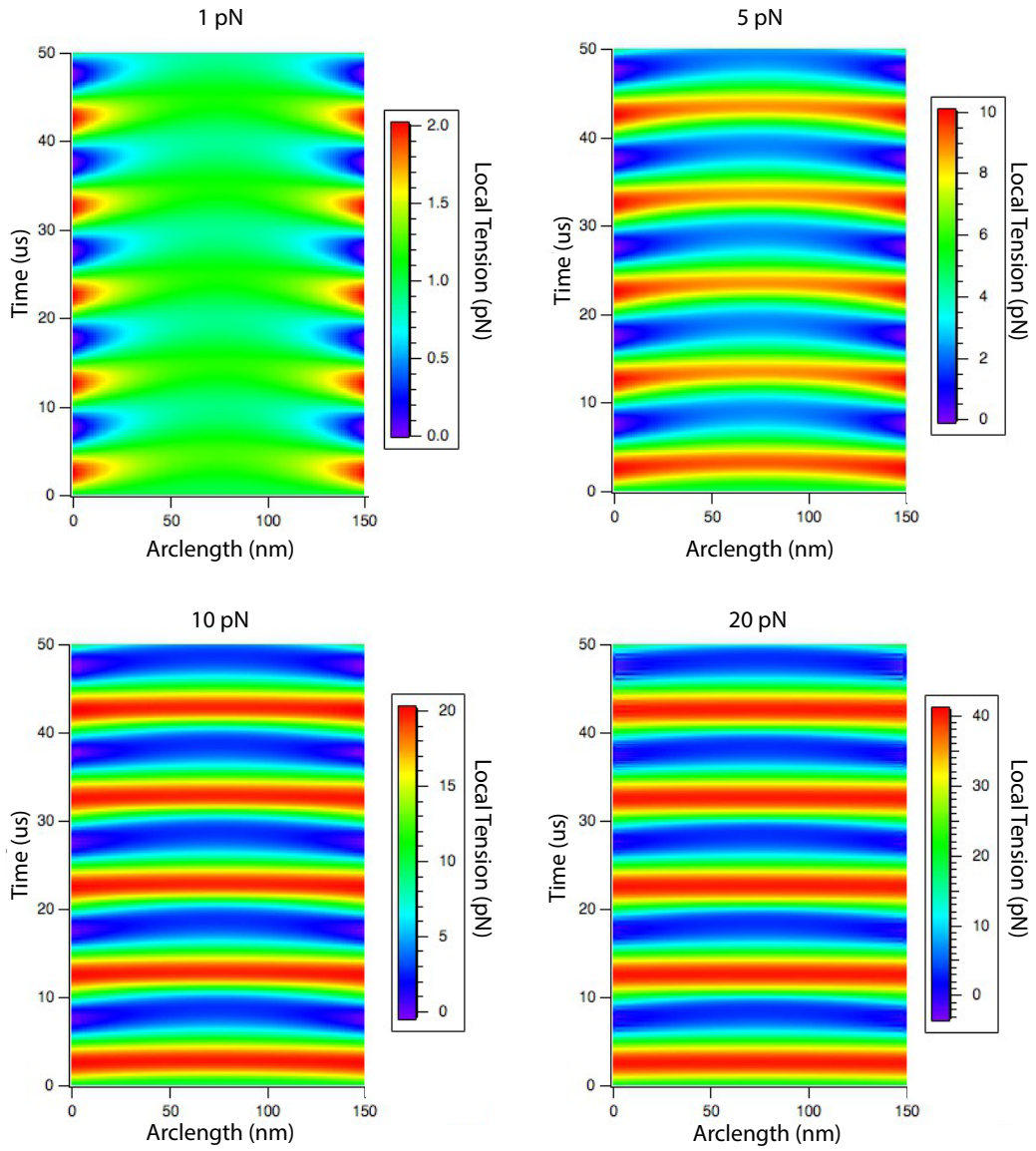


Figure 4.6: **Tension Profiles For Tip-Link-Like Polymers Under Tension IV** Identical numerical computation as in Figure 4.3 (100 kHz), but with increased sinusoidal forcing amplitude equal to the entirety of the resting tension. Even though the value of the pulling tension as increased by a factor of 10, the qualitative shape of the tension profiles remains the same. The notable changes from the small forcing cases are in the 5 pN resting-tension profile, where the force is close to equilibrium at the center of the chain, and in the 10 pN resting tension profile, where significant asymmetry presents in the midpoint wavefront.

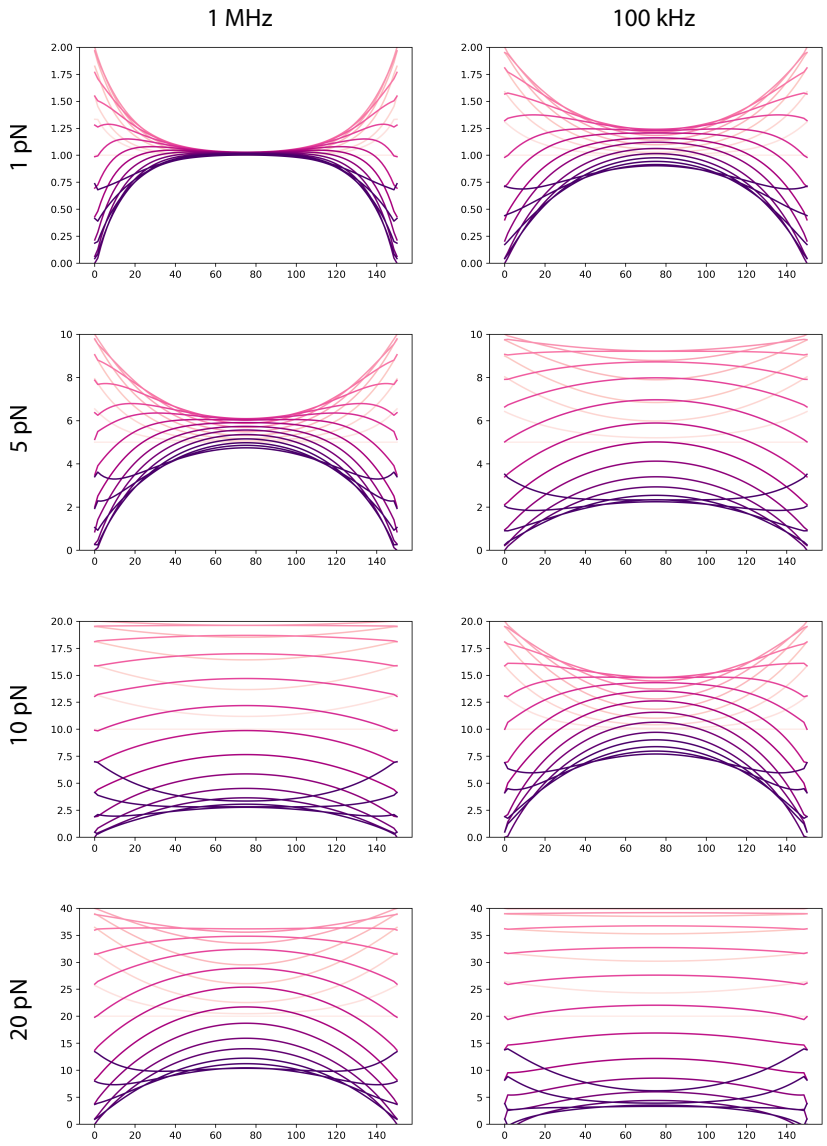


Figure 4.7: **Snapshots of Tension Profiles** Tension profile snapshots taken roughly at the same time point along the first oscillation of pulling force. Timescales were generated independently for each calculation, and profiles were chosen using a nearest neighbor sorting algorithm in the time domain. For the 1 MHz condition and 100 kHz condition, the time-points were chosen spaced 50 ns and 500 ns apart, respectively. The "finger trap" characteristic shape of many sequential snapshots reflects the inability for the chain to come to equilibrium. As the finger trap widens, the entire chain is closer to equilibrium. Surprisingly, the finger trap shape does not widen monotonicaly with increasing resting tension, but first widens and then contracts at sufficiently high tensions. The behavior of the overall 100 kHz snapshots closely mirrors that of the next highest resting tension condition in the 1 MHz case (for instance, 100 kHz and $f_0 = 1$ pN resembles 1 MHz and $f_0 = 5$ pN). In many cases, individual tension profile snapshots are found with a "W" shape.

## 4.8 Numerical Solutions to $\Delta\rho$ Profiles

The changes in local stored-length density $\Delta\rho$ are necessarily calculated as a byproduct of our numerical strategy outlined in Section 4.3. In particular, the computation of the error $E$ requires explicit calculation of the right hand side of Equation (4.1). We verified the validity of our approach by backtesting on the arclength curvature of the time integrated local tension, which matched well to our solutions. The most significant differences occurred at the boundaries, where numerical errors near the boundaries caused the curvature to fluctuate. The effect was diminished significantly by averaging over every other time point, smoothing the resulting tension profiles.

In Figure 4.8, 4.9, 4.10, and 4.11, we show the companion stored-length density changes to the local tensions shown in Figure 4.4, 4.5, 4.6, and 4.7. Under low resting tensions, the change in stored-length density propagated further into the bulk than the associated pulling tension. This is reflective of the relationship of the change in stored-length density to the curvature of the tension profile, rather than the value of the local tension itself. In the case of instantaneous step pulling, we observed the curvature of the force profile changed significantly at the center of the chain before the tension was "lifted". This property allowed the stored-length density to propagate much further than considerations of the local tension alone would anticipate.

Like the low-resting-tension cases, the stored-length density change propagated slowly down the length of the chain under the release condition (corresponding to an increase in the stored-length density). The rapid shift in local tension at the ends, although seemingly equilibrated under examination of the tension profile, causes phase shifts in response. Small phase shifts have an amplified effect on the stored-length density change.

In only one condition did we find that the stored-length density change remained in equilibrium – the small $f_0/10$ pulling amplitude condition under 100 kHz sinusoidal forcing (Figure 4.10). Similar to the tension profile, the stored-length approaches a "90's striped-shirt"

pattern at high resting tensions, while for low resting tensions $\Delta\rho$ is unable to propagate along the chain. Under high $f_0$ pulling amplitudes, the observed behavior of the tension and stored-length density diverged (Figure 4.11). While $\Delta\rho$ propagated into the bulk upon extension of the chain, the opposite under extension was not true.

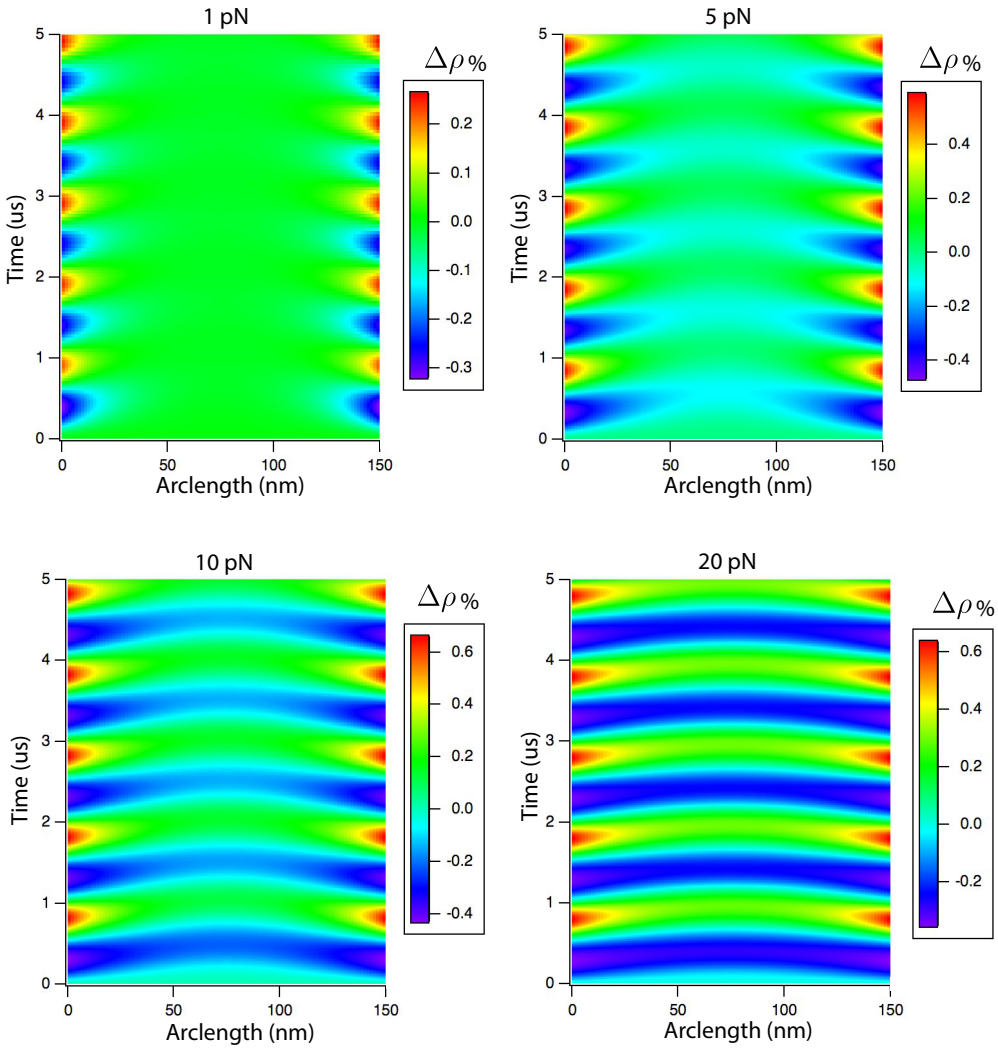


Figure 4.8: **Stored-Length Density For Tip-Link-Like Polymers Under Tension I** Identical numerical calculation as in Figure 4.3 (1 MHz), but showing the stored-length density change calculated through explicit integration. Alternatively calculating the stored-length density change by differentiation of the time integrated tension profile yielded similar results. Due to the relation between the stored-length density change and the time integrated tension, rather than just the local line tension, the stored-length density is sensitive to phase lag effects. This is most evident in the 10 pN case, where phase lag causes significant bowing of the wavefront. Short lasting effects at the onset of oscillation are a result of the heavy tailed memory of the chain to its past tension history, which was assumed constant going back to the beginning of time. Large changes in stored-length density, where the chain is in a crumpled configuration, have difficulty penetrating deep into the bulk of the chain. This is due to the slower process of tension relaxation in comparison to extension.

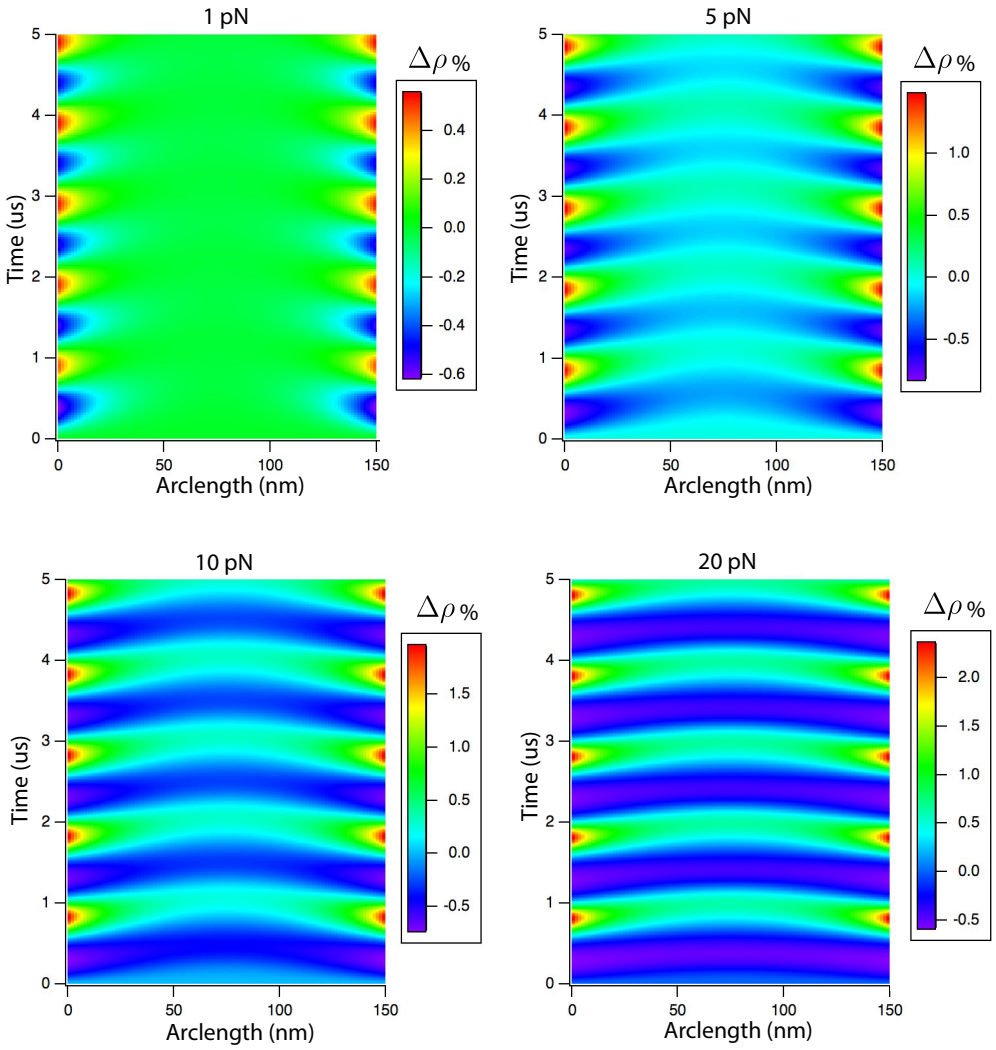


Figure 4.9: **Stored-Length Density For Tip-Link-Like Polymers Under Tension II** Additional stored-length density profiles for the case of forcing amplitude equal to the resting force, $f(s = 0, l_c) = f_0 + f_0 \sin(\omega t)$ for the 1 MHz pulling case. In the low, 1 pN resting tension computation, the profile remains nearly identical to that of the low amplitude pulling condition in Figure 4.4. The wavefronts of higher tensions are more prominent at intermediate resting tensions, with caveat that the extrema value of change at the boundaries do not propagate far into the bulk.

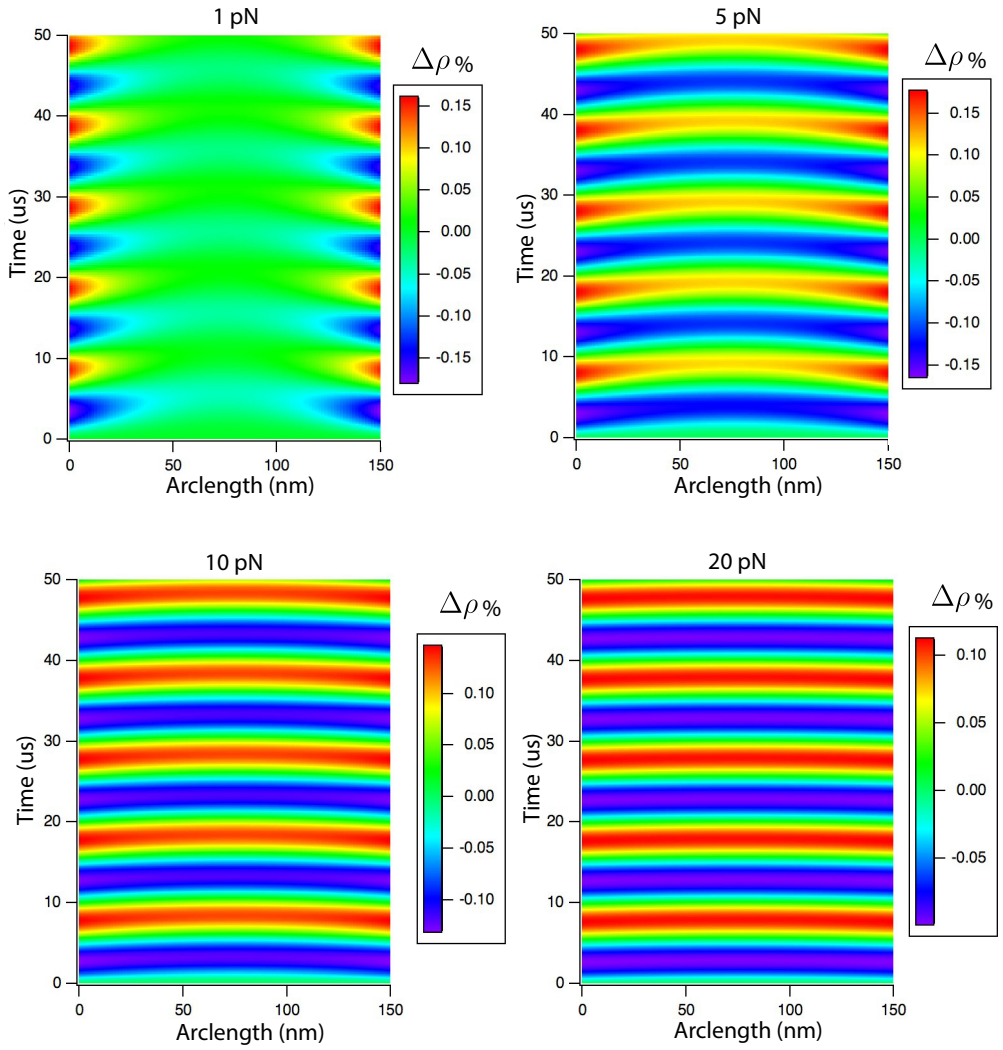


Figure 4.10: **Stored-Length Density For Tip-Link-Like Polymers Under Tension III** Identical numerical computation as in Figure 4.5 (100 kHz), but showing the stored-length density change instead of the tension profile. The map is inverted in comparison to Figure 4.5, reflecting the inverse correspondence between local line tension and stored-length density, but otherwise shows no significant qualitative shifts. Under low 1 pN resting tensions, the stored-length density does not extend far into the bulk, while at high 20 pN resting tensions, the stored-length density is in equilibrium at all times along the chain. Slight bowing of wavefronts at intermediate resting tensions suggests some tension propagation effects, which correspond to decreases in the end-to-end distance change amplitude

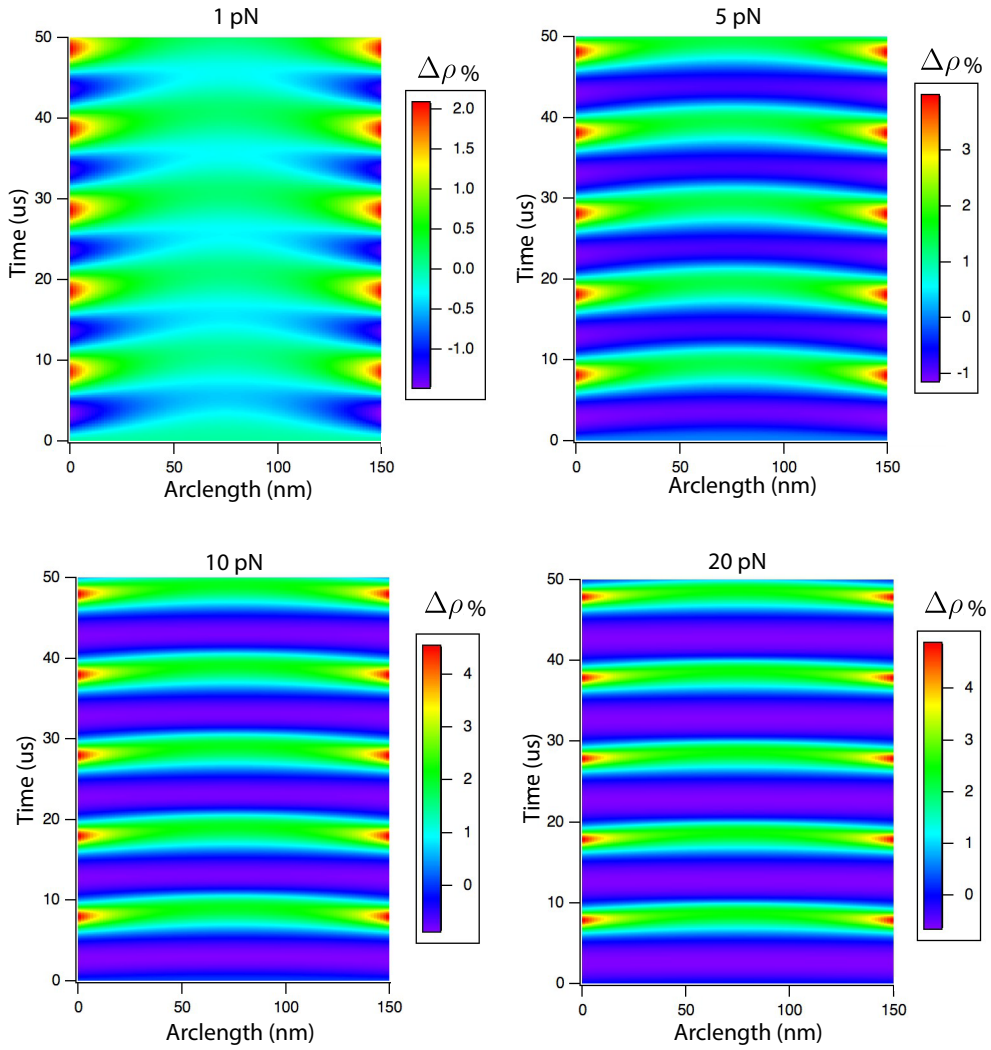


Figure 4.11: **Stored-Length Density Change Profiles For Tip-Link-Like Polymers Under Tension IV** The same numerical calculations as in Figure 4.10 (100 kHz), but with forcing amplitude equal to the resting tension. The store length density profile shows extension into the bulk in the low 1 pN resting tension case, but with significant delay of positive changes at the center of the chain. At high 20 pN resting tension, the stored-length density of the chain is unable to come to equilibrium, even though the resting tension in the identical calculation in Figure 4.6 qualitatively suggests the resting tension is close to equilibrium. Subtle changes in resting tension propagation into the bulk correspond to large changes in stored-length density, due to the slow process of tension relaxation.

## 4.9 Equilibrium at Low Frequencies and High Resting Tensions

Again we chose values that approximated the mammalian tip link, with $l_c = 150$ nm, $l_p = 10$ nm, and effective tangential drag-coefficient-per-unit-length $\zeta_\perp = 100$ mN·s·m$^{-2}$. We applied a variety of sinusoidal stimuli at frequencies ranging from 10 kHz up to 100 kHz, with forces $f_0 = 1$ pN, $f_{\text{offset}} = 5$ pN, $f_{\text{amp}} = 5$ pN, and observed slight deviations from equilibrium (Figure 4.12 a,b) consistent with our findings in previous sections. Even under lower frequency stimulation, at 20 kHz, we observed a wavefront emerge in both the tension profiles and $\Delta\rho(s)$ profiles indicating that drag does play a minor role in keeping the system from equilibrium. We also note an asymmetry in the response; although the profiles respond quickly to an increase in tension at the boundaries, the response at the midpoint lagged behind when the tension was quickly ramped down. The profiles of stored-length density change (Figure 4.12) showed deep extension into the bulk with increasing tension. The converse was not true; during decreasing tension at the ends, the stored-length density did not follow suit in the bulk, especially at lower frequencies (Fig 4.12 c). As we increased the frequency of stimulation at the ends, we observed increasingly symmetric end to end distance changes, while the amplitude of limit cycle displacement decreased. We conclude the possibility that under low prestress and moderate forcing amplitudes, the tip link may exhibit some non-equilibrium properties.

The exact prestress – or resting tension – under which the tip link is held varies along the tonotopic axis of the mammalian cochlea, with larger prestress observed in tip links gating higher frequency tuned hair bundles [38]. With this knowledge, we conclude that high resting tension enables the chain to remain at equilibrium well beyond the limit of the human auditory range. Conversely, lowering resting tension introduces significant drag effects into the system, which cause the behavior to deviate significantly from quasi-static behavior. In Chapter 5, we will systematically address how changing resting tension effects

the response of a polymer in the linearized viscoelastic, or small forcing, regime.

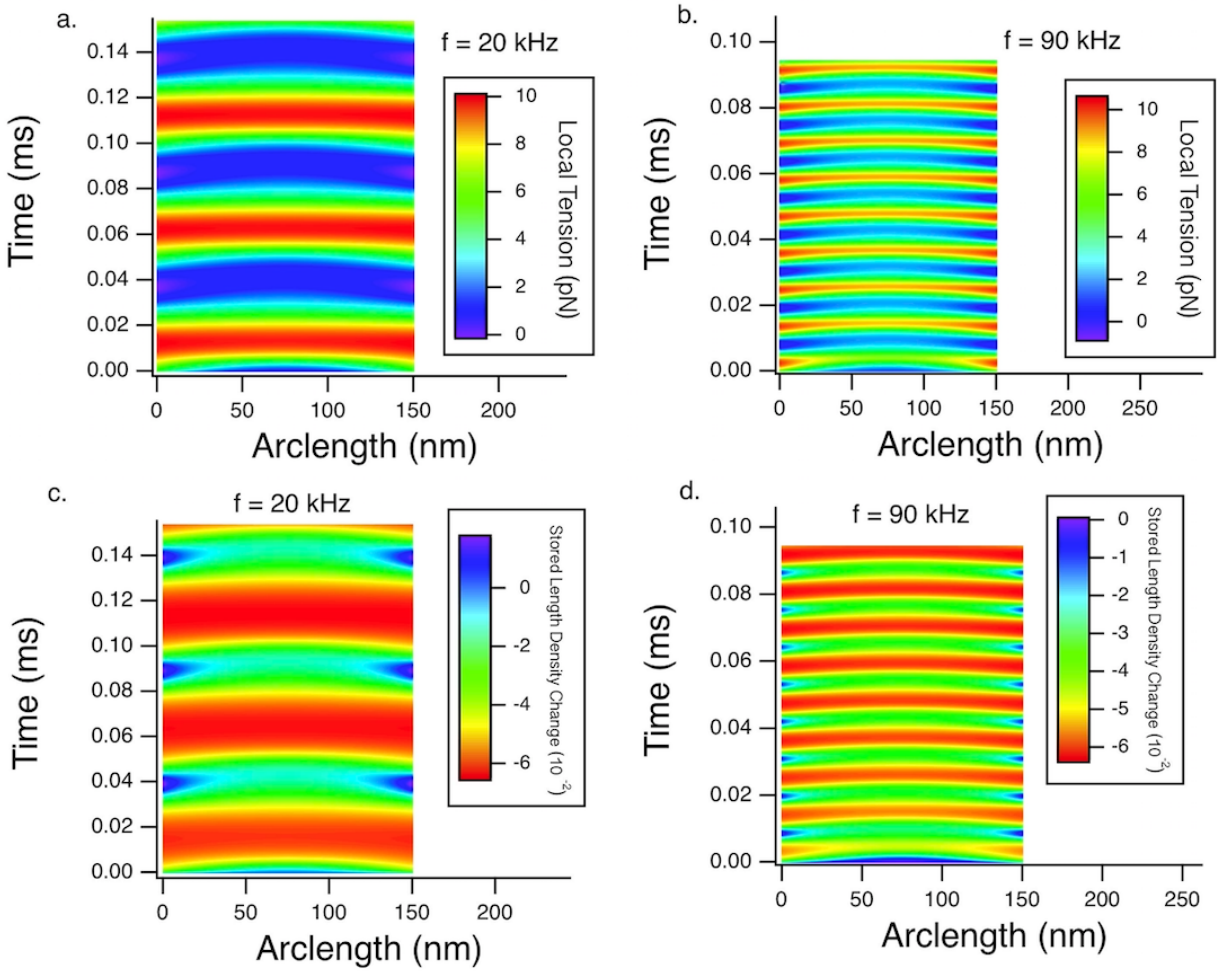


Figure 4.12: **Tip-Link-Like Polymers Under Physiological Stimuli** Numerical tension profiles and stored-length density change profiles calculated as solutions to Equation (4.1) under sinusoidal forcing conditions, for parameter values more closely aligned to that of the tip link. At time 0, the tension at the boundaries jumps from 1 pN to 5 pN, and oscillates around this value with an amplitude of 5 pN. Parameters values used in model were $l_p = 10$ nm, $l_c = 150$ nm, and $\gamma_\perp = 100$ mN·s·m$^{-2}$. In (a) and (b), heatmaps of the tension profiles for frequencies of 20 kHz and 90 kHz, respectively. Here, the tension profiles are equilibrated almost everywhere for the slower frequency condition, but undergo a significant phase shift between the midpoint and the ends. In the faster frequency condition, we find a decay in the low tension extension into the bulk of solution, but otherwise only subtle differences. In (c) and (d), the same numerical solutions as in (a) and (b), but showing the stored-length density change $\Delta\rho$ from its initial value.

## 4.10 Recovering the Force-Extension Relationship

To naively recover the force-extension relationship, we should follow the procedure given in Equation (4.4). Doing so yields end-to-end distance changes that are far smaller than the results we expect for a polymer under equilibrium oscillating between a low and high resting tension. The result of this discrepancy arises from the definition of the stored-length density, which measures the *local* stored-length in the chain, rather than the global stored-length. In the limit of low forces and low persistence length, the chain is more closely approximated by a flexible chain with significant thermal bends . We may still use Equation (4.4) to model the resting tension on a local scale, but concede that the global configuration of the chain is inaccessible to our approximation. Indeed, the change in local stored-length density only reflects a fraction of the total length change, unless the entire chain is close to the semiflexible limit. The flexible case corresponds to a constantly changing coordinate system, where the direction of $\hat{r}_{||}(s)$ has arclength dependence.

One solution is to combine the numerically calculated local backbone tension with the tension blob picture described in Chapters 2 and expanded to the WLC model in Chapter 3. Gradients in backbone force separate the chain into tension blobs of size $l_{\mathrm{blob}(s,t)} \approx \sqrt{\frac{k_B T}{l_p f(s,t)}}$, where we now both the local blob size and the backbone tension to have arclength and time dependence. In Figure 4.13, we consider the blob picture in the case of some characteristic force profiles observed in our numerical calculations. The first, for the stereotypical pulling experiment, shows a "beaded-pearl necklace" configuration of tension blobs (Figure 4.13(a)). In the second, we consider the atypical behavior we observed in some fast sinusoidal forcing scenarios, in which the tension profile resembled an elongated "W". In this case, the blob size is small at the edges and the middle, but increases one-third and two-thirds down the length of the chain.

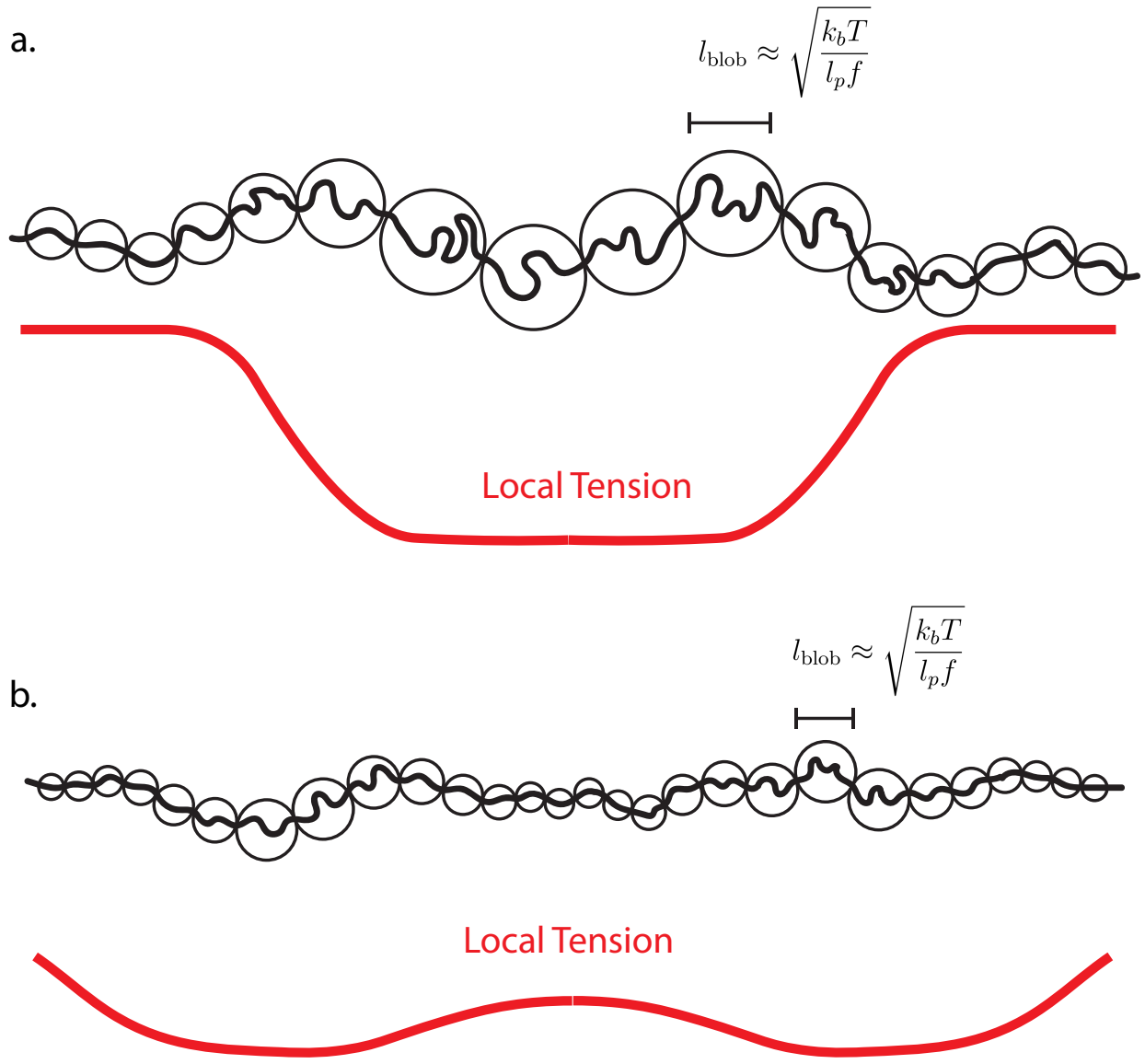


Figure 4.13: **Tension Blob Representation of Force Profiles** Example tension blob schematics for characteristic tension profiles observed in numerical computations. In (a), the tension is equilibrated near the ends but decreases towards the center of the chain. Correspondingly, the blob size increases towards the middle of the chain as $l_{\text{blob}} \propto \sqrt{1/f}$. This "beaded-pearl necklace" configuration is characteristic of fast tension changes. In (b), the tension forms an extended "W" pattern like those seen in Figure 4.7. In this case, the blob size does not monotonically increase towards the middle of the chain, but gets largest one-third and two-thirds down the length of the chain.

## 4.11 Numerical Solutions to Combined Sinusoidal Stimuli with Force Jumps

We solved Equation (4.1) for a variety of parameters to get a full picture of the possible dynamics of the system under sinusoidal forcing conditions

$$f(0,t) = f(l_c,t) = \begin{cases} f_0, & \text{if } t \leq 0. \\ f_{\text{offset}} + f_{\text{amp}} \sin(2\pi\omega t + \phi) & \text{if } t > 0. \end{cases} \tag{4.18}$$

where $f_{\text{offset}}$ is the mean force delivered at the ends over many cycles, $f_{\text{amp}}$ is the amplitude of forcing, and $\omega$ and $\phi$ are the angular frequency and phase of the stimulus. Our results (Figure 4.14) show the possibility of non-equilibrium responses under high-amplitude and high-frequency stimuli. In these computations, the mean force $f_{\text{offset}}$ was not chosen equal to the prestress $f_0$, and thus we observed a response that has two components; first, the system was far from equilibrium and exhibited the properties of the force jump with an overlaid oscillation, and second, the system approached a stable limit cycle in which tension changes along the filament could only propagate into a bulk with a characteristic penetration depth that was highly dependent on the stimulus frequency. Snapshots revealed nontrivial tension profiles along the chain, where much of the nonlinearity was concentrated near the ends. Under parameters studied, the solutions always approached stable limit cycles after an initial ramping of behavior.

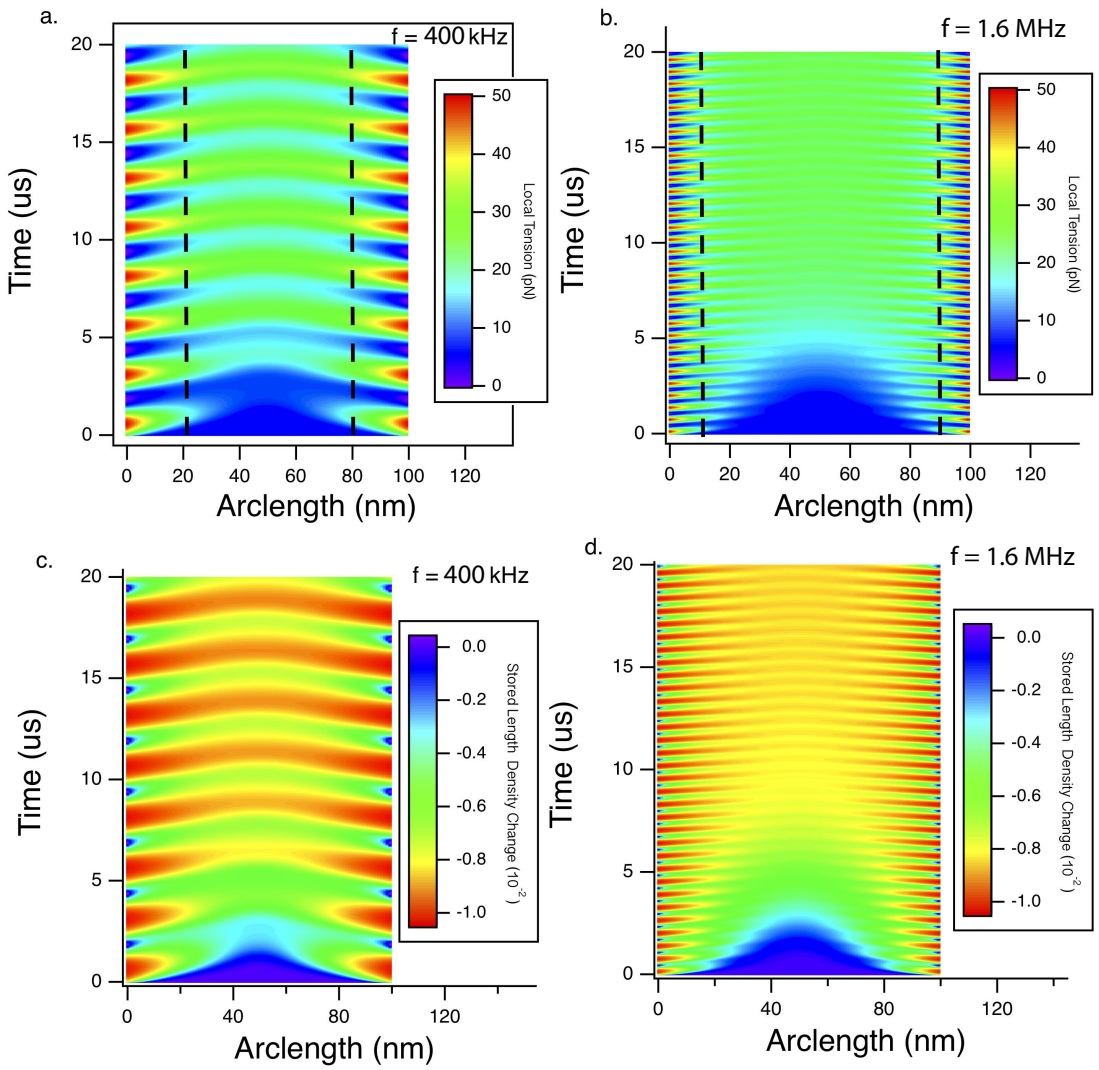


Figure 4.14: **Combined Force Jump and Sinusoidal Forcing** Numerical tension profiles and stored-length density change profiles calculated as solutions to Equation (4.1) under sinusoidal forcing conditions. At time 0, the tension at the boundaries jumps from 5 pN to 25 pN, and oscillates around this value. Parameters values used in model were $l_p = 1$ nm, $l_c = 100$ nm, and $\gamma_\perp = 100$ mN·s·m$^{-2}$. In (a) and (b), heatmaps of the tension profiles for frequencies of 400 kHz and 1.6 MHz, respectively. The rapid oscillations of tension at the boundaries are unable to extend far into the bulk due to the effects of drag. Dashed lines indicate roughly where the tension has died off to half its maximum value. This penetration depth is deeper for slower stimuli. After a short time, the solutions approach a stable limit cycle. In (c) and (d), the same numerical solutions as in (a) and (b), but showing the stored-length density change $\Delta\rho$ from its initial value. The stored-length density change extends far into the bulk for when tension is increasing, but fails to extend far when the tension is decreasing.

## 4.12 Conclusions

An open question in auditory biophysics is whether the tip link itself may act as the gating spring. In order for the tip link to have the right stiffness value to match that of the gating spring, the effects of entropic elasticity must contribute to its compliance in a nontrivial way. Indeed, studies of the enthalpic elasticity of cadherin domains precludes any significant novel unfurling of the chain that would act like a compliant spring, besides a kink found in the crystal structure of EC8 – EC10 [127] and full unfolding of EC domains. An open question has been whether entropic elasticity can react fast enough to support the entire auditory range, and if not, what effects this might have on auditory physiology and hair-bundle mechanics. Here, we addressed the first question by modeling the tip link as a semiflexible polymer, and subjecting it to high oscillatory stresses. In agreement with our asymptotic analysis in Chapter 3, the rate of tension propagation down the tip link was highly dependent on initial resting tension. We showed that under low, but still physiological resting tensions on the order of 1 pN, the tip-link's resting tension did not equilibrate globally, and the stored-length density measuring the crimping from thermal undulations took even longer to respond. Under high resting tension of the order 10 pN, however, these effects became minimal, drawing the tip link into a regime of complete equilibrium well past the human auditory range of frequencies. These finding suggest that by regulating resting tension, the hair bundle may adjust the operating regime of the tip link to always remain in equilibrium.

In this chapter, we subjected polymers to high forces well outside the physiological range. These forces were deliberately chosen, because methods do not currently exist to probe this high-frequency, high-tension regime. Although our computational approach allowed us to generate novel solutions over reasonable computational timescales, there exist other methods to probe the small forcing limit. In the next chapter, we will shift focus to this linearized regime, and discuss the viscoelastic behavior under small forcing amplitudes more in line with auditory stimuli.

# Chapter 5: Viscoelastic Properties of Tip Links

In the previous chapter, we discussed the numerical solutions to polymer dynamics in systems that were far from equilibrium. Although this gave insight into some unexpected behaviors, and provided a full picture of the tension across the polymer at any given moment of time for a variety of pulling forces, we consider now the reaction of the linearized system. In the context of the auditory system, this corresponds to acoustic stimuli up to 60 dB, well within the range of normal human speech [128]. In fact, most audible sounds oscillate a hair bundle on the order of only nanometers, corresponding to a small sinusoidal oscillation that is superimposed upon an average resting position. For low-frequency tuned hair bundles in the American bullfrog sacculus, large spontaneous oscillations may cause motions of the kinociliary bulb with amplitudes of 20 nm [55], corresponding to a 2.5 nm displacement of the end-to-end distance of the tip link. For cochlear hair bundles, prestin-based electromotility in the outer hair cells can extend the length of the cell body by tens of nanometers, again corresponding to small displacements of the intersterociliary distance [129].

For these reasons, it is necessary to examine the response of polymers in general, and tip links specifically, to small sinusoidal oscillations away from their operating resting tension $f_0$. We begin with a review of basic viscoelastic theory, and move onto experimental evidence

that implicates the tip link as a viscoelastic element [130]. Viscoelastic properties can give rise to diverse behaviors - most notably, they may give rise to the phenomena of subdiffusion, in which over considerable timescales the mean-squared end-to-end distance change $\langle (x_t - x_0)^2 \rangle$ grows with time dependence $\propto t^\nu$ with $\nu < 1$. Next, we consider the solution for the viscoelastic compliance for a generic semiflexible chain, with tunable parameters. We show that the operating regime of the tip link exists at a critical point in the viscoelastic behavior, enabling it to act as a nonlinear tuning fork that can vary its force sensitivity by only slightly adjusting its resting tension. We conclude with a discussion of the implications of this model in the context of auditory frequency tuning, and consider a model that combines well studied basilar membrane mechanics [3] with an updated model of the tip link as a viscoelastic element.

## 5.1 Linear Viscoelastic Theory

The field of viscoelastic theory is wide, with applications in material design, biological modeling, and engineering [131, 132]. We consider here general viscoelastic behavior, in which a material may exhibit both elastic (energy-storing) properties, and viscous (energy-depleting) properties. A classic, joyous example is Silly Putty©, which behaves elastically on short timescales and may act as bouncy rubber ball to infuriate parents, but exhibits creeping flow on longer timescales that may cause it to drip off the side of a table to pool on a priceless Persian rug. Viscoelastic materials behave differently depending on the rate at which we apply stress.

The theory of linear viscoelasticity can be summarized in the following equation. We suppose that there is a linear relationship between the force applied to a material (in this

case, a polymer) and the distance it is displaced. Furthermore, we allow this relationship to depend on the entire history of forces that we have applied to the material:

$$x = \int_{-\infty}^{t} K(t-t')f(t')dt' \tag{5.1}$$

where K is a memory kernel or response function, and $f(t)$ is the time history of the force applied. The meaning of this equation becomes clear in the Fourier domain, where we may take:

$$\hat{x}(\omega) = \hat{K}(\omega)\hat{f}(\omega) \tag{5.2}$$

by the unilateral Convolution Theorem [133]. Technically, the Fourier transform was taken unilaterally, but for simplicity we leave the notation unchanged. Rearranging this equation for clarity, and defining $\hat{J}(\omega) = \hat{K}(\omega)$, we invert to find:

$$\hat{f}(\omega) = \frac{1}{\hat{J}(\omega)}\hat{x}(\omega) \tag{5.3}$$

which is equivalent to the equation for a Hookean spring with spring constant $1/\hat{J}$. Equation (5.1) therefore defines the equation for a spring. Unlike a conventional spring, however, this spring has a frequency dependence, and can have both real (in-phase) and complex (out-of-phase) components. We rename the spring constant $1/\hat{J} = \hat{G}$ and call it the "viscoelastic modulus", and call $\hat{J}$ the "viscoelastic compliance". In the time domain, $J(t-t')$ is often written as $\chi(t-t')$ and labeled the linear-response function. Equivalently, it is the Green's function for the differential equation. We may also write the viscoelastic compliance as:

$$\hat{J}(\omega) = \frac{\hat{x}(\omega)}{\hat{f}(\omega)} \tag{5.4}$$

As an example, we examine the response to a sinusoidal stimuli with frequency $\omega_0$, $x(t) = e^{iw_0 t}$. In Fourier space, this equals $\delta(\omega_0 - \omega)$, in which $\delta(x)$ is the delta function.

Substituting this expression, and taking the inverse Fourier transform, we find:

$$\mathcal{F}\big[\hat{f}(\omega)\big] = f(t) = \mathcal{F}\big[\hat{G}(\omega)\delta(\omega_0 - \omega)\big] = \hat{G}(\omega_0)e^{i\omega_0 t} \tag{5.5}$$

which defines the equation for sinusoidal motion. $\hat{G}(w)$ measures the frequency-dependent response of a system to a sinusoidal force stimulus. Both $\hat{G}(\omega)$ and $\hat{J}(\omega)$ can have both real and imaginary components, which we explicitly write out as $\hat{G}(\omega) = \hat{G}'(\omega) + i\hat{G}''(\omega)$ and $\hat{J}(\omega) = \hat{J}'(\omega) + i\hat{J}''(\omega)$. Substituting into Equation (5.6) and taking only the real part, we find:

$$f(t) = \hat{G}'(\omega_0)\cos(\omega_0 t) + \hat{G}''(\omega_0)\cos(\omega_0 t + \pi/2) \tag{5.6}$$

in which it now becomes clear that $\hat{G}'(\omega)$ corresponds to the amplitude of the in-phase response, and $\hat{G}''(\omega)$ corresponds to the amplitude of the out-of-phase response. We refer to these as the storage modulus, since $\hat{G}'(\omega)$ represents the elastic response of the system, and the loss modulus, since $\hat{G}''(\omega)$ represents the viscous response of the system. Similarly, the compliance can be divided into an storage compliance $\hat{J}'(\omega)$ and a loss compliance $\hat{J}''(\omega)$.

The viscoelastic modulus, or equivalently the viscoelastic compliance, is sufficient to predict the linearized response of a system to a small force or small displacement. To gain intuition, we consider the viscoelastic compliance of simple system described by:

$$\zeta\dot{x} = -\kappa x + f \tag{5.7}$$

which describes the motion of a bead trapped in a harmonic potential undergoing diffusion. Taking the Fourier transform of both sides, and rearranging terms gives a compliance of the form:

$$\hat{J}(\omega) = \frac{1}{\kappa - i\omega\zeta} = \frac{\kappa}{\kappa^2 + \omega^2\zeta^2} + i\frac{\omega\zeta}{\kappa^2 + \omega^2\zeta^2} \tag{5.8}$$

In the low-frequency limit, the storage compliance is constant, whereas the dissipative compliance scales as $\omega$. In the high-frequency limit, the storage compliance falls off as $1/\omega^2$, and the dissipative compliance falls off as $1/\omega$. We will see similar effects when we examine the viscoelastic compliances of polymers in Section 5.4.

## 5.2 Subdiffusion in the Hair Bundle

In solution, thermal motion bombards the hair bundle and causes it to fluctuate over time. The process by which the hair bundle moves is stochastic in nature, and resembles a continuous random walk in a confining potential. This motion is interchangeably known as Brownian motion or diffusion. We first address the simple diffusive case, and move onto more complex cases as the section progresses.

In the absence of a confining potential, and without correlations in drag, the hair bundle undergoes free Brownian motion. What is the cause of this Brownian motion? It is due to the extreme number and independence of thermal bombardment by water molecules. In the low-Reynold's number limit, the (simplified) equation of motion for a hair bundle in one dimension is:

$$\zeta \dot{X}_t = F_{\text{th}} \tag{5.9}$$

where $\zeta$ is a drag coefficient, $F_{\text{th}}$ is the instantaneous force due to the water molecules, and $\dot{X}$ is the time derivative of the particle's position. In solution, water molecules bombard the hair bundle with an average energy $k_B T$, but there is no net directionality to the force involved. Additionally, the force exerted by the water molecules has no temporal correlations – an assumption that breaks down at very small time scales on the order of picoseconds,

but which we will ignore. Formally, we may write $\langle F_{\text{th}} \rangle = 0$ and $\langle F_{\text{th}}(t) F_{\text{th}}(t') \rangle = g\delta(t - t')$. We make no claim that the individual force distribution is normal over short time scales – in fact, it is very likely non-Gaussian. However, as each force is an independent identically distributed random variable, we may invoke the Central Limit Theorem to claim that upon integration over small timescales, the integrated force becomes normally distributed [134]. Upon integrating Equation (5.9), we find that the integral of the force $W(t) = \int_0^t F_{\text{th}}(t')dt'$ has the following properties:

$$\begin{aligned} &(1)\text{: } W_0 = \int_0^0 F_{\text{th}}\ dt = 0 \\ &(2)\text{: } \langle (W_{t+s} - W_t) W_u \rangle = 0 \text{ for } u < t \\ &(3)\text{: } W_{t+s} - W_t \sim \mathcal{N}(0, g) \end{aligned} \tag{5.10}$$

where properties 2 and 3 can be shown explicitly by substitution of the definition of $W(t) = \int_0^t F_{\text{th}}(t')dt'$, and $g$ is set by the Fluctuation Dissipation Theorem as $g = 2k_B T\zeta s$. These properties, along with the physical constraint that the hair bundle does not "jump" from one position to the next, allow us to identify $W(t)$ formally as a Weiner process [135], or a Brownian motion. Upon differentiation, we identify $dW/dt = \xi_t$ as the derivative of Brownian motion, which is discontinuous everywhere. Equation (5.9) is a stochastic differential equation.

The stochastic differential equation may be solved using Ito's Isometry [135] to find the variance:

$$\mathbf{E}[X_t^2] = \int_0^t (\sqrt{2k_b T/\zeta})^2 dt = \frac{2k_b T}{\zeta} t = 2Dt \tag{5.11}$$

where we have used the Einstein relation $k_B T/\zeta = D$, with $D$ the diffusion constant of the

hair bundle. The mean-squared displacement (MSD) is equivalent to the variance in this case, if we define $X_0 = 0$. In the free diffusion case, then, MSD(t) $\propto t^\nu$ with $\nu = 1$.

The addition of confining potentials can significantly change the shape of the MSD. For instance, for a hair bundle in a harmonic potential with energy $E = \frac{1}{2}\kappa x^2$, again using Ito's Isometry the MSD(t) is given by:

$$\text{MSD(t)} = \frac{k_B T}{\kappa}(1 - e^{-2\kappa t/\zeta}) + x_0^2(1 + e^{-2\kappa t/\zeta} - 2e^{-\kappa t/\zeta}) \tag{5.12}$$

where the hair bundle does not necessarily start at position $x_0 = 0$ at the time of measurement. At short times, the hair bundle undergoes effectively free diffusion (or superdiffusion in some cases), while at long times, the MSD plateaus to a constant value $k_B T/\kappa$.

Actual interferometric measurements of hair bundle fluctuations by (Kozlov et al. 2012) showed anomalous diffusion properties over timescales ranging from $\tau = 0.1$ ms up to $\tau = 10$ ms, with scaling MSD(t) $\propto t^\alpha$ where $\alpha < 1$ [130]. Predictions based on a simple model of hair bundle diffusion in a harmonic potential do not agree with this behavior, as plateauing occurs over less than an order of magnitude in timescale. During their measurements, treatment of hair bundles with BAPTA – causing tip-link breakage – removed the subdiffusive behavior. Blocking channels with 5 mM amiloride did not remove the subdiffusive behavior, ruling out the possibility of channel gating as the primary source. They suggest that the tip link, or something in series with the tip link, acts as a viscoelastic element. Since subdiffusive or superdiffusive behavior must still obey the Fluctuation-Dissipation theorem, they suggest that the driving motion is a fractional brownian motion (fBM) with Hurst parameter $H < 1/2$ that characterizes subdiffusion [136].

In light of these findings, we may ask how the compliance of a system relates to its MSD and power spectral density. From Equation (5.1), we see that the memory kernal $K(t - t')$ relates the displacement $x$ to the driving force $f$. We showed previously that in free conditions, the thermal force is the derivative of a standard Wiener process, such that:

$$x_t \propto \int_{-\infty}^{t} K(t-t')dW_t \tag{5.13}$$

To find the MSD, then, we let:

$$\text{MSD(t)} \propto \mathbf{E}[(x_t - x_0)^2] = \mathbf{E}\Big[\Big(\int_0^t K(t-t')dW_t\Big)^2\Big] \tag{5.14}$$

Again using the Ito Isometry, we find:

$$\text{MSD(t)} \propto \int_0^t K^2(t')dt' \tag{5.15}$$

One can easily confirm that in the case of free diffusion ($K(t-t') = 1$), that the MSD(t) $\propto t^\nu$ with $t^\nu = 1$. This corresponds to a compliance of $\hat{J} = 1/i\omega$, indicating a purely viscous response. In particular, Brownian motion has a flat power spectrum, and Brownian noise (the derivative of the Weiner process) has a power spectral density that decays as $1/\omega^2$. The mean squared displacement, then, may be written as:

$$\text{MSD(t)} \propto \int_0^t \mathcal{F}_u^{-1}[\hat{J}^2(\omega)]dt \tag{5.16}$$

where $\mathcal{F}_u^{-1}$ is the unilateral inverse Fourier transform. Clearly, if $\hat{J} \propto \omega^\alpha$ with $\alpha \neq 1$, then the MSD will scale non-linearly with time.

Although Equation (5.16) is easily found for simple systems in which the Green's function is solvable in the time domain, complications arise when attempting to convert discrete measurements of either experimentally or analytically obtained viscoelastic compliance or modulus data. The inverse unilateral Fourier transform is closely related to the inverse Laplace transform, which in general is difficult to solve even for exact functional forms. As shown in Appendix A, the inverse Laplace transform can be solved by taking a contour integral in the complex plane, and summate all poles in the system. Unfortunately, in many circumstances finding the poles in the complex plane requires extensive computational effort

(in Section 2.6, we were able to find the poles only because the continued fraction could be rewritten in an easily analyzed polynomial form).

There is another way to recover contact with experimental data from the viscoelastic compliance: through the Fluctuation-Dissipation theorem, which relates the power spectral density of thermal fluctuations of the tip of the hair bundle to the viscoelastic loss compliance:

$$\mathcal{F}[x(t)]\mathcal{F}[x(t)]^* = S_x(\omega) = \frac{2k_BT}{\omega}\hat{J}''(\omega) \tag{5.17}$$

In the case of our toy system of a bead in a harmonic potential considered in Section 5.1, we found $\hat{J}'' = \frac{\omega\zeta}{\kappa^2+\omega^2\zeta^2}$. The power spectral density, then, would be given by $S_x(\omega) = 2k_BT/(\kappa^2 + \omega^2\zeta^2)$. This is the classical lorentzian power spectral density, confirming the validity of the approach. In the case where in which the loss compliance is a complex function that is only discretely sampled, the power spectral density is still trivially computed.

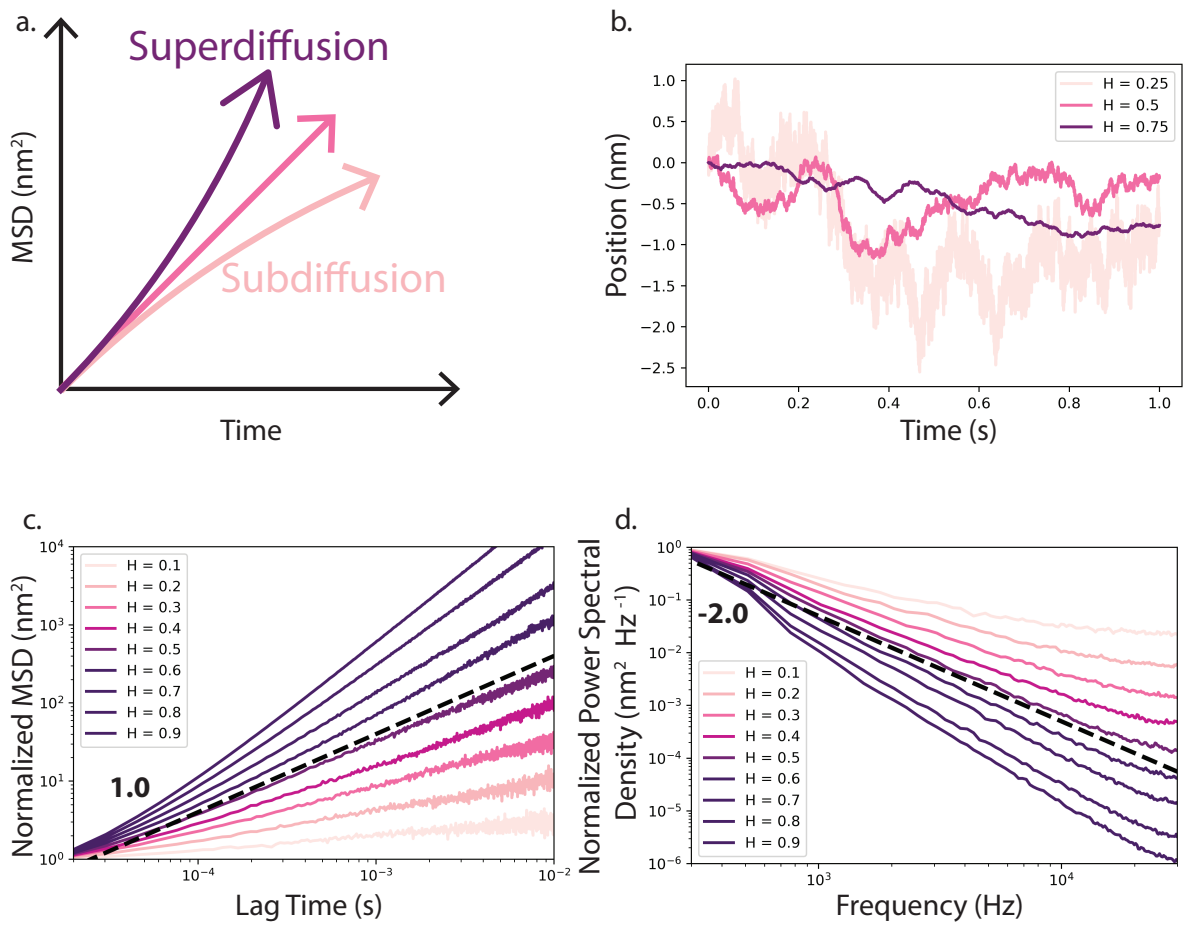


Figure 5.1: **Anomalous Diffusion** In (a), a schematic of the general classes of diffusive behavior. The middle pink line represents standard brownian motion, which has a MSD that scales linearly with time, MSD $\propto$ t. Any process with a MSD that scales slower than this, with MSD $\propto t^{\alpha}$ where $\alpha < 1$, is termed subdiffusive, whereas anything with $\alpha > 1$ is termed superdiffusive. On short timescales, diffusive motion appears superdiffusive due to ballistic motion before sufficient thermal motion takes place to dampen acceleration [137]. Subdiffusive behavior has been found in a variety of contexts, including trapped particles [138] and in the motion of entire hair bundles of the Bullfrog sacculus [130]. (b) Sample traces of fractional Brownian motion generated through the fbm Python package [139] using the Davies-Harte method [155], with different Hurst parameters. Number of points generated $N = 2^{16}$. The $H = 1/2$ condition corresponds to standard Brownian motion, whereas $H < 1/2$ corresponds to subdiffusive Brownian motion and $H > 1/2$ corresponds to superdiffusive Brownian motion. (c). MSDs of sample traces calculated through standard independent increment without overlap averaging algorithm, for Hurst parameters from 0.1 to 0.9. MSDs were normalized to begin at the same position. In black dashed, a line with MSD $\propto t^1$ is plotted for comparison. (d). The power spectral densities of sample traces, normalized to begin at the same position. In black dashed, a line with $PSD \propto \omega^{-2}$ corresponding to the viscous damping of a normal Brownian motion.

## 5.3 Viscoelastic Behavior of a Semiflexible Polymer

The viscoelastic behavior of a semiflexible polymer following Equation (3.26) has been solved for both the inextensible and extensible cases [83]. Here, to consider the results for the extensible case, we define a backbone stiffness $\kappa_s$ as the backbone elastic spring constant, consistent with our notation in Section 3.8. We consider the situation in which we apply a small sinusoidal force $f = f_0 + \delta f \sin(\omega t)$, where $\delta f < f_0$. The results for the elastic and loss compliance are as follows [83]:

$$\hat{J}''(x) = \frac{2}{x}\mathrm{Im}\Big[\sqrt{\phi_c^{1/2}\hat{M}(ix)}\tanh\sqrt{\frac{1}{4}\phi_c^{1/2}\hat{M}(ix)}\Big] \tag{5.18}$$

$$\hat{J}'(x) = \frac{2}{x}\mathrm{Re}\Big[\sqrt{\phi_c^{1/2}\hat{M}(ix)}\tanh\sqrt{\frac{1}{4}\phi_c^{1/2}\hat{M}(ix)}\Big] \tag{5.19}$$

where x $= \omega\zeta_\perp\kappa/f_0^2$, $\phi_c$ is the ratio of the prestress to the critical force $f_c = \kappa l_p^2/\hat{\zeta}^2 l_c^4$, and $\hat{M}$ is an integral defined as [83]:

$$\hat{M}(ix) = \frac{1}{\pi}\int_0^\infty dk\Big[\frac{2k^2}{k^2+1} - \frac{4k^4}{k^2(k^2+1)+ix}\Big] + i\phi_x^{3/2}x \tag{5.20}$$

with $\phi_x$ the ratio of the prestress to the overstretched force scale $f_x = k_B T \kappa_s^{2/3}/l_p^{1/3}$. $\kappa_s$ is related to the elastic spring constant $k_s$ by $\kappa_s = k_s/k_B T$. The change in end-to-end distance $\delta R$ due to this sinusoidal forcing is given by:

$$\delta R(t) = \delta f \frac{\kappa}{\hat{\zeta} l_c f_0^2}\Big[\hat{J}'(\omega\zeta_\perp\kappa/f_0^2)\sin(\omega t) - \hat{J}''(\omega\zeta_\perp\kappa/f_0^2)\cos(\omega t)\Big] \tag{5.21}$$

The inverse equation can also be solved in terms of the viscoelastic modulus $\hat{G}$. In this case we stimulate the polymer by applying the necessary force to extend its end-to-end distance by a set amount $\delta x$. We find:

$$\delta f(t) = \delta x \frac{\hat{\zeta} l_c f_0^2}{\kappa} \Big[ \hat{G}'(\omega \zeta_\perp \kappa / f_0^2) \sin(\omega t) - \hat{G}''(\omega \zeta_\perp \kappa / f_0^2) \cos(\omega t) \Big] \tag{5.22}$$

The maximal change in force applied to the chain by oscillating it by $\delta x$ can be easily calculated as:

$$\delta f_{\max}(\omega) \approx \delta x \frac{\hat{\zeta} l_c f_0^2}{\kappa} \sqrt{\hat{G}'^2(\omega \zeta_\perp \kappa / f_0^2) - \hat{G}''^2(\omega \zeta_\perp \kappa / f_0^2)} \tag{5.23}$$

We also calculate a new measure, the force sensitivity $\chi_f$, which measures by what fraction the force has changed from its resting tension due to a given oscillatory motion. The force sensitivity is defined as:

$$\chi_f(\omega) = \frac{\delta f_{\max}}{f_0 \delta x} = \frac{\hat{\zeta} l_c f_0}{\kappa} \sqrt{\hat{G}'^2(\omega \zeta_\perp \kappa / f_0^2) - \hat{G}''^2(\omega \zeta_\perp \kappa / f_0^2)} \tag{5.24}$$

which has units of $\mathrm{m}^{-1}$. In the context of the auditory system, this force sensitivity represents the change in force on a MET channel when a hair bundle is sheared a set distance. At the level of an individual hair bundle, this shearing motion induces a change in the end-to-end distance of each tip link, transducing force to the channel to regulate its open probability. Channels are sensitive to changes in force from the resting tension, $f_0$, and thus this force sensitivity reflects how sensitive a channel is to oscillations at different frequencies.

## 5.4 Numerical Solutions of Viscoelastic Behavior for the Tip Link

Equations (5.18) can be solved for typical values of the tip link, with $l_c = 150$ nm, $l_p = 10$-$50$ nm, and $\kappa_s = k_s / k_B T \approx 15$ nm$^{-2}$. Figure (5.1) shows the results after numerical integration

of Equation (5.20) for resting tension values ranging from 0.1 to 10 pN. With these values, $f_x$ ranges from 6.8 pN to 11.6 pN scaling $l_p$ from 50 to 10 nm, and $f_c$ ranges from 4 fN to 30 aN, again scaling $l_p$ from 50 to 10 nm. The results of our calculations show the existence of a crossover regime for both the viscoelastic compliance and viscoelastic modulus $\hat{J}$ and $\hat{G}$, where at low frequencies the behavior is governed by the elastic response, but above a crossover frequency the behavior becomes dominated by the viscous response. For high values of resting tension, the frequency at which this crossover occurs increases by orders of magnitude for a small change in force. The viscoelastic modulus shows similar behavior, in which the elastic component remains constant before increasing above a certain frequency. This behavior corresponds to the polymer not having sufficient time to come to equilibrium, causing large tension spikes at the ends and resulting in local stretching of the backbone. This is similar to the behavior that we observed in Chapter 4, in which the penetration depth of tension into the bulk of the chain decreased at high frequencies of forcing. We may directly compare the results of our model, in Figure 5.2, with the modulus found for the entire hair bundle [130]. Impressively, the hair bundles rheological properties follow a similar pattern to that observed in our model, with crossover frequency occurring shortly before an increase in the elastic modulus. Our model does not capture all behaviors, which is expected inasmuch as it considers a polymer as the sole viscoelastic element in the system.

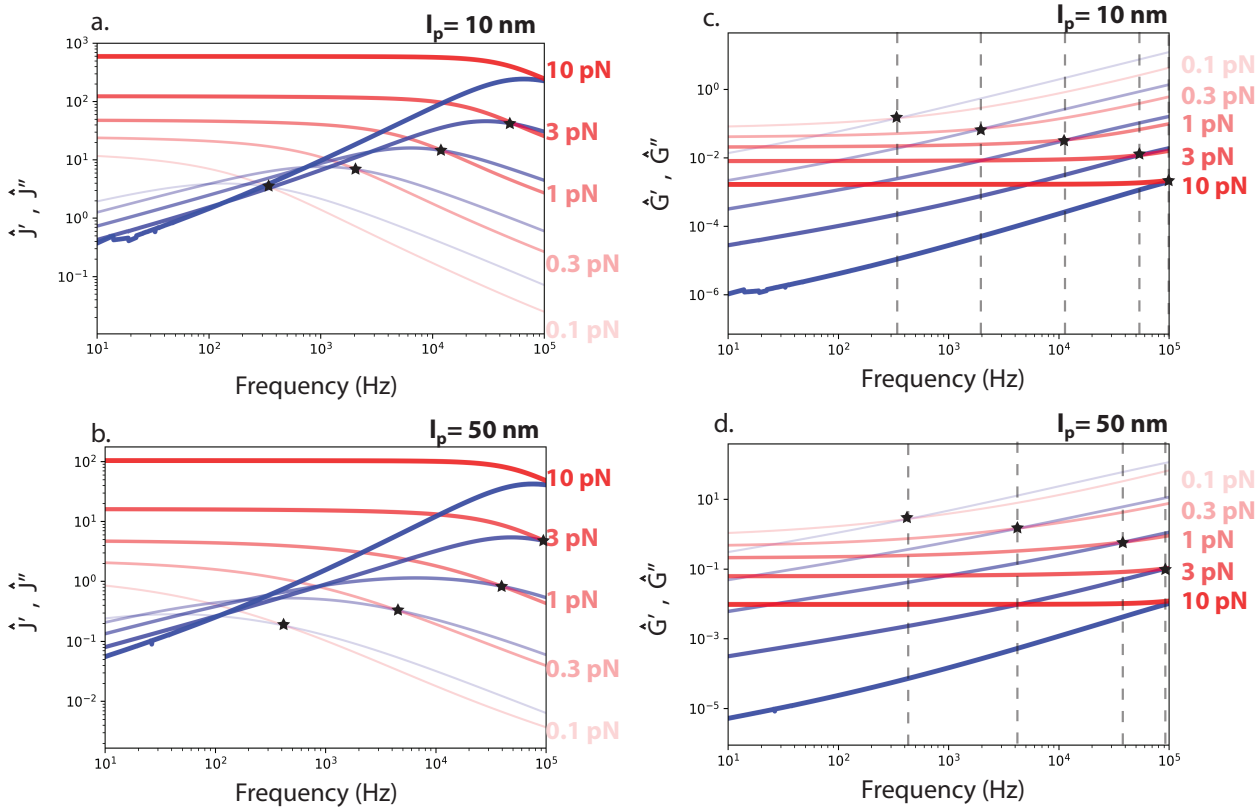


Figure 5.2: **Viscoelastic Properties of a Tip-Link-Like Polymer** Viscoelastic compliance $\hat{J}$ and modulus $\hat{G}$ are shown for a polymer with values taken close to those known for a tip link ($\zeta_\perp = 100$ mN$\cdot$ s $\cdot$ m$^{-2}$, $l_c = 150$ nm,$k_s = 60$ mN/m). (a,b) The viscoelastic compliance of the polymer as a function of stimulus frequency (Hz). In red, the real, in-phase component of the compliance $\hat{J}'$. In blue, the out-of-phase dissipative component $\hat{J}''$. The two components reverse order at critical frequencies denoted by stars. These points represent the frequencies above which compliance from the dissipative component outweighs the compliance of the elastic stretching. Changing the persistence length by a factor of 5 does little to change the qualitative behavior, but shifts the frequency cutoffs to lower values. Gradient of opacity curves represents different values of $f_0$ chosen roughly on a logarithmic scale (0.1 pN, 0.3 pN, 1 pN, 3 pN, 10 pN). (c,d) The viscoelastic modulus of the polymer, defined as $\frac{1}{\hat{J}'+i\hat{J}''}$. In red and blue, the in- and out-of-phase elastic moduli $\hat{G}'$ and $\hat{G}''$. The elastic response remains constant at low frequencies, whereas the dissipative component rises due to increasing heat dissipation into the bath. At high frequencies, the effective spring constant of the polymer becomes dominated by viscous effects. Increasing resting tension shifts the frequency at which this occurs to progressively higher values, spaced roughly equal on the logarithmic scale.

The effect of this change in viscoelastic behavior is elucidated further by considering the force sensitivity $\chi_f(\omega)$ defined in the previous section. Using our standard parameter values, we numerically solve the force sensitivity for the $l_p = 10$ nm model and the $l_p = 50$ nm model (Figure 5.2). At slow resting tensions (lightly shaded), the force sensitivity immediately rises, and eventually scales with frequency as $\chi_f(\omega) \propto \omega^\alpha$ with $\alpha \approx 0.7 - 0.85$ (scaling $l_p$ from 50 to 10 nm). For higher values of resting tension, the frequency at which the sensitivity scales progressively shifts upwards. After this crossover frequency, which we term the amplification frequency, the sensitivity again begins to rise with the same fractional exponent. At much higher resting tensions, the model enters into the overstretched limit, in which the increased force causes a shift downward in sensitivity for all frequencies. This downward shift is to be expected, since at very high resting tensions, the chain begins to act like a hookean spring with constant spring constant given by the backbone tension. The frequency sensitivity thus scales as $\chi_f \propto 1/f_0$, in the overstretched limit. In the model of $l_p = 10$ nm, the force at which this crossover occurs is around 10 pN, and thus the effect is not strongly felt. In the model of $l_p = 50$ nm, the effect can become large.

The amplification frequency at which the polymer begins to become more sensitive increases dramatically as a function of resting tension $f_0$. In Figure 5.3, we show the frequency at which the sensitivity has changed 20% from its base value at low frequencies. Strikingly, we observe that shifting resting tension by two orders of magnitude results in almost a four-order-of-magnitude change in the amplification frequency. These forces are well within the range of tensions that have been observed for individual tip links in the cochlea [38], and are easily regulated by tuning the strength of myosin motors in the insertional plaque. For instance, a polymer with a resting tension of 1 pN would respond to a 4 nm change in end-to-end distance with force of 0.08 pN at 100 Hz, whereas at 10 kHz it would respond at 0.8 pN. On this scale of the resting tension of 1 pN, this represents a massive change, yet on a global biological scale, it is well within the range we would expect to be relevant and measurable by biological processes.

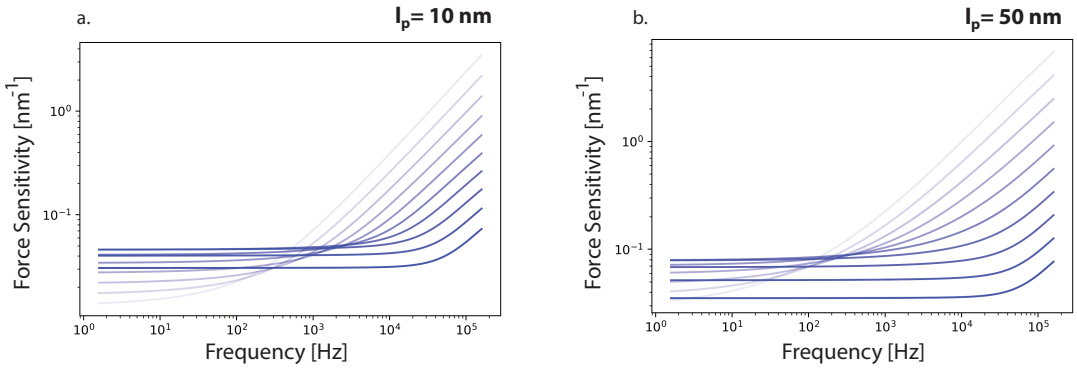


Figure 5.3: **Force Sensitivity of Polymers** The force sensitivity curves $\chi_f(\omega/2\pi)$ for tip-link-like polymers with values $\zeta_\perp = 100$ mN$\cdot$ s $\cdot$ m$^{-2}$, $l_c = 150$ nm,$k_s = 60$ mN/m. Force sensitivity is defined as the fractional change in maximum force necessary to change the end-to-end distance of a chain by set amount $\delta x$, given by $\chi_f(\omega/2\pi) = \delta x f_{\max}/f_0$ (a) The force sensitivity curve for a low persistence length model, for values of resting tension $f_0$ ranging from 0.1 pN to 10 pN on a logarithmic scale (light to dark: 0.100 pN, 0.167 pN, 0.278 pN, 0.465 pN, 0.774 pN, 1.292 pN, 2.154 pN, 3.594 pN, 5.995 pN, 10 pN). Higher sensitivity corresponds to greater changes in force at the ends of the chain. At characteristic resting tension dependent frequencies, the sensitivity changes from a constant value and increases exponentially. As resting tension increases, the frequency at which the sensitivity changes also increases exponentially. This "folded sheet" like diagram corresponds to a frequency dependent reversal of the resting tension sensitivity ordering. (b) The same values as in a, but for a larger persistence length. At high resting tensions (10 pN), the sensitivity decreases everywhere, indicating the chain is approaching the overstretched limit in which stochastic random motion plays a diminished role in its behavior.

In order to gain further insight into possible mechanisms by which the auditory system may tune its resonant frequency along the tonotopic axis, we examined the predicted force that would be transferred to a channel upon hair-bundle deflection at different resting tensions of the tip link, and for several frequencies chosen on a logarithmic scale (Figure 5.5). Along the tonotopic axis, the resting tension of the tip links are known to increase from the apex to the base of the cochlea, and correspondingly from low to high frequency. We replicated a characteristic change in resting tension that would be observed along the spiral of the cochlea, within our range of working parameters from 0.1 pN to 10 pN. Whereas the

actual resting tension of the tip links have been measured to be higher [38], which according to our model would indicate the tip link would be in the stretched limit, we assume at least some tip links are under low tension by being partially unfolded, or else imagine a scenario in which the actual persistence length of some segments is far less than we anticipate for the fully folded tip link. Additionally, one may imagine a mechanism in which $Ca^{2+}$ feedback regulates the strength or slippage rate of myosin motors within the insertional plaque, allowing some tip links to retain low resting tensions to become more sensitive to high-frequency stimuli.

For polymers under low resting tensions, we find that stimulating the end-to-end distance with progressively higher frequencies leads to and increased force-transfer function, defined as $\mathcal{F}_t = \chi_x \cdot f_0$, which represents the change in force applied to the channel per length unit of extension (measured here in nanometers). The low-tension chains have very low force transfer values at low frequencies of stimulation, which then increase dramatically at higher frequencies of stimulation. The high-tension chains are resistant to changes in frequency, and begin to shift their response only once they are driven at frequencies in the range of 10 kHz. This change in behavior is consistent with our other measures of force sensitivity. For some special frequencies, within the range of 100 Hz to 2 kHz, we find that the force transfer takes on local minima.

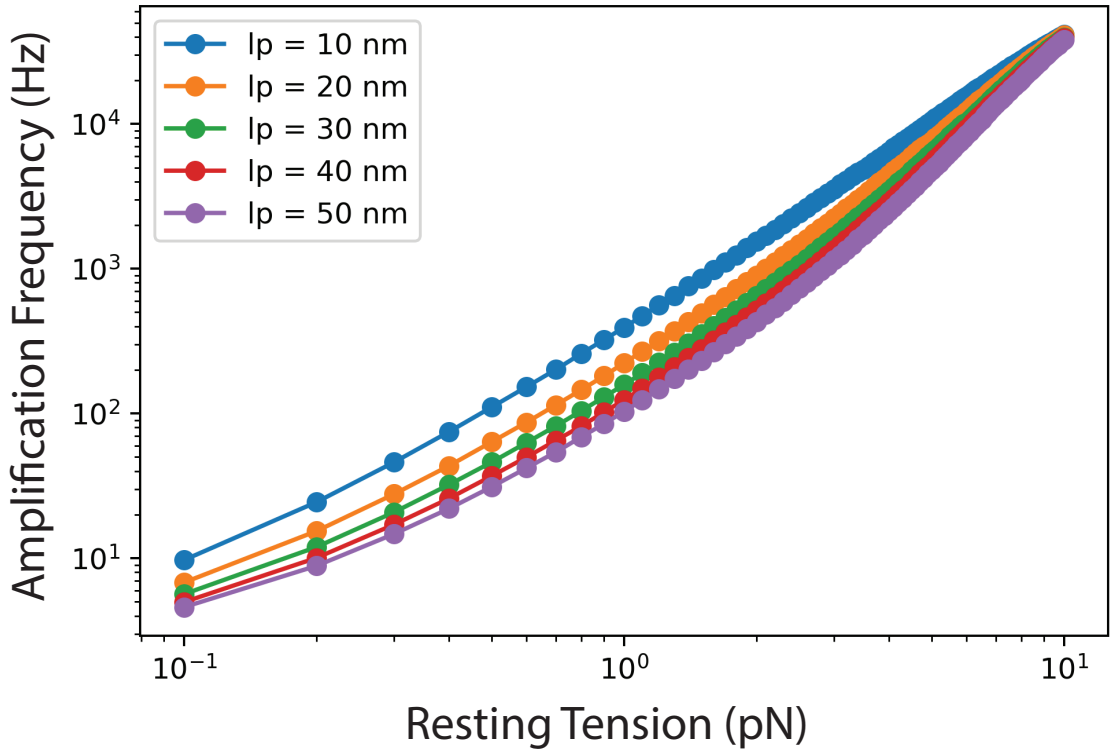


Figure 5.4: **Amplification Frequency** The lowest frequency at which the chain increases force sensitivity $\chi_f(\omega/2\pi)$ by 20%. As resting tension increases from easily regulated physical values from 0.1 pN to 10 pN, the frequency at which amplification begins (the amplification frequency) increases orders of magnitude from 10 Hz to 50 kHz, spanning the entirety of the human auditory range and beyond. Traces also shown for various physically relevant possible persistence lengths $l_p$, showing that the effect is largely model independent.

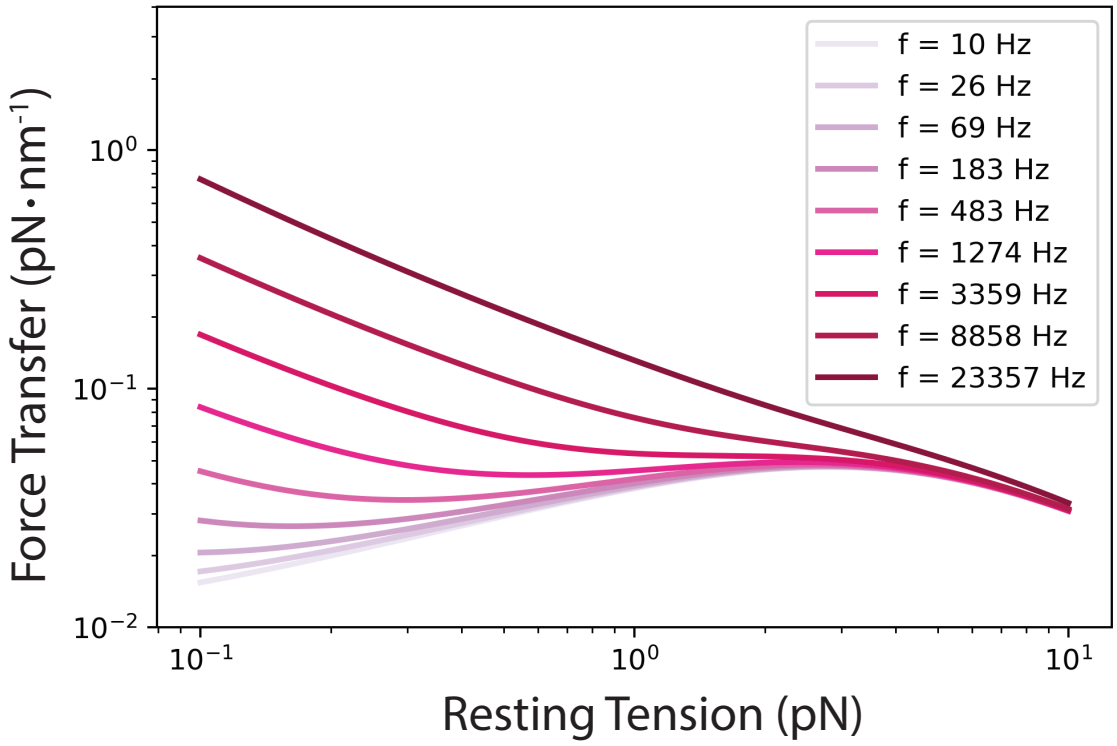


Figure 5.5: **Predicted Force Transfer to Channel**. The predicted force transfer function $\mathcal{F}_t = \chi_f \cdot f_0$, which measures the change in force at the end of the polymer per unit of distance oscillation. At high resting tensions, the polymer is insensitive to changes in frequency, and responds with the same force. At lower resting tensions, the polymer is insensitive to changes in frequency up to a particular cutoff frequency, whereafter it begins to rise. The auditory system of mammals possesses both gradients in resting tension and in frequency sensitivity, from low-frequency sensitivity and low resting tension at the apex, to high-frequency sensitivity and high resting tension at the base. As resting tension increases, the force transfer attenuates and approaches the overstretched limit not captured by the model. By lowering the resting tension, a polymer is able to increase its sensitivity to high frequencies. At certain frequencies of oscillation around the 1 kHz regime, the force transfer takes on nonextrema local minimum.

Finally, to make contact with experiments that suggest the hair bundle may undergo a subdiffusive motion, we calculate the power spectral density from the viscoelastic compliance by using the Fluctuation-Dissipation Theorem given in Equation (5.17) (Figure 5.6). We vary the resting tension $f_0$ logrithmically from 0.1 to 10 pN, and again consider the low

frequency and high frequency limit of scaling. In the limit of high frequency, the PSD of all resting tensions scales as $PSD \propto \omega^{-1.75}$, which indicates subdiffusive motion with a Hurst parameter of $H \approx 0.4$. This subdiffusive motion is identical to that found for the entire hair bundle, and agrees with previous analysis of end-to-end distance fluctuations for semiflexible polymers [109]. Surprisingly, our results also show a regime in which the PSD scaling changes from $\omega^{-1.75}$ to $\omega^{-0.6}$, with the size of the crossover regime and frequency position being dependent on resting tension. This crossover regime can manifest as a region of extended subdiffusion with changing Hurst parameter depending on the lag time.

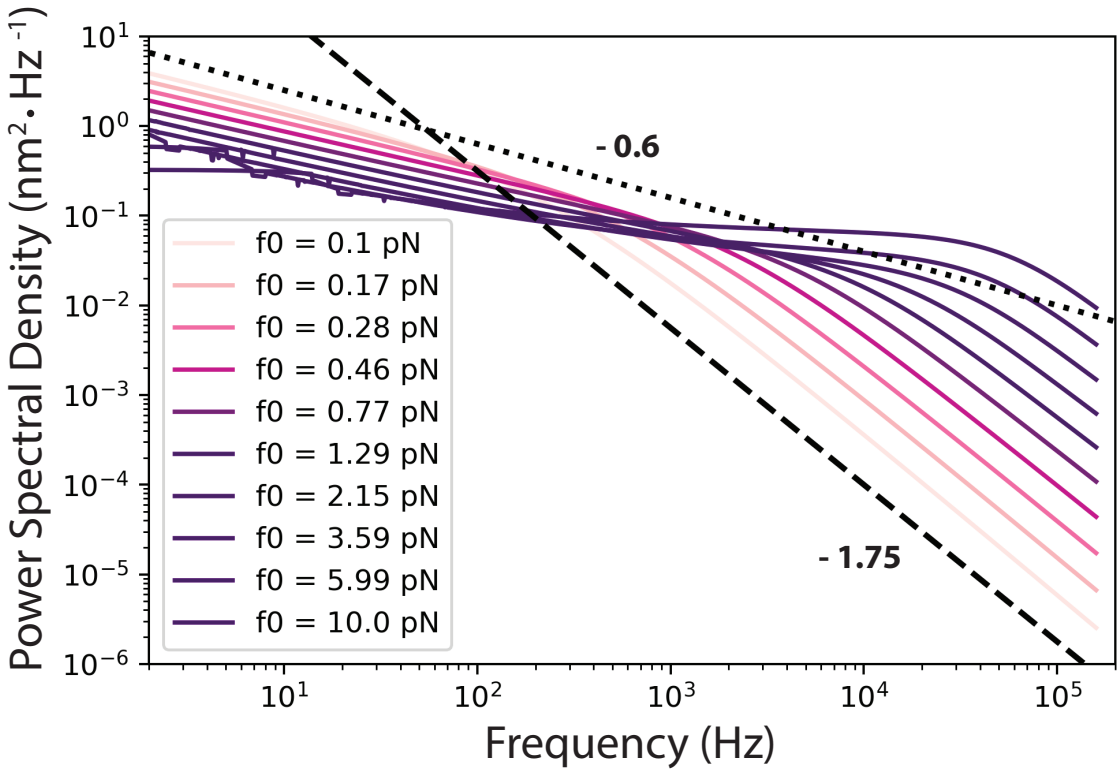


Figure 5.6: **Power Spectral Density of Polymers Under Tension** The predicted power spectral density of measurements of the end-to-end distance change of a fluctuating polymer in solution under an average tension $f_0$. In color, the values calculated from using the Fluctuation-Dissipation Theorem for polymers under varying amounts of tension. In dashed black and dotted black, for comparison, functions that scale as $H(\omega) \propto \omega^{\alpha}$ with $\alpha = -1.75$ and $\alpha = -0.6$ respectively. The fractional dependence at high frequencies (with $\alpha = -1.75$) manifests as subdiffusive behavior in the MSD [140]. At lower frequencies, the PSD does not level off, but retains some frequency dependence with fractional exponent $\alpha \approx -0.6$. The frequency range over which the $\alpha = -1.75$ regime occurs decreases with increasing average tension. As with the force sensitivity, the tension dependent crossover frequency where the two regimes diverge varies over several orders of magnitude. In this crossover regime, the value of alpha is rapidly shifting, causing the anomalous diffusion to change in character. Numerical errors caused irregular behavior in extreme cases, reflecting the breakdown of the theory at high resting tensions and low frequencies as the overstretched limit was approached.

## 5.5 Combined Basilar Membrane Mechanics

The entire basilar membrane does not oscillate in response to a pure tone of discrete frequency. A traveling wave is induced along the cochlea due to pressure changes between the scala tympani and scala media, which decelerates and peaks at a characteristic position along the cochlea. This waveform has been calculated from first principles, showing that the wave envelope has significant weight to the base of the characteristic position, and rapidly deteriorates towards the apex [141].

In light of our findings, we suggest that the resting tension in the tip link might act as a further source of frequency discrimination basal to the characteristic position. As we showed in the previous section, a tip link that has the capacity to tune its resting tension can change the frequency beyond which it becomes more force-sensitive. We take force-sensitive here to mean the force that will be exerted on the MET channel by oscillation of the tip link. Consider a tone at an intermediate frequency, of around 1 kHz, which stimulates a position at the start of the second turn of the cochlea. Towards the apex from this point lie tip links with low average resting tension. These tip links, we have shown, become extremely sensitive to frequencies greater than their hair bundle's characteristic frequency. Due to the rapid tapering of the traveling wave envelope, however, the oscillation amplitude of these tip links is effectively zero, and the hair bundles do not respond. Towards the base the tip links are highly tightened, and respond similarly to low- and high- frequency oscillations. These tip links are stimulated by the tone, but because the frequency is not sufficiently high, their response remains constant. The hair bundles that are stimulated maximally at this tone, then, should try to tune their resting tensions to the point where the tone has significantly begun to impact their force sensitivity.

It is worth noting again that these values of resting tension are not typically seen in experimental measurements of the entire hair bundle. This does not, however, preclude the use of this mechanism in the auditory system. Through actions of cadherin domain unfolding,

myosin motor slippage, and heterogeneous resting tension distributions within an individual hair bundle, at least some tip links may be in a low resting tension state in even high frequency hair bundles.

## 5.6 Conclusions

In this chapter, we reviewed linear viscoelastic theory to analyze the behavior of a tip-link-like polymer under small oscillatory motion. We additionally reviewed the topics of diffusion and subdiffusion, in order to relate our models to experimental data. We found that tip links are poised at parameter values appropriate to allow for a unique frequency-dependent behavior that is tightly regulated by the average resting tension.

This concludes our formal discussion of tip-link models, and we will review our conclusions again in Chapter 7. In the following chapter, we take a detour into the realm of Monte Carlo sampling of polymer configurations in thermal equilibrium. At the end, we discuss strategies we hope to implement in the future to extend Monte Carlo sampling into the time domain, so that we may probe the conformation distribution of a polymer undergoing fast dynamic stretching.

# Chapter 6: Fast Monte Carlo Sampling of Polymers

The late twentieth century saw a reinvigoration in the study of single-chain polymers, catalyzed by the advent of optical-force and atomic-force microscopy, which permit the measurement of real biopolymers [142]. As a prototypical example, a single strand of DNA or protein is glued between either two beads in solution, or a functionalized glass surface and a single bead. The bead is then pulled slowly, using either optical-trapping force or magnetic force, which applies constant tension to the chain. The position of the bead is recorded, allowing for precise determination of the resulting extension.

Although these experiments and calculations provide information about the end-to-end distance of the chain, they are not capable of providing a detailed picture of the entire chain's conformation. Although unimportant over long timescales where the polymer fluctuates in equilibrium, the details of the chain conformation can play a critical role in fast dynamic processes. For instance, after a polymer under tension is instantaneously released, the rate of recoil is tied closely to the conformation of the chain near the ends [85]. Additionally, constraints on the local tangents at the ends of the chain can influence global-chain conformations and can significantly alter the behavior of a polymer under tension [143, 108]. For contour lengths $l_c$ much greater than the persistence length $l_p$ of a polymer, these boundary

conditions play a negligible role, but for short chains and over short timescales, the conformation near the boundary is critically important to predicting the resulting end-to-end distribution.

Due to their microscopic size and shape, visualization of real polymers can be difficult [144, 145], relying either on electron microscopy or sparse markers to visualize portions of the chain. As an alternative, one may build a model for a specific polymer of interest, and after construction of its hamiltonian, computationally simulate a chain configuration from first principles. Configurations can be generated "directly", whereby they are drawn independently from the distribution, or can be generated sequentially, through use of a Markov Chain Monte Carlo (MCMC) algorithm. For polymers in equilibrium with no constraints, the MCMC procedure is straightforward – we start from an allowable configuration and adjust slightly the position of every point along the chain. If the energy has decreased, we accept the move, and if the energy has increased, we accept it with a probability proportional to the ratio of the two configurations' Boltzmann factors.

As discussed in Section 2.4, physical constraints limit the viability of the traditional MCMC technique, due to the excessively high rate of proposed-configuration rejection [99, **?**]. In contrast, MCMC pivot algorithms – whereby large portions of the polymer configuration moves at once – have comparatively low rejection rates and allow fast sampling of diverse polymer conformations. Pivot algorithms, however, are restricted to use in lattice models of polymers, for which positions may only take on discrete values.

In this chapter we will discuss a novel algorithm for sampling the configurations of polymers in equilibrium subject to a fixed end-to-end-distance constraint. We focus primarily on the FJC model, but also address subtle complications when attempting to extend the procedure to the WLC model. Key to our algorithm will the accurate determination of the midpoint distribution. We make use of a pseudo-direct procedure, whereby each conformation sample is independent from the previous, but which makes use of MCMC in determining where to place points along a particular conformation.

## 6.1 Random Flights

As the cornerstone of our sampling algorithm, we first consider the probability distribution of random flights in $\mathbb{R}^2$ and $\mathbb{R}^3$ for an arbitrary number of steps $N$. The random flight model is identical to the discretized FJC model described in Section 2.1, consisting of $N+1$ beads linked together by $N$ bonds, and where each bond vector is free to rotate. The total length of the uncoiled chain is denoted by $l_c$, the contour length of the chain. Consequently, the length of each bond, or the step size of each flight, is given by $b = l_c/N$. By definition of the model, we assume freely-jointed segments, such that there is no energetic cost to bending of adjacent segments, and segments are free to rotate. The statistics of the chain are thus governed solely by entropic effects. In arbitrary dimensions, the correlation between adjacent segments is given by $\left\langle \vec{r}_i \cdot \vec{r}_{i+1} \right\rangle = 0$.

In Section 2.1, we found the probability density for the end-to-end distance for a chain with a large number of segments $N$ to be:

$$p_N(r) = 4\pi r^2 \Big(\frac{3}{2\pi N b^2}\Big)^{3/2} e^{-\frac{3r^2}{2Nb^2}} \tag{6.1}$$

In $\mathbb{R}^3$. Similarly, in $\mathbb{R}^2$, the end-to-end distance distribution is given by:

$$p_N(r) = \Big(\frac{2r}{\pi N b^2}\Big) e^{-\frac{r^2}{Nb^2}} \tag{6.2}$$

The probability distributions above were derived in the limit that $N \to \infty$. Clearly, as $N$ becomes small, these probability densities fail to hold and obey the arclength constraint set by $Nb = l_c$. In the case of a small numbers of segments, the probability distributions deviate significantly from the large-chain limit. The breakdown occurs at approximately

$N = 8$ for chains in $\mathbb{R}^2$, and at $N = 6$ for chains in $\mathbb{R}^3$. We begin by exactly solving the small-$N$ cases, and give formulas as $N$ approaches intermediate values. For convenience, we normalize all chain lengths to be $l_c = 1$, such that the probability of the end-to-end distance vector magnitude $P(r \leq 1) = 1$

Probability densities of short random flights were considered long ago by Kluyver, who expressed the densities of an $N$-step random walk in terms of Bessel functions [146, 147]:

$$p_N(r) = \int_0^\infty rtJ_0(rt)J_0^N(t)dt \tag{6.3}$$

where $J_0$ is a Bessel function of the first kind of order 0. Although these formula are solvable numerically, we also wish to gain an intuitive understanding behind the procedure of determining these probability densities. To that end, we show the analytic calculation for the density for small $N = 1$ and 2.

In the case that $N = 1$, the probability density is given by:

$$p_{N=1}(r, \theta) = \frac{\delta(\|r\| - 1)}{2\pi} \tag{6.4}$$

where $\|r\|$ is the magnitude of the end to end distance vector $\vec{r}$. As required, the total probability for the vector to lie in the circular plane of radius one is given by

$$P(r \leq 1) = \int_0^\infty \int_0^{2\pi} p(r, \theta)d\theta dr = \int_0^\infty \int_0^{2\pi} \frac{\delta(\|r\| - 1)}{2\pi} d\theta dr = \int_0^{2\pi} \frac{1}{2\pi} d\theta = 1 \tag{6.5}$$

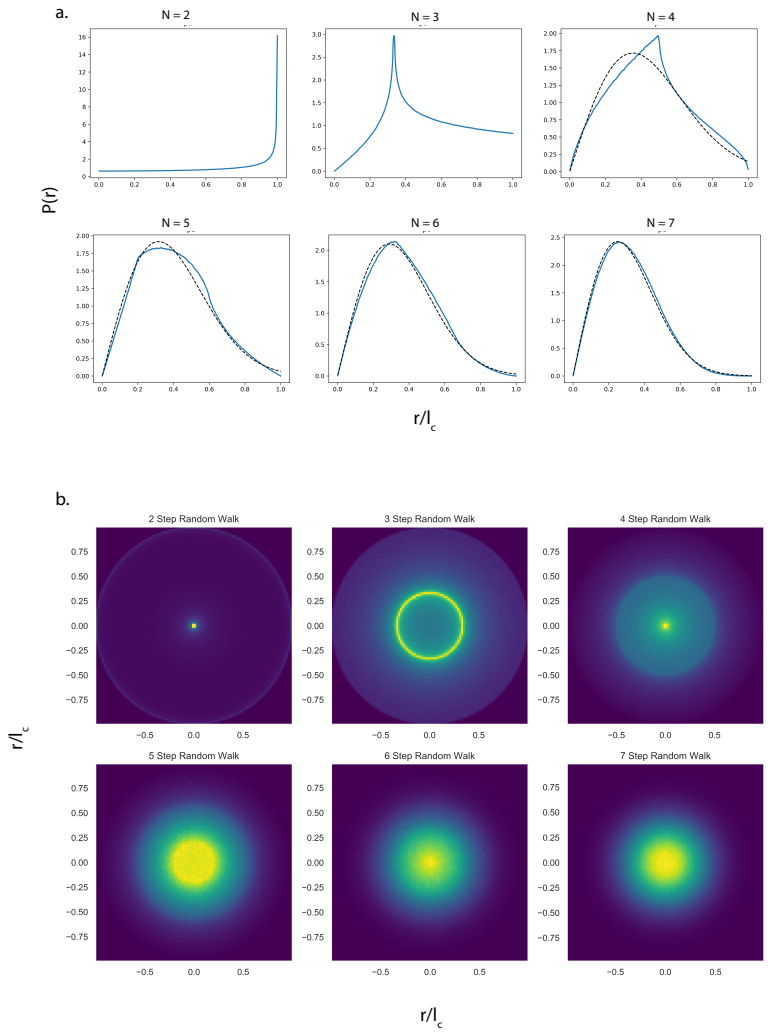


Figure 6.1: **Short Random Walks In Two Dimensions** The probability density of short random walks simulated directly and independently. In (a), the probability density of an end-to-end distance $r$ for an $N$-step random walk with total walk length equal to unity. Blue traces were constructed by taking $10^7$ independent samples, converted into a cumulative distribution function, and numerically differentiated and smoothed. Fits to the Gaussian approximation (dashed black line), for comparison. In (b), the raw two-dimensional histograms of the $N$-step random walks.

For the case of $N$=2, we may determine the probability density by constructing the joint probability of taking a $N$=1 step given a starting position drawn from the random distribution of Equation (6.4). Integrating over all possible positions of the $N = 1$ step then gives the probability distribution of the $N = 2$ position.

$$p_{N=2}(r,\theta) = \int_0^\infty \int_0^{2\pi} p(r_2,\theta_2|r_1,\theta_1)p(r_1,\theta_1)dr_1 d\theta_1 \tag{6.6}$$

Because the probability of a single $N$=1 step from $(r_1,\theta_1)$ to $(r_2,\theta_2)$ is given by Equation (6.4) with a shifted origin, we may write the transition probability $p(r_2,\theta_2|r_1,\theta_1)$ as $\delta(\|\vec{r}_1 - \vec{r}_2\| - 1)/2\pi$, or in polar coordinates, $\delta(\sqrt{r_1^2 + r_2^2 - 2r_1 r_2 \cos\theta_1 - \theta_2} - 1)/2\pi$. Combining this form with Equation (6.6) gives

$$p_{N=2}(r,\theta) = \frac{1}{4\pi^2}\int_0^\infty \int_0^{2\pi} \delta(r_1 - 1)\delta\left(\sqrt{r_1^2 + r_2^2 - 2r_1 r_2 \cos\theta_1 - \theta_2} - 1\right) dr_1 d\theta_1 \tag{6.7}$$

Integrating over both variables, with the property that the integral of $\delta(r_1 - 1)f(r_1) = f(1)$, we find

$$p_{N=2}(r,\theta) = \frac{1}{\pi^2\sqrt{1-r^2}} \tag{6.8}$$

where we have rescaled in the final equation such that the maximum magnitude of $\vec{r}$ is 1. The probability distribution is again independent of $\theta$ as expected, but its radial dependence is nontrivial. The probability of any vector, $\vec{r}$, is given by the probability density for the radius divided by the surface area of the circle

$$p_{N=2}(\vec{r},\theta) = p_{N=2}(r,\theta)/2\pi r = \frac{1}{2\pi^3 r\sqrt{1-r^2}} \tag{6.9}$$

where $r$ is the magnitude of the vector $\vec{r}$. This equation predicts a peak in probability at the midpoint and again towards the edges of the circle.

For the case of $N = 3$, the probability is again constructed by taking the joint probability of taking a $N = 1$ step given a starting position drawn from the random distribution of Equation (6.8). Analytically, this may be expressed as

$$p_{N=3}(r,\theta) = \int_0^\infty \int_0^{2\pi} p(r_3,\theta_3|r_2,\theta_2)p(r_2,\theta_2)dr_2 d\theta_2 \tag{6.10}$$

We may again express the transition probability $p(r_3,\theta_3|r_2,\theta_2)$ as $\delta(\sqrt{r_2^2+r_3^2-2r_2r_3\cos\theta_2-\theta_3}-1)/2\pi$. Combining this with the expression for the probability density of the $N = 2$ step random walk, we find

$$p_{N=3}(r,\theta) = \frac{1}{2\pi^3}\int_0^\infty \int_0^{2\pi} \frac{1}{\sqrt{1-r_2^2}}\delta\left(\sqrt{r_2^2+r_3^2-2r_2r_3\cos\theta_2-\theta_3}-1\right)dr_2 d\theta_2 \tag{6.11}$$

Unlike the previous integrals, Equation (6.11) cannot be solved through naive integration. Instead, we may resort to using numerical techniques to evaluate the integral given in Equation (6.3). In general, the analytical forms of Equation (6.3) are difficult to find, and have only recently been found in closed form solution for $N = 3$ and $N = 4$ [147]:

$$p_{N=3}(r,\theta) = \frac{6\sqrt{3}}{\pi}\frac{r}{(3^3+r^2)}{}_2F_1\left(\frac{1}{3},\frac{2}{3},1\middle|\frac{r^2(9^2-r^2)^2}{(3^3+r^2)^3}\right) \tag{6.12}$$

$$p_{N=4}(r,\theta) = \frac{2}{\pi^2}\frac{\sqrt{256-r^2}}{r}{}_2\mathrm{Re}_3F_2\left(\frac{1}{2},\frac{1}{2},\frac{1}{2},\frac{5}{6},\frac{7}{6}\middle|\frac{4(256-r^2)^3}{27r^4}\right) \tag{6.13}$$

where the $F$'s are hypergeometric functions. The complexity of the closed-form solutions for short random walks reflects the modularity of the density function, which changes character at specific points in $r$.

As an alternative to direct integration, we computationally simulated $N$-step random walks to generate probability distributions of the end-to-end distance vector $\vec{r}$. Figure 6.1 shows these computations, each of which was preformed by taking $10^7$ direct samples. Start-

ing from the origin, we randomly sampled points spaced a distance $1/N$ away by drawing two independent samples from a Gaussian distribution and rescaling their magnitude [148]. The process was repeated $N$ times to give a total random walk of length unity. Probability densities were constructed first by discretizing the $r$ coordinate and calculating the cumulative distribution by sequential ordering of samples, and then by numerical differentiation. Raw probability densities were jagged, and were subsequently smoothed using a linear Savitzky  Golay filter with window length of 11 points. Figure 6.1a shows the probability density functions for $N = 2$, 3, 4, 5, 6, and 7 steps. While the two-step random walk reflects our derivation found previously, the $2 < N < 6$ random walks are both non-gaussian and modular, consisting of piecewise continuous non-analytical functions that join at different values of $r$. For these short walks, we compared the results to those predicted by the $N \to \infty$ limit. By the seven-step walk, the result is nearly gaussian. Figure 6.2b shows the raw two-dimensional histograms found by the direct sampling approach, which give an intuitive picture of where the walk is likely to conclude. For short walks, the most probable areas form concentric rings and circles, reflecting the nonintuitive statistics of short random walks. By the seven-step random walk, however, the system has converged close to a Gaussian distribution.

We repeated the procedure outlined above, but for the random walk in $\mathbb{R}^3$, this time sampling three independent Gaussian random variables for each step (Figure 6.3). Here we show the raw cumulative distribution functions, as well as the probability densities. The probability densities are qualitatively different than those found in $\mathbb{R}^3$, especially for the small two and three step cases. As the step size increases to four steps, the probability distributions quickly converge onto the $N \to \infty$ gaussian limit. These results have been well characterized in previous work, but remain an active area of study.

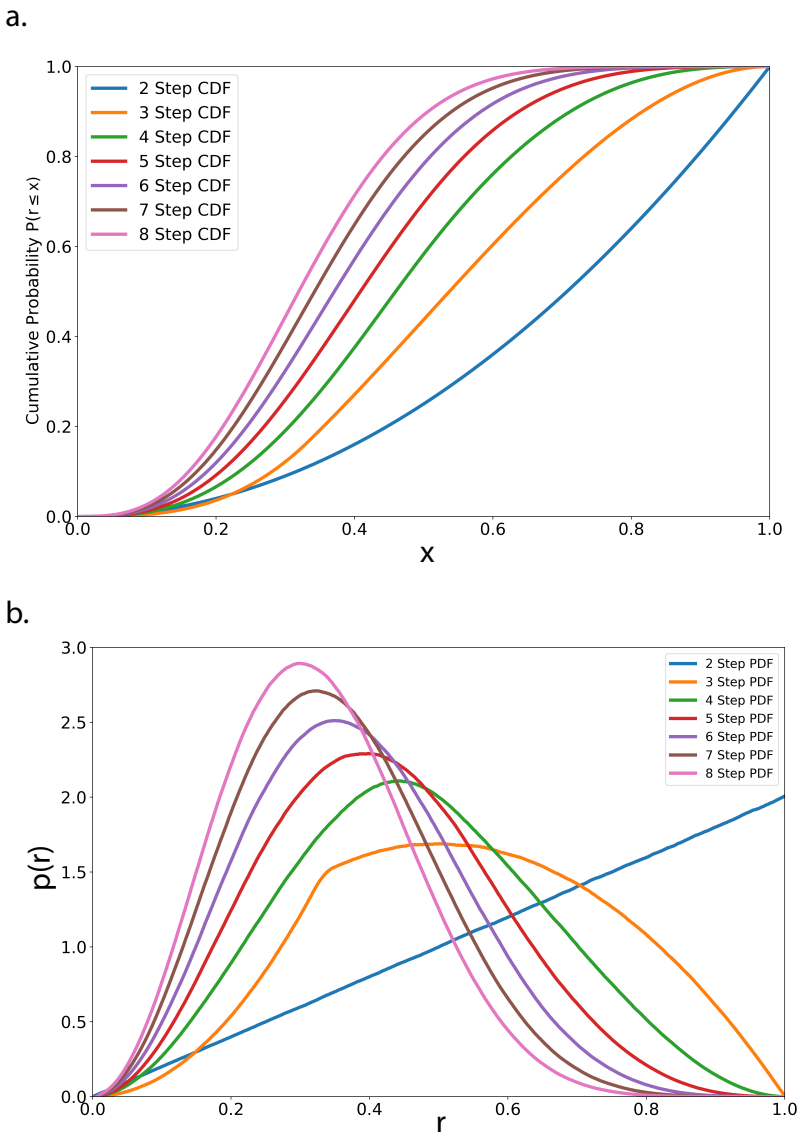


Figure 6.2: **Short Random Walks In Three Dimensions** Short random walks of step number $N$ in three dimensions were calculated identically to those for the two-dimensional case, and with number of independent samples $10^8$. In (a), the raw cumulative distribution function calculated by sorting algorithm. In (b), the resulting probability densities of end-to-end distance $r$.

## 6.2 Midpoint Distribution of the Random Flight

The midpoint distributions of the short random walks considered in the previous section are nontrivial, but can be calculated computationally with minimal effort once the probability distributions of the short random flights are in hand. We first review the result for the large-$N$ limit, and then move to the small-$N$ limit.

The midpoint distribution of a random walk is dependent on three parameters: the end-to-end distance vector $\vec{R}$, the total walk length $l_c$, and the number of steps $N$. For simplicity, we always orient the end-to-end distance vector along the $\hat{x}$ axis, corresponding to a rotation of our coordinate system, and let $R$ be the distance in the new $\hat{x}$ direction. Clearly, the step size $b$ must be given by $b = l_c/N$. By definition, the random walk cannot extend further than the total walk length $l_c$, so $R \leq l_c$.

Here, we consider the case in which we fix the ends of the walk to be exactly a distance $R$ apart. In the limit that $R \to l_c$, the walk must collapse to a straight line. When $R < l_c$, the walk can take significant deviations, but is forced back towards the $\vec{R}$ direction by the necessity of progress towards its ultimate destination. This is similar to the Levy construction of a brownian bridge, and is closely related to the midpoint of a brownian sheet, but has subtle differences that change the physics significantly [149]. Notably, the fixed step length sets an additional constraint on the system that must be obeyed.

The midpoint distribution of such a random walk with fixed $R$ is given by the product of the probability of two walks of length $l_c/2$ and with $N/2$ number of steps meeting at position $\vec{r}$:

$$p_{N,\text{mid}}(\vec{r}) = p_{N/2}(|\vec{r}|)p_{N/2}(|\vec{R} - \vec{r}|) \tag{6.14}$$

In simpler terms, the probability of finding the midpoint at position $\vec{r}$ is equivalent to the probability of a random walk of $N/2$ steps traveling from the origin to the position $\vec{r}$, and also independently having another random walk travel from $\vec{R}$ to $\vec{r}$. The lack of correlations

in direction of the step vector guarantees that the walks are independent. This simplifies the analysis considerably, but will change when we consider the WLC.

In the limit of $N \to \infty$, the radial distribution function in $\mathbb{R}^2$ is given by Equation (6.2). The midpoint distribution, then, is given by:

$$\lim_{N\to\infty} p_{N,\text{mid}}(\vec{r}) = \frac{8N^4}{\pi^2 l_c^4} |\vec{r}| \cdot |\vec{R} - \vec{r}| \cdot e^{-\frac{N}{l_c^2}(R^2 + |\vec{R}-\vec{r}|^2)} \tag{6.15}$$

This density may be sampled for any midpoint position, and yields a gaussian centered at $\vec{R}/2$.

In the case of a short random walk, the probability density cannot be sampled from a convenient analytical form. Instead, we rely on our results from Section 6.1, in which we generated probability densities for short random walks. These probability densities were generated assuming that the length of the walk was exactly unity, but can be scaled isotropically a distance $l_c/2$. Once the short random walk probability densities are sufficiently resolved, they need not be calculated again.

In Figure 6.3, we present the midpoint densities for a $N = 4$-, 8-, 16-, and 32-step random walk, where the ends were held exactly a distance unity apart, and where we scaled the total walk length to $l_c = 2$, 4, and 8. The midpoint distributions, like the individual probability densities, display intricate ring and circle patterns. Even for a relatively large number of steps, up to $N = 16$, the midpoint distributions are far from the gaussian limit of large $N$, instead creating interference patterns. The results shown in Figure 6.3 were generated through a $10^6$ step MCMC Metropolis algorithm, though we identically could compute the midpoint distribution by multiplying the probability densities calculated in the previous section. We chose this MCMC method in order to estimate the correlation between subsequent steps in the Markov chain, for use in our algorithm discussed next.

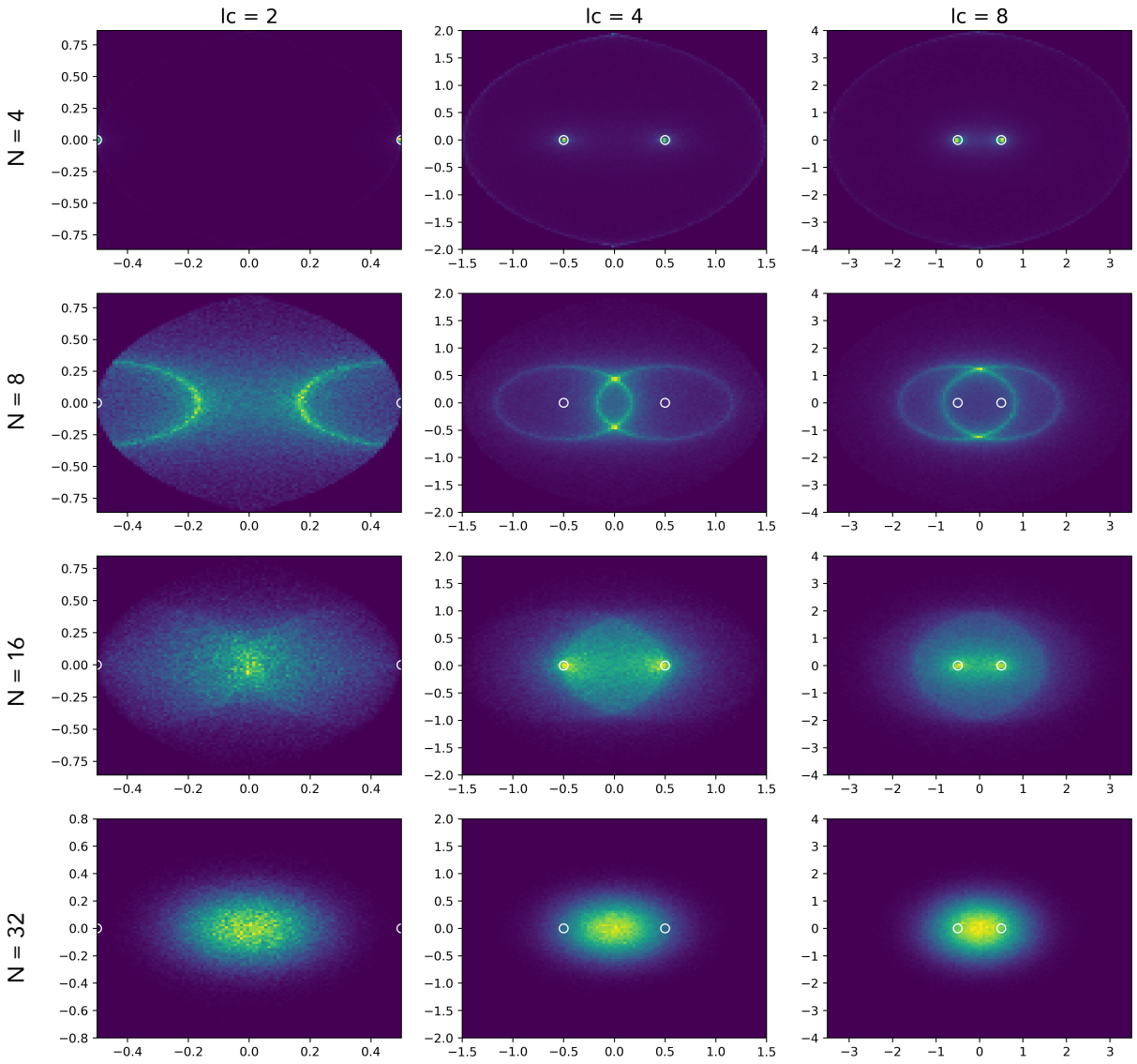


Figure 6.3: **Midpoint Distributions of the Random Flight in Two Dimensions** The midpoint probability density sampled through a Metropolis algorithm with $10^6$ sampling steps. Each instantiation assumed the ends were fixed at positions (-0.5,0) and (0.5,0) (white circles). The probability distributions used were given by the results from Section 2.2, with computationally derived densities for $N = 4$, 8, and 16, and analytically derived densities for $N = 32$. The contour length was varied from $l_c = 2$ to $l_c = 8$, in order to explore the effect of total chain length on the distributions.

## 6.3 The Middle-Out Algorithm

In the previous sections, we discussed the midpoint probability distributions for random walks with any number of segments $N$. We argued that the midpoint distribution, due to the lack of correlation between adjacent step angles, was given by the probability of one chain having end-to-end distance $\vec{x}_0 - \vec{x}_{\text{mid}}$ multiplied by the probability of the second chain having end-to-end distance $\vec{x}_1 - \vec{x}_{\text{mid}}$. The midpoint distribution will play a pivotal role in our algorithm.

In this section, we provide an algorithm for directly sampling confirmations of a simple polymer model consisting of $N$ uncorrelated steps with fixed endpoints. The goal of the sampling algorithm we construct is to utilize analytical and computational results for probability distributions in order to reduce the number of unaccepted moves in a typical MCMC algorithm. Because the primary barrier for fast conformation sampling is the frequency of unaccepted moves, we circumvent the problem by pseudo-direct sampling, and by making use of the fractal self-affine nature of a FJC. Having chosen an end-to-end distance for the chain, we proceed to break the chain into two equal segments. This procedure is equivalent to modeling the entire chain as having only three points (Figure 6.4). Given the number of links chosen and the entire chain length, the midpoint distribution will change. After choosing the midpoint, we treat each new segment formed as a new independent chain with half the remaining number of links, and again sample the midpoint distribution for each new segment. This procedure can be used to generate chain samples $2^n$ long, with $n$ an integer.

Consider a FJC with fixed end-to-end distance $\vec{R}$, with total chain length $l_c$ and bond length $b$ chosen so that the total number of links is equal to $N = 2^n$, where $n$ is an integer. The configuration of bond vectors at the start of the simulation is unknown, but we wish to sample it from a distribution that mirrors the probability distribution found in equilibrium. The constraint that the total chain length be exactly $l_c$ is in general difficult to enforce, and precludes any algorithm that would attempt to snake the chain from one end to the other.

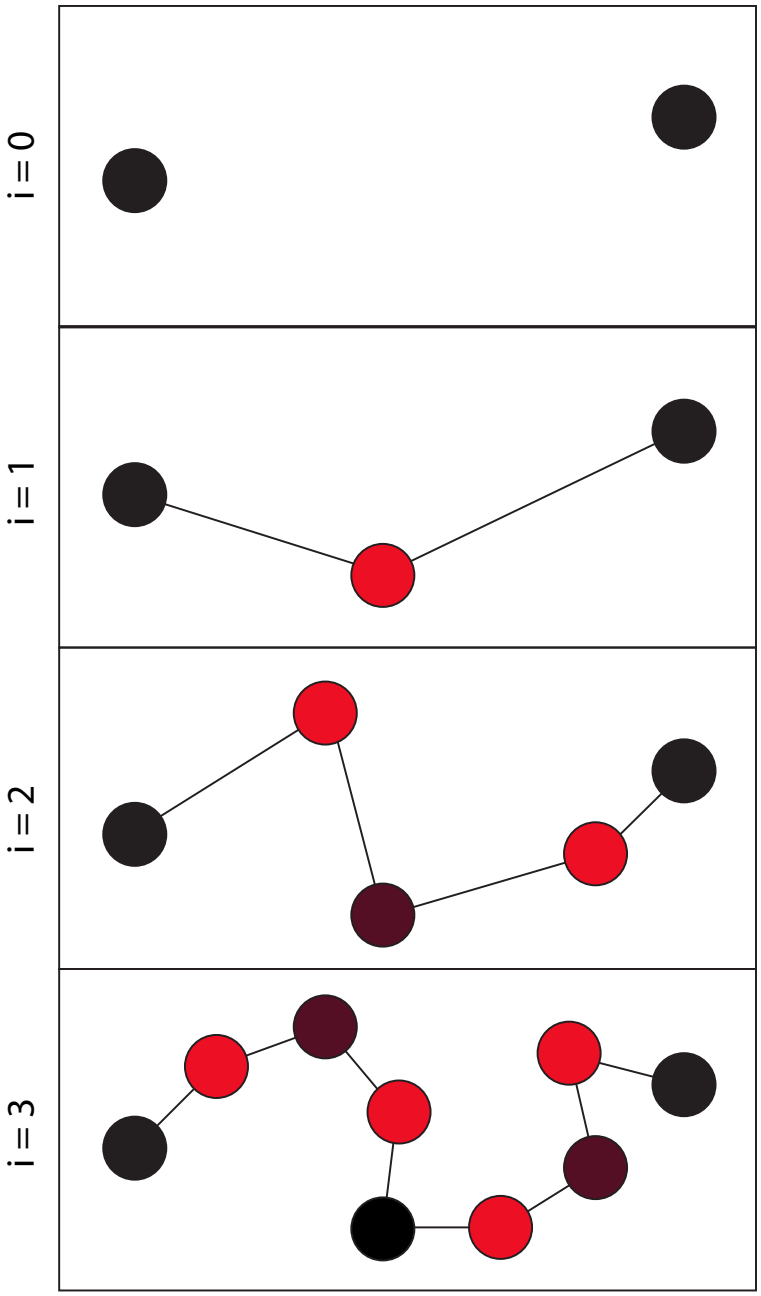


Figure 6.4: **Schematic of Middle-out Algorithm** Given two points, represented as black circles in the first panel, the algorithm described in Section 6.3 fills in a configuration linking the two points by sampling the successive midpoints. In the second $i = 1$ panel, a red point is drawn from a probability distribution and locked in place. Next, the chain is broken into two segments, each with half the number of links. In the following $i = 2$ panel, two new points are sampled independently at the midpoint of each half segment. In the $i = 3$ panel, the chain is complete.

Instead, we take advantage of the fractal nature of the chain to successively fill in additional structure. We begin by considering the midpoint of the chain, which can be drawn from the distributions considered in Section 6.1. If the number of links $N$ is very large, this probability distribution collapses to the midpoint distribution found in Equation (6.14). In the limit that $N$ is small, we must sample from the midpoint distribution dictated by the specific number of steps $N$.

To sample from the midpoint distribution, we use the MCMC Metropolis algorithm with variable step size chosen to approach a reject rate of $\frac{\#\text{ Accepted moves}}{\text{Total }\#\text{ moves}} \approx \frac{1}{2}$. Correlations among moves deteriorates quickly, and we empirically choose the total number of moves $N = 200$, which represents a tradeoff between accurate independent sampling and computational efficiency. The combined act of choosing a midpoint "directly" at the level of the chain, and sampling the midpoint distribution through an MCMC algorithm, allows us to minimize the number of rejections to just those encountered sampling the midpoint distributions.

Once the midpoint has been chosen, the new prior configuration of the chain is shuffled down to the newly sampled three-point configuration (Figure 6.4). Effectively, we have approximated the entire chain with just three positions, $\vec{x}(0)$, $\vec{x}(l_c/2)$, and $\vec{x}(l_c)$. If $l_c \ll ||\vec{R}||$, then there is a high probability that there is still significant slack in on either side of the chain, such that $||\vec{x}(0) - \vec{x}(l_c/2)|| \ll l_c$ and $||\vec{x}(l_c/2) - \vec{x}(l_c)|| \ll l_c$. Because the midpoint that we chose is locked in place, we have shifted the problem of finding a chain conformation to two new problems of finding the midpoint distribution between $\vec{x}(0)$ and $\vec{x}(l_c/2)$, and between $\vec{x}(l_c/2)$ and $\vec{x}(l_c)$, each with contour length $l_c/2$ and $N_1 = N/2$ segments. Thus, starting from the center, we build the chain from the "middle-out" by successively sampling new midpoints.

The process is iterated $n$ times, with successive points being chosen on the basis of the newly sampled midpoints. A transition in the algorithm occurs when the number of segments between two adjacent points $N_i \leq 16$. In this case, the probability distribution of midpoints that we sample from necessarily deviates from the large-$N$ probability distribution

limit. Now it becomes apparent why we spent so long examining the midpoint probability distributions of small numbers of steps. We may use our same methodology as before, using the MCMC Metropolis algorithm to sample the midpoint distribution, though we transition to using the probability distribution estimated by randomly generated two-, four-, and eight-step random walks. The probability distributions in this case were taken from the previous section, where we generated $N = 10^7$ independent random walks in two dimensions and calculated a discretized cumulative distribution function of the observed radial distance realizations. The total midpoint probability distribution, then, was again given by the multiplication of probability of the two independent chains meeting at the midpoint, each with $N_i = N/2i$ number of steps and total contour length $l_{c,i} = l_c/2i$.

Successive convergences demonstrate that the end-to-end distance between two adjacent sampled points on the chain, $\vec{x}_j - \vec{x}_{j+1}$, never exceed the chain length $l_{c,i}$ between them. This is because the midpoint-probability distributions explicitly forbid this scenario from happening. The converse scenario, in which $||\vec{x}_j - \vec{x}_{j+1}|| < l_{c,i}$ is always true. However, as $N_i \to 1$, $||\vec{x}_j - \vec{x}_{j+1}||$ does not converge to $l_{c,i}$ as we approach the end of the algorithm. This is not a bug, but an expected feature, for any correlation of adjacent vector angles is solely influenced by the total end-to-end vector $\vec{R}$. As such, care must be taken in order to enforce the total chain length $l_c$. In our framework this enforcement is relatively simple, and corresponds to a choice of final midpoints such that each bond has length $l_c/N$. For the two-dimensional chain, this corresponds to two points in $\mathbb{R}^2$ that are chosen from with equal probability. For a three-dimensional chain, this corresponds from sampling a point along a circle in $\mathbb{R}^3$, and in higher dimensions sampling from spheres and hyper-spheres.

In Figure 6.5, we show sample configurations drawn using our algorithm, in which we fix the end-to-end distance vector to be equal to unity, and scale the total length of the chain. We find that even for small chain lengths, significant deviations exist from the straight conformation. Looping behavior begins around $l_c = 1.5$, for which value the chain has enough excess length in order to make complete rotations. The corresponding variance of

end-bond vector angles decreases after this cutoff length, resulting in a phase transition that we are in the process of investigating.

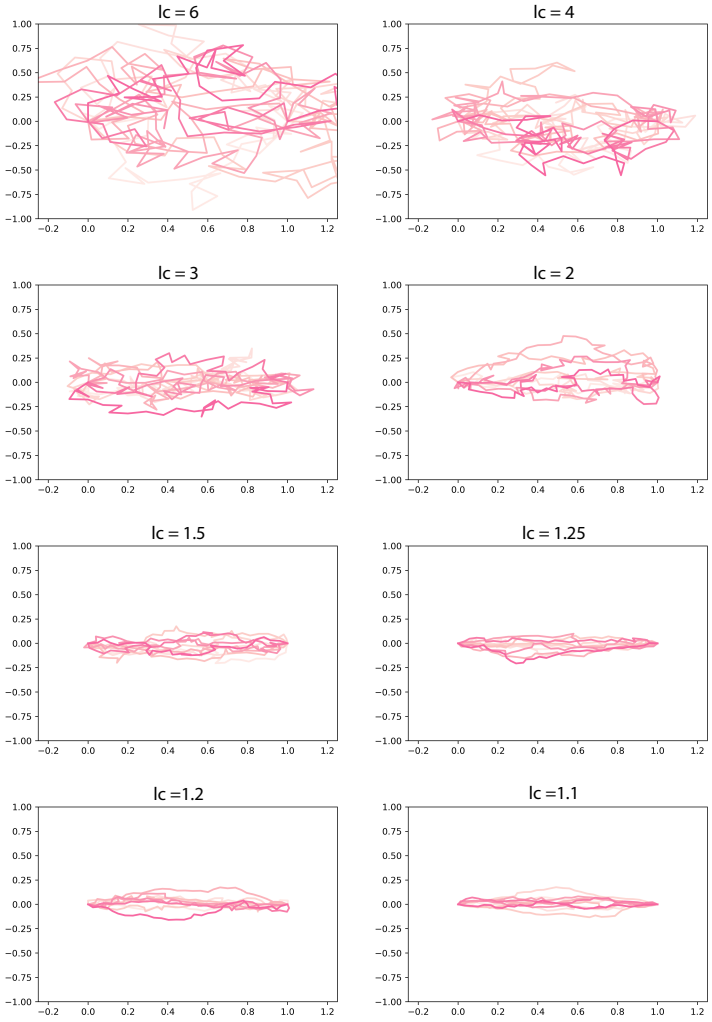


Figure 6.5: **Samples of the FJC with Fixed Ends** Samples of a FJC with variable contour length drawn using the middle-out algorithm. $n = 5$, with $N = 2^5$ bonds or 30 sampled positions, and fixed end-to-end distance of unity.

## 6.4 Midpoint Distribution of the Worm-Like Chain

The midpoint of a WLC cannot be solved through the method employed in Section 6.2, for which we naively allowed the probability density of the midpoint to be the union of two independent probability distributions. In addition to the WLC having energetic costs associated with bending, which can significantly change the midpoint probability found though an MCMC algorithm, the WLC has the additional constraint that the tangent to the curve remain continuous everywhere. Not only does the *position* have to match, but the *angle* at which the two chains meet must match.

In cases for which $l_p \ll l_c$, the tangent constraint represents a minimal perturbation to the midpoint distribution. In many cases, and by necessity of the algorithm, we must at some point confront the case in which $l_c \ll l_p$; or even more disturbingly, when $l_c \approx l_p$. Atypical behaviors are common in this regime, especially under end-point tangent constraints. The constraint that the angle must be fixed introduces considerable complexity, and suspends any hope of progress through naive calculation.

In order to solve for the midpoint distribution, we make sure of the pioneering work by Spakowitz and Wang in exactly solving the end-to-end distance vector probability for a semiflexible polymer with arbitrary $l_p$ and $l_c$, subject to fixed-end orientations [108]. To summarize, they found the Green's function in Fourier-Laplace space for a semiflexible chain in two-dimensions with a single fixed-end orientation to be given by:

$$G(\vec{k}|\vec{u}_0;p) = \frac{1}{2\pi}G_0^0(K;p) + \frac{1}{\pi}\sum_{m=1}^{\infty}\cos(\chi)G_0^m(K;p) \tag{6.16}$$

where $\vec{u}_0$ is taken to be the orientation of the polymer at one end, $\chi$ is the angle of the wave-vector $\vec{k}$, $K = 2l_p||k||$, and $p$ is the Laplace conjugate variable to $N = l_c/(2l_p)$. As we saw in Section 2.7, the value of $G_0^0$ is given by [108]:

$$G_0^0 = \cfrac{1}{P_0(p) + \cfrac{K^2/2}{P_1(p) + \cfrac{K^2/4}{P_2(p) + \cfrac{K^2/4}{P_3(p) + \cfrac{K^2/4}{\cdots}}}}} \tag{6.17}$$

with $P_i(p) = p + n^2$. The additional $G_0^m$ terms are defined as:

$$G_0^m = G_0^0 \left(\frac{iK}{2}\right)^m \cfrac{1}{P_1(p) + \cfrac{K^2/4}{P_2(p) + \cfrac{K^2/4}{\cdots}}} \cfrac{1}{P_2(p) + \cfrac{K^2/4}{P_3(p) + \cfrac{K^2/4}{\cdots}}} \cdots \cfrac{1}{P_m(p) + \cfrac{K^2/4}{P_{m+1}(p) + \cfrac{K^2/4}{\cdots}}}. \tag{6.18}$$

Solving Equation (6.16) involves a similar procedure to that in Section 2.7. We first truncate the infinite continued fraction, and then find the poles of the subsequent rational function and calculate their residues. Upon summing the residues, we recover the inverse Laplace transform back into $N$-space. Next, we calculate the inverse Fourier transform, which is not spherically symmetric due to the inclusion of the $\cos\chi$ term. The procedure can be carried out for any value of $N$, which measures the ratio of the chain length to the persistence length.

To recover the midpoint distribution of a WLC, we shift reference frames to the midpoint, oriented with the $\hat{x}$ direction facing the direction of the local tangent. The probability of finding the chain a position ($r$,$\theta$) away subject to this fixed orientation is given by the Green's function described above. Since the local tangent constraint is satisfied by construction of the problem, we may now write the midpoint probability as the joint probability of two chains having end-to-end vectors chosen with respect to the local tangent such that $\vec{r}_{\text{mid}\to 0} - \vec{r}_{\text{mid}\to l_c} = \vec{r}_{0\to l_c}$. Although this seems woefully complicated, we are rescued by the realization that the tangent angle is not fixed, but must be summed over to find the total probability of the midpoint, which can exist with tangents in any orientation. The final probability density for the midpoint, then, is given by:

$$P(\vec{r}|\vec{r}_N, l_p) = \int_0^{2\pi} G(r,\theta)\hat{\mathbf{H}}_\phi G(|\vec{r} + \vec{r}_N|, \theta) d\theta \tag{6.19}$$

where the operator $\hat{\mathbf{H}}_\phi$ represents a rotation an angle $\phi$ of the two-dimensional probability distribution. Using this procedure we may construct the midpoint probability distribution of a WLC between two fixed endpoint, which is valid in both the stiff limit and weakly-bending limit. Construction of these distributions is an ongoing area of research.

## 6.5 Conclusions

In this chapter, we constructed a new, hybrid algorithm to sample the confirmations of a FJC between two fixed-end points. Due to the arbitrary positioning of the end points, the conformations that obey both the end constraint and in-extensibility constraint represent a infinitesimal subset of all available conformations. By construction, the algorithm immediately discards conformations that do not meet the constraint criteria, greatly lowering the (computational) energetic cost of sampling. Central to our algorithm was the construction of atypical short-random-walk probability distributions, which allowed us to sample successive midpoint distributions of a fixed-end polymer. The literature on midpoint distributions of polymers is sparse, and their calculation cannot trivially be obtained by modal decomposition due to the in-extensibility constraint.

We plan to extend our algorithm into the time domain, such that it may be used to generate conformations of a polymer under end-to-end distance changes. We hope our current algorithm may be used to help understand the role of steric interactions in the dimeric tip link, and may find applicability in future computational polymer physics, especially after being extended to the worm-like chain.

# Chapter 7: Concluding Remarks

The auditory system has evolved to detect stimuli across a broad range of frequencies and intensities, with acute sensitivity and discriminatory capabilities. Integral to the proper functioning of the auditory receptor cells is the gating of mechanically-sensitive ion channels that regulate the rate of ion flow into the cell and subsequent depolarization. If the compliant element through which hair-bundle moment is converted to force on this channel is too stiff, the apparatus forfeits its dynamic range and is biased strongly towards either the entirely open or closed state. If the compliant element is too soft, then the channel will be insensitive to low-intensity signals. Therefore, the compliant element must have a carefully tuned and regulated stiffness as well as the capacity to extend several tens of nanometers in response to force.

The tip link is a prime candidate for the compliant element, for it extends 100-200 nm and directly transduces force to the stereociliary tip. Although crystallographic, electron-microscopic, and molecular-dynamic evidence suggests extracellular cadherin domains and linker regions are too stiff and too inflexible to contribute sufficient elasticity to support audition, measurements of the lower one-third of the tip link by high-precision optical-trap experiments reveal that entropic elasticity, rather than enthalpic elasticity, dominates the low-force extension relation. This line of evidence suggested that the entire tip link could act as a semiflexible entropic spring and could store excess length within thermal undulations

along its contour.

To address this possibility, we examined the literature and identified a suitable theoretical model for study; the dynamic worm-like chain, which has found historical success in predicting biopolymer behavior. The tip link, however, is unique in several ways: its resting tension may be dynamically modulated, its end-to-end distance is entrained to the motion of the hair bundle, and its operating range reaches many tens of kilohertz. These considerations led us to new scaling regimes, and to numerically solve the backbone tension along a polymer for arbitrary force stimuli.

Our results underscore the central role that resting tension plays in determining the frequency-dependent behavior of a polymer. We uncovered through asymptotic analysis a new scaling regime for polymers under significant resting tension subjected to a step change in force, which revealed that the time for a polymer to come to equilibrium scales as $t^* \propto l_c^{4/3} f_0^{-2/3}$, in contrast to the unstressed regime in which the same time scales as $t^* \propto l_c^4$. This qualitative shift occurs because resting tension suppresses the longest-wavelength oscillatory modes, which also take the longest to come to equilibrium. Therefore, the application of resting tension to the tip link plays a critical role in its frequency-dependent behavior.

Our numerical calculations of force propagation along the tip link for high-frequency oscillatory stimuli revealed a shear-thickening response, in which resting tension was again found to play a critical role in keeping the polymer in equilibrium. Under low resting tensions, high-frequency and high-amplitude stimuli prevented the pulling force from extending into the bulk of the chain. Along with numerous other subtle behaviors, we uncovered regimes in which the chain appeared close to equilibrium, but still exhibited non-equilibrium behavior in its stored-length density and upon tension release.

The systematic examination of small sinusoidal stimuli shows how resting tension dramatically changes the viscoelastic response of the polymer. Recognizing that *local* tension influences the open probability of the channel, we examined the force required to stretch a polymer at auditory frequencies. Mirroring our numerical results, we found that lowering

the resting tension dramatically increases the viscous resistance encountered: in light of our numerical results, low tension causes tension to pool at the ends of the polymer and not extend into the bulk. In order for the modestly prestressed polymer to extend under high frequency, its local end-tension must dramatically increase, causing the enthalpic stretching of bonds and the channel into an open configuration. Increasing resting tension dramatically shifts the frequency above which this effect occurs, suggesting one mechanism by which the auditory system tunes its frequency-dependent response.

How does this examination of tip-link behavior fit in with existing models? For one, the tip link's structure does not suggest a traditionally compliant element in analogy with proteins such as ankryin. If the tip link is to act as the gating spring, then, the entropic elasticity caused by thermal bends must exert itself fast enough to support the full auditory frequency. Our results confirm that under sufficient resting tension, this is indeed the case - the chain is effectively in equilibrium. Under low resting tension, however, the chain exhibits viscoelastic properties that alter its frequency dependent response, but in such a way that they actually increase the tension at the ends of the tip link. In addition, our results allow us to visualize how tension propagates along the tip link on average, and implicates the experimentally observed unfolding of extracellular cadherin domains as occurring more probably towards the ends of the tip link.

We conclude with an outlook to the future, in which we hope that additional questions may be answered by our fast sampling algorithm of fixed end-to-end distance freely-jointed chains. Although we have not yet extended the algorithm to the time domain to examine dynamic effects, we may use the algorithm to test the role of steric interactions in the dimeric tip link. We hope this method finds many uses in computational polymer physics, especially after it is extended to sample confirmations of the worm-like chain.

# Appendix A: Inverse Fourier-Laplace Transform

Solutions of Equation (2.15) are found by Laplace inversion from p into the $N = 1/2l_p$ space, and Fourier inversion from the wave-vector $\vec{k}$ back to the real space $\vec{r}$.

The Laplace inversion may be found by use of the Bromwich integral [150]:

$$f(N) = L^{-1}\{F(p)\}(t) = \frac{1}{2\pi i} \lim_{T\to\infty} \int_{\gamma-iT}^{\gamma+iT} e^{pN} F(p) dp \tag{A.1}$$

where $L^{-1}$ is the inverse Laplace transform, and $\gamma$ is a real number chosen such that all poles of $F(p)$ lie to the left of the line $p = \gamma$ in the complex plane. One approach to solving the Bromwich integral is to expand the integral into a contour integral around a hemicircle in the complex plane from the line $p = \gamma$ out to $-\infty$. By Cauchy's residue theorem, the closed contour integral is proportional to the sum of the residues at its poles, which in this case are all simple poles [108].

The poles of the function $G(\vec{K}, p)$ may be calculated by truncating the infinite continued fraction, typically after 10 fractions, and computing its polynomial expansion by use of recursions relations. Viskovatoff's method can be used to convert any rational function into a finite continued fraction, and inversely, any finite continued fraction can be expressed as a rational function. In particular, we may rewrite the expression $G(\vec{K}, p)$ in the form:

$$G(\vec{K}, p) = b_0 + \frac{a_1}{b_1 + \frac{a_2}{b_2 + \frac{a_3}{b_3 + \ldots}}} \tag{A.2}$$

The convergents of the truncated continued fraction series are defined as the value after after n number of fractions have been evaluated. For instance, the first convergent $G_0 = b_0$, and the second convergent $G_1 = b_0 + a_1/b_1$. The convergents may also be expressed in the form $G_n = A_n/B_n$, where $A_n$ and $B_n$ are given by the recursion formulas [151]:

$$\begin{aligned} A_n &= b_n A_{n-1} + a_n A_{n-2} \\ B_n &= b_n B_{n-1} + a_n B_{n-2} \end{aligned} \tag{A.3}$$

which in our case has initial values $A_{-1} = 1$, $A_0 = 0$, $B_{-1} = 0$, $B_0 = 1$.

It is useful to note that the convergents of the continued fraction may always be expressed as a rational function, and more specifically, that $A_n$ and $B_n$ are already given in polynomial form. To compute the convergents, we use the SymPy library which allows for fast manipulation of polynomials. Applying the recursion relations Eq (A.3), we find the first few convergents for the 2 dimensional case to be:

$$\begin{aligned} G_0 &= 0 \\ G_1 &= \frac{1}{p} \\ G_2 &= \frac{p+1}{p^2 + p + .5K^2} \\ G_3 &= \frac{p^2 + 5p + .25K^2 + 4}{p^3 + 5p^2 + (.75K^2 + 4)p + 2K^2} \\ G_4 &= \frac{p^3 + 14p^2 + (.5K^2 + 49)p + 2.5K^2 + 36}{p^4 + 14p^3 + (K^2 + 49)p^2 + (9K^2 + 36)p + .125K^4 + 18K^2} \\ &\ldots \end{aligned} \tag{A.4}$$

Even for low order convergents like $G_3$, the expressions become nontrivial. Additionally, the poles of $G_n$ do not scale simply with $K$ (Figure 2.4), and must be computed numerically. We utilize the deflation through subtraction algorithm [152] in order to compute the partial-fraction expansion of $G_n$. Doing so allows for fast computation of residues, which may be multiplied by the exponential of the pole position $e^{p_i N}$ and summed to extract the inverse-Laplace transform at $N$. As the pole positions and residue values are only dependent on $K$ and are independent of $N$, the additional evaluation of the inverse-Laplace transform at several values of $N$ minimally effects the computation time. In contrast, the scaling of $l_p$ in traditional calculations results in qualitative shifts in approximation schemes.

With $G(K, N)$ calculated for discrete values of $K$, the inverse Fourier transform is easily evaluated due to the angular symmetry of the problem. It is given by, in dimension D:

$$G(r, N) = \frac{\mathrm{SA}_D(r)}{(2\pi N^2)^{D/2}} \int_0^\infty dK K^{D-1} \frac{J_{D/2-1}(NrK)}{(NrK)^{D/2-1}} G(K, N) \tag{A.5}$$

where $\mathrm{SA}_D(r)$ is the surface area of a sphere in D dimensions, and $J_{D/2-1}$ is a Bessel function of the first kind with order $D/2 - 1$. As the analytical form of $G(K, N)$ is not known, we convert the integral into a sum and preform the numerical approximation to the integral.

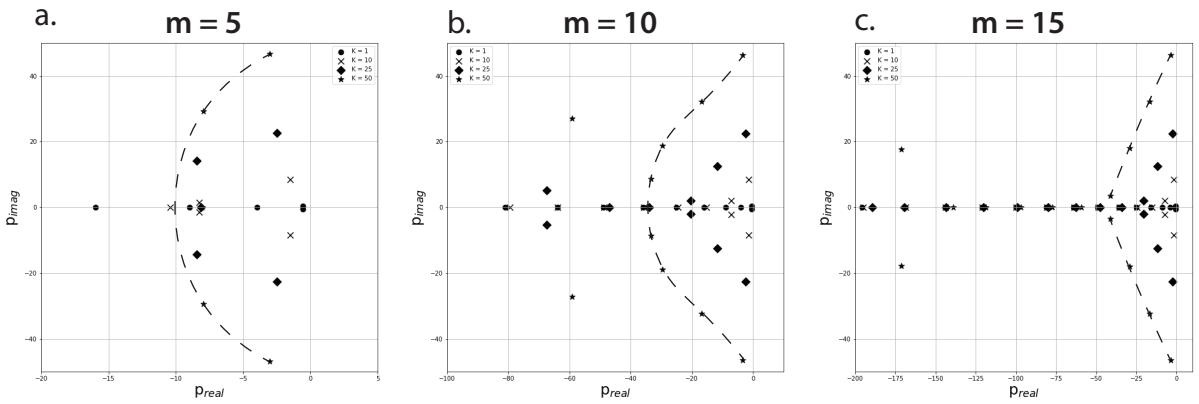


Figure A.1: **Poles of the Continued Fraction Approximates**. Poles found in the complex plane for different values of $K$ and $m$, the number of fractions to compute before truncation. In (a), the fraction was truncated quickly, and shows that as $K$ increased, the number of poles with imaginary components increased ($K = 1$ circle, $K = 10$ X, $K = 25$ diamond, and $K = 50$ star). In (b,c), the result of taking more continued fractions. In black dotted, arcs that show convergence of pole positions as $K$ gets large.

# Appendix B: Sample Python Code

## B.I: Probability Distributions of Worm-Like Chains

```
import numpy as np
from numpy import linalg as LA
import scipy
import random
import matplotlib.pyplot as plt
from scipy import signal as signal
import sympy as sym
import scipy.special as special


Alpha = lambda sub: sub**2/(4*sub**2 - 1) # In 3D
P = lambda p,sub: p + sub*(sub+1) # In 3D


## Function Definitions
def returnpoly_new(m_start,m_end):
    p = sym.Symbol('p')
    k = sym.Symbol('k')

    a = [0,1]
    b = [0]
    if m_start == 0:
        a.append(Alpha(1)*k**2)
        for i in range(m_end + 1):
            a.append(Alpha(i+2)*k**2)
            b.append(P(p,i))

    else:
        for i in range(m_start,m_end + 1):
            a.append(.25*k**2)
            b.append(P(p,i))

```

```
    A = [1, b[0]]
    B = [0, 1]
    for i in range(m_end-m_start):
        A.append(A[-1]*b[i+1] + A[-2]*a[i+1])
        B.append(B[-1]*b[i+1] + B[-2]*a[i+1])

    a = sym.Poly(sym.simplify(np.array(B)[-1]),p)
    #polycoef_a = a.coeffs()

    b = sym.Poly(sym.simplify(np.array(A)[-1]),p)
    #polycoef_b = b.coeffs()

    return a, b

def convert_poly(polys):
    polycoef_a = polys[0].coeffs()
    polycoef_b = polys[1].coeffs()
    return polycoef_a,polycoef_b

def fast_inverse_laplace(polys,Kvals,Ns):
    polycoef_a = polys[0]
    polycoef_b = polys[1]
    inverse_array = np.zeros((len(Kvals),len(Ns)))
    kcount = 0
    ncount = 0
    for K in Kvals:
        polycoef_a_K = [term.evalf(subs={'k':K}) for term in polycoef_a]
        polycoef_b_K = [term.evalf(subs={'k':K}) for term in polycoef_b]

        results = scipy.signal.residue(polycoef_b_K,polycoef_a_K)
        roots = results[1]
        residues = results[0]

        for N in Ns:
            inverse_array[kcount,ncount] = sum(residues*np.exp(roots*N))
            ncount +=1
        ncount = 0
        kcount +=1

    return inverse_array


def allterms(numterms, Kvals,Ns):
    term_array = []
    for i in range(numterms):
        if i == 0:
            poly1 = returnpoly_new(0,12)
        else:
            poly2 = returnpoly_new(i,12-i)
            poly1 = (poly1[0]*poly2[0],poly1[1]*poly2[1])
        fullpoly = convert_poly(poly1)
        term_array.append(fast_inverse_laplace(fullpoly,Kvals,Ns))
        print('term # ', i, ' done')
    return term_array
```

```
1086
1087
1088 #Generate the laplace transforms for chosen values of N and K
1089 Nvals = [0.5,1,1.5,2,2.5,3,3.5,4,4.5,5,5.5,6,6.5,7,20]
1090 Kvals = np.logspace(-2,3.74,5001)
1091 terms3d = allterms(1,Kvals,Nvals)
1092
1093
1094
1095 # Inverse Fourier transform to evaluate the vector probability density
1096 P0 = np.zeros((len(Nvals),1000))
1097 r = np.linspace(.001,1,1000)
1098 for j in range(len(Nvals)):
1099     count = 0
1100     for rval in r:
1101         intvals = []
1102         for k in range(len(Kvals)):
1103             intvals.append(terms3d[0].T[j][k]*Kvals[k]**2 *(float(Kvals[k]*
    rval*Nvals[j]))**(-1/2)*special.jv(0.5,float(Kvals[k]*rval*Nvals[j])))
1104         P0[j,count] = Nvals[j]**3 * np.trapz(intvals,Kvals[0:len(Kvals)])
1105         count += 1
```

## B.II: Middle-out Sampling

```
# Monte Carlo Sampling of FJC with fixed endpoints
# Daniel Firester 2020


#Functional Definitions
def dist(j1,j2): #Find distance beteween two points (2d or 3d)
    j1,j2 = np.array(j1),np.array(j2)
    return np.sqrt(np.dot(j1 - j2,j1-j2))

def equidistant(r1,r2,D): #Find the two points allowed distance d between two fixed points
    r1, r2 = np.array(r1),np.array(r2)
    rm = (r1 + r2)/2
    rdiff = r2 - r1
    r_cw = np.array([rdiff[1],-rdiff[0]])
    r_cw = r_cw/np.linalg.norm(r_cw)

    r_first = rm + r_cw*np.sqrt(D**2 - dist(rm,r1)**2)
    r_second = rm - r_cw*np.sqrt(D**2 - dist(rm,r1)**2)
    return list(r_first),list(r_second)

def find_nearest(array, value): #Find nearest index to a specific value requested
    array = np.asarray(array)
    idx = (np.abs(array - value)).argmin()
    return idx

def p_converter(pdf,xlims,r): #Convert raw probabilities
    x_array = (xlims[:-1] + xlims[1:])/2
    idx = find_nearest(x_array,r)
    return pdf[idx]/x_array[idx]


#Sample the midpoint between two fixed points
# Probability densities must be loaded in for proper functioning
def sample_midpoint(exp,r0,rN,lc,numsamps,delta):
    num_links = 2**exp

    r = list((np.array(r0) + np.array(rN))/2)
    if exp == 0:
        points = equidistant(r0,rN,lc/2)

        choice = np.random.randint(0,2)
        return points[choice]
    elif exp == 1:
        def log_P(r):
            try:
                return np.log(p_converter(pdf_2,xvals,dist(r,r0)/(lc/2))*p_converter(pdf_2,xvals,dist(r,rN)/(lc/2)))
            except:
                return -1e5
```

```
    elif exp == 2:
        def log_P(r):
            try:
                return np.log(p_converter(pdf_4,xvals,dist(r,r0)/(lc/2))*
    p_converter(pdf_4,xvals,dist(r,rN)/(lc/2)))
            except:
                return -1e5
    elif exp == 3:
        def log_P(r):
            try:
                return np.log(p_converter(pdf_8,xvals,dist(r,r0)/(lc/2))*
    p_converter(pdf_8,xvals,dist(r,rN)/(lc/2)))
            except:
                return -1e5
    else:
        def log_P(r):
            try:
                return -((dist(r,r0)**2 + dist(r,rN)**2)/((lc/2)**2 * (1/
    num_links))) + np.log(dist(r,r0)) + np.log(dist(r,rN)) - 2*np.log(((lc/2)
    **2 * (1/num_links)))
            except:
                return -1e5

    switch = False
    while switch == False:
        reject = 0
        for i in range(numsamps):
            rnew = [r[0] + delta*random.uniform(-1,1),r[1] + delta*random.
    uniform(-1,1)]
            if (dist(rnew,r0) > lc/2) or (dist(rnew,rN) > lc/2):
                reject +=1
            else:
                newP = log_P(rnew)
                P = log_P(r)
                if np.random.uniform(0,1) < np.exp(newP - P):
                    r = rnew
                else:
                    reject +=1
        if reject/numsamps < .3:
            delta = delta*5
        elif reject/numsamps > .7:
            delta = delta/5
        else:
            switch = True
    return r

# Sample the FJC
def semi_direct_worm_free(N,lc,r0,rN):
    worm = [r0,rN]
    lcval = lc
    delta = .1
    for i in range(1,N+1):
        leftworm = np.append([[0,0]],worm,axis=0)
        new_links = []
```

```
1097
1098            for j in range(1,len(worm)):
1099
1100                new = sample_midpoint(N-i,leftworm[j],worm[j],lcval,100,delta)
1101                new_links.append(new)
1102            lcval = lcval/2
1103
1104
1105            newworm = [None]*(len(worm) + len(new_links))
1106            newworm[::2] = worm
1107            newworm[1::2] = new_links
1108            worm = newworm
1109        return worm
```

## B.III: Numerical Solutions to PIDE

```
# Module for use in numerically computing solutions to the PIDE for a polymer under tension
# Daniel Firester 2020

import numpy as np
import sys
import time
import scipy.integrate as integrate
import scipy.special as special
from multiprocessing import Pool

# Here we define the integrands to be used in the computation of the solution
def jp1(x,t,F_t,f0,k):
    return 2*x**2*(np.exp(-2*x**2*(x**2 *t + F_t))) / (x**2 + f0/k)

def jp2(x,t,ti,tim1,F_t,F_ti,F_tim1):
    return (2*x**2/(x**2 + (F_ti - F_tim1)/(ti - tim1))) * (np.exp(-2*x**2*(x**2*(t-ti) + F_t - F_ti)) - np.exp(-2*x**2*(x**2*(t-tim1) + F_t - F_tim1)))

def jp2_1(x,t,ti,tim1,F_t,F_ti,F_tim1):
    return (1/(x**2 + (F_ti - F_tim1)/(ti - tim1))**2)*(1/(ti - tim1))*(1 - np.exp(-2*x**2*(x**2*(ti-tim1) + F_ti - F_tim1))) + ((2*x**2)/(x**2 + (F_ti - F_tim1)/(ti - tim1)))*np.exp(-2*x**2*(x**2*(ti-tim1) + F_ti - F_tim1))

def p1(x,t,F_t,f0,k):
    return (1-np.exp(-2*x**2*(x**2 * t + F_t)))/(x**2 + f0/k)

def p2(x,t,ti,tim1,F_t,F_ti,F_tim1):
    return -(1/(x**2 + (F_ti - F_tim1)/(ti - tim1))) * (np.exp(-2*x**2*(x**2*(t-ti) + F_t - F_ti)) - np.exp(-2*x**2*(x**2*(t-tim1) + F_t - F_tim1)))


def integral(args):
    tn = args[0]
    ti = args[1]
    tim1 = args[2]
    F_test = args[3]
    F_target_k_1 = args[4]
    F_target_k = args[5]
    I = integrate.quad(p2,0,np.inf,args=(tn,ti,tim1,F_test,F_target_k_1,F_target_k))
    return I[0]

def integralJ(args):
    tn = args[0]
    ti = args[1]
    tim1 = args[2]
    F_test = args[3]
    F_target_k_1 = args[4]
    F_target_k = args[5]
    if tn == ti:
```

```
1045            I = integrate.quad(jp2_1,0,np.inf,args=(tn,ti,tim1,F_test,F_target_k_1
    ,F_target_k))
1046        else:
1047            I = integrate.quad(jp2,0,np.inf,args=(tn,ti,tim1,F_test,F_target_k_1,
    F_target_k))
1048        return I[0]
1049
1050
1051 class Polymer(object):
1052        '''Creates a polymer object to simulate. The specific polymer has an
    associated persistent length and
1053        contour length, along with relevant boundary conditions (pulling protocols
    ) that govern its behavior '''
1054        # Class Attributes
1055        lcl_dx = None
1056        N = None
1057        f0 = None
1058        real_dt = None
1059        numT = None
1060        fastpull = False
1061        fastpullforce = None
1062        sinpull = False
1063        etepull = False
1064        sinpullfreq = None
1065        sinpullmid = None
1066        sinpullamp = None
1067        k_ends = None
1068        ten_prof = []
1069        F_prof = []
1070        boundry = []
1071        error = []
1072        sld = []
1073        lcl_dt = []
1074        lp = []
1075        tdrag = []
1076        ldrag = []
1077
1078
1079        # Initalizer / Instance Attributes
1080        def __init__(self,lc):
1081            '''Construct a Polymer object.
1082                Args:
1083                    lp: The persistance length of the chain
1084                    lc: The contour length of the chain '''
1085            self.lc = lc
1086
1087        # Allow user to set the transverse drag along the chain
1088        def setdrag(self, tdrag,frac=.5):
1089            self.tdrag = tdrag
1090            self.ldrag = frac*tdrag
1091
1092        # Allow user to set the persistence length along the chain
1093        def setlp(self,lp):
1094            self.lp = lp
```

```
1095
1096    # Set values for the simulation
1097    def setValues(self,dt,N,f0,numT):
1098        '''Set the values for the simulation, including the time step, the
    number of points along the arclength,
1099        the initial holding force/prestress, and the number of simulation
    points
1100        Args:
1101                dt: The real timestep
1102                N: The number of points to simulate along the length of the
    chain
1103                f0: The prestress/holding force of the chain before the
    simulation begins
1104                numT: The number of timepoints to take in the simulation'''
1105        self.lcl_dx = self.lc/(N-1)
1106        self.N = N
1107        self.real_dt = dt
1108        self.lcl_dt = dt*self.k/self.tdrag
1109        self.f0 = f0
1110        self.numT = int(numT)
1111
1112    # Set value for the spring constant at ends (when looking at end to end
    boundry conditions)
1113    def setkend(self,k_end):
1114        self.k_end = k_end
1115
1116    # Allow user to independently set the time step of the simulation
1117    def setdt(self,dt):
1118        ''' Set the time step to use in the simulation. This is the scaled
    time step, which ranges from
1119        .01 to 10-100, depending on the pulling force and speed. Also
    calculate the real time step in real time
1120        Args:
1121                dt: The rescaled timestep
1122                '''
1123        self.lcl_dt = dt
1124        self.real_dt = dt*self.tdrag/self.k
1125
1126    @property
1127    def k(self):
1128        ''' Return the value of the bending modulus, based on the persistance
    length'''
1129        return self.lp*4.114
1130
1131    # Allow user to set the number of points to break the simulation into
    along the arclength coordinate
1132    def setNx(self,N):
1133        ''' Set the number of points to break the simulation into along the
    arclength, as well as
1134        calculate the size of the spacial step in real length
1135        Args:
1136                N: The number of points to simulate along the length of the
    chain
1137                '''
```

```
1138         self.lcl_dx = self.lc/(N-1)
1139         self.N = N
1140 
1141 
1142     def fastpullProtocol(self,force):
1143         '''Set the boundry conditions to a jump in force (real force)'''
1144         self.fastpull = True
1145         self.fastpullforce = force
1146 
1147 
1148     def sinProtocol(self,freq,mid,amp):
1149         '''Set the boundary conditions to a sinusoidal stimulus, with real
    frequency, force amplitude, and force offset
1150         Args:
1151                 freq: The real frequency of stimulation
1152                 mid: The offset of the amplitude
1153                 amp: Amplitude of sinusoidal stimulus'''
1154         self.sinpull = True
1155         self.sinpullfreq = freq
1156         self.sinpullmid = mid
1157         self.sinpullamp = amp
1158 
1159     def sinEndtoEndProtocol(self,freq,amp):
1160         '''Set the boundary conditions to a sinusoidal end to end distance
    stimulus, with real frequency and end to end amplitude
1161         Args:
1162                 freq: The real frequency of stimulation
1163                 mid: The offset of the amplitude
1164                 amp: Amplitude of sinusoidal stimulus'''
1165 
1166         self.etepull = True
1167         self.sinpullfreq = freq
1168         self.sinpullamp = amp
1169 
1170     @property
1171     def J1m(self):
1172         matrix = np.zeros((self.N,self.N))
1173         for i in range(0,self.N):
1174             matrix[i,i] = -2
1175             if i-1 > -1:
1176                 matrix[i,i-1] = 1
1177             if i+1 < self.N:
1178                 matrix[i,i+1] = 1
1179 
1180 
1181         transform_Matrix = np.outer(1/self.tdrag, self.tdrag)
1182         return transform_Matrix*matrix/self.lcl_dx**2
1183 
1184 
1185 
1186 
1187     def Simulation(self,numthreads):
1188         numT = int(self.numT)
1189         dt = self.real_dt
```

```
1190        J2m = np.zeros((self.N, self.N))
1191        self.ten_prof = np.zeros((self.N,numT))
1192        self.sld = np.zeros((self.N,numT))
1193        f_test = np.zeros(self.N)
1194        self.F_prof = np.zeros((self.N,numT))
1195        self.error = np.zeros((self.N,numT))
1196        F_test = np.zeros(self.N)
1197        error = np.zeros(self.N)
1198        P = np.zeros(self.N)
1199        P1 = np.zeros(self.N)
1200        P2 = np.zeros(self.N)
1201        P1J = np.zeros(self.N)
1202        P2J = np.zeros(self.N)
1203        transformed_Curvature = np.zeros(self.N)
1204        tosubtract = np.zeros(self.N)
1205        self.ten_prof[:,0] = self.f0/self.k
1206        self.F_prof[:,0] = 0
1207        timetable = np.zeros(numT)
1208        numberofpoints = np.zeros(self.N)
1209
1210
1211        dx_chain = 0  # initalize the start of the chain change to zero
1212
1213        # INITIATE THE TEST VALUE TO START
1214        if self.fastpull == True:
1215            f_test = np.linspace(self.fastpullforce/self.k[0],self.
    fastpullforce/self.k[self.N-1],self.N)
1216        if self.sinpull == True:
1217            f_test = np.linspace(self.sinpullmid/self.k[0],self.sinpullmid/
    self.k[self.N-1],self.N)
1218
1219        p = Pool(numthreads)
1220
1221        starttimes = np.zeros(numT)
1222        starttimes[0] = time.time()
1223        # j indexes the time axis. We compute the target f_target for each
    time point, then move on
1224        for j in range(1,numT):
1225            print('time elapsed:',time.time() - starttimes[j-1])
1226            starttimes[j] = time.time()
1227
1228            print(j)
1229
1230            timetable[j] = timetable[j-1] + dt
1231            for trial in range(0,1000):
1232
1233                # CALCULATE THE VALUE OF THE TEST INTEGRAL FOR THE GIVEN TEST
    FUNCTION AND PREVIOUS ANSWERS
1234                F_test[:] = 0
1235                F_test[:] = self.F_prof[:,j-1]
1236                F_test[:] = F_test[:] + (dt*self.k/self.tdrag)*(f_test[:] +
    self.ten_prof[:,j-1])/2
1237
1238                self.F_prof[:,j] = F_test[:]
```

```
1239
1240                #CALCULATE THE RHS OF THE EQUATION: THE INVERSE TRANSFORM FROM
     WAVE NUMBER TO S
1241                #EACH SPATIAL POINT IS INDEPENDENT, SO WE CAN CALCULATE EACH
    ONE IN TURN
1242
1243                for i in range(0,self.N):
1244
1245                    #Calculate part 1 of the RHS of equation, a simple
    integral
1246                    I = integrate.quad(p1,0,np.inf,args=(timetable[j]*self.k[i
    ]/self.tdrag[i],F_test[i],self.f0,self.k[i]))
1247                    P1[i] = I[0]
1248
1249                    E = integrate.quad(jp1,0,np.inf,args=(timetable[j]*self.k[
    i]/self.tdrag[i],F_test[i],self.f0,self.k[i]))
1250                    P1J[i] = E[0]
1251
1252
1253                    #Calculate part 2 of the RHS of equation: need to compute
    sum of integrals
1254
1255
1256                    #To calculate which integrals to preform, we will always
    take the first 30 points and the
1257                    #0 point. After that, we want to compute the curvature at
    each point, and if it is above
1258                    #A certain threshold, we will break the integrals into
    small pieces around that
1259                    #point. The curvature cutoff should be based on some sort
    of exponential, so that
1260                    #the further in the past we are, the less we care (except
    for extreme steps), but
1261                    #for now we will just take an absolute cutoff (of 0.01)
1262                    parameters = []
1263                    indexlist = [0] #Always add the first point
1264                    minval = max(0,j-30)
1265                    for k in range(minval,j+1): #Always add the previous 60
    points to the list
1266                        indexlist.extend([k])
1267
1268                    if j > 30: #After the 30th point, begin sparsely sampling
    points
1269                        m = j - 30
1270                        step = 1
1271                        while m > 0:
1272                            indexlist.extend([m])
1273                            m = m - step
1274                            step +=1
1275
1276
1277                    indexlist = np.unique(indexlist) #np.unique will cut out
    any duplicates, and arrange the list
1278
```

```
                    for k in range(1,len(indexlist)): #Extend the list of paramaters to compute integrals for
                        parameters.extend([[timetable[j]*self.k[i]/self.tdrag[i],timetable[int(indexlist[k])]*self.k[i]/self.tdrag[i],timetable[int(indexlist[k-1])]*self.k[i]/self.tdrag[i],F_test[i],self.F_prof[i,int(indexlist[k])],self.F_prof[i,int(indexlist[k-1])]]])

                    #Compute sum of P2 integrals
                    results_pooled = list(p.map(integral,parameters))
                    results = list(results_pooled)
                    P2[i] = sum(results)

                    #Compute sum of jacobian P2 integrals
                    results_pooled_J = list(p.map(integralJ,parameters))
                    results_J = list(results_pooled_J)
                    P2J[i] = sum(results_J)



                # Sum the two contributions
                P = P1 + P2



                for i in range(0,self.N):
                    J2m[i,i] = (P1J[i] + P2J[i])*(1/(2*self.lp[i]*np.pi))

                Jacobian = self.J1m - J2m




                #TAKE 2ND DERIVATIVE OF THE TEST FUNCTION, TO COMPUTE CURVATURE

                #Compute the curvature of the test F, locally transformed on a point by point
                #basis
                for i in range(0,self.N):
                    dxdy = np.gradient(F_test*self.tdrag/self.tdrag[i])
                    curvature = (1/self.lcl_dx**2)*np.gradient(dxdy)
                    transformed_Curvature[i] = curvature[i]
                for i in range(0,self.N):
                    if np.abs(transformed_Curvature[i]) > 1e5:
                        transformed_Curvature[i] = transformed_Curvature[i-1]

                error = transformed_Curvature - (1/(2*self.lp*np.pi))*P
                error[0] = 0
                error[self.N - 1] = 0

                if (j == 1):
                    error_Threshold = 1e-4
                else:
                    error_Threshold = 1e-3
```

```
                error_Threshold
                if ((np.sum(abs(error)))) < error_Threshold:


                    dx_chain = sum(P[1:-2])*self.lcl_dx


                    self.ten_prof[:,j] = f_test
                    self.F_prof[:,j] = F_test
                    self.error[:,j] = error
                    self.sld[:,j] = P




                    storage = np.zeros((self.N,j))
                    for k in range(0,j):
                        storage[:,k] = self.ten_prof[:,k]*self.k
                    np.savetxt('ten_vals.txt',storage)
                    for k in range(0,j):
                        storage[:,k] = self.F_prof[:,k]*self.tdrag
                    np.savetxt('f_vals.txt',self.F_prof)
                    for k in range(0,j):
                        storage[:,k] = self.sld[:,k]*self.ldrag/(np.pi * self.
    lp)
                    np.savetxt('sld.txt',storage)
                    print('success')
                    print('dx chain = ',dx_chain)
                    print('dx walls = ',dx_walls)
                    print('Num Trials:',trial)

                    np.savetxt('error.txt',self.error)
                    np.savetxt('times.txt',timetable)

                    if trial < 5:
                        dt = dt*1.1
                    if trial > 8:
                        dt = dt*.9

                    break #Move on to next time step



                tosubtract = (np.dot(np.linalg.pinv(Jacobian),error))
                F_test = F_test - tosubtract


                f_test = (2/(dt*self.k/self.tdrag))*(F_test - self.F_prof[:,j
    -1]) - self.ten_prof[:,j-1]


                if self.fastpull == True:
                    f_test[0] = self.fastpullforce/self.k[0]
                    f_test[self.N-1] = self.fastpullforce/self.k[self.N-1]
```

```
1379                 if self.sinpull == True:
1380                     forceval = self.sinpullmid + self.sinpullamp*np.sin(2*np.
    pi*timetable[j]*self.sinpullfreq)
1381                     f_test[0] = forceval/self.k[0]
1382                     f_test[self.N-1] = forceval/self.k[self.N-1]
1383                 if self.etepull == True:
1384                     dx_walls = self.sinpullamp*np.sin(2*np.pi*timetable[j]*
    self.sinpullfreq)
1385                     fval = .5*self.k_end*(dx_walls + 5 - dx_chain)
1386                     f_test[0] = fval/self.k[0]
1387                     f_test[self.N-1] = fval/self.k[self.N-1]
1388 
1389         p.terminate()
```

# References


[1] Nin, F., Reichenbach, T., Fisher, J. A. N., & Hudspeth, A. J. (2012). Contribution of active hair-bundle motility to nonlinear amplification in the mammalian cochlea. Proceedings of the National Academy of Sciences, 109(51), 2107621080.

[2] Fettiplace, R. (2006). Active hair bundle movements in auditory hair cells. The Journal of Physiology, 576(Pt 1), 2936.

[3] Reichenbach, T., & Hudspeth, A. J. (2014). The physics of hearing: Fluid mechanics and the active process of the inner ear. Reports on Progress in Physics. Physical Society.

[4] Eguluz, V. M., Ospeck, M., Choe, Y., Hudspeth, A. J., & Magnasco, M. O. (2000). Essential nonlinearities in hearing. Physical Review Letters, 84(22), 52325235.

[5] Dalhoff, E., D. Turcanu, H.-P. Zenner, & A. W. Gummer. 2007. Distortion Product Otoacoustic Emissions Measured as Vibration on the Eardrum of Human Subjects. Proceedings of the National Academy of Sciences 104 (5): 154651.

[6] Harris, G. G. (1968). Brownian Motion in the Cochlear Partition. The Journal of the Acoustical Society of America, 44(1), 176186.

[7] Knudsen, V. O. (1923). The Sensibility of the Ear to Small Differences of Intensity and Frequency. Physical Review, 21(1), 84102.

[8] Spiegel, M. F., & Watson, C. S. (1984). Performance on frequency?discrimination tasks by musicians and nonmusicians. The Journal of the Acoustical Society of America, 76(6), 16901695.

[9] Oppenheim, J., & Magnasco, M. (2012). Human Time-Frequency Acuity Beats the Fourier Uncertainty Principle. Physical Review Letters, 110.

[10] Luers, J. C., & Hüttenbrink, K. (2016). Surgical anatomy and pathology of the middle ear. Journal of Anatomy, 228(2), 338353.

[11] Guest, H., Munro, K. J., Couth, S., Millman, R. E., Prendergast, G., Kluk, K., Murray, C., & Plack, C. (2019). No Effect of Interstimulus Interval on Acoustic Reflex Thresholds. Trends in Hearing, 23.

[12] Macas, S., Hechavarra, J. C., & Kssl, M. (2016). Sharp temporal tuning in the bat auditory midbrain overcomes spectral-temporal trade-off imposed by cochlear mechanics. Scientific Reports, 6.

[13] Linnenschmidt, M., & Wiegrebe, L. (2019). Ontogeny of auditory brainstem responses in the bat, Phyllostomus discolor. Hearing Research, 373, 8595.

[14] Raufer, S., Guinan, J. J., & Nakajima, H. H. (2019). Cochlear partition anatomy and motion in humans differ from the classic view of mammals. Proceedings of the National Academy of Sciences, 116(28), 1397713982.

[15] Nin, F., Hibino, H., Doi, K., Suzuki, T., Hisa, Y., & Kurachi, Y. (2008). The endocochlear potential depends on two K+ diffusion potentials and an electrical barrier in the stria vascularis of the inner ear. Proceedings of the National Academy of Sciences, 105(5), 17511756.

[16] Choi, C.-H., & Oghalai, J. S. (2008). Perilymph Osmolality Modulates Cochlear Function. The Laryngoscope, 118(9), 1621.

[17] Motallebzadeh, H., Soons, J. A. M., & Puria, S. (2018). Cochlear amplification and tuning depend on the cellular arrangement within the organ of Corti. Proceedings of the National Academy of Sciences, 115(22), 57625767.

[18] Kolla, L., Kelly, M. C., Mann, Z. F., Anaya-Rocha, A., Ellis, K., Lemons, A., Palermo, A. T., So, K. S., Mays, J. C., Orvis, J., Burns, J. C., Hertzano, R., Driver, E. C., & Kelley, M. W. (2020). Characterization of the development of the mouse cochlear epithelium at the single cell level. Nature Communications, 11(1), 2389.

[19] Lim, D. J. (1986). Functional structure of the organ of Corti: A review. Hearing Research, 22(1), 117146.

[20] Oghalai, J. S. (2004). The cochlear amplifier: Augmentation of the traveling wave within the inner ear. Current Opinion in Otolaryngology & Head and Neck Surgery, 12(5), 431438.

[21] McPherson, D. R. (2018). Sensory Hair Cells: An Introduction to Structure and Physiology. Integrative and Comparative Biology, 58(2), 282300.

[22] Martin, P., & Hudspeth, A. J. (1999). Active hair-bundle movements can amplify a hair cells response to oscillatory mechanical stimuli. Proceedings of the National Academy of Sciences, 96(25), 1430614311.

[23] Gillespie, P. G., & Hudspeth, A. J. (1991). High-purity isolation of bullfrog hair bundles and subcellular and topological localization of constituent proteins. Journal of Cell Biology, 112(4), 625640.

[24] Han, W., Shin, J.-O., Ma, J.-H., Min, H., Jung, J., Lee, J., Kim, U.-K., Choi, J. Y., Moon, S. J., Moon, D. W., Bok, J., & Kim, C. H. (2020). Distinct roles of stereociliary links in the nonlinear sound processing and noise resistance of cochlear outer hair cells. Proceedings of the National Academy of Sciences, 117(20), 1110911117.

[25] Chiappe, M. E., Kozlov, A. S., & Hudspeth, A. J. (2007). The Structural and Functional Differentiation of Hair Cells in a Lizards Basilar Papilla Suggests an Operational Principle of Amniote Cochleas. The Journal of Neuroscience, 27(44), 1197811985.

[26] Ricci, A. J., Crawford, A. C., & Fettiplace, R. (2002). Mechanisms of Active Hair Bundle Motion in Auditory Hair Cells. Journal of Neuroscience, 22(1), 4452.

[27] Hudspeth, A. J. (1985). The cellular basis of hearing: The biophysics of hair cells. Science, 230(4727), 745752.

[28] Kachar, B., Parakkal, M., Kurc, M., Zhao, Y., & Gillespie, P. G. (2000). High-resolution structure of hair-cell tip links. Proceedings of the National Academy of Sciences of the United States of America, 97(24), 1333613341.

[29] Liu, S., Wang, S., Zou, L., Li, J., Song, C., Chen, J., Hu, Q., Liu, L., Huang, P., & Xiong, W. (2019). TMC1 is an essential component of a leak channel that modulates tonotopy and excitability of auditory hair cells in mice. ELife, 8, e47441.

[30] Fettiplace, R. (2016). Is TMC1 the Hair Cell Mechanotransducer Channel? Biophysical Journal, 111(1), 39.

[31] Qiu, X., & Müller, U. (2018). Mechanically Gated Ion Channels in Mammalian Hair Cells. Frontiers in Cellular Neuroscience, 12.

[32] Giese, A. P. J., Tang, Y.-Q., Sinha, G. P., Bowl, M. R., Goldring, A. C., Parker, A., Freeman, M. J., Brown, S. D. M., Riazuddin, S., Fettiplace, R., Schafer, W. R., Frolenkov, G. I., & Ahmed, Z. M. (2017). CIB2 interacts with TMC1 and TMC2 and is essential for mechanotransduction in auditory hair cells. Nature Communications, 8(1), 43.

[33] Kazmierczak, P., Sakaguchi, H., Tokita, J., Wilson-Kubalek, E. M., Milligan, R. A., Müller, U., & Kachar, B. (2007). Cadherin 23 and protocadherin 15 interact to form tip-link filaments in sensory hair cells. Nature, 449(7158), 8791.

[34] Maeda, R., Kindt, K. S., Mo, W., Morgan, C. P., Erickson, T., Zhao, H., Clemens-Grisham, R., Barr-Gillespie, P. G., & Nicolson, T. (2014). Tip-link protein protocadherin 15 interacts with transmembrane channel-like proteins TMC1 and TMC2. Proceedings of the National Academy of Sciences, 111(35), 1290712912.

[35] Grillet, N., Xiong, W., Reynolds, A., Kazmierczak, P., Sato, T., Lillo, C., Dumont, R. A., Hintermann, E., Sczaniecka, A., Schwander, M., Williams, D., Kachar, B., Gillespie, P. G., & Müller, U. (2009). Harmonin mutations cause mechanotransduction defects in cochlear hair cells. Neuron, 62(3), 375387.

[36] Gillespie, P. G., & Cyr, J. L. (2004). Myosin-1c, the Hair Cells Adaptation Motor. Annual Review of Physiology, 66(1), 521545.

[37] Martin, P., Bozovic, D., Choe, Y., & Hudspeth, A. J. (2003). Spontaneous Oscillation by Hair Bundles of the Bullfrogs Sacculus. The Journal of Neuroscience, 23(11), 45334548.

[38] Tobin, M., Chaiyasitdhi, A., Michel, V., Michalski, N., & Martin, P. (2019). Stiffness and tension gradients of the hair cells tip-link complex in the mammalian cochlea. ELife, 8, e43473.

[39] Zampini, V., Rüttiger, L., Johnson, S. L., Franz, C., Furness, D. N., Waldhaus, J., Xiong, H., Hackney, C. M., Holley, M. C., Offenhauser, N., Fiore, P. P. D., Knipper, M., Masetto, S., & Marcotti, W. (2011). Eps8 Regulates Hair Bundle Length and Functional Maturation of Mammalian Auditory Hair Cells. PLOS Biology, 9(4), e1001048.

[40] Lelli, A., Michel, V., Boutet de Monvel, J., Cortese, M., Bosch-Grau, M., Aghaie, A., Perfettini, I., Dupont, T., Avan, P., El-Amraoui, A., & Petit, C. (2016). Class III myosins shape the auditory hair bundles by limiting microvilli and stereocilia growth. Journal of Cell Biology, 212(2), 231244.

[41] Jacobs, R. A., & Hudspeth, A. J. (1990). Ultrastructural correlates of mechanoelectrical transduction in hair cells of the bullfrogs internal ear. Cold Spring Harbor Symposia on Quantitative Biology, 55, 547561.

[42] Gold, T. (1948). Hearing. II. The physical basis of the action of the cochlea. Proceedings of the Royal Society B: Biological Sciences, 135(881), 492498.

[43] Denk, W., Keolian, R. M., & Webb, W. W. (1992). Mechanical response of frog saccular hair bundles to the aminoglycoside block of mechanoelectrical transduction. Journal of Neurophysiology, 68(3), 927932.

[44] Davis, H. (1983). An active process in cochlear mechanics. Hearing Research, 9(1), 7990.

[45] Manley, G. A. (2000). Cochlear mechanisms from a phylogenetic viewpoint. Proceedings of the National Academy of Sciences, 97(22), 1173611743.

[46] Manley, G. A. (2001). Evidence for an active process and a cochlear amplifier in non-mammals. J. Neurophysiol. 86, 541-549.

[47] Martin, P. and Hudspeth, A.J. (2001). Compressive nonlinearity in the hair bundle's active response to mechanical stimulation. Proc Natl Acad. Sci. USA 98:128101.

[48] David T Kemp (2011). Otoacoustic emissions, their origin in cochlear function, and use. Br. Med. Bull. 63(1): 223-241

[49] W. Fritze (1938). On the frequency-distribution of spontaneous cochlear emissions. HEARING Phys. Bases and Psycho. Phys. Springer

[50] Retzlus, G. (1884). Das Gehororgan der Wirbelthiere. II¿.Das Gehorogan der Reptilien, der Vogel und der Saugethiere. Samson and Wallin, 354.

[51] Ospeck, M., Eguluz, V. M., & Magnasco, M. O. (2001). Evidence of a Hopf Bifurcation in Frog Hair Cells. Biophysical Journal, 80(6), 25972607.

[52] Daibhid O Maoileidigh, Ernesto M. Nicola, and A. J. Hudspeth (2012). The diverse effects of mechanical loading on active hair bundles. Proc. Natl Acad. Sci. USA 109(6): 1943-1948.

[53] Camalet, S., Duke, T., Jülicher, F. and Prost, J. (2000). Auditory sensitivity provided by self-tuned critical oscillations of hair cells. Proc. Natl Acad. Sci. USA 97, 31833188.

[54] Kern, A. and Stoop, R. (2003). Essential role of couplings between hearing nonlinearities. Phys. Rev. Lett. 91,128101

[55] Salvi J.D, Maoileidigh D.O., Fabella B.A., Tobin M., A.J. Hudspeth (2015). Control of a hair bundle's mechanosensory function by mechanical load. Proc Natl Acad. Sci. USA 112(9):E1000-E1009.

[56] Walker, D. P. (1978). Studies in Musical Science in the Late Renaissance. Warburg Institute

[57] Helmholtz, H. L. F (1954). On the Sensations of Tone.

[58] Jaramillo, F., Markin, V. S., Hudspeth, A. J. (1993). Auditory illusions and the single hair cell. Nature 364, 527-529.

[59] Barral, J., Martin, P. (2012). Phantom tones and suppressive masking by active nonlinear oscillations of the hair-cell bundle. Proc. Natl Acad. Sci. USA 109, E1344-E1351.

[60] Hudspeth, A. J. (1992). Hair-bundle mechanics and a model for mechanoelectrical transduction by hair cells. Society of General Physiologists Series, 47, 357370.

[61] Vilfan, A., & Duke, T. (2003). Two Adaptation Processes in Auditory Hair Cells Together Can Provide an Active Amplifier. Biophysical Journal, 85(1), 191203.

[62] Stepanyan, R., & Frolenkov, G. I. (2009). Fast Adaptation and Ca2+ Sensitivity of the Mechanotransducer Require Myosin-XVa in Inner But Not Outer Cochlear Hair Cells. The Journal of Neuroscience, 29(13), 40234034.

[63] Howard, J., & Hudspeth, A. J. (1988). Compliance of the hair bundle associated with gating of mechanoelectrical transduction channels in the Bullfrogs saccular hair cell. Neuron, 1(3), 189199.

[64] Bausch, A. R., & Kroy, K. (2006). A bottom-up approach to cell mechanics. Nature Physics, 2(4), 231238.

[65] Fletcher, D. A., & Mullins, R. D. (2010). Cell mechanics and the cytoskeleton. Nature, 463(7280), 485492.

[66] Pritchard, R. H., Huang, Y. Y. S., & Terentjev, E. M. (2014). Mechanics of biological networks: From the cell cytoskeleton to connective tissue. Soft Matter, 10(12), 18641884.

[67] Saotome, K., Murthy, S. E., Kefauver, J. M., Whitwam, T., Patapoutian, A., & Ward, A. B. (2018). Structure of the mechanically activated ion channel Piezo1. Nature, 554(7693), 481486.

[68] Zhao, Q., Zhou, H., Chi, S., Wang, Y., Wang, J., Geng, J., Wu, K., Liu, W., Zhang, T., Dong, M.-Q., Wang, J., Li, X., & Xiao, B. (2018). Structure and mechanogating mechanism of the Piezo1 channel. Nature, 554(7693), 487492.

[69] Jin, P., Bulkley, D., Guo, Y., Zhang, W., Guo, Z., Huynh, W., Wu, S., Meltzer, S., Cheng, T., Jan, L. Y., Jan, Y.-N., & Cheng, Y. (2017). Electron cryo-microscopy structure of the mechanotransduction channel NOMPC. Nature, 547(7661), 118122.

[70] Zhao, Y., Yamoah, E. N., & Gillespie, P. G. (1996). Regeneration of broken tip links and restoration of mechanical transduction in?hair?cells. Proceedings of the National Academy of Sciences of the United States of America, 93(26), 1546915474.

[71] Hackney, C. M., & Furness, D. N. (2013). The composition and role of cross links in mechanoelectrical transduction in vertebrate sensory hair cells. Journal of Cell Science, 126(8), 17211731.

[72] Oroz, J., Galera-Prat, A., Hervs, R., Valbuena, A., Fernndez-Bravo, D., & Carrin-Vzquez, M. (2019). Nanomechanics of tip-link cadherins. Scientific Reports, 9(1), 13306.

[73] Sotomayor, M., Corey, D. P., & Schulten, K. (2005). In search of the hair-cell gating spring elastic properties of ankyrin and cadherin repeats. Structure (London, England: 1993), 13(4), 669682.

[74] Sotomayor, M., Weihofen, W. A., Gaudet, R., & Corey, D. P. (2010). Structural determinants of cadherin-23 function in hearing and deafness. Neuron, 66(1), 85100.

[75] Sotomayor, M., Weihofen, W. A., Gaudet, R., & Corey, D. P. (2012). Structure of a Force-Conveying Cadherin Bond Essential for Inner-Ear Mechanotransduction. Nature, 492(7427), 128132.

[76] Sakaguchi, H., Tokita, J., Müller, U., & Kachar, B. (2009). Tip links in hair cells: Molecular composition and role in hearing loss. Current Opinion in Otolaryngology & Head and Neck Surgery, 17(5), 388393.

[77] Assad JA, Shepherd GM, Corey DP. Tip-link integrity and mechanical transduction in vertebrate hair cells. Neuron. 1991;7:98594.

[78] Goodyear RJ, Richardson GP. A novel antigen sensitive to calcium chelation that is associated with the tip links and kinocilial links of sensory hair bundles. J Neurosci. 2003;23:487887.

[79] Di Palma, F., Holme, R. H., Bryda, E. C., Belyantseva, I. A., Pellegrino, R., Kachar, B., Steel, K. P., & Noben-Trauth, K. (2001). Mutations in Cdh23, encoding a new type of cadherin, cause stereocilia disorganization in waltzer, the mouse model for Usher syndrome type 1D. Nature Genetics, 27(1), 103107.

[80] Alagramam, K. N., Yuan, H., Kuehn, M. H., Murcia, C. L., Wayne, S., Srisailpathy, C. R., Lowry, R. B., Knaus, R., Van Laer, L., Bernier, F. P., Schwartz, S., Lee, C., Morton,

C. C., Mullins, R. F., Ramesh, A., Van Camp, G., Hageman, G. S., Woychik, R. P., Smith, R. J., & Hagemen, G. S. (2001). Mutations in the novel protocadherin PCDH15 cause Usher syndrome type 1F. Human Molecular Genetics, 10(16), 17091718.

[81] Sotomayor, M., Corey, D. P., & Schulten, K. (2005). In search of the hair-cell gating spring elastic properties of ankyrin and cadherin repeats. Structure (London, England: 1993), 13(4), 669682.

[82] Bartsch, T. F., Hengel, F. E., Oswald, A., Dionne, G., Chipendo, I. V., Mangat, S. S., Shatanofy, M. E., Shapiro, L., Müller, U., & Hudspeth, A. J. (2019). Elasticity of individual protocadherin 15 molecules implicates tip links as the gating springs for hearing. Proceedings of the National Academy of Sciences, 116(22),

[83] Obermayer, B., & Frey, E. (2009). Tension dynamics and viscoelasticity of extensible wormlike chains. Physical Review E, 80(4), 040801.

[84] Yang, S., Witkoskie, J. B., & Cao, J. (2002). Single-molecule dynamics of semiflexible Gaussian chains. The Journal of Chemical Physics, 117(24), 1101011023.

[85] Hallatschek, O., Frey, E., & Kroy, K. (2007). Tension dynamics in semiflexible polymers. Part I: Coarse-grained equations of motion. Physical Review. E, Statistical, Nonlinear, and Soft Matter Physics, 75, 031905.

[86] Hallatschek, O., Frey, E., & Kroy, K. (2007). Tension dynamics in semiflexible polymers. II. Scaling solutions and applications. Physical Review. E, Statistical, Nonlinear, and Soft Matter Physics, 75(3 Pt 1), 031906.

[87] Bockelmann, U., Thomen, Ph., Essevaz-Roulet, B., Viasnoff, V., & Heslot, F. (2002). Unzipping DNA with Optical Tweezers: High Sequence Sensitivity and Force Flips. Biophysical Journal, 82(3), 15371553.

[88] Uyeda, T. Q. P., Iwadate, Y., Umeki, N., Nagasaki, A., & Yumura, S. (2011). Stretching Actin Filaments within Cells Enhances their Affinity for the Myosin II Motor Domain. PLoS ONE, 6(10).

[89] Wu, D. Y., Meure, S., & Solomon, D. (2008). Self-healing polymeric materials: A review of recent developments. Progress in Polymer Science, 33(5), 479522.

[90] Morton, M. (1981). History of Synthetic Rubber. Journal of Macromolecular Science: Part A - Chemistry, 15(7), 12891302.

[91] Staudinger, H. (1920). Über Polymerisation. Berichte Der Deutschen Chemischen Gesellschaft (A and B Series), 53(6), 10731085.

[92] Belgacem MN, Gandini A. Monomers, Polymers and Composites from Renewable Resources. Elsevier; 2011.

[93] Brown, A. E., & Reinhart, K. A. (1971). Polyester Fiber: From Its Invention to Its Present Position. Science, 173(3994), 287293.

[94] M. Doi, S. F. Edwards (1986) The Theory of Polymer Dynamics, Oxford Science Publications

[95] P.G de Gennes, Scaling Concepts in Polymer Physics, (Cornell Univ. Press 1979)

[96] P.J. Flory, Statistical Mechanics of Chain Molecules, (Wiley 1969)

[97] Papadopoulos, G. J., & Thomchick, J. (1977). On a path integral having application in polymer physics. Journal of Physics A: Mathematical and General, 10(7), 11151121.

[98] Vilgis, T. A. (2000). Polymer theory: Path integrals and scaling. Physics Reports, 336(3), 167254.

[99] Clisby, N. (2010). Efficient Implementation of the Pivot Algorithm for Self-avoiding Walks. Journal of Statistical Physics, 140(2), 349392.

[100] Kratky, O., & Porod, G. (1949). Diffuse small-angle scattering of x-rays in colloid systems. Journal of Colloid Science, 4(1), 3570.

[101] Marko, J. F., & Siggia, E. D. (1995). Stretching DNA. Macromolecules, 28(26), 87598770.

[102] M. Rubinstein, Ralph H. Colby (2003) Polymer Physics, Oxford University Press

[103] Rowghanian, P., & Grosberg, A. Y. (2011). Force-Driven Polymer Translocation through a Nanopore: An Old Problem Revisited. The Journal of Physical Chemistry B, 115(48), 1412714135.

[104] Flory, P. J., J. Chem. Phys. 17, 303 (1949)

[105] Flory, P. J., Principles of Polymer Chemistry. Cornell Univ. Press, Ithaca (1953)

[106] Clisby, N. (2010). Accurate Estimate of the Critical Exponent v for Self-Avoiding Walks via a Fast Implementation of the Pivot Algorithm. Physical Review Letters, 104, 055702.

[107] Guillou, J. C. L., & Zinn-Justin, J. (1985). Accurate critical exponents from the ?-expansion. Journal de Physique Lettres, 46(4), 137141.

[108] Spakowitz, A. J., & Wang, Z.-G. (2005). End-to-end distance vector distribution with fixed end orientations for the wormlike chain model. Physical Review E, 72(4), 041802.

[109] Broedersz, C. P., & MacKintosh, F. C. (2014). Modeling semiflexible polymer networks. Reviews of Modern Physics, 86(3), 9951036.

[110] L. D. Landau and E. M. Lifshitz, Statistical Physics, Part 1, 3rd ed. Pergamon Press, 1988.

[111] Wilhelm, J., & Frey, E. (1996). Radial Distribution Function of Semiflexible Polymers. Physical Review Letters, 77.

[112] Spakowitz, A. J., & Wang, Z.-G. (2004). Exact Results for a Semiflexible Polymer Chain in an Aligning Field. Macromolecules, 37(15), 58145823.

[113] Mehraeen, Shafigh, Bariz Sudhanshu, Elena F. Koslover, and Andrew J. Spakowitz. End-to-End Distribution for a Wormlike Chain in Arbitrary Dimensions. Physical Review E 77, no. 6 (June 9, 2008): 061803.

[114] Petrosyan, R. (2017). Improved approximations for some polymer extension models. Rheologica Acta, 56(1), 2126.

[115] A. Grosberg, A. Khokhlov (1994) Statistical Physics of Macromolecules, AIP Press

[116] E. Engel, R.M. Dreizler, Density Functional Theory, Theoretical and Mathematical Physics, pp. 403531 (2011)

[117] Hou, T. Y., Luo, W., Rozovskii, B., Zhou, H.-M. (2006). Wiener Chaos expansions and numerical solutions of randomly forced equations of fluid mechanics. Journal of Computational Physics, 216(2), 687706.

[118] Hinczewski, M., Schlagberger, X., Rubinstein, M., Krichevsky, O., & Netz, R. R. (2009). End-monomer Dynamics in Semiflexible Polymers. Macromolecules, 42(3), 860875.

[119] Wang, M. D., Yin, H., Landick, R., Gelles, J., & Block, S. M. (1997). Stretching DNA with optical tweezers. Biophysical Journal, 72(3), 13351346.

[120] Kojima, H., Ishijima, A., & Yanagida, T. (1994). Direct measurement of stiffness of single actin filaments with and without tropomyosin by in vitro nanomanipulation. Proceedings of the National Academy of Sciences, 91(26), 1296212966.

[121] Siemens, J., Lillo, C., Dumont, R. A., Reynolds, A., Williams, D. S., Gillespie, P. G., & Müller, U. (2004). Cadherin 23 is a component of the tip link in hair-cell stereocilia. Nature, 428(6986), 950955.

[122] Sotomayor, M., & Schulten, K. (2008). The Allosteric Role of the Ca2+ Switch in Adhesion and Elasticity of C-Cadherin. Biophysical Journal, 94(12), 46214633.

[123] Dionne, G., Qiu, X., Rapp, M., Liang, X., Zhao, B., Peng, G., Katsamba, P. S., Ahlsen, G., Rubinstein, R., Potter, C. S., Carragher, B., Honig, B., Müller, U., & Shapiro, L. (2018). Mechanotransduction by PCDH15 Relies on a Novel cis-Dimeric Architecture. Neuron, 99(3), 480-492.e5.

[124] Obermayer, B., Hallatschek, O., Frey, E., & Kroy, K. (2007). Stretching dynamics of semiflexible polymers. The European Physical Journal E, 23(4), 375388.

[125] Travis E. Oliphant. A guide to NumPy, USA: Trelgol Publishing, (2006)

[126] Moore, E. H. (1920). "On the reciprocal of the general algebraic matrix". Bulletin of the American Mathematical Society. 26 (9): 39495.

[127] Araya-Secchi, R., Neel, B. L., & Sotomayor, M. (2016). An elastic element in the protocadherin-15 tip link of the inner ear. Nature Communications, 7.

[128] Warren, R. L., Ramamoorthy, S., Ciganovi?, N., Zhang, Y., Wilson, T. M., Petrie, T., Wang, R. K., Jacques, S. L., Reichenbach, T., Nuttall, A. L., & Fridberger, A. (2016). Minimal basilar membrane motion in low-frequency hearing. Proceedings of the National Academy of Sciences, 113(30), E4304E4310.

[129] Zheng J, Shen W, He DZ, Long KB, Madison LD, Dallos P. Prestin is the motor protein of cochlear outer hair cells. Nature. 2000;405(6783):149-155.

[130] Kozlov, A. S., Andor-Ard, D., Hudspeth, A. J. (2012). Anomalous Brownian motion discloses viscoelasticity in the ears mechanoelectrical-transduction apparatus. Proceedings of the National Academy of Sciences, 109(8), 28962901.

[131] Chim, Y. H., Mason, L. M., Rath, N., Olson, M. F., Tassieri, M., Yin, H. (2018). A one-step procedure to probe the viscoelastic properties of cells by Atomic Force Microscopy. Scientific Reports, 8(1), 14462.

[132] Adalja, S. B., Otaigbe, J. U., Thalacker, J. (2001). Glass-polymer melt hybrids. I: Viscoelastic properties of novel affordable organic-inorganic polymer hybrids. Polymer Engineering and Science, 41(6), 10551067.

[133] Oppenheim, Alan V.; Schafer, Ronald W.; Buck, John R. (1999). Discrete-time signal processing (2nd ed.). Upper Saddle River, N.J.: Prentice Hall. ISBN 0-13-754920-2

[134] Trotter, H. F. "An Elementary Proof of the Central Limit Theorem." Arch. Math. 10, 226-234, 1959.

[135] Shreve, S. (2004). Stochastic Calculus for Finance II: Continuous-Time Models. Springer-Verlag

[136] Grigolini, P., Rocco, A., & West, B. J. (1999). Fractional calculus as a macroscopic manifestation of randomness. Physical Review E, 59(3), 26032613.

[137] Li, T., & Raizen, M. (2013). Brownian motion at short time scales. Annalen Der Physik, 525.

[138] Chepizhko, O., & Peruani, F. (2013). Diffusion, Subdiffusion, and Trapping of Active Particles in Heterogeneous Media. Physical Review Letters, 111(16), 160604.

[139] Flynn, C. 2019. "Fractional Brownian Motion Realizations". PyPi

[140] Krapf, D., Lukat, N., Marinari, E., Metzler, R., Oshanin, G., Selhuber-Unkel, C., Squarcini, A., Stadler, L.-M., Weiss, M., Xu, X. (2019). Spectral Content of a Single Non-Brownian Trajectory.

[141] Reichenbach, T., & Hudspeth, A. J. (2010). Dual Contribution to Amplification in the Mammalian Inner Ear. Physical Review Letters, 105(11), 118102.

[142] Smith, S. B., Finzi, L., Bustamante, C. *Science* 1992, 258, 1122

[143] Seol, Y., Li, J., Nelson, P. C., Perkins, T. T., & Betterton, M. D. (2007). Elasticity of Short DNA Molecules: Theory and Experiment for Contour Lengths of 0.67 $\mu$m. Biophysical Journal, 93(12), 43604373.

[144] Kumaki, J. Observation of polymer chain structures in two-dimensional films by atomic force microscopy. Polym J 48, 314 (2016).

[145] Price, A. C., Pilkiewicz, K. R., Graham, T. G. W., Song, D., Eaves, J. D., & Loparo, J. J. (2015). DNA Motion Capture Reveals the Mechanical Properties of DNA at the Mesoscale. Biophysical Journal, 108(10), 25322540.

[146] J. C. Kluyver, A local probability problem. In: Royal Netherlands Academy of Arts and Sciences, Proceedings, 8 I, 1905, pp. 341350.

[147] Borwein, J. M., Straub, A., Wan, J., Zudilin, W., & Zagier, D. (2012). Densities of Short Uniform Random Walks. Canadian Journal of Mathematics, 64(5), 961990.

[148] Werner Krauth, Algorithms and Computations, 2006, Oxford University Press

[149] Sommer, S., Arnaudon, A., Kühnel, L., Joshi, S. 2017, September 14. Bridge Simulation and Metric Estimation on Landmark Manifolds.

[150] Arfken, G. "Inverse Laplace Transformation." 15.12 in Mathematical Methods for Physicists, 3rd ed. Orlando, FL: Academic Press, pp. 853-861, 1985.

[151] Baumann, H. (2019). Generalized continued fractions: A unified definition and a Pringsheim-type convergence criterion. Advances in Difference Equations, 2019(1), 406.

[152] J. F. Mahoney, B. D. Sivazlian, Partial fractions expansion: a review of computational methodology and efficiency, Journal of Computational and Applied Mathematics, Vol. 9, 1983.

[153] Rouse, J. Chem. Phys. 21, 1273 (1953)

[154] Bender, C. M., & Orszag, S. A. (1999). Advanced Mathematical Methods for Scientists and Engineers I: Asymptotic Methods and Perturbation Theory. Springer-Verlag.

[155] Davies, Robert B., and D. S. Harte. Tests for Hurst effect. Biometrika 74, no. 1 (1987): 95-101.

[156] Bartsch, T. F., & Hudspeth, A. J. (2018). A New Twist on Tip Links. Neuron, 99(3), 423425.